THESE

En vue de l'obtention du

DOCTORAT DE L'UNIVERSITÉ DE TOULOUSE

Délivré par :
Institut National Polytechnique de Toulouse (INP Toulouse)

Discipline ou spécialité :
Énergétique et transferts

Présentée et soutenue par :
Matthieu LEYKO
Le 21/05/2010

Titre :
Mise en œuvre et analyse de calculs aéroacoustiques de type SGE pour la prévision du bruit de chambres de combustion aéronautiques

---

Ecole doctorale :
Mécanique, Energétique, Génie civil et Procédés (MEGeP)

Unité de recherche :
CERFACS

Directeur(s) de Thèse :
Thierry POINSOT (Directeur de Recherche à l'IMF de Toulouse)
Co-directeur : Franck NICOUD (Professeur à l'Université Montpellier II)

Rapporteurs :
Sébastien CANDEL (Professeur à l'Ecole Centrale Paris)
Christophe BAILLY (Professeur à l'Ecole Centrale Lyon)

Autre(s) membre(s) du jury :
Friedrich BAKE (Dr-Ing. au DLR de Berlin, Allemagne)
Wolfgang SCHROEDER (Professeur à l'Université de Aachen, Allemagne)
Stéphane MOREAU (Professeur à l'Université de Sherbrooke, Canada)
Alexandre VUILLEMIN (Ingénieur à SNECMA Villaroche)

Résumé

Une part importante du bruit généré par les moteurs d'avion est liée à la combustion. Afin de réduire cette source de bruit, une compréhension fine des phénomènes associés est nécessaire. Deux mécanismes générateurs de bruit, et ayant pour origine la combustion, ont été identifié dans les moteurs d'avions dans les années 1970: un premier mécanisme dit direct, qui est lié directement à un dégagement de chaleur instationnaire, et l'autre dit indirect qui est lié aux interactions entre les étages de turbine et les fluctuations de température en sortie de chambre, également produites par la combustion. Des méthodes analytiques et des simulations numériques sont utilisées ici à la fois pour montrer l'importance du bruit de combustion indirect par rapport au bruit direct, et pour donner des limites de validité des approches analytiques qui sont basées sur l'hypothèse de tuyère compacte. Trois configurations différentes sont étudiées dans un premier temps: une tuyère quasi-1-D, une tuyère axi-symétrique 2-D, ainsi qu'une aube de turbine 2-D. Finalement, un secteur de chambre de combustion 3-D réelle (SNECMA) est calculé à l'aide de la Simulation aux Grandes Echelles. Les fluctuations en sortie du brûleur sont utilisées pour évaluer le bruit total généré par la combustion (direct et indirect) à l'aide des approches analytiques précédemment étudiées. **Mots clefs : Bruit de combustion, bruit indirect, tuyères compactes, Simulation aux Grandes Echelles.**

Abstract

An important part of the noise generated by aero-engines is caused by the combustion. To decrease this source of noise, a precise comprehension of the underlying phenomenon is required. Two different mechanisms generating noise in aero-engines because of the combustion have been identified in the 1970's: the direct mechanism that is directly related to the unsteady heat release, and the indirect one that is caused by the interactions between the turbine stages and the temperature fluctuations also produced by the combustion. Analytical methods and numerical simulations are used here both to show the importance of the indirect combustion noise compared with the direct one, and to provide some validity limits of compact nozzles analytical approaches. Three different configurations dealing with indirect noise are investigated: quasi-1-D nozzle, axisymmetric 2-D nozzle and 2-D turbine blade. Finally, an actual 3-D combustion chamber sector (SNECMA) is addressed with Large-Eddy Simulation. Fluctuations at the outlet of the combustor are used to compute the overall noise caused by the combustion (direct and indirect), by means of the investigated analytical models. **Keywords: Combustion noise, indirect noise, compact nozzles, Large-Eddy Simulation.**

Contents

Acknowledgements

Acknowledgements / Remerciements

Je remercie chaleureusement Friedrich Bake, Wolfgang Schroeder, Stéphane Moreau, Christophe Bailly et Sébastien Candel d'avoir participé à l'évaluation de cette thèse. Je voudrais en particulier remercier Christophe Bailly et Sébastien Candel pour l'examen du manuscrit. J'ai été vraiment honoré par la présence de ces grands noms dans mon jury de thèse.

Un grand merci à Jean-Claude André pour m'avoir accueilli au sein du CERFACS, ainsi qu'à Thierry Poinsot (directeur de thèse), Franck Nicoud (co-directeur de thèse) et (last but not least) Stéphane Moreau (coco ... directeur de thèse) pour leurs encadrements. Merci à tous les trois pour vos conseils avisés tout au long de ces trois ans (bon d'accord : trois ans et huit mois).

Merci également à l'équipe de l'administration, Chantal Nasri, Michèle Campasens et Marie Labadens pour la gestion de toutes ces tâches qui me dépassent. Merci à l'équipe du support informatique toujours souriante et super efficace, j'ai nommé Patrice Laporte, Fabrice Fleury, Gérard Déjean et Isabelle d'Ast.

Merci à l'équipe acoustique de Snecma avec le chef d'orchestre Maxime Lebrun, l'acousticien chevronné Guillaume Bodard, la Fan d'harmoniques complexes Hélène Posson et Alexandre Vuillemin qui m'a encadré durant ces trois ans sans fausses notes.

Je tiens à remercier tous les doctorants et post-doctorants du Cerfacs avec qui j'ai pu échanger, passer du bon temps, courir, faire du roller, du badminton, du vélo, des flammes de diffusion, liftées, puis prémélangées; des plus jeunes aux moins jeunes, Ignacio Duran, David Barré, Elena Collado, Fabien Wlassow, Benedetta Franzelli, Stéphane Jauré, Elsa Gullaud, Camillo Silva, Kerstin Wieczorek, Jorge Amaya, Claude Sensiau, Jacques Lavedrine, Guillaume Boudier, Thomas Schmidt, Marta Garcia, Matthieu Boileau, Sébastien Roux, Alois Sengissen, Mauro Porta, Laurent Benoit, Eleonor Riber, Antoine Dauptain, Gabriel Staffelback, Olivier Vermorel.

Une spéciale dédicace aux personnes des "algecos", Marlène Sanjosé qui rendait ces lieux si "vivant" et l'imperturbable Felix Jeagle, l'athlétique Guilheme Lacaze et son collègue de flamme épaissie Benoit Enaux, le globe-trotteur Olivier Cabrit et la bête de travail Jean-Mathieu Soener.

Un grand merci à mes trois collègues de bureau (et assimilés) Anthony Roux, Florant Duchaine et Nicolas Lamarque. Merci à vous, et à vos femmes respectives Anne, Mélanie et

Lara, pour avoir supporté mes nombreuses séances de questions, mes expérimentations farfelues, et le plus dur : mes "blagues" ("dans le cosson ... tout est bon !"). Ce fut un grand plaisir de partager ces trois années avec vous, à la fois pour la science et la rigolade.

Je remercie mon père, ma mère et mon frère Jacky d'avoir cru en moi et de m'avoir supporté pendant les moments difficiles. Enfin, un grand merci à Manu qui a énormément participé à ce travail, de manière "directe" et "indirecte" ;-), et c'est intégralement à elle (de moins l'infini à plus l'infini) que je dédie cette thèse.

List of symbols

Roman letters

$\dot{Q}$	global heat release rate, W
$\dot{q}$	heat release rate, $W.m^{-3}$
ℓ_{in}	length of the EWG inlet duct
ℓ_{out}	length of the EWG outlet duct
ℓ_n	nozzle length, m
ℓ_x	axial blade length, m
$\vec{k}$	wave vector
$\dot{m}$	mass flow rate, $kg.s^{-1}$
$\mathcal{A}$	cross-section area, m^2
$\mathcal{E}$	efficiency function
$\mathcal{F}$	thickening factor
$\mathcal{R}$	reflection coefficient
$\mathcal{S}$	flame sensor
$\mathcal{Y}$	acoustic admittance
$\mathcal{Z}$	acoustic impedance
A	acoustic power
P	vector of primitive variables for CHORUS
W	vector of characteristic variables (waves)
w^-	upstream propagating acoustic wave

w^+	downstream propagating acoustic wave
w^{S}	entropy wave
w^{V}	vorticity wave
A	pre-exponentional factor, $c.g.s$
c	speed of sound, $m.s^{-1}$
c_p	specific heat at constant pressure, $J.kg^{-1}.K^{-1}$
c_v	specific heat at constant volume, $J.kg^{-1}.K^{-1}$
E	specific energy, $J.kg^{-1}$
e	specific sensible energy, $J.kg^{-1}$
E_a	activation energy, $J.mol^{-1}$
f	frequency, Hz
f_0	reference frequency, Hz
h	specific enthalpy, $J.kg^{-1}$
i	the standard imaginary unit ($i^2 = -1$)
$J_{j,k}$	j-th component of the diffusive molecular flux for species k, $mol.s^{-1}.m^{-2}$
K	dimensionless wave vector
k	wave vector magnitude (in part II and III)
K_f	forward reaction constant
K_r	reverse reaction constant
K_{eq}	equilibrium constant
L	transformation matrix primitive-to-characteristic (in Chap. 5)
L_x	blade spacing, m
L_y	blade spacing, m
M	number of reactions
N	number of species
N_B	number of burners
N_k	number of frequencies

N_P	number of temporal portions
N_t	number of periods
p	pressure, Pa
p_t	stagnation pressure, Pa
q_j	j-th component of the diffusive heat flux, $W.m^{-2}$
Q_r	radiation energy source term, $W.m^{-3}$
R	mean radius, m
R	transformation matrix characteristic-to-primitive (in Chap. 5)
r	radius (in part II and III), m
r	specific gas constant, $J.kg^{-1}.K^{-1}$
s	specific entropy, $J.kg^{-1}.K^{-1}$
S_{ij}	strain rate tensor, s^{-1}
$S_{l,0}$	laminar flame speed, $m.s^{-1}$
S_{xx}	power spectral density
S_{xy}	cross-spectral density
T	temperature, K
t	time, s
t_d	time delay for fluid-particles, s
T_t	stagnation temperature, K
U	vector of conservative variables
u	axial velocity, $m.s^{-1}$
u_i	i-th component of the velocity vector, $m.s^{-1}$
V	vector of primitive variables
v	transversal velocity, $m.s^{-1}$
V_n	vector of primitive variables normal to the boundary
W	molar mass (in Chap. 2 and 3), $kg.mol^{-1}$
w	magnitude of the velocity, $m.s^{-1}$

X	molar fraction
x	axial space coordinate, m
Y	mass fraction
y	space coordinate, m
z	space coordinate, m

Greek letters

α	angle in the circumferential direction, rad
β	blade row model constant
β'	flame sensor constant
δ	Dirac delta distribution
δ_{ij}	Kronecker's delta
δ_l	laminar flame thickness, m
$\dot{\omega}_k$	production rate of species k, $kg.m^{-3}.s^{-1}$
η	ratio between the indirect and the direct combustion noise
Γ	pseudo-reaction rate constant
γ	specific heats ratio
Γ_{xy}	coherence function
κ	relaxation coefficient, s^{-1}
λ	heat conduction coefficient, $W.m^{-1}.K^{-1}$
μ	dynamic viscosity, $N.m^2.s$
ν	angle of the vector wave, rad
ν	kinematic viscosity, $m^2.s^{-1}$ (in part I)
ν''_{kj}	reverse stochiometric coefficient
ν'_{kj}	forward stochiometric coefficient
ν_{kj}	global stochiometric coefficient
ν_t	kinematic turbulent sub-grid scale viscosity, $m^2.s^{-1}$
Ω	dimensionless angular frequency (in Chap. 7)

Ω	pseudo-reaction rate
ω	angular frequency, $rad.s^{-1}$
$\dot{\omega}_T$	chemical heat release rate, $W.m^{-3}$
ϕ	local equivalence ratio
ψ	POD eigenfunction
ρ	mass density, $kg.m^{-3}$
ρ_e	excess mass density, $kg.m^{-3}$
τ	relaxation time of an entropy pulse, s
τ_0	reference period, s
τ_{ij}	component i,j of the stress tensor, Pa
Θ	dimensionless temperature
θ	angle in the transversal direction, rad
ξ'	vorticity fluctuation, s^{-1}

Dimensionless numbers

$\mathcal{M}$	Mach number
Pr	Prandtl number
Re	Reynolds number
Sc	Schmidt number

Operators

$\hat{\hat{f}}$	double Fourier-tranform
$\hat{f}$	Fourier-tranform
$\langle \cdot \rangle$	spatial integration
$\overline{f}$	Reynolds average
$\widetilde{f}$	Favre filtering

Subscripts

∞	quantity taken at infinity
F	related to the fuel

O	related to the oxidizer

Superscripts

$'$	related to the temporal fluctuation
I	inviscid terms
t	turbulent sub-grid scale contribution
V	viscous terms

Abbreviations

ACARAE	Advisory Council for Aeronautics Research in Europe
BC	Boundary Condition
CFD	Computational Fluid Dynamics
CFL	Courant-Friedrichs-Lewy
CRZ	Central Recirculating Zone
DAC	Dual Annular Combustor
DLR	Deutsches zentrum für Luft- und Raumfahrt
DNS	Direct Numerical Simulation
DTF	Dynamically Thickened Flame
EPN	Effective Perceived Noise
EWG	Entropy Wave Generator
HPC	High-Pressure Compressor
HPT	High-Pressure Turbine
HPTN	High-Pressure Turbine Nozzle
ICAO	International Civil Aviation Organization
LES	Large-Eddy Simulation
LODI	Local One-Dimensional Inviscid
LPC	Low-Pressure Compressor
LPT	Low-Pressure Turbine
LW	Lax-Wendroff

NS	Navier-Stokes
NSCBC	Navier-Stokes Characteristic BC
PFT	Pressure in the Flame Tube
POA	Pressure in the Outer Annulus
POD	Proper Orthogonal Decomposition
PSD	Power Spectral Density
PVC	Precessing Vortex Core
RANS	Reynolds Averaged Navier-Stokes
RMS	Root Mean Square
SAC	Single Annular Combustor
SPL	Sound Pressure Level
SRA	Strategic Research Agenda
TF	Thickened Flame
TFLES	Thickened Flame model for LES
TTG	Two-step Taylor-Galerkin

Chapter 1

General introduction

The weakest sound that can be perceived by a young human commonly reaches a pressure level of 2×10^{-5} Pa, and this value constitutes the basis to the noise measurements (0 dB). On the opposite side, the pressure level encountered by a person working with a jackhammer, or during a rock concert, can reach 20 Pa (120 dB). From this level, sound is considered as painful [101]. With regards to the high sensibility of the human hearing (more than six order of magnitude), the nowadays intense acoustic environment have inevitably an important impact on human health and life quality. Beyond the possible permanent hearing loss involved by very loud sounds, regular exposure to moderate noise level can have influence on health, as well as mental capacities. As highlighted in [120], children chronically exposed to aircraft noise have significant deficits in reading, and chronic noise may also lead to deficits in children's speech acquisition [44].

1.1 Noise regulation

According to the projections of the International Civil Aviation Organization (ICAO) [53], the air traffic (number of departures and flown distance) is expected to more than double over the 2005-2025 period. This traffic directly leads to increase the annoyance felt by the population leaving in the vicinity of airports. Since more than 30 years, the ICAO designs standards related to aircraft noise, in order to anticipate the developpement of the civil aviation, and then to propose economically feasible emission rules (noise and pollutant).

In concertation with ICAO and the aeronautic industry, the Advisory Council for Aeronautics Research in Europe (ACARE) proposes objectives related to the emissions reduction (Strategic Research Agenda - SRA), and the current ones are to reduce noise per aircraft of 10 EPNdB[1]

---

[1] Effective Perceived Noise in Decibels (EPNdB) is an annoyance based certification metric. It accounts for human response to spectral shape, intensity, tonal content and duration of noise from an aircraft. EPNdB cannot be directly measured, and has to be evaluated in a standard manner (Annex 16 of the ICAO standards).

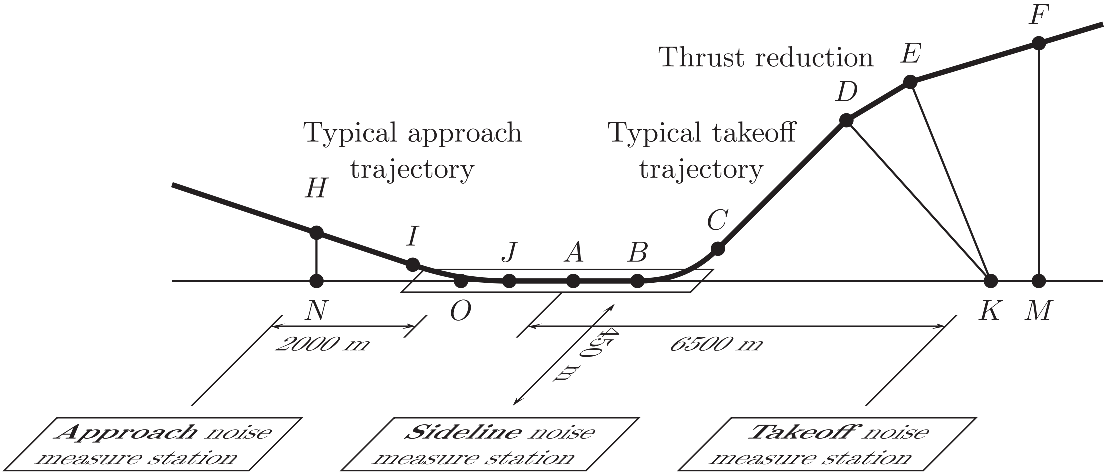

Figure 1.1 - *Positions of the three points of measurements for the noise certification.*

over the 2001-2020 period. Manufacturers are strongly involved in reaching these objectives, and deploy numerous research activities to handle these points.

Although, the regulation authorities (ICAO) define maximum noise levels[2], it concerns the whole aircraft and there is no individual certification for the engine. The propulsion system manufacturer performs his own noise measurements (see Fig.1.2) in collaboration with the aircraft manufacturer, but there isn't acoustic regulation specifically for the engine (just for the entire aircraft), even if it represents the main source of noise. The noise caused by the airframe (high-lift devices, landing gears, etc.) is in the order of the one generated by the engine at approach, but it is clearly prevalent at takeoff (see Fig. 1.1).

1.2 Noise sources in turbofans

The jet has been the major source of noise of turbojets, but it has strongly decreased using turbofans with high bypass ratio[3]. The jet-noise scales as the jet velocity to the power of height, so that slower, but with a greater mass-flux, exhaust gases have a benefit effect on the noise reduction. Nowadays, the addition of *mixers* and *plugs* also participates in reducing the noise generated by the engine. The theoretical background in this field has been investigated during many decades and it is quite mature, even if a lot of new technologies are coming like micro-jets control, that rise new challenges.

The large fans used on the current engine are also important sources of noise, essentially at

---

[2] The current standard is related to ICAO Appendix 16, Volume 1, Chapter 4. The three certification points are concerned (see Fig. 1.1) depending on the commissioning date of the aircraft, as well as the weight of the aircraft and type of the motorization (two turbojets, four turbojets, etc.)

[3] The ratio between the primary and the secondary fluxes (see Fig. 1.4)

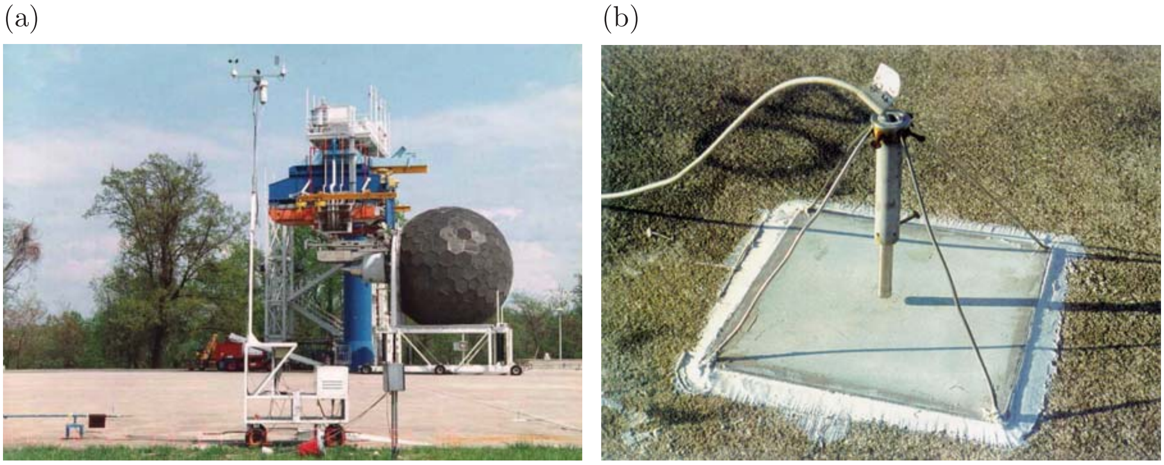

Figure 1.2 - *(a) Engine equipped with flow-straighter during acoustic measurements, and (b) one of the microphone mounted on the ground all around the engine.*

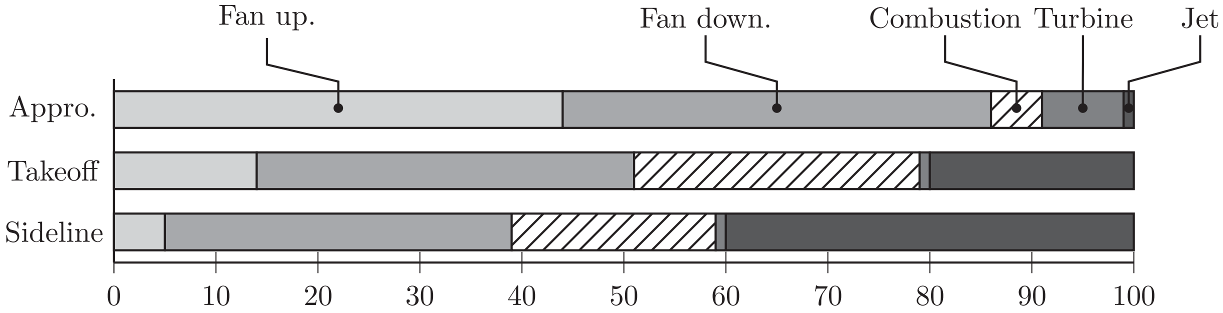

Figure 1.3 - *Example of the repartition of the acoustic power of the different noise sources in percent (A320/CFM56-5B). Combustion noise in hatched style.*

takeoff. Acoustic treatment on the interior of the nacelles and optimization of the design of the fan blades and engine cycle make this source of noise smaller but it can generate a very strong tonal sound. Turbines generate a very specific sound (because of the rotation speed and the blade clocking) and appear to be the less important source. The combustion noise is not the major source of noise, but it is clearly not negligible (see Fig. 1.3).

1.3 Combustion noise

Combustion noise participates to the global noise of the engine, but is not the main source for the moment, as mentioned in Sec. 1.2. The noise caused by the combustion *stricto sensu* is actually not known, and it is often obtained subtracting the other sources from global noise of the engine. That is the reason why one often talk of *core noise* and not of *combustion noise* since detailed measurements of the pure noise generated by the combustion are generally not

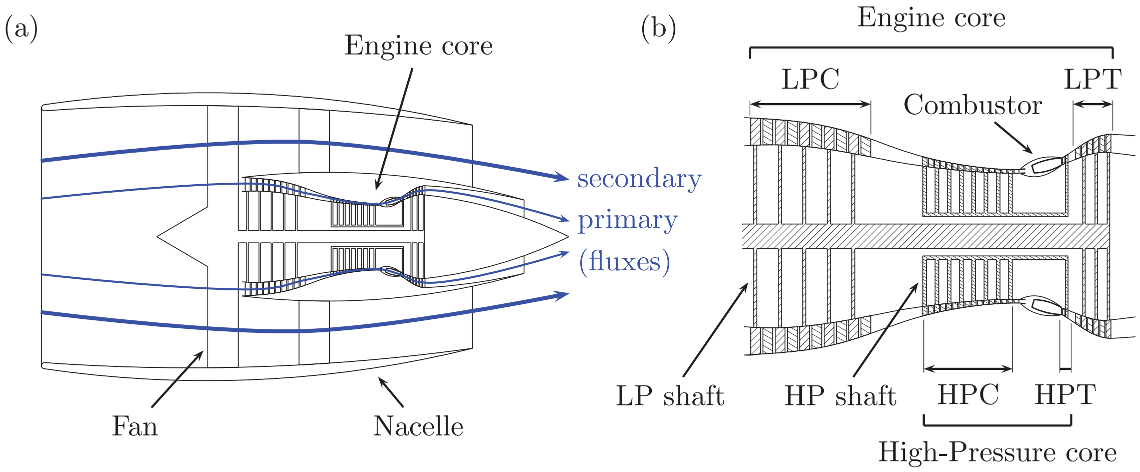

Figure 1.4 - *(a) Schematic diagram of a two-shaft high-bypass-ratio turbofan engine. (b) Details of the engine core: HPC and HPT stand for High-Pressure Compressor and Turbine, whereas LPC and LPT stand for Low-Pressure devices.*

available. The engine manufacturer generally uses simple empirical laws (based on numerous engines and operating conditions) to evaluate the combustion noise, mainly because it is not well understood. These relations mostly show that the combustion produces a low-frequency (100-1000 Hz) broadband noise. This kind of laws, providing the acoustic power A_{360} in the outlet plane of the combustor, can for instance be written (SNECMA):

$$\mathrm{A}_{360} = 10\log(\dot{m}_{360}) + 20\log\left(\frac{T_{400} - T_{300}}{T_{300}}\, p_{300}\right) - 0.4 \tag{1.1}$$

where $\dot{m}$, T and p are respectively the mass flow rate, the temperature and pressure. Subscripts 300, 360 and 400 respectively stand for HPC outlet, combustor inlet and combustor outlet (see Fig. 1.4). It is then assumed for instance that each turbine stage leads to a noise attenuation of about 2 dB. Therefore, only passive treatment of the combustion noise is nowadays under development. Figure 1.5 shows such acoustic absorbents (for both combustion and turbine noise) that could eventually equip nozzle centre plugs of turbofans [54].

Few actual evaluations of the core noise, based on a theoretical background, can be found in the literature [19, 37, 85, 49], and it appears from these studies that the main source of noise generated by the engine core is not caused directly by the combustion process itself (direct combustion noise), but to the interaction between the temperature fluctuations, also produced by the combustion, and the turbine stages (indirect combustion noise). However, it is still not clear if this statement is correct because of the assumptions made to achieve core noise evaluation in a theoretical framework.

1.4 Motivations and objectives of the thesis

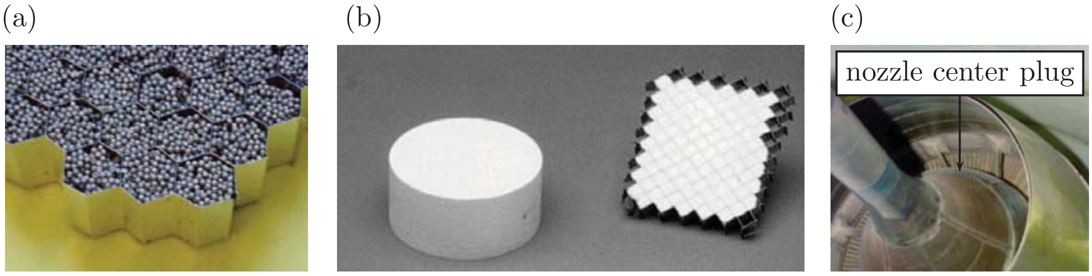

Figure 1.5 - *(a) Acoustic absorbent made of micro-balls. (b) Acoustic absorbent made of ceramic foam. (c) Prototype of an acoustically treated nozzle centre plug reducing turbine and combustion noise.*

In the 1990's, the new emissions regulation has led to the introduction of low-NO_x combustion chambers. The reduction of NO_x emissions (also regulated by ICAO) has been achieved using dual annular combustor (DAC) instead of the standard single annular combustor (SAC): both are depicted in Fig. 1.6. The pilot stage is optimized to operate lightly-loaded as required for idle, altitude re-light and start-up engine conditions, whereas the main stage is optimized for high-loaded conditions [41]. The first acoustic measurements on the CFM56-B engine equipped with the above-mentioned low-NO_x combustor, show that the former exhibits much more noise than SAC [49]. The engines operating with DAC were noisier of about 5-8 dB than SAC for part load operation (approach), and about 10-15 dB SPL for some peaks in the spectrum and there were almost no differences for fully-loaded operation (sideline and takeoff). It has led to a missed attempt of acoustic certification of the Airbus 319. More generally, it was observed that low-NO_x combustors are noisier than the standard ones [49].

This example shows how the design of the engine already is, and is going to be more and more challenging. On one hand there is a strong will and need to reduce the emissions of NO_x (80% before 2020 according to the ACARE SRA), and on the other hand noise emissions have to be reduced of 10 EPNdB. The new concepts of combustor could have a very important impact on the noise emissions as mentioned previously, and thus they also have to be handled at the development stage of an acoustic point of view, and not only in a passive manner. Even if the core noise is not nowadays the main source of noise, the potential impact on the acoustic emissions of the engine has first to be controlled with regards to the improvements made on the combustion (pollutant emission), before dealing with the core noise reduction.

It is clear that the methods available for the evaluation of the noise due to the combustion mentioned in Sec. 1.3 are not able to deal with such technological effects. Geometrical details of the combustor have to be taken into account, as well as unsteady behavior of the phenomena inherent to the combustion process. Therefore, Large-Eddy Simulation (LES) has been selected to solve the reacting flow within the combustion chamber. Especially, the aim of this PhD thesis is to investigate the relations between the direct and the indirect noise mentioned in Sec. 1.3 and to provide a high-fidelity method to address core noise generation with LES.

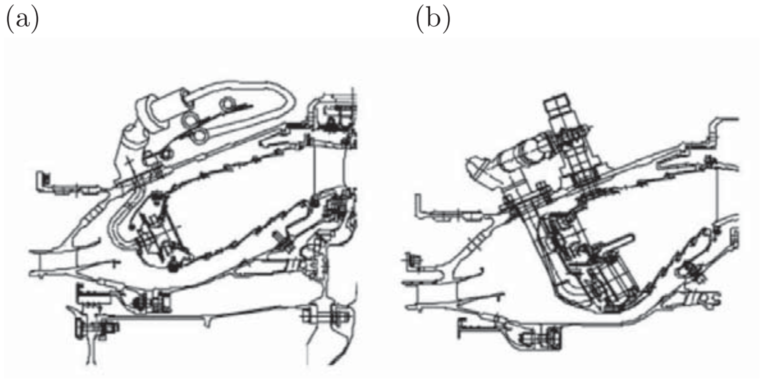

Figure 1.6 - *(a) Single annular combustor (SAC), (b) Dual annular low-NO_x combustor (DAC) of CFM56 engine.*

1.5 Organization of the document

This manuscript is organized into three different parts which present first the numerical tool used for this thesis, then theoretical aspects of the combustion noise in aero-engines and finally an application of the developed method on an actual combustor (see Fig. 1.7 for more details):

- The first part describes the numerical solver AVBP used in the second and the third part. The general equations are presented followed by the modelling underlying the LES approach: the sub-grid scale model is detailed as well as the combustion one. Finally, the boundary conditions and their acoustic behaviour are described, since the reflection coefficients need to be control precisely in the second part. This part is mainly numerical so that readers interested only in combustion noise can begin reading at Part II.
- The theoretical aspects of combustion noise are addressed in the second part. It is especially focusing on the noise generation (indirect noise) and transmission (direct noise) through the turbine. A comparison between the mentioned direct and indirect combustion noise is performed in a first step in a well-defined theoretical framework (a one-dimensional model combustor). The indirect combustion appearing as major source of noise for aero-engine operating conditions, the second section of this part is dedicated to the investigation of the indirect combustion noise in a mainly one-dimensional nozzle. Numerical and analytical calculations are performed and compared with an experimental set-up operated at the DLR. The theoretical method, based on the work of Marble and Candel [70], provides good results which proves that such approaches can be used for aero-engines. Therefore in the last section of this part, simulations are performed to investigate more elaborated analytical models for an actual turbine device: an isolated turbine blade nozzle. The analytical model of Cumpsty and Marble [37] is compared with two-dimensional simulations and a good agreement is found for low frequencies, as expected from the assumptions required for such approaches.
- The last part is dedicated to the development and the application of a method to evaluate

the noise caused by the combustion in an actual aeronautical combustor. The tool based on this method is called CHORUS. The combustor investigated here is fed with kerosene, so that the chemical scheme to handle this fuel is first presented. Large-Eddy Simulation of a single burner is performed with AVBP and the main fluctuations are extracted using CHORUS. CHORUS also integrates the analytical model [37] investigated in the second part to evaluate direct and indirect noise. Results show that indirect noise is still the main source of noise and an estimation of the acoustic power at the outlet of the high-pressure turbine nozzle is provided.

The flowchart presenting the main steps of the present work is depicted in Fig 1.7.

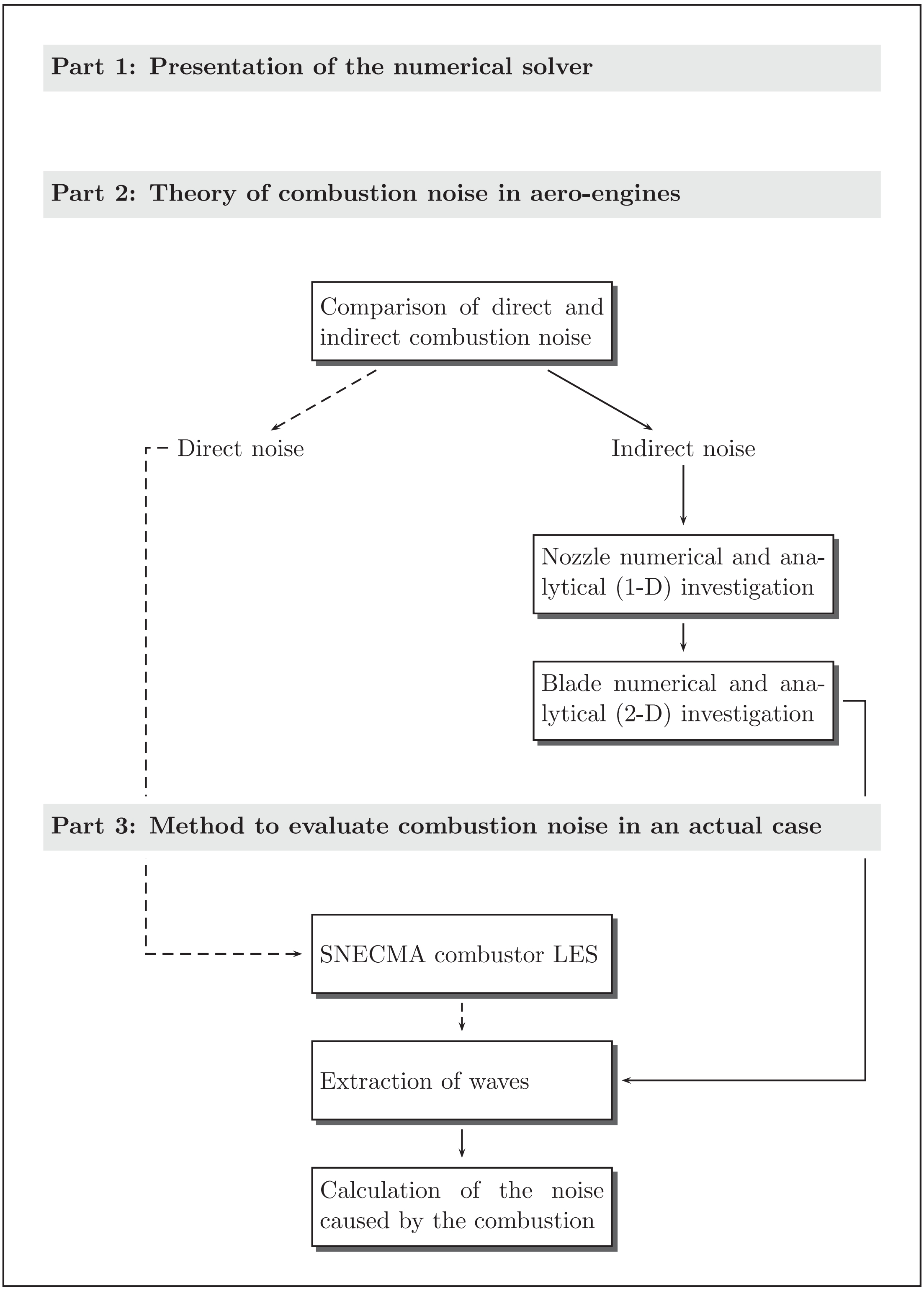

Figure 1.7 - *Flowchart of the PhD thesis.*

Part I

Equations, modelling and simulation of reacting flows

Table of Contents

Chapter 2

Equations for reacting flows

2.1 Equations and conservative variables

This chapter describes the governing equations that are solved by the numerical solver AVBP used in this thesis to solve the compressible Navier-Stokes equations. The index notation is adopted (Einstein summation convention) for almost all the variables and equations. The exception concerns the index k that is related to species and traditional summation symbol is used in this case, and N is the related number of species.

The set of equations that defines the evolution of a compressible and reacting flow (respectively momentum, energy and species balance equations) can be written as follows:

$$\frac{\partial}{\partial t}(\rho u_i) + \frac{\partial}{\partial x_j}(\rho u_i u_j) = -\frac{\partial}{\partial x_j}(p\delta_{ij} - \tau_{ij}) \tag{2.1}$$

$$\frac{\partial}{\partial t}(\rho E) + \frac{\partial}{\partial x_j}(\rho E u_j) = -\frac{\partial}{\partial x_j}\left[u_i(p\delta_{ij} - \tau_{ij}) + q_j\right] + \dot{\omega}_T + Q_r \tag{2.2}$$

$$\frac{\partial \rho_k}{\partial t} + \frac{\partial}{\partial x_j}(\rho_k u_j) = -\frac{\partial J_{j,k}}{\partial x_j} + \dot{\omega}_k \tag{2.3}$$

where ρ, u_i, p and E are respectively the mass density, the i-th component of the velocity vector, the thermodynamic pressure and the energy per mass unit (specific internal and kinetic energy). $\rho_k = \rho Y_k$ where Y_k is the mass-fraction of the species k. δ_{ij} is the Kronecker's delta. The fluid is assumed to be Newtonian (viscous stress tensor linearly dependent of the strain rate tensor) and the bulk viscosity is neglected, so that the viscous stress tensor τ_{ij} is:

$$\tau_{ij} = 2\mu\left(S_{ij} - \frac{1}{3}S_{ll}\right) \tag{2.4}$$

where μ is the shear dynamic viscosity and S_{ij} is the strain rate tensor that is defined as:

$$S_{ij} = \frac{1}{2}\left(\frac{\partial u_i}{\partial x_j} + \frac{\partial u_j}{\partial x_i}\right) \tag{2.5}$$

The terms q_j and $J_{j,k}$ respectively correspond to the heat and molecular diffusion fluxes. The source term $\dot{\omega}_T$ is related to the heat release rate, whereas $\dot{\omega}_k$ is related to the production rate of the species k. Q_r is the energy source term due to electromagnetic radiation, but it is not taken into account all along this thesis. The former diffusion and source terms are described in the next sections.

Equations (2.1) to (2.3) are generally written in a more compact form using the vector U of conservative variables $(\rho u_1, \rho u_2, \rho u_3, \rho E, \rho_1, \ldots, \rho_N)^T$, the matrix of fluxes F (which will be further separated into convective and diffusive fluxes parts) and the source terms vector S:

$$\frac{\partial U_i}{\partial t} + \frac{\partial F_{ij}}{\partial x_j} = S_i \tag{2.6}$$

2.2 Thermodynamic variables

The energy used in Eq. (2.2) corresponds to the summation of the sensible internal energies $e_{s,k}$ of the different species and the kinetic energy, and it is written:

$$E = \sum_{k=1}^{N} Y_k e_{s,k} + \frac{u_i u_i}{2} \tag{2.7}$$

The sensible energies $e_{s,k}(T_i)$ of the species k are defined for discrete temperature values. The sensible energy is tabulated for temperatures T_i using the reference JANAF data from 0 K up to 5000 K by steps of 100 K (i ranging from 0 up to 51). These energies are defined as follows:

$$e_{s,k}(T_i) = \int_{T_0=0\mathrm{K}}^{T_i} c_{v,k}(T)dT = h_{s,k}(T_i) - r\ T_i \tag{2.8}$$

The energies $e_{s,k}$ are interpolated linearly so that one assumes that the species specific heat $c_{v,k}(T_i)$ are constant between T_i and T_{i+1}. These energies are defined as:

$$e_{s,k}(T) = T_i + (T - T_i)\frac{e_{s,k}(T_{i+1}) - e_{s,k}(T_i)}{T_{i+1} - T_i} \tag{2.9}$$

Specific entropy s_k as well as specific enthalpies $h_{s,k}$ are also tabulated and interpolated like for $e_{s,k}$. As mentioned previously, the sensible energy of the mixture is written:

$$\rho e_s = \sum_{k=1}^{N} \rho_k e_{s,k} = \rho \sum_{k=1}^{N} Y_k e_{s,k} \tag{2.10}$$

2.3 Ideal-gas state equation

The state equation used in AVBP is ideal gas that writes:

$$p = \rho r T \tag{2.11}$$

where r is the specific gas constant of the mixture, that depends on space and time since it is a function of the molar mass W of the mixture and is equal to $r = R/W$, where R is the molar gas constant that is 8.314472 J/K/mol. The molar mass of the mixture is calculated as follows:

$$\frac{1}{W} = \sum_{k=1}^{K} \frac{Y_k}{W_k} \tag{2.12}$$

The different thermodynamic coefficients of the mixture are also calculated by summing the specific values for the species weighted by the mass fractions. One defines the mixture specific heat at constant pressure c_p and volume c_v as:

$$c_p = \sum_{k=1}^{K} Y_k \ c_{p,k} \quad ; \quad c_v = \sum_{k=1}^{K} Y_k \ c_{v,k} \tag{2.13}$$

The specific heats ratio is noted γ and is defined as the ratio between specific heat at constant pressure and volume c_p/c_v. It also depends on space and time because of the temperature and the mixture. The speed of sound of the mixture c for the ideal gas is calculated according to the following derivative of the pressure at constant entropy:

$$c^2 = \left.\frac{\partial p}{\partial \rho}\right)_s = \gamma r T \tag{2.14}$$

2.4 Multi-species molecular diffusion

Mass conservation within a multi-components fluid, implies the following relation:

$$\sum_{k=1}^{N} Y_k \ V_i^k = 0 \tag{2.15}$$

where V_i^k is i-th component of the diffusion velocity of the species k. These velocities are often expressed as a function of the molar fractions gradients and the exact linear problem for species diffusion is replaced with the approximation of Hirschfelder and Curtiss when $N > 2$, which leads to:

$$X_k V_i^k = -D_k \frac{\partial X_k}{\partial x_i} \tag{2.16}$$

where X_k is the molar fraction of the species k, expressing $X_k = Y_k\, W/W_k$. Therefore, Eq. (2.16) can be written in terms of mass fractions:

$$Y_k V_i^k = -D_k \frac{W_k}{W} \frac{\partial X_k}{\partial x_i} \tag{2.17}$$

The summation for all species k doesn't necessary imply the relation Eq. (2.15), related to the mass conservation. To address this point, one adds a correction velocity V_i^c to the diffusion flux $J_{i,k}$, and it is simply defined as:

$$V_i^c = \sum_{k=1}^{N} D_k \frac{W_k}{W} \frac{\partial X_k}{\partial x_i} \tag{2.18}$$

Finally, the diffusion flux for species k is computed as follows:

$$J_{i,k} = -\rho \left(D_k \frac{W_k}{W} \frac{\partial X_k}{\partial x_i} - Y_k\, V_i^c \right) \tag{2.19}$$

where D_k are the diffusion coefficients of each species within the mixture. These coefficients are defined in the next sections.

2.5 Heat diffusion

Another heat flux must be taken into account for a multi-component mixture, in addition to the Fourier conduction flux. It is due to the transport of heat because of the diffusion of the species. Soret (diffusion of species due to a gradient of temperature) and Dufour (diffusion of heat due to a gradient of species) effects are neglected here. The final diffusion heat flux is:

$$q_i = \underbrace{-\lambda \frac{\partial T}{\partial x_i}}_{\text{Fourier}} - \underbrace{\rho \sum_{k=1}^{N} J_{i,k}\, h_{s,k}}_{\text{Diffusion of species}} \tag{2.20}$$

where λ is the heat conduction coefficient of the mixture.

2.6 Diffusive transport coefficients

The dynamic viscosity μ is often assumed to be independent of the mixture and close to air composition. Therefore the Sutherland law can be used and it is written:

$$\mu = \mu_{\text{ref}} \frac{T_{\text{ref}} + C}{T + C} \left(\frac{T}{T_{\text{ref}}} \right)^{3/2} \tag{2.21}$$

where μ_{ref} (also noted c_1 in AVBP) and C (or c_2) must be determined so as to fit the real viscosity of the mixture. For air for example, $T_{\text{ref}} = 273$ K, $\mu_{\text{ref}} = 1.71^{-5}$ kg/m.s and $C = 110.4$

K [121]. However, another expression for the viscosity is used here, called power law:

$$\mu = \mu_{\text{ref}} \left(\frac{T}{T_{\text{ref}}} \right)^b \tag{2.22}$$

where b ranges from 0.5 up to 1.0. In the present study, $b = 0.6695$ and the other parameters are $T_{\text{ref}} = 473$ K, $\mu_{\text{ref}} = 2.5034^{-5}$ kg/m.s. The heat conduction coefficient of the mixture λ is calculated using the Prandlt number of the mixture Pr:

$$\lambda = \frac{\mu \ c_p}{Pr} \tag{2.23}$$

The Prandlt number is defined as an input, and it is assumed to be constant in space and time ($Pr = 0.739$ for standard computation during this PhD thesis).

The computation of the molecular diffusion coefficient D_k should theoretically be expressed using the binary coefficient D_{jk} obtained from the kinetic theory (Hirschfelder *et al.* [51]). The mixture diffusion coefficient for species k, D_k , is computed as (Bird *et al.* [11]):

$$D_k = \frac{1 - Y_k}{\sum_{j=k}^{K} X_j / D_{jk}} \tag{2.24}$$

The coefficients D_{ij} are complex functions of collision integrals and thermodynamic variables. For a DNS code using complex chemistry, using Eq. (2.24) makes sense. However in most cases, DNS uses a simplified chemical scheme and modelling diffusivity in a precise way is not needed so that this approach is much less attractive. Therefore, a simplified approximation is used in AVBP for D_k. The Schmidt numbers Sc_k of the species are supposed to be constant so that the binary diffusion coefficient for each species is computed as:

$$D_k = \frac{\mu}{\rho \ Sc_k} \tag{2.25}$$

Moreover, it will be seen in Sec. 2.8 that the Schmidt numbers for all species need to be equal to perform the reacting flow computations with reduced chemical schemes.

2.7 Chemical kinetics

The combustion model in AVBP is based on an Arrhenius law written for N reactants named $\mathcal{M}_k$ and for M reactions as:

$$\sum_{k=1}^{N} \nu'_{kj} \mathcal{M}_k \rightleftharpoons \sum_{k=1}^{N} \nu''_{kj} \mathcal{M}_k, \quad j = 1, M \tag{2.26}$$

The reaction rate $\dot{\omega}_k$ of the species k corresponds to the sum of the rates $\dot{\omega}_{k,j}$ produced by all M reactions:

$$\dot{\omega}_k = \sum_{j=1}^{M} \dot{\omega}_{kj} = \sum_{j=1}^{M} W_k \nu_{kj} \mathcal{Q}_j \tag{2.27}$$

where $\nu_{kj} = \nu''_{kj} - \nu'_{kj}$ and $\mathcal{Q}_j$ is the progress rate of reaction j and it is written:

$$\mathcal{Q}_j = \underbrace{K_{f,j} \prod_{k=1}^{N} \left(\frac{\rho Y_k}{W_k} \right)^{\nu'_{kj}}}_{\text{forward}} - \underbrace{K_{r,j} \prod_{k=1}^{N} \left(\frac{\rho Y_k}{W_k} \right)^{\nu''_{kj}}}_{\text{reverse}} \tag{2.28}$$

In Eq. (2.28), $K_{f,j}$ and $K_{r,j}$ are respectively the forward and reverse rates of reaction j. The forward rate $K_{f,j}$ is calculated using the Arrhenius empirical equation as mentioned previously:

$$K_{f,j} = A_{f,j} T^{\beta_j} \exp\left(-\frac{E_{a,j}}{RT} \right) \tag{2.29}$$

where $A_{f,j}$ is the pre-exponentional factor (in cgs units), β_j is the temperature exponent and $E_{a,j}$ is the activation energy. The reverse reaction rate $K_{r,j}$ is obtained from the assumption of equilibrium that leads to:

$$K_{r,j} = K_{f,j} / K_{\text{eq}} \tag{2.30}$$

where the equilibrium constant K_{eq} is defined from the minimum of the Gibbs free energy ($G = H - TS$), and it yields:

$$K_{\text{eq}} = \left(\frac{p_0}{RT} \right)^{\sum_{k=1}^{K} \nu_{kj}} \exp\left(\frac{\Delta S_j^0}{R} - \frac{\Delta H_j^0}{RT} \right) \tag{2.31}$$

The reference pressure $p_0 = 10^5$ Pa. The enthalpy change ΔH_j^0 and the entropy change ΔS_j^0 for reaction j are:

$$\Delta H_j^0 = \sum_{k=1}^{K} \nu_{kj} W_k (h_{s,k}(T) + \Delta h_{f,k}^0) \quad \text{and} \quad \Delta S_j^0 = \sum_{k=1}^{K} \nu_{kj} W_k s_k(T) \tag{2.32}$$

where $\Delta h_{f,k}^0$ is the specific enthalpy of formation of species k (zero for pure elements like O_2 for example) at temperature $T_0 = 0$ K. Finally, the heat release is calculated summing energy differences induced by each species:

$$\dot{\omega}_T = - \sum_{k=1}^{K} \dot{\omega}_k \Delta h_{f,k}^0 \tag{2.33}$$

2.8 Mixture fraction and equivalence ratio

The reduced chemical scheme used for the simulation of the actual combustor (Chap. 11) needs to be adapted locally as a function of the equivalence ratio. In this section, the definition of this quantity is provided. This definition is based on a passive scalar built from the species equation Eq. (2.3), and equal Schmitd numbers, ie. $D_k = D$ are required. In this case, the correction velocity V_i^c of Eq. (2.18) becomes:

$$V_i^c = D \, \frac{1}{W} \frac{\partial W}{\partial x_i} \tag{2.34}$$

The equations governing the species (2.3) thus become:

$$\frac{\partial}{\partial t}(\rho Y_k) + \frac{\partial}{\partial x_j}(\rho Y_k u_j) = \frac{\partial}{\partial x_j}\left(\rho D \frac{\partial Y_k}{\partial x_i}\right) + \dot{\omega}_k \tag{2.35}$$

The molar mass of species k is calculated by summing the molar masses of the different atoms:

$$W_k = \sum_{a=1}^{A} n_{k,a}^A W_a^A \tag{2.36}$$

where $n_{k,a}^A$ is the number of atoms a in the species k, and W_a^A is the molar weight of atom a. Therefore, one can define the mass fraction Z_a of an atom a within the mixture as:

$$Z_a = \sum_{k=1}^{K} n_{k,a}^A \frac{W_a^A}{W_k} Y_k \tag{2.37}$$

Multiplying Eq. (2.35) by $n_{k,a}^A W_a^A / W_k$ and summing all species lead to the equation of a passive scalar (convection and diffusion only). The source term vanishes, since the conservation of mass implies that $\sum_k \dot{\omega}_k = 0$, and the equation for Z_a writes:

$$\frac{\partial}{\partial t}(\rho Z_a) + \frac{\partial}{\partial x_j}(\rho Z_a u_j) = \frac{\partial}{\partial x_j}\left(\rho D \frac{\partial Z_a}{\partial x_i}\right) \tag{2.38}$$

The passive scalar Z_a is independent on the reactions within the flow, and thus can be used to define a local equivalence ratio $\phi(\vec{x}, t)$. It is usual to handle combustion of hydrocarbons, to consider atoms of carbon C in comparison with reference values on *oxidizer* (noted O) and *fuel* (noted F) sides. One defines a normalized quantity for the atoms of carbon C, the mixture fraction z_C, that is defined as follows:

$$z_C = \frac{Z_C - Z_C^O}{Z_C^F - Z_C^O} \tag{2.39}$$

The quantity z_C is 0 on *oxidizer* side (pure air for example) and 1 on *fuel* side (pure hydrocarbon for example). Finally, it is common to use the equivalence ratio ϕ that writes:

$$\phi = \frac{z_C}{1 - z_C} \phi_{\mathrm{st}} \tag{2.40}$$

where ϕ_{st} is defined for the combustion of hydrocarbons as:

$$\phi_{\mathrm{st}} = \left(n_{F,C}^A + n_{F,H}^A / 4\right) \frac{W_O}{W_F} \frac{Y_F}{Y_O} \tag{2.41}$$

Equation (2.40) is used in Chap. 11 to define the equivalence ratio.

Chapter 3

Equations for Large-Eddy Simulation

This chapter presents the equations solved in the LES approach of reacting flows in AVBP. First, the filtered equations solved by AVBP for a turbulent non-reacting flow are addressed in Sec. 3.1). Section 3.2 presents the models used for unclosed terms. Sections 3.3 and 3.4 describe specifically the models for flame/turbulence interactions (the TF and DTF models) and show how these models are coupled to the filtered equations.

3.1 LES equations for gaseous phase

Large Eddy Simulation (LES) [89, 100] is nowadays recognized as an intermediate approach in comparison with the more classical Reynolds Averaged Navier-Stokes (RANS) approaches. Although conceptually very different, these two approaches aim at providing new systems of governing equations to mimic the characteristics of turbulent flows.

The derivation of the new governing equations is obtained by introducing operators to be applied to the set of compressible Navier-Stokes equations. Unclosed terms arise from these manipulations and models need to be supplied for the problem to be solved. The major differences between RANS and LES come from the operator used for the derivation. In RANS the operation consists of a temporal or ensemble average over a set of realizations of the studied flow [25, 89]. The unclosed terms are representative of the physics taking place over the entire range of frequencies present in the ensemble of realizations under consideration. In LES, the operator is a spatially localized time independent filter of given size, Δ, to be applied to a single realization of the studied flow. Resulting from this ”spatial average” is a separation between the large (greater than the filter size) and small (smaller than the filter size) scales. The unclosed terms are in LES representative of the physics associated with the small structures (with high frequencies) present in the flow. Figure 3.1 illustrates the conceptual differences between (a) DNS and (b) LES and (c) RANS when applied to a homogeneous isotropic turbulent field.

Due to the filtering approach, LES allows a dynamic representation of the large scale mo-

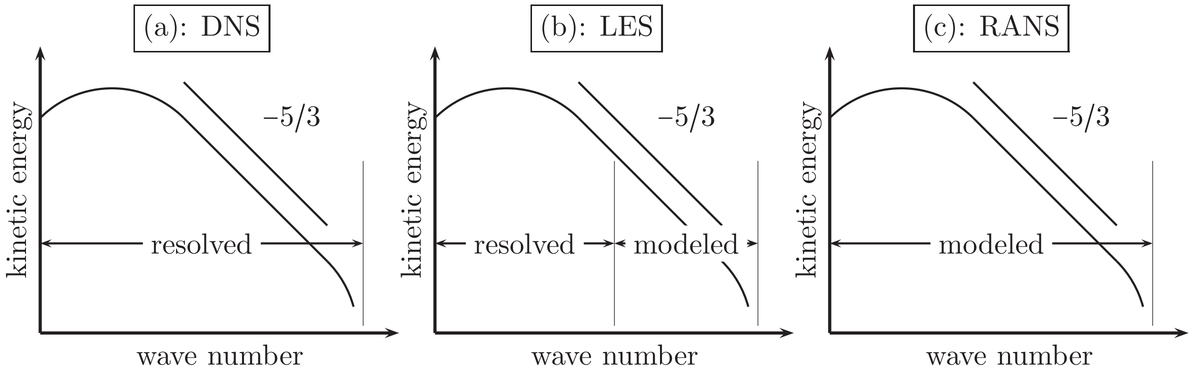

Figure 3.1 - *Conceptual differences between (a) DNS, (b) LES and (c) RANS on homogeneous isotropic turbulence kinetic energy spectrum.*

tions whose contributions are critical in complex geometries. The LES predictions of complex turbulent flows are henceforth closer to the physics since large scale phenomena such as large vortex shedding and acoustic waves are embedded in the set of governing equations [87].

For the reasons presented hereabove, LES has a clear potential in predicting turbulent unsteady flows encountered in aero-engine combustors. Such possibilities are however restricted by the hypothesis introduced while constructing LES models.

3.1.1 Filtering

The filtered quantity $\bar{f}$ is resolved in the numerical simulation whereas $f' = f - \bar{f}$ is the subgrid scale part due to the unresolved flow motion. For variable density ρ, a mass-weighted Favre filtering is introduced such as:

$$\tilde{f} = \frac{\overline{\rho f}}{\overline{\rho}} \tag{3.1}$$

The balance equations for large eddy simulations are obtained by filtering the instantaneous balance equations (2.1), (2.2) and (2.3):

$$\frac{\partial}{\partial t}(\overline{\rho}\tilde{u}_i) + \frac{\partial}{\partial x_j}\left(\overline{\rho}\tilde{u}_i\tilde{u}_j\right) = -\frac{\partial}{\partial x_j}\left(\overline{\rho}\tilde{u}_i\tilde{u}_j\right)\left(\overline{p}\delta_{ij} - \overline{\tau}_{ij} - \overline{\tau}^t_{ij}\right) \tag{3.2}$$

$$\frac{\partial}{\partial t}(\overline{\rho}\tilde{E}) + \frac{\partial}{\partial x_j}\left(\overline{\rho}\tilde{u}_j\tilde{E}\right) = -\frac{\partial}{\partial x_j}\left[\overline{u_i\left(p\delta_{ij} - \tau_{ij}\right)} + \overline{q}_j + \overline{q}^t_j\right] + \overline{\dot{\omega}_T} + \overline{Q_r} \tag{3.3}$$

$$\frac{\partial}{\partial t}(\overline{\rho}\tilde{Y}_k) + \frac{\partial}{\partial x_j}\left(\overline{\rho}\tilde{u}_j\tilde{Y}_k\right) = -\frac{\partial}{\partial x_j}\left[\overline{J}_{j,k} + \overline{J}^t_{j,k}\right] + \overline{\dot{\omega}_k} \tag{3.4}$$

where a repeated index implies summation over this index (Einstein's rule of summation). Note also that throughout the document, the index is reserved to refer to the species and does not follow the summation rule (unless specifically mentioned). The filtered chemical source terms are mentioned, even if the combustion model used here implies modifications of the diffusive terms in Eq. (3.3) and (3.4). Indeed, a specific implementation is done for the standard AVBP models for flame/turbulence interactions (TF and DTF) as it will be seen in sections 3.3 and 3.4. The cut-off scale corresponds to the mesh size (implicit filtering). As usually done, the filter operator and the partial derivative are assumed to commute.

In Eqs. (3.2) to (3.4), the flux tensor can be divided into three parts: the inviscid part, the viscous part and the subgrid scale turbulent part.

3.1.2 Inviscid terms

The three spatial components of the inviscid flux tensor are the same than in DNS but based on the filtered quantities:

$$\begin{pmatrix} \overline{\rho}\tilde{u}_i\tilde{u}_j + \overline{p}\delta_{ij} \\ \overline{\rho}\tilde{u}_j\tilde{E} + \overline{pu_j}\delta_{ij} \\ \overline{\rho}_k\tilde{u}_j \end{pmatrix} \tag{3.5}$$

3.1.3 Viscous terms

The components of the viscous flux tensor take the following form:

$$\begin{pmatrix} -\overline{\tau}_{ij} \\ -\overline{u_i\tau_{ij}} + \overline{q}_j \\ \overline{J}_{j,k} \end{pmatrix} \tag{3.6}$$

Filtering the balance equations leads to unclosed quantities, which need to be modelled.

3.1.4 Sub-grid scale turbulent terms

The components of the turbulent sub-grid scale flux take the following form:

$$\begin{pmatrix} -\overline{\tau}_{ij}^{t} \\ \overline{q}_j^{t} \\ \overline{J}_{j,k}^{t} \end{pmatrix} \tag{3.7}$$

The filtered diffusion terms are (see T. Poinsot and D. Veynante, Chapter 4 [87]) :

- the laminar filtered stress tensor $\tilde{\tau}_{ij}$ is given by the following relations:

$$\overline{\tau}_{ij} = \overline{2\mu\left(S_{ij} - \frac{1}{3}\delta_{ij}S_{ll}\right) \approx 2\overline{\mu}\left(\tilde{S}_{ij} - \frac{1}{3}\delta_{ij}\tilde{S}_{ll}\right)} \tag{3.8}$$

with:

$$\tilde{S}_{ij} = \frac{1}{2}\left(\frac{\partial \tilde{u}_j}{\partial x_i} + \frac{\partial \tilde{u}_i}{\partial x_j}\right) \tag{3.9}$$

- the diffusive species flux vector in non-reacting flows is:

$$\overline{J}_{i,k} = -\overline{\rho\left(D_k \frac{W_k}{W}\frac{\partial X_k}{\partial x_i} - Y_k V_i^c\right)} \approx \overline{\rho}\left(\overline{D}_k \frac{W_k}{W}\frac{\partial \tilde{X}_k}{\partial x_i} - \tilde{Y}_k \tilde{V}_i^c\right) \tag{3.10}$$

  where higher order correlations between the different variables of the expression are assumed to be negligible.

- the filtered heat flux is:

$$\overline{q}_i = -\overline{\lambda\frac{\partial T}{\partial x_i}} + \sum_{k=1}^{N} \overline{J_{i,k} h_{s,k}} \approx -\overline{\lambda}\frac{\partial \tilde{T}_k}{\partial x_i} + \sum_{k=1}^{N} \overline{J}_{i,k}\tilde{h}_{s,k} \tag{3.11}$$

  These forms assume that the spatial variations of molecular diffusion fluxes are negligible and can be modelled through simple gradient assumptions.

3.2 Sub-grid scale models

As highlighted above, filtering the transport equations yields a closure problem evidenced by the so-called "Sub-Grid Scale" (SGS) turbulent fluxes (see Eq. 3.2). For the system to be solved numerically, closures need to be supplied. Details on the forms and models available in AVBP are given in this section.

- the Reynolds tensor is:

$$\overline{\tau}_{ij}^t = -\overline{\rho}\left(\widetilde{u_i u_j} - \tilde{u}_i \tilde{u}_j\right) \tag{3.12}$$

  The influence of the SGS on the resolved motion is taken into account in AVBP by a SGS model based on the introduction of a turbulent viscosity ν_t (Boussinesc assumption), and thus the Reynolds tensor is written:

$$\overline{\tau}_{ij}^t = 2\overline{\rho}\nu_t \tilde{S}_{ij} - \frac{1}{3}\delta_{ij}\overline{\tau}_{ll}^t \tag{3.13}$$

  The modelling of ν_t is explained in section 3.2.1.

- the sub-grid scale diffusive species flux vector:

$$\overline{J}_{i,k}^t = \overline{\rho}\left(\widetilde{u_i Y_k} - \tilde{u}_i \tilde{Y}_k\right) \tag{3.14}$$

  this term is modelled by analogy to laminar form:

$$\overline{J}_{i,k}^t = \overline{\rho}\left(D_k^t \frac{W_k}{W}\frac{\partial \tilde{X}_k}{\partial x_i} - \tilde{Y}_k \tilde{V}_i^{c,t}\right) \tag{3.15}$$

where:

$$D_k^t = \frac{\nu_t}{Sc_k^t} \tag{3.16}$$

The turbulent Schmidt Sc_k^t number is the same for all species and is here equal to 0.6.

- the sub-grid scale heat flux vector:

$$\overline{q_i}^t = \overline{\rho}\left(\widetilde{u_i E} - \tilde{u}_i \tilde{E}\right) \tag{3.17}$$

the modelling for $\overline{q_i}^t$ is written:

$$\overline{q}_i^t = \lambda^t \frac{\partial \tilde{T}}{\partial x_i} + \sum_{k=1}^{N} \overline{J}_{i,k}^t \tilde{h}_{s,k} \tag{3.18}$$

with:

$$\lambda^t = \frac{c_p\ \nu_t}{Pr^t} \tag{3.19}$$

The turbulent Prandtl number Pr^t is also 0.6 here.

3.2.1 Model for the sub-grid stress tensor

A description of the characteristics of the most known sub-grid stress tensor model (Smagorinsky) is given in the next section. This LES model is derived on the theoretical ground that the LES filter is spatially and temporally invariant. Variations in the filter size due to non-uniform meshes or moving meshes are not directly accounted for in the LES models. Change of cell topology is only accounted for through the use of the local cell volume, that is $\Delta = \sqrt[3]{V_{cell}}$.

The filtered compressible Navier-Stokes equations exhibit sub-grid scale (SGS) tensors and vectors describing the interaction between the non-resolved and resolved motions. The influence of the SGS on the resolved motion is taken into account in AVBP by a SGS model based on the introduction of a turbulent viscosity, ν_t, as mentioned in Sec. 3.2. Such an approach assumes the effect of the SGS field on the resolved field to be purely dissipative.

The most common model to deal with the turbulent viscosity, and the one which is used hereafter, is the Smagorinsky model. This viscosity writes:

$$\nu_t = (C_S \Delta)^2 \sqrt{2 \tilde{S}_{ij} \tilde{S}_{ij}} \tag{3.20}$$

where Δ denotes the filter characteristic length (cube-root of the cell volume), C_S is the model constant set to 0.18 but can vary between 0.1 and 0.18 depending on the flow configuration. The Smagorinsky model [108] was developed in the 1960's and heavily tested for multiple flow configurations. This closure has the particularity of supplying the right amount of dissipation of kinetic energy in homogeneous isotropic turbulent flows. Locality is however lost and only global quantities are maintained. It is known as being "too dissipative" and transitioning flows are not suited for its use [100].

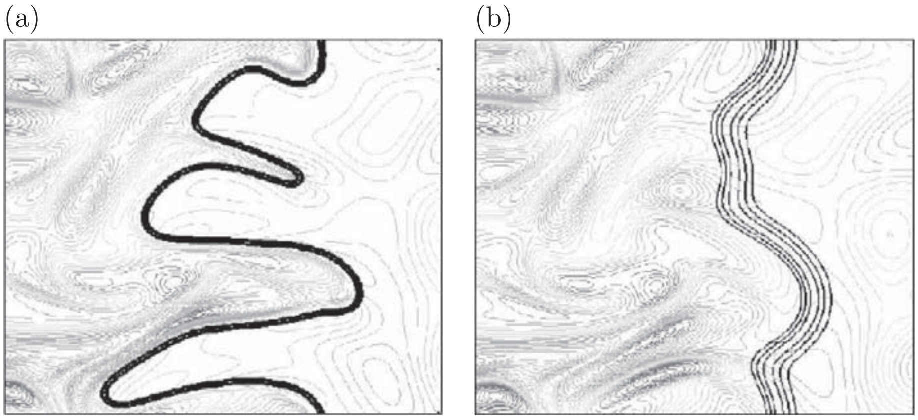

Figure 3.2 - *Direct Numerical Simulation of flame/turbulence interactions by Angelberger* et al. *[2] and Poinsot and Veynante [87]. (a) non-thickened flame and, (b) thickened flame ($\mathcal{F} = 5$).*

3.3 Models for turbulent combustion

A difficult problem is encountered for Large Eddy Simulation of premixed flames: the thickness δ_L^0 of a premixed flame is generally smaller than the standard mesh size Δ_x used for LES. For this reason, the Thickened Flame (TF) model has been developed so as to resolve the flame fronts on a LES mesh. The former is thickened by multiplying the diffusive fluxes by a thickening factor $\mathcal{F}$. However, in turbulent flows, the interaction between turbulence and chemistry is altered: eddies smaller than δ_L^0, do not interact with the flame any longer. As a result, the thickening of the flame reduces the ability of the vortices to wrinkle the flame front. As the flame surface is decreased, the reaction rate is underestimated. In order to correct this effect, an efficiency function $\mathcal{E}$ has been developed [27] from DNS results and implemented into AVBP (see Fig. 3.2). It is described in the next subsection.

3.3.1 The combustion sub-grid scale model

A complete description of the efficiency function is given in reference [27]. The underlying model philosophy can be summarized through three main steps:

- The wrinkling factor of the flame surface Ξ is estimated from the flame surface density $\bar{\Sigma}$, assuming an equilibrium between the turbulence and the sub-scale flame surface:

$$\Xi \approx 1 + \alpha \frac{\Delta_e}{s_L^0} \langle a_T \rangle_s \tag{3.21}$$

  where $\langle a_T \rangle_s$ is the sub-grid scale strain rate, Δ_e is the filter size (ie. larger than Δ_x) and α is a model constant.

- $\langle a_T \rangle_s$ is estimated from the filter size Δ_e and the sub-grid scale turbulent velocity u'_{Δ_e}: $\langle a_T \rangle_s = \Gamma u'_{\Delta_e} / \Delta_e$. The function Γ corresponds to the integration of the effective strain rate induced by all scales affected by the artificial thickening, i.e. between the Kolmogorov η_K and the filter Δ_e scales (see also [73]). Γ is written as:

$$\Gamma\left(\frac{\Delta_e}{\delta_L^1}, \frac{u'_{\Delta_e}}{s_L^0}\right) = 0.75 \exp\left[-\frac{1.2}{(u'_{\Delta_e}/s_L^0)^{0.3}}\right]\left(\frac{\Delta_e}{\delta_L^1}\right)^{\frac{2}{3}} \tag{3.22}$$

Finally, the efficiency function is defined as the wrinkling ratio between the non-thickened reference flame and the thickened flame:

$$\mathcal{E} = \frac{\Xi(\delta_L^0)}{\Xi(\delta_L^1)} = \frac{1 + \alpha\Gamma\left(\frac{\Delta_e}{\delta_L^0}, \frac{u'_{\Delta_e}}{s_L^0}\right)\frac{u'_{\Delta_e}}{s_L^0}}{1 + \alpha\Gamma\left(\frac{\Delta_e}{\delta_L^1}, \frac{u'_{\Delta_e}}{s_L^0}\right)\frac{u'_{\Delta_e}}{s_L^0}} \tag{3.23}$$

s_L^0 and δ_L^0 are the laminar flame speed and the laminar flame thickness, respectively, when $\mathcal{F} = 1$ and $\delta_L^0 = \mathcal{F}\delta_L^0$.

$\mathcal{E}$ varies between 1 (weak turbulence) and $\mathcal{E}_{max} \approx \mathcal{F}^{2/3}$ (large wrinkling at the sub-grid scale). In turbulent premixed zones, the efficiency function is determined to ensure that the turbulent flame speed will be $\mathcal{E}s_L^0 = s_T$. The efficiency function is required when the vortex size r is defined by $\delta_L^0 > r > \delta_L^c$ for the flame and by $\delta_L^1 = \beta\mathcal{F}\delta_L^0 > r > \delta_L^c$ for a thickened flame. δ_L^c is a cut-off length scale: for vortices lower than δ_L^c, the flame remains unaffected. δ_L^c, is defined in [27].

- The filter size Δ_e corresponds to the greatest scale affected by the flame thickening, that is to say δ_L^1. In practice, $\Delta_e = 10\Delta_x$ with $\Delta_x = \sqrt[3]{V}$. The sub-grid scale turbulent velocity u'_{Δ_e} is based on the rotational of the velocity field to remove the dilatational part of the velocity which must not be counted as "turbulence". The operator used to define the velocity u'_{Δ_e} is the following:

$$u'_{\Delta_e} = c_2\Delta_x^3\left|\frac{\partial^2}{\partial x_j \partial x_j}\left(\epsilon_{lmn}\frac{\partial \overline{u}_n}{\partial x_m}\right)\right| \tag{3.24}$$

with $c_2 \approx 2$ and where ϵ_{lmn} stands for the Levi-Civita symbol.

3.3.2 Estimation of the model constant α

The model constant α is estimated to match the asymptotic behavior of the wrinkling factor Ξ versus RMS velocity u' for thin flames when Δ_e goes to the integral length scale l_t, the flame wrinkling Ξ goes to Ξ_{max} defined by:

$$\Xi_{max} = 1 + \beta u'/s_L^0 \tag{3.25}$$

with u' the velocity at length scale $l_t\alpha$ is then deduced from Eq. (3.25):

$$\alpha = \beta\frac{2\ln(2)}{3c_{ms}\left[\sqrt{Re_t} - 1\right]} \tag{3.26}$$

where $Re_t = u' l_t / \nu$ is the turbulent Reynolds number and $c_{ms} = 0.28$. The reader is referred to [27] for more details.

Other forms of efficiency function have been derived by Charlette *et al.* [23, 24] but are not used here.

3.3.3 Implementation of the standard Thickened Flame (TF) model

The filtered equations for total energy and for species [Eqs. (3.3) and (3.4)] must be modified in reactive flows when the TF or DTF model is used. In this case, only the filtered equations for momentum (Eq. 3.2) are unchanged. For the species and energy, the filtered equations are replaced by the thickened equations as follows:

Viscous terms

- the filtered diffusive species flux vector is given by:

$$\overline{J}_{i,k} = -\mathcal{E}\mathcal{F}\frac{\overline{\mu}}{Sc_k}\frac{W_k}{W}\frac{\partial \tilde{X}_k}{\partial x_i} + \overline{\rho}_k \tilde{V}_i^c \tag{3.27}$$

  with

$$\tilde{V}_i^c = -\mathcal{E}\mathcal{F}\sum_{k=1}^{N}\frac{\overline{\mu}}{\overline{\rho} Sc_k}\frac{W_k}{W}\frac{\partial \tilde{X}_k}{\partial x_i} \tag{3.28}$$

- the filtered heat flux is:

$$\overline{q}_i = -\mathcal{E}\mathcal{F}\frac{c_p\,\overline{\mu}}{Pr}\frac{\partial \tilde{T}}{\partial x_i} + \sum_{k=1}^{N}\overline{J}_{i,k}\tilde{h}_{s,k} \tag{3.29}$$

Source terms

The filtered source term vector is written:

$$\begin{pmatrix} 0 \\ \frac{\mathcal{E}}{\mathcal{F}}\dot{\omega}_T(\tilde{Y}_k, \tilde{T}) \\ \frac{\mathcal{E}}{\mathcal{F}}\dot{\omega}_k(\tilde{Y}_k, \tilde{T}) \end{pmatrix} \tag{3.30}$$

where $\dot{\omega}_T(\tilde{Y}_k, \tilde{T})$ and $\dot{\omega}_k(\tilde{Y}_k, \tilde{T})$ are reaction rates computed with the Arrhenius expression and the filtered values of $\tilde{Y}_k$ and $\tilde{T}$. Note that this model should be used only for perfectly premixed cases since mixing in the fresh gases, for example, is modified by thickening and not correctly handled with the filtered terms of Eqs. (3.3) and (3.4). The actual transport equations for the TF model are summarized below.

The use of the TF model implies the following relation for the correction diffusion velocities:

$$\tilde{V}_i^c + \tilde{V}_i^{c,t} = \sum_{k=1}^{N}\mathcal{E}\mathcal{F}\frac{\overline{\mu}}{\overline{\rho} Sc_k}\frac{W_k}{W}\frac{\partial \tilde{X}_k}{\partial x_i} \tag{3.31}$$

3.3.4 Final equations solved for the TF model

The final set of LES equations solved when performing LES of reacting flows with the TF model finally writes:

$$
\begin{aligned}
\frac{\partial}{\partial t}(\overline{\rho}\tilde{u}_i) + \frac{\partial}{\partial x_j}(\overline{\rho}\tilde{u}_i\tilde{u}_j) =& \frac{\partial}{\partial x_j}\left[\overline{p}\delta_{ij} - 2(\overline{\mu} + \mu_t)(\tilde{S}_{ij} - 1/3\ \tilde{S}_{ll}\delta_{ij})\right] && (3.32)\\
\frac{\partial}{\partial t}(\overline{\rho}\tilde{E}) + \frac{\partial}{\partial x_j}(\overline{\rho}\tilde{E}\tilde{u}_j) =& \frac{\partial}{\partial x_j}\left[\tilde{u}_i\overline{p}\delta_{ij} - 2\overline{\mu}\tilde{u}_i(\tilde{S}_{ij} - 1/3\ \tilde{S}_{ll}\delta_{ij})\right] \\
&+ \frac{\partial}{\partial x_j}\left[\mathcal{E}\mathcal{F}\frac{c_p\overline{\mu}}{Pr}\frac{\partial \tilde{T}}{\partial x_j}\right] \\
&+ \frac{\partial}{\partial x_j}\left[\sum_{k=1}^{N}\left(\mathcal{E}\mathcal{F}\frac{\overline{\mu}}{Sc_k}\frac{W_k}{W}\frac{\partial \tilde{X}_k}{\partial x_j} - \overline{\rho}\tilde{Y}_k(\tilde{V}_j^c + \tilde{V}_j^{c,t})\right)\tilde{h}_{s,k}\right] \\
&+ \frac{\mathcal{E}}{\mathcal{F}}\dot{\omega}_T(\tilde{Y}_k, \tilde{T}) && (3.33)\\
\frac{\partial}{\partial t}(\overline{\rho}\tilde{Y}_k) + \frac{\partial}{\partial x_j}(\overline{\rho}\tilde{Y}_k\tilde{u}_j) =& \frac{\partial}{\partial x_j}\left[\mathcal{E}\mathcal{F}\frac{\overline{\mu}}{Sc_k}\frac{W_k}{W}\frac{\partial \tilde{X}_k}{\partial x_j} - \overline{\rho}\tilde{Y}_k(\tilde{V}_j^c + \tilde{V}_j^{c,t})\right] \\
&+ \frac{\mathcal{E}}{\mathcal{F}}\dot{\omega}_k(\tilde{Y}_k, \tilde{T}) && (3.34)
\end{aligned}
$$

3.4 The Dynamically Thickened Flame (DTF) model for LES

The TF model is adequate to simulate perfectly premixed flames. For partially premixed cases, this model is not suitable and must be adjusted for different reasons:

- In non-reactive zones, where only mixing takes place, the molecular and thermal diffusion are overestimated by a factor $\mathcal{F}$. In these zones, the thickening factor should be corrected to go to unity. Moreover, turbulent sub-grid scale terms should be added (they have been totally omitted in Eqs. (3.27) and (3.29) where they are replaced by the thickened terms).
- In the flame zone, the thickening allows resolving the diffusion and the source terms. Thus, the sub-grid scale turbulent terms can be set to zero.

In other words, the TF model can remain unchanged in the flame zone but must be adapted outside the flame region. The DTF model has been developed to take into account these points (Legier *et al.* [61]). Its application is addressed in Fig. 3.3. The thickening factor $\mathcal{F}$ is not a constant anymore but it goes to $\mathcal{F}_{max}$ in flame zones and decreases to unity in non-reactive zones. The $\mathcal{F}_{max}$ parameter can be fixed by the user or can be computed, according to the local mesh spacing, using the following relation:

$$
\mathcal{F}_{max} = \frac{N_c \Delta_x}{\delta_L^0} \qquad (3.35)
$$

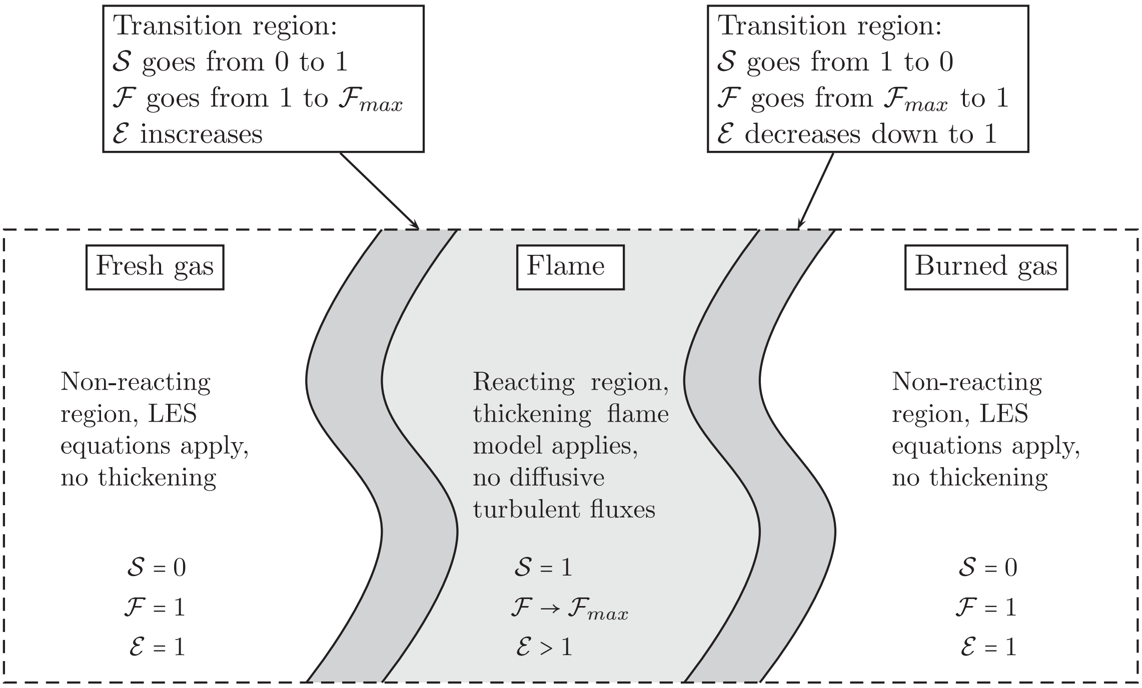

Figure 3.3 - *Schematic representation of the different regions found in a partially premixed flame and as defined for the DTF model.*

where N_c is the number of cells used to resolve the flame front and Δ_x is the local mesh size. An appropriate value for δ_L^0 is therefore required, and it is provided by the user.

The local thickening factor $\mathcal{F}$ is then obtained as follows:

$$\mathcal{F} = 1 + (\mathcal{F}_{max} - 1)\mathcal{S} \tag{3.36}$$

where $\mathcal{S}$ is a sensor depending on the local temperature and mass fractions.

$$\mathcal{S} = \tanh\left(\beta' \frac{\Omega}{\Omega_0}\right) \tag{3.37}$$

where Ω is a sensor function detecting the presence of a reaction front. One possible method to construct this sensor is to use the kinetic parameters of the fuel breakdown reaction:

$$\Omega = Y_F^{\nu'_F} Y_O^{\nu'_O} \exp\left(-\Gamma \frac{E_a}{RT}\right) \tag{3.38}$$

Although Ω looks like a reaction rate function, it is actually quite different. This form is only one convenient way to identify the flame zone but other functions could be used as long as they track correctly the zones where combustion occurs.

Γ is used to start the thickening before the reaction, that's why $\Gamma < 1$ (usually $\Gamma = 0.5$). The β' factor is set in AVBP ($\beta' = 500$). $\mathcal{S}$ varies between 0 in non-reactive zones and 1 in flames. Ω_0 is specified by the user by measuring it on a 1D premixed non-thickened flame (see Chap. 11).

3.4.1 Implementation of the Dynamically Thickened Flame (DTF) model

When the DTF model is applied, the filtered diffusive species flux vector is given by:

$$\overline{J}^t_{i,k} = -(1-\mathcal{S})\frac{\mu_t}{Sc^t_k}\frac{W_k}{W}\frac{\partial \tilde{X}_k}{\partial x_i} + \overline{\rho}\tilde{Y}_k\tilde{V}^{c,t}_i \tag{3.39}$$

with

$$\tilde{V}^{c,t}_i = (1-\mathcal{S})\sum_{k=1}^{N}\frac{\mu_t}{\overline{\rho}Sc^t_k}\frac{W_k}{W}\frac{\partial \tilde{X}_k}{\partial x_i} \tag{3.40}$$

and the filtered heat flux is:

$$\overline{q}^t_i = -(1-\mathcal{S})\frac{c_p\mu_t}{Pr^t}\frac{\partial \tilde{T}}{\partial x_i} + \sum_{k=1}^{N}\overline{J}^t_{i,k}\tilde{h}_{s,k} \tag{3.41}$$

while the source term becomes:

$$\begin{pmatrix} 0 \\ \frac{\mathcal{E}}{\mathcal{F}}\dot{\omega}_T(\tilde{Y}_k,\tilde{T}) \\ \frac{\mathcal{E}}{\mathcal{F}}\dot{\omega}_k(\tilde{Y}_k,\tilde{T}) \end{pmatrix} \tag{3.42}$$

The use of the DTF model implies the following relation for the correction diffusion velocities:

$$\tilde{V}^c_i + \tilde{V}^{c,t}_i = \sum_{k=1}^{N}\left(\mathcal{E}\mathcal{F}\frac{\overline{\mu}}{\overline{\rho}Sc_k} + (1-\mathcal{S})\frac{\mu_t}{\overline{\rho}Sc^t_k}\right)\frac{W_k}{W}\frac{\partial \tilde{X}_k}{\partial x_i} \tag{3.43}$$

3.4.2 Final equations solved for the DTF model

It is interesting here again to rewrite the final transport equations resulting from the DTF model. The different convective terms are the same as for the TF model. The final set of LES equations solved when performing LES of reacting flows with the DTF model finally writes:

$$\frac{\partial}{\partial t}(\overline{\rho}\tilde{u}_i) + \frac{\partial}{\partial x_j}(\overline{\rho}\tilde{u}_i\tilde{u}_j) = \frac{\partial}{\partial x_j}\left[\overline{p}\delta_{ij} - 2(\overline{\mu}+\mu_t)(\tilde{S}_{ij} - 1/3\ \tilde{S}_{ll}\delta_{ij})\right] \tag{3.44}$$

$$\begin{aligned}\frac{\partial}{\partial t}(\overline{\rho}\tilde{E}) + \frac{\partial}{\partial x_j}(\overline{\rho}\tilde{E}\tilde{u}_j) =& \frac{\partial}{\partial x_j}\left[\tilde{u}_i\overline{p}\delta_{ij} - 2\overline{\mu}\tilde{u}_i(\tilde{S}_{ij} - 1/3\ \tilde{S}_{ll}\delta_{ij})\right] \\ &+ \frac{\partial}{\partial x_j}\left[c_p\left(\mathcal{E}\mathcal{F}\frac{\overline{\mu}}{Pr} + (1-\mathcal{S})\frac{\mu_t}{Pr_t}\right)\frac{\partial \tilde{T}}{\partial x_j}\right] \\ &+ \frac{\partial}{\partial x_j}\left[\sum_{k=1}^{N}\left(\left[\mathcal{E}\mathcal{F}\frac{\overline{\mu}}{Sc_k} + (1-\mathcal{S})\frac{\mu_t}{Sc^t_k}\right]\frac{W_k}{W}\frac{\partial \tilde{X}_k}{\partial x_j} - \overline{\rho}\tilde{Y}_k(\tilde{V}^c_j + \tilde{V}^{c,t}_j)\right)\tilde{h}_{s,k}\right] \\ &+ \frac{\mathcal{E}}{\mathcal{F}}\dot{\omega}_T(\tilde{Y}_k,\tilde{T})\end{aligned} \tag{3.45}$$

$$\begin{aligned}\frac{\partial}{\partial t}(\overline{\rho}\tilde{Y}_k) + \frac{\partial}{\partial x_j}(\overline{\rho}\tilde{Y}_k\tilde{u}_j) =& \frac{\partial}{\partial x_j}\left[\left(\mathcal{E}\mathcal{F}\frac{\overline{\mu}}{Sc_k} + (1-\mathcal{S})\frac{\mu_t}{Sc^t_k}\right)\frac{W_k}{W}\frac{\partial \tilde{X}_k}{\partial x_j} - \overline{\rho}\tilde{Y}_k(\tilde{V}^c_j + \tilde{V}^{c,t}_j)\right] \\ &+ \frac{\mathcal{E}}{\mathcal{F}}\dot{\omega}_k(\tilde{Y}_k,\tilde{T})\end{aligned} \tag{3.46}$$

This implementation shows that the DTF model is a hybrid formulation:

- outside the flame zones, the sensor Ω is zero and $\mathcal{S}$ is zero. The thickening factor $\mathcal{F}$ is one, the efficiency $\mathcal{E}$ goes to 1 and the DTF equations recover the standard LES form to handle mixing.
- in flame zones, detected by non-zero values of Ω, the sensor $\mathcal{S}$ goes to unity, the model behaves like the classical TF model.

Chapter 4

Numerical approach

The computational code AVBP is used for all the numerical studies performed during this PhD thesis. This code has been created by the OUCL (Oxford University Computing Laboratory) and the CERFACS in 1993, it is now owned by the IFP (Institut Français du Pétrole) and the CERFACS which maintain and develop it together. It has been designed to solve compressible Navier-Stokes equations on a non-structured grid and hybrid elements, in order to provide the maximum of freedom in the choice and discretization of the computational domain. AVBP has been written, from the beginning, to be used on parallel machine, which explains its high performance on super-computers [103, 109]. The numerical methods of AVBP have been implemented by Rudgyard and Schönfeld, following the work concerning cell-vertex type finite-volume methods of the Oxford team [84, 98, 67, 35, 34].

This chapter presents briefly the cell-vertex method (section 4.1) and the numerical schemes used in this thesis (section 4.2). The reader can refer to the PhD. thesis of Lamarque [58] for a detailed description of the numerics in AVBP.

4.1 *Cell-vertex* discretization

The flow solver used for the discretization of the governing equations is based on the ”finite volume” (FV) method. There are three common techniques for implementing FV methods: the cell-centered, the vertex-centered and the so-called cell-vertex formulation. In the first two ones, not used in AVBP, discrete solution values are stored at the center of the control volumes (or grid cells), and neighboring values are averaged across cell boundaries in order to calculate fluxes. In the alternative cell-vertex technique, used as underlying numerical discretization method of AVBP, the discrete values of the conserved variables are stored at the cell vertices (or grid nodes). The mean values of the fluxes are then obtained by averaging along the cell edges.

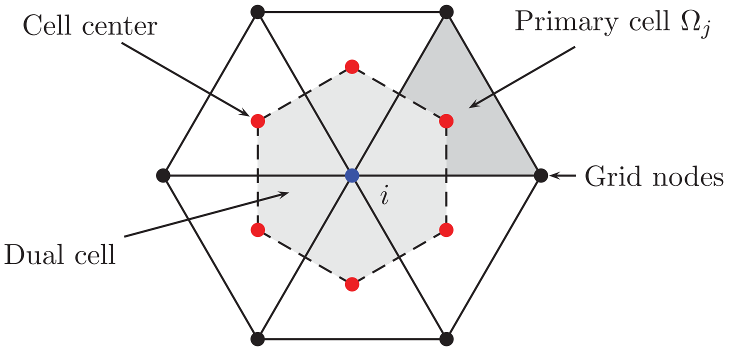

Figure 4.1 - *Cell-vertex cells.*

4.1.1 Weighted Cell Residual Approach

For the description of the weighted cell-residual approach, the laminar Navier-Stokes equations are considered in their conservative formulation:

$$\frac{\partial U}{\partial t} + \nabla \cdot F = 0 \tag{4.1}$$

where $U = (\rho u_i, \rho E, \rho_k)$ is the vector of conserved variables and F is the corresponding flux tensor. For convenience, the latter is divided into an inviscid and a viscous part, $F = F^I(U) + F^V(U, \nabla U)$. Different formulations to compute $F^V(U, \nabla U)$ can be used in AVBP, but they are not presented here. The following sections are dedicated to the convection schemes. The spatial terms of the equations are approximated in each control volume Ω_j (see Fig. 4.1) to give the cell residual R_{Ω_j}, using the Green-Gauss theorem:

$$R_{\Omega_j} = \frac{1}{V_{\Omega_j}} \int_{\partial \Omega_j} F \cdot n dS \tag{4.2}$$

where $\partial \Omega_j$ denotes the boundary of Ω_j with n, the outward normal to $\partial \Omega_j$. V_{Ω_j} is the volume of cell j.

The cell-vertex approximation is readily applicable to arbitrary cell types and is hence straightforward to apply on hybrid grids. The residual in Eq. (4.2) is first computed for each element performing a simple integration rule applied to the faces. For triangular faces, a straightforward mid-point rule is used, which is equivalent to the assumption that the individual components of the flux vary linearly on these faces. For quadrilateral faces, where the nodes may be not coplanar, each face is divided into four triangles (two divisions along the two diagonals) and the integration is performed over each triangle (see Fig. 4.2). The flux value is then obtained from the average of the four contributions. This so-called "linear preservation property" plays an important part in the global discretization, because it ensures that accuracy is not lost on irregular meshes. Computationally, it is useful to write the discrete integration Eq. (4.2) over

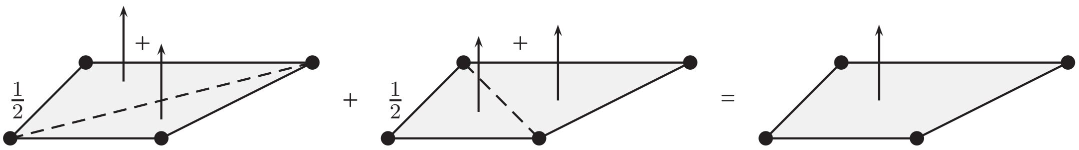

Figure 4.2 - *Calculation of normals for non-coplanar vertex.*

an arbitrary cell Ω_j as:

$$R_{\Omega_j} = -\frac{1}{n_d V_{\Omega_j}} \sum_{k|k\in\Omega_j} F_k \cdot S_k \tag{4.3}$$

where F_k is an approximation of F at the nodes, n_d represents the number of space dimensions and $\{k \in \Omega_j\}$ are the vertices of the cell Ω_j. In this formulation, the geometrical information has been included into the S_k terms that are associated with individual nodes of the cell Ω_j. For triangular elements, the normal of node k (internal to the element) corresponds to the surface-weighted external normal of the face opposite to node k. Note that for consistency one has $\sum_{k|k\in\Omega_j} S_k = 0$.

A linear preserving approximation of the divergence operator is obtained if the volume V_{Ω_j} is defined consistently as:

$$V_{\Omega_j} = -\frac{1}{n_d^2} \sum_{k|k\in\Omega_j} x_k \cdot S_k \tag{4.4}$$

since $\nabla \cdot x = n_d$. And the control volume around the node i (median dual cell) is defined as: $V_i = \sum_{k|k\in\Omega_j} V_{\Omega_j}/n_v(\Omega_j)$.

Once the cell residuals are calculated, one can obtain R_i, the nodal residual at node i, as the volume average of the cell residuals:

$$R_i = \frac{1}{V_i} \sum_{j|i\in\Omega_j} D_{i|\Omega_j} V_{\Omega_j} R_{\Omega_j} \tag{4.5}$$

where $D_{i|\Omega_j}$ is a distribution matrix that weighs the cell residual from cell centre Ω_j to node i (scatter operation). The form of matrix $D_{i|\Omega_j}$ determines the numerical scheme employed. Finally, the semi-discrete scheme (with perfect time advancement) can be defined as:

$$\frac{dU_i}{dt} = -R_i \tag{4.6}$$

and conservation is guaranteed if $\sum_{j|i\in\Omega_j} D_{i|\Omega_j} = I$ (identity matrix). The following sections are dedicated to the discretization of convective fluxes (hyperbolic part of the Navier-Stokes equations) according to the numerical schemes available in AVBP, and used hereafter.

4.2 Numerical schemes

4.2.1 The Lax-Wendroff scheme

The form of the distribution matrix $D_{i|\Omega_j}$ determines the different numerical schemes available in AVBP. Hereafter, $D_{i|\Omega_j}$ is derived for the Lax-Wendroff scheme [59]. The Lax-Wendroff scheme (second order accurate in space and time) is based on a Taylor expansion in time of the solution U.

$$U^{n+1} = U^n + \Delta t \left(\frac{\partial U}{\partial t} \right)^n + \frac{1}{2} \Delta t^2 \left(\frac{\partial^2 U}{\partial t^2} \right)^n + O\left(\Delta t^3\right) \tag{4.7}$$

Considering Eq. (4.7), the first temporal derivative can be expressed as:

$$\frac{\partial U}{\partial t} = -\nabla \cdot F \tag{4.8}$$

In a similar manner, the second derivative can be recast as:

$$\frac{\partial^2 U}{\partial t^2} = \frac{\partial}{\partial t} (-\nabla \cdot F) = -\nabla \cdot \frac{\partial F}{\partial t} = -\nabla \cdot \left[\mathscr{A} \left(\frac{\partial U}{\partial t} \right) \right] = \nabla \cdot [\mathscr{A} (\nabla \cdot F)] \tag{4.9}$$

assuming that temporal and spatial derivatives can be exchanged and defining $\mathscr{A} = \partial F / \partial U$ as the Jacobian matrix. Hence, substituting Eqs. (4.8) and (4.9) into Eq. (4.7) the solution at time $n+1$ can be written as:

$$U^{n+1} = U^n - \Delta t \left\{ \nabla \cdot F - \frac{1}{2} \Delta t \nabla \cdot [\mathscr{A} (\nabla \cdot F)] \right\} \tag{4.10}$$

In discrete form, remembering the basic principle of the cell-vertex approach, the nodal residual R_i is obtained by summing the contributions of all the surrounding elements. The value is then scaled by the nodal volume V_i.

$$R_i = \frac{1}{V_i} \sum_{j|i \in \Omega_j} R_{i|\Omega_j} \tag{4.11}$$

The residual contribution to node i of element j can be written as:

$$R_{i|\Omega_j} = R_{\Omega_j} \frac{V_{\Omega_j}}{n_v(\Omega_j)} - LW_{i|\Omega_j} \tag{4.12}$$

The first term in Eq. (4.12) is the cell residual computed as in Eq. (4.3). It is weighed by the volume of the cell divided by the number of vertex of the element. The $LW_{i|\Omega_j}$ term is computed on the dual cell $\mathscr{C}_i$ taking advantage of the Green-Gauss theorem.

$$LW_{i|\Omega_j} = \frac{1}{2} \Delta t \iiint_{\Omega_j \cap \mathscr{C}_i} \nabla \cdot [\mathscr{A} (\nabla \cdot F)] \, dV = \frac{1}{2} \Delta t \iint_{\partial \mathscr{C}_i} [\mathscr{A} (\nabla \cdot F)] \, dS \tag{4.13}$$

This term is then discretized to give:

$$LW_{i|\Omega_j} \simeq \frac{1}{2} \Delta t \, [\mathscr{A} (\nabla \cdot F)]_{\Omega_j} \frac{S_{i|\Omega_j}}{n_d} \tag{4.14}$$

where $S_{i|\Omega_j}$ is the normal associated to node i, and cell j; it is computed according to the scaling by n_d. It should be noticed that no weighing is required for the LW term because it is computed on the dual cell. Substituting Eq. (4.3) and Eq. (4.14) into Eq. (4.12) leads to:

$$R_{i|\Omega_j} = \left(I - \frac{\Delta t}{2n_d} \frac{n_v(\Omega_j)}{V_{\Omega_j}} \mathscr{A}_{\Omega_j} \cdot S_{i|\Omega_j} \right) R_{\Omega_j} \frac{V_{\Omega_j}}{n_v(\Omega_j)} \tag{4.15}$$

Recalling now Eq. (4.5) the distribution matrix takes the form:

$$D_{i|\Omega_j} = \frac{1}{n_v(\Omega_j)} \left(I - \frac{\Delta t}{2n_d} \frac{n_v(\Omega_j)}{V_{\Omega_j}} \mathscr{A}_{\Omega_j} \cdot S_{i|\Omega_j} \right) \tag{4.16}$$

4.2.2 The TTG4A and TTGC numerical schemes

Taylor-Galerkin (TG) schemes were first derived by Donea [38, 39], the key idea of the method being the coupling between a Taylor expansion in time and a Galerkin discretization in space. Selmin and Quartapelle [105, 92] extended this approach, and proposed the family of Two-step Taylor Galerkin (TTG) schemes. The TTG4A scheme developed by Quartapelle reaches third-order accuracy in space and fourth-order in time. The TTGC scheme is third-order both in space and time and has been developed by Colin and Rudgyard [28]. The general form of the TTG schemes is the following:

$$\tilde{U}^n = U^n + \alpha \Delta t \left(\frac{\partial U}{\partial t} \right)^n + \beta \Delta t^2 \left(\frac{\partial^2 U}{\partial t^2} \right)^n \tag{4.17}$$

$$U^{n+1} = U^n + \Delta t \left[\theta_1 \left(\frac{\partial U}{\partial t} \right)^n + \theta_2 \left(\frac{\partial \tilde{U}}{\partial t} \right)^n \right] + \Delta t^2 \left[\epsilon_1 \left(\frac{\partial^2 U}{\partial t^2} \right)^n + \epsilon_2 \left(\frac{\partial^2 \tilde{U}}{\partial t^2} \right)^n \right] \tag{4.18}$$

where $\alpha = 1/3$, $\beta = 1/12$, $\theta_1 = 1$, $\theta_2 = 0$, $\epsilon_1 = 0$ and $\epsilon_2 = 1/2$ for the TTG4A scheme, and $\alpha = 0.49$, $\beta = 1/6$, $\theta_1 = 0$, $\theta_2 = 1$, $\epsilon_1 = 0.01$ and $\epsilon_2 = 0$ for TTGC. The first and the second order temporal derivatives are replaced by spatial derivatives like for the Lax-Wendroff scheme. The Galerkin method is then applied on the resulting equations which makes the mass-matrix appear in the left-hand-side. More details about the derivation of these schemes can be found in the thesis of Lamarque [58].

Chapter 5

Boundary conditions

5.1 Characteristic boundary conditions

5.1.1 Generalities

When considering the Navier-Stokes equations for the unsteady and compressible flows, one cannot define a simple mathematical framework. The convective part has properties of hyperbolic systems, whereas the diffusive part provides elliptic properties to the system. The source terms turn the system of equations into a non-homogeneous one. It also involves self-transport of the velocity which makes the equations strongly non-linear. Therefore, even the theoretical definition of the boundary conditions is not obvious and a special treatment is required. Oliger and Sundstrom [82], Dutt [42], Strikwerda [113] have theoretically found the number of conditions which have to be satisfied depending on the system of equations to be solved, the boundary and the flow speed (described in Table 5.1).

Performing a clear separation of the contribution of variables having a different domain of influence is not possible for the Navier-Stokes equations. For instance, imposing the gradient of temperature for a solid boundary can affect the heat transfer as well as the acoustics. The

Boundary	Non-reacting Euler	Non-reacting Navier-Stokes	Reacting Navier-Stokes
Subsonic inflow	4	5	$5 + N$
Subsonic outflow	1	4	$4 + N$
Supersonic inflow	5	5	$5 + N$
Supersonic outflow	0	4	$4 + N$

Table 5.1 - *Number of conditions required for a well-defined 3-D problem. N is the number of species for the reacting flow.*

decomposition into waves for the Euler equations is presented in Thompson [116] and is called Euler Characteristic Boundary Conditions (ECBC). Poinsot and Lele [86] provided a way to deal with waves for the non-reacting Navier-Stokes equations, even if the characteristic waves definition is of course theoretically questionable for such equations. The authors only consider the hyperbolic part of the equations for the characteristic treatment in a first step, and the contributions of the other terms are added in a second step. These Navier-Stokes Characteristic Boundary Conditions (NSCBC) have been extended to multi-components flow (reacting) by Baum *et al.* [9] and also described by Moureau *et al.* [75]. The mentioned approaches consider only waves normal to the boundary, but for example Yoo and Im [122] have developed a method to handle correctly the acoustic waves when transversal fluctuations or source terms are present. Lodato *et al.* [64] have also developed boundary conditions to take into account three-dimensional effects (3D-NSCBC).

In addition to handling properly the boundary conditions, how the system surrounding the computational domain interacts with the numerical simulation should theoretically be known (heat transfers, acoustic reflections, etc.). However, such informations are often not available because of experimental measurements or modelling limits. The boundary conditions can have a first-order influence on the results, especially when acoustics is involved, that is the reason why they are presented in this section. The approach followed by Poinsot and Lele, and Moureau *et al.* [75], is described since it corresponds the best to the coding made in the ideal-gas version of AVBP. It provides to the reader some elementary concepts that are required hereafter.

5.1.2 Characteristic form of the Navier-Stokes equations

The aim of the decomposition into characteristic waves is to separate the information ingoing or outgoing the computational domain. As mentioned previously, this decomposition cannot be performed directly on the Navier-Stokes (NS) equations. Instead, one can only consider the Euler part of the NS equations for the characteristic treatment and then add the sources and diffusive terms afterwards. This can be done writing the Euler part of the equations that are solved:

$$\frac{\partial U_i}{\partial t} + \frac{\partial F_{ij}}{\partial x_j} = 0 \tag{5.1}$$

and expressing it in a characteristic form:

$$\frac{\partial W_i}{\partial t} + D\frac{\partial W_i}{\partial n} = 0 \tag{5.2}$$

where D is a diagonal matrix, which contains the eigenvalues of the system, that is to say the speed of propagation of the different characteristic variables, also called *waves* here. In Eq. (5.2) only the derivatives normal to the boundary are kept: the Local One-Dimensional Inviscid (LODI) assumption is used. In such form the waves are independent and are governed by their own equation. Depending on the direction of propagation of the wave (ingoing or outgoing), one can *physically* handle the boundary conditions. The ingoing waves are set in order to impose the desired flow properties (temperature, pressure, etc.), whereas the outgoing waves are left untouched. The treatment of the boundaries is done in three steps: transformation of the conservative variables predicted by the numerical scheme into characteristic variables; correction of the ingoing waves; transformation of the corrected characteristic variables into conservative variables. The transformation matrices used for the characteristic decomposition are presented in the next section.

5.1.3 Transformation into characteristic variables

The conservative variables $U = (\rho u, \rho v, \rho w, \rho E, \rho_1 \dots \rho_k \dots \rho_N)$ are first transformed into primitive variables $V = (u, v, w, p, \rho_1 \dots \rho_N)$ using the matrix M. This matrix is built using the total differential form of the conservative variables, that can be written for the first element of U for instance:

$$dU_1 = \frac{\partial U_1}{\partial V_1} dV_1 + \cdots \frac{\partial U_1}{\partial V_{5+k}} dV_{5+k} + \cdots \tag{5.3}$$

Identification of the different partial derivatives in Eq. (5.3) leads to the matrix M. Details to establish this matrix can be found in the PhD thesis of Porta [90]. The inverse matrix M^{-1} can easily be defined using the same approach to write the primitive variables as a function of the conservative ones. These two transformation matrices are:

$$M = \frac{\partial U}{\partial V} \quad \text{and} \quad M^{-1} = \frac{\partial V}{\partial U} \tag{5.4}$$

The primitive variables V are defined in the global system of coordinates $X = (x, y, z)$ whereas one needs to express these variables in a system of coordinates normal to the boundary $X_n = (n, t_1, t_2)$: the jacobian matrix is diagonalizable when considering one direction only and we are mainly interested by waves normal to the boundary. The matrix for the transformation of the primitive variables into primitive variables in X_n, $V_n = (u_n, u_{t1}, u_{t2}, p, \rho_1 \dots \rho_N)$, is noted Ω_V^{-1} and the inverse matrix is noted Ω_V:

$$\Omega_V = \frac{\partial V}{\partial V_n} \quad \text{and} \quad \Omega_V^{-1} = \frac{\partial V_n}{\partial V} \tag{5.5}$$

These rotation matrices are built using simple geometrical considerations and are also detailed in [90]. The transformation of the variables V_n into characteristic variables $W = (w^+, w^-, w^{t1}, w^{t2}, w^1 \dots w^N)$ is detailed hereafter since the relationships between both are frequently used in the next sections. The Euler part of the NS equations can be written for primitive variables in the basis normal to the boundary:

$$\left[\frac{\partial}{\partial t} + \underbrace{\begin{pmatrix} u_n & 0 & 0 & \frac{1}{\rho} & 0 & \cdots & 0 \\ 0 & u_n & 0 & 0 & 0 & \cdots & 0 \\ 0 & 0 & u_n & 0 & 0 & \cdots & 0 \\ \rho c^2 & 0 & 0 & u_n & 0 & \cdots & 0 \\ \rho_1 & 0 & 0 & 0 & u_n & \cdots & 0 \\ \vdots & \vdots & \vdots & \vdots & \vdots & \ddots & \vdots \\ \rho_N & 0 & 0 & 0 & 0 & \cdots & u_n \end{pmatrix}}_{N} \frac{\partial}{\partial n} + T_1 \frac{\partial}{\partial t_1} + T_2 \frac{\partial}{\partial t_2}\right] \begin{pmatrix} u_n \\ u_{t1} \\ u_{t2} \\ p \\ \rho_1 \\ \vdots \\ \rho_N \end{pmatrix} = 0 \tag{5.6}$$

Diagonalization of the normal jacobian matrix of flux for primitive variables N leads to the matrix D containing the eigenvalues $\lambda = (u_n + c, u_n - c, u_n, u_n \dots u_n)$ of the system. Then, one defines the transformation matrices L and R as:

$$L = \frac{\partial W}{\partial V_n} \quad \text{and} \quad R = \frac{\partial V_n}{\partial W} \tag{5.7}$$

Equation. (5.6) can be expressed in terms of the characteristic variables W by multiplying the former by L and noting that $N = RDL$:

$$\left[\frac{\partial}{\partial t} + D\frac{\partial}{\partial n} + LT_1R\frac{\partial}{\partial t_1} + LT_2R\frac{\partial}{\partial t_2}\right]W = 0 \tag{5.8}$$

To obtain Eq. (5.2), the LODI assumption is used. It means that the transversal derivatives of W are neglected, so that only the temporal derivative remains as well as the normal derivative with the diagonal matrix. The speeds of propagation of the different characteristic variables are thus well-defined. The transformation matrices L and R can be written as follows:

$$L = \begin{pmatrix} 1 & 0 & 0 & \frac{1}{\rho c} & 0 & \cdots & 0 \\ -1 & 0 & 0 & \frac{1}{\rho c} & 0 & \cdots & 0 \\ 0 & 1 & 0 & 0 & 0 & \cdots & 0 \\ 0 & 0 & 1 & 0 & 0 & \cdots & 0 \\ 0 & 0 & 0 & -\frac{\rho_1}{\rho c^2} & 1 & \cdots & 0 \\ \vdots & \vdots & \vdots & \vdots & \vdots & \ddots & 0 \\ 0 & 0 & 0 & -\frac{\rho_N}{\rho c^2} & 0 & \cdots & 1 \end{pmatrix} \quad \text{and} \quad R = \begin{pmatrix} \frac{1}{2} & -\frac{1}{2} & 0 & 0 & 0 & \cdots & 0 \\ 0 & 0 & 1 & 0 & 0 & \cdots & 0 \\ 0 & 0 & 0 & 1 & 0 & \cdots & 0 \\ \frac{\rho c}{2} & \frac{\rho c}{2} & 0 & 0 & 0 & \cdots & 0 \\ \frac{\rho_1}{2c} & \frac{\rho_1}{2c} & 0 & 0 & 1 & \cdots & 0 \\ \vdots & \vdots & \vdots & \vdots & \vdots & \ddots & 0 \\ \frac{\rho_N}{2c} & \frac{\rho_N}{2c} & 0 & 0 & 0 & \cdots & 1 \end{pmatrix} \tag{5.9}$$

Finally, the matrices $L_U = M^{-1}\Omega_V^{-1}L$ and $R_U = M\Omega_V R$ are defined to perform the characteristic treatment on the conservative variables within the solver. The different steps of the decomposition into waves are presented in Table 5.2. The reader must keep in mind that only the final expression of the matrices L_U and R_U (not shown here) are used within the solver. Using the expression of the matrix L defined in Eq. (5.9), simple relations between the waves and the primitive variables related to the system of coordinates of the boundary can be written:

$$\partial w^+ = \partial p/\rho c + \partial u_n \tag{5.10}$$

$$\partial w^- = \partial p/\rho c - \partial u_n \tag{5.11}$$

$$\partial w^{t1} = \partial u_{t1} \tag{5.12}$$

$$\partial w^{t2} = \partial u_{t2} \tag{5.13}$$

$$\partial w^k = \partial \rho_k - \rho_k \partial p/\rho c^2 \tag{5.14}$$

The waves $w^\pm$ propagate with the velocity $u_n \pm c$ and are considered to be acoustic. The waves w^{t1} and w^{t2} propagate at the velocity of the flow crossing the boundary and are related to the vortical perturbations, then they are called shear or vorticity waves. The summation of the species waves w^k, which are also convected through the boundary, yields to the entropy wave w^{S}:

$$\partial w^{\mathrm{S}} = \partial \rho - \partial p/c^2 \tag{5.15}$$

Conservative		Primitive		Primitive in a normal basis		Characteristic
∂U		∂V		∂V_n		∂W
$\partial \begin{pmatrix} \rho u \\ \rho v \\ \rho w \\ \rho E \\ \rho_1 \\ \vdots \\ \rho_N \end{pmatrix}$	$\begin{matrix} M^{-1} \\ \rightarrow \\ \leftarrow \\ M \end{matrix}$	$\partial \begin{pmatrix} u \\ v \\ w \\ p \\ \rho_1 \\ \vdots \\ \rho_N \end{pmatrix}$	$\begin{matrix} \Omega_V^{-1} \\ \rightarrow \\ \leftarrow \\ \Omega_V \end{matrix}$	$\partial \begin{pmatrix} u_n \\ u_{t1} \\ u_{t2} \\ p \\ \rho_1 \\ \vdots \\ \rho_N \end{pmatrix}$	$\begin{matrix} L \\ \leftarrow \\ \rightarrow \\ R \end{matrix}$	$\partial \begin{pmatrix} w^+ \\ w^- \\ w^{t1} \\ w^{t2} \\ w^1 \\ \vdots \\ w^N \end{pmatrix}$
	$\leftarrow$ $\rightarrow$		L_U R_U		$\leftarrow$ $\rightarrow$	

Table 5.2 - *Relations between the different sets of variables.*

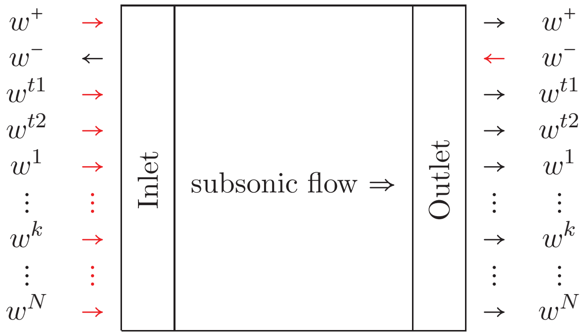

Figure 5.1 - *Example of the decomposition into waves at the inlet and outlet of a subsonic case*

An example of the decomposition into waves at the inlet and outlet of a typical subsonic configuration is described in Fig. 5.1. It can be seen that $4 + N$ waves are ingoing at the inlet, whereas only one wave is ingoing at the outlet. The ingoing waves have to be imposed to make the problem well-posed, and one can see in this example that the number of conditions to be defined for this case agrees with Table 5.1. How the ingoing waves are defined to impose the flow conditions is addressed in the next section. The resulting acoustic behaviour is especially investigated.

5.2 Acoustics of the characteristic boundary conditions

5.2.1 Acoustic variables

As a preliminary step to study the acoustic behavior of the different boundary conditions available in AVBP, some common acoustic variables are defined. A one-dimensional axially oriented configuration is assumed in this section. The specific acoustic impedance $\mathcal{Z}$[1] is first defined that is written as:

$$\mathcal{Z}(i\omega) = \frac{1}{\bar{\rho}\bar{c}} \frac{\hat{p}}{\hat{u}} \tag{5.16}$$

where $\hat{p}$, respectively $\hat{u}$, is the Fourier-transform of the pressure, respectively of the axial velocity component. It can be noticed that the concept of impedance is a general physical one, which can be found in many other fields like electricity or mechanical sciences. Generally speaking, the impedance is representative of the ratio between a *force* and a *flux*, that is to say of the potential power involved in the system. The electrical impedance is the ratio between the electromotive force and the electric current whereas the mechanical impedance is the ratio between the force acting on a solid body and its displacement velocity. At this point, the concept of *real* and *imaginary* mechanical work related to the impedance of an interface has to be introduced. If one considers a mono-dimensional pipe with a fluid at rest (in a steady point of view) and an imaginary membrane of surface $\mathcal{A}$, the steady complex mechanical power $\bar{P}$ exchanged by this membrane can simply be written:

$$\bar{P}(i\omega) = \mathcal{A}\ \hat{p}(i\omega)\ \hat{u}^*(i\omega) \tag{5.17}$$

where $\hat{u}^*$ is the complex conjugate of $\hat{u}$. Substituting the expression of the pressure defined from Eq. (5.16) into Eq. (5.17) leads to:

$$\bar{P}(i\omega) = \bar{\rho}\bar{c}\mathcal{A}\ |\hat{u}|^2\ \mathcal{Z}(i\omega) \tag{5.18}$$

The *real* steady mechanical (or acoustic) power exchanged by the membrane (corresponding to a loss or gain of mechanical or acoustic energy) is directly related to the real part of the impedance:

$$\Re\left\{\bar{P}(i\omega)\right\} = \bar{\rho}\bar{c}\mathcal{A}\ |\hat{u}|^2\ \Re\left\{\mathcal{Z}(i\omega)\right\} \tag{5.19}$$

As mentioned previously, the concepts related to the impedance are general physical concepts and several analogies can be found with the other scientific fields. If the relationship Eq. 5.19 is considered in an electrical point of view for instance (where $\hat{u}$ is replaced by the Fourier-transform of the electric current, and $\Re\{\mathcal{Z}(i\omega)\}$ by the electrical resistance), one obtains the well-known Joule's first law providing the thermal power generated by an electric current flowing through a conductor. Therefore, the impedance is defined in the general form:

$$\mathcal{Z} = R + iX \tag{5.20}$$

where R is the resistive part of the impedance (resistance) and where X is the reactive part (reactance). This last part is representative of the *storage* of the energy at the interface. Positive reactance relates to the inductance, whereas it relates to the capacitance when it is negative. According to the relationship Eq. (5.19), passive physical systems have a positive real part of the impedance. The physical systems of interest are mostly passive, so that the resistance is known to be always positive, but it can be negative here if the system has an internal source of energy (as it can be the case in fluid mechanics of reacting flows for instance). In the acoustic domain,

---

[1] The specific acoustic impedance is often noted ζ in the literature.

many authors (as Candel [20] does), define the normal component of the steady acoustic energy flux $\mathscr{F}_n$ as follows:

$$\mathscr{F}_n = \frac{1}{2}|\hat{u}|^2 \left[\Re\{\mathcal{Z}(i\omega)\ \}(1+\bar{\mathcal{M}}^2) + \bar{\mathcal{M}}(1+|\mathcal{Z}(i\omega)|^2)\right] \tag{5.21}$$

where $\bar{\mathcal{M}}$ is the steady Mach number of the flow related to the normal component of the velocity. Equation (5.21) providing the steady acoustic energy flux will be used in the section hereafter. The specific acoustic admittance $\mathcal{Y}$[2] is defined as the inverse of the impedance Eq. (5.16):

$$\mathcal{Y} = \frac{1}{\mathcal{Z}} \tag{5.22}$$

The steady acoustic energy flux $\mathscr{F}_n$ can also be written as a function of the Fourier-transform of pressure $\hat{p}$ and the admittance $\mathcal{Y}$ in the same form as in Eq. (5.21) (see Sec. 5.2.3). The reflection coefficient $\mathcal{R}$ is defined as the ratio between the Fourier-transform of the acoustic ingoing wave (w^- for an outlet and w^+ for an inlet) and the outgoing one (w^+ for an outlet and w^- for an inlet) as defined in section Sec. 5.1:

$$\mathcal{R}(i\omega) = \left[\frac{\hat{w}^-}{\hat{w}^+}\right]_{\text{outlet}} \quad \text{or} \quad \left[\frac{\hat{w}^+}{\hat{w}^-}\right]_{\text{inlet}} \tag{5.23}$$

The acoustic variables mentioned above, namely the acoustic impedance $\mathcal{Z}$, the acoustic admittance $\mathcal{Y}$ or the reflection coefficient $\mathcal{R}$, are defined for harmonic regimes. It is important to notice that it is equivalent writing the ratio of the Fourier-transforms of the different quantities, or writing the Fourier-transforms of the temporal derivatives of the corresponding quantities, since $(\cdot)_t \equiv i\omega$. Especially, the reflection coefficient $\mathcal{R}$ can also be expressed as follows:

$$\mathcal{R}(i\omega) = \left[\frac{\widehat{w_t}^-}{\widehat{w_t}^+}\right]_{\text{outlet}} \quad \text{or} \quad \left[\frac{\widehat{w_t}^+}{\widehat{w_t}^-}\right]_{\text{inlet}} \tag{5.24}$$

According to relationships of section Sec. 5.1, the waves $\widehat{w_t}^+$ and $\widehat{w_t}^-$ can be expressed as a function of the pressure and velocity variations in the equation of the reflection coefficient. The reflection coefficient can be written as a function only of the impedance dividing both the numerator and the denominator by the velocity variations. After some algebra, it leads to the following relation between the impedance and the reflection coefficient [87]:

$$\mathcal{Z} = \left[\frac{\mathcal{R}+1}{\mathcal{R}-1}\right]_{\text{inlet}} \tag{5.25}$$

5.2.2 Boundary condition with relaxation of the pressure or the velocity

The decomposition of the conservative variables of the flow into characteristic waves detailed in section Sec. 5.1 can be used to determine the number of conditions to prescribe on a boundary. This decomposition assumes that the convective part of the equations contains the most important part of the flow information (decomposition based on the Euler equations). One can show

---

[2] The specific acoustic admittance is often noted β in the literature.

in this case that four independent quantities have to be imposed at the inlet of a subsonic 3-D and single-species flow, and only one for an outlet [86]. It is usual to impose the three velocity components and the temperature at the inlet, and the pressure at the outlet. However imposing in a *strong* way these quantities leads to an acoustically reflective boundary conditions. Indeed if one considers for instance a one-dimensional, single-species and subsonic flow at the outlet (in this case only two independent quantities have to be imposed at inlet, but still one at the outlet), the pressure variation ∂p can be written in the following manner (as seen in section Sec. 5.1):

$$\partial p = \partial w^+ + \partial w^- \tag{5.26}$$

If the pressure is imposed in a *strong* way ($\partial p = 0$), the boundary condition is acoustically fully-reflective since the modulus of the reflection coefficient $\mathcal{R}$ is unity:

$$\mathcal{R}(i\omega) = \frac{\hat{w}^+}{\hat{w}^-} = -1 \tag{5.27}$$

Therefore, both for physical and numerical reasons, the pressure at the outlet is generally not directly imposed since it would lead to an acoustically closed system (if all the other boundaries are also fully-reflective). Acoustic energy can be produced in fluid mechanics of reactive flows so that it would lead to a physically or numerically unstable system (even if it can be true for real systems). To avoid this issue, a relaxation on the pressure can be introduced [99]. At the outlet, only the wave w^- can be imposed, and since it involves pressure and velocity variations:

$$\partial w^- = \frac{1}{\rho c}\partial p + \partial u \tag{5.28}$$

the relaxation of the pressure based on the term ∂p is justified. If an ideal numerical temporal integration is assumed, the ingoing acoustic wave at the outlet w^- with relaxation of pressure is, for this boundary condition, written as follows:

$$w_t^- = -\frac{2\kappa_p}{\rho c}\left(p - \bar{p}\right) \tag{5.29}$$

where κ_p is the relaxation coefficient on the pressure and $\bar{p}$ is defined as both the target and the steady pressure at the outlet. Selle *et al.* [104] have shown that such a boundary condition behaves like a first-order filter, with the relaxation coefficient κ_p as the cut-off angular frequency. The demonstration of Selle *et al.* is developed below, and it is generalized to the boundary conditions used hereafter.

Let's consider small harmonic perturbations of pressure p, velocity u and mass-density ρ around the steady state noted $\bar{(\cdot)}$:

$$\begin{aligned} p &= \bar{p} + \hat{p}\exp\{-i\omega t\} \\ u &= \bar{u} + \hat{u}\exp\{-i\omega t\} \\ \rho &= \bar{\rho} + \hat{\rho}\exp\{-i\omega t\} \end{aligned} \tag{5.30}$$

The assumption of small perturbations means that $\hat{(\cdot)}/\bar{(\cdot)} \ll 1$. Using Eqs. (5.29) and (5.30), one can obtain the expression of the Fourier-transform of the outgoing acoustic wave[3] $\widehat{w_t}^+$ at

---

[3] w, $\widehat{w}$ and $\widehat{w_t}$ are all called *waves* in the present manuscript.

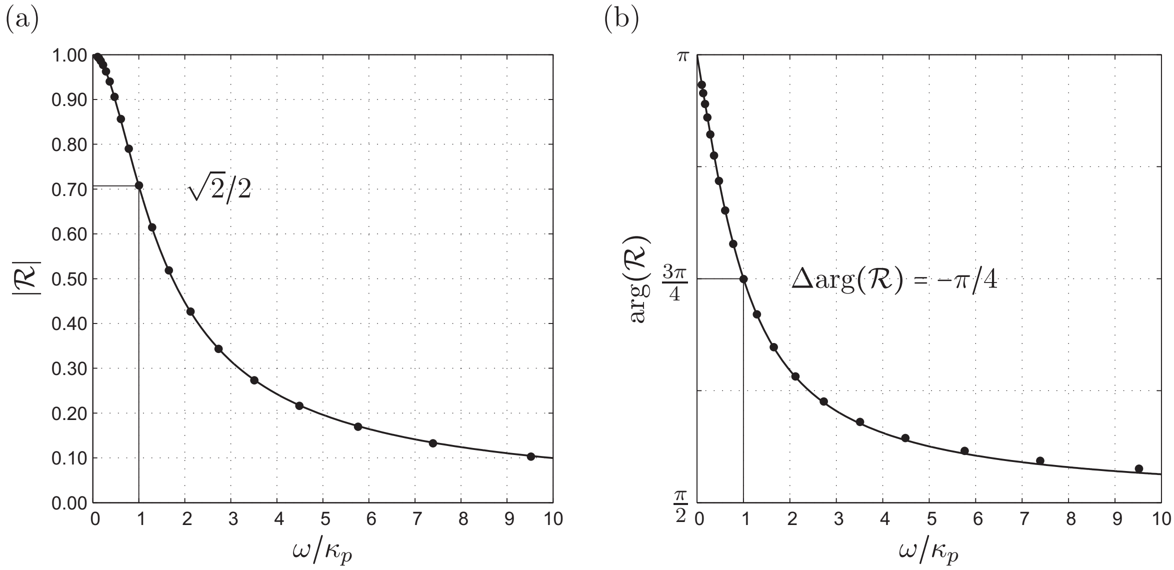

Figure 5.2 - *Reflection coefficient of the boundary condition at the outlet with relaxation of the pressure, with (a) the modulus and (b) the argument, for a steady Mach number $\bar{\mathcal{M}}$ of 0.5. Theoretical results (—); Numerical calculations with AVBP (•).*

the first-order, as a function of the ingoing one and the pressure perturbation $\hat{p}$:

$$\widehat{w_t}^+ = -\widehat{w_t}^- - \frac{2}{\bar{\rho}\bar{c}} i\omega\hat{p} \tag{5.31}$$

One obtains the general form of the reflection coefficient $\mathcal{R}$ at the outlet:

$$\mathcal{R}(i\omega) \quad = \quad -\frac{1}{1 + \frac{2}{\bar{\rho}\bar{c}} i\omega\hat{p}/\widehat{w_t}^-} \tag{5.32}$$

For the boundary condition with relaxation of pressure at the outlet, the first-order Fourier-transform of the ingoing wave $\widehat{w_t}^-$ can be written as:

$$\widehat{w_t}^- = -\frac{2\kappa_p}{\bar{\rho}\bar{c}}\hat{p} \tag{5.33}$$

Finally, the expression of Selle *et al.* [104] is recovered, providing the reflection coefficient at the outlet as a function of the angular frequency ω and the relaxation coefficient κ_p:

$$\mathcal{R}(i\omega) = -\frac{1}{1 - i\omega/\kappa_p} \tag{5.34}$$

Selle *et al.* [104] focus on the acoustic properties of an outlet boundary condition with relaxation of pressure, but the same approach can be followed to investigate the acoustic behavior of an inlet boundary condition with relaxation on the velocity, or the mass-flow as shown in the next section. At the inlet, it two quantities need to be imposed for a 1-D, mono-species subsonic flow, which are generally the velocity and the temperature (or the mass-flow and the temperature). The temperature is imposed by means of the entropy wave w^{S}, so that it is not directly involved in the acoustics of the boundary. However, the velocity is imposed by the means of the ingoing acoustic wave w_t^+, with usually a relaxation on the velocity:

$$w_t^+ = -2\kappa_u \left(u - \bar{u}\right) \tag{5.35}$$

where κ_u is the relaxation coefficient on the velocity. From the general relations of Sec. 5.1, one can write the first-order Fourier-transform of the outgoing acoustic wave $\widehat{w_t}^-$as a function of the ingoing one and the velocity perturbation $\hat{u}$:

$$\widehat{w_t}^- = \widehat{w_t}^+ + 2i\omega\hat{u} \tag{5.36}$$

Therefore, one obtains the general form of the reflection coefficient $\mathcal{R}$ at the inlet:

$$\mathcal{R}(i\omega) \quad = \quad \frac{1}{1 + 2i\omega\hat{u}/\widehat{w_t}^+} \tag{5.37}$$

For the boundary condition with the relaxation of the velocity at the inlet, the first-order Fourier-transform of the ingoing wave $\widehat{w_t}^+$ can be written in the following manner:

$$\widehat{w_t}^+ = -2\kappa_u\hat{u} \tag{5.38}$$

Finally, the expression obtained for this boundary condition is very similar to the one obtained for the outlet with relaxation on pressure by Selle *et al.* [104], since it simply involves a phase-difference of π radians and expresses as follows:

$$\mathcal{R}(i\omega) = \frac{1}{1 - i\omega/\kappa_u} \tag{5.39}$$

The modulus (a) and the argument (b) of the reflection coefficient of the outlet boundary condition with relaxation on pressure plotted versus reduced angular frequency ω/κ_p can be observed in Fig. 5.2. The former reflection coefficient is calculated both theoretically and measured in a dedicated numerical computation with AVBP, with a steady Mach number $\bar{\mathcal{M}}$ of 0.5. The same behavior would be found for the inlet boundary condition with relaxation of the velocity, with however additional π radians for the argument. As mentioned before, these boundary conditions behave like a first-order low-pass filter, so that the power rolloff approaches 20 dB per decade in the limit of high frequencies, and the cut-off angular frequency (defined for -3dB) is the relaxation coefficient κ.

5.2.3 Boundary condition with relaxation of the mass-flow

Imposing the mass-flow rate at the inlet of a computational domain instead of the velocity can be preferred in most practical cases. This is especially the case when the computational case involves a choked flow. Indeed, for a choked flow the mass-flow rate $\dot{m}$ is directly proportional to the inlet thermodynamic conditions by the relationship:

$$\rho u \equiv \frac{p_t}{\sqrt{T_t}} \tag{5.40}$$

Therefore, the flow within the computational domain no longer depends on the outlet boundary conditions. If the velocity is imposed, and a deviation in the computation occurs on the main flow, it could impact on the mass-flow, which can be a problem for the equivalence ratio. The ingoing acoustic wave w_t^+ is for this boundary condition defined as follows:

$$w_t^+ = -\frac{2\kappa_{\rho u}}{\rho(1-\mathcal{M})}\left(\rho u - \overline{\rho u}\right) \tag{5.41}$$

where $\kappa_{\rho u}$ is the relaxation coefficient of the mass-flow. One can easily show that like for the previous boundary conditions, the general form of the reflection coefficient can be written as follows:

$$\mathcal{R}(i\omega) \quad = \quad -\frac{1}{1+\frac{2}{\bar{\rho}\bar{c}} i\omega\hat{p}/\widehat{w_t}^+} \tag{5.42}$$

Equation (5.41) can be written for small perturbations of the velocity $\hat{u}$ and mass-density $\hat{\rho}$, and the resulting expression of the Fourier-transform of the ingoing acoustic wave $\widehat{w_t}^+$ is:

$$\widehat{w_t}^+ = -\frac{2\kappa_{\rho u}}{\bar{\rho}(1-\bar{\mathcal{M}})}\left(\hat{\rho}\bar{u} + \bar{\rho}\hat{u}\right) \tag{5.43}$$

The mass-density fluctuation can be replaced according to the isentropic relation $\hat{\rho}/\bar{\rho} = \hat{p}/\gamma\bar{p}$ and Eq (5.43) leads to:

$$\widehat{w_t}^+ = -\frac{2\kappa_{\rho u}}{\bar{\rho}\bar{c}(1-\bar{\mathcal{M}})}(\bar{\mathcal{M}} + \underbrace{\bar{\rho}\bar{c}\hat{u}/\hat{p}}_{\mathcal{Z}^{-1}})\hat{p} \tag{5.44}$$

The acoustic impedance $\mathcal{Z}$ and the relationship between $\mathcal{Z}$ and the reflection coefficient $\mathcal{R}$ of Eq. (5.25) are used in Eq. (5.44). After some algebra, the following expression is obtained:

$$\mathcal{R}(i\omega) \quad = \quad -\frac{1}{1-(i\omega/\kappa_{\rho u})\frac{1-\bar{\mathcal{M}}}{\frac{\mathcal{R}-1}{\mathcal{R}+1}+\bar{\mathcal{M}}}} \tag{5.45}$$

Finally, the expression of the reflection coefficient for an inlet boundary condition with relaxation of the mass-flow rate can be written:

$$\mathcal{R}(i\omega) \quad = \quad \frac{1-\bar{\mathcal{M}}}{1+\bar{\mathcal{M}}}\frac{1}{1-(i\omega/\kappa_{\rho u})\frac{1-\bar{\mathcal{M}}}{1+\bar{\mathcal{M}}}} \tag{5.46}$$

Figure. 5.3 shows the modulus (a) and the argument (b) of the reflection coefficient of the inlet boundary condition with relaxation on the mass-flow rate, plotted versus reduced angular frequency $\omega/\kappa_{\rho u}$ calculated theoretically and measured in a numerical computation test case,

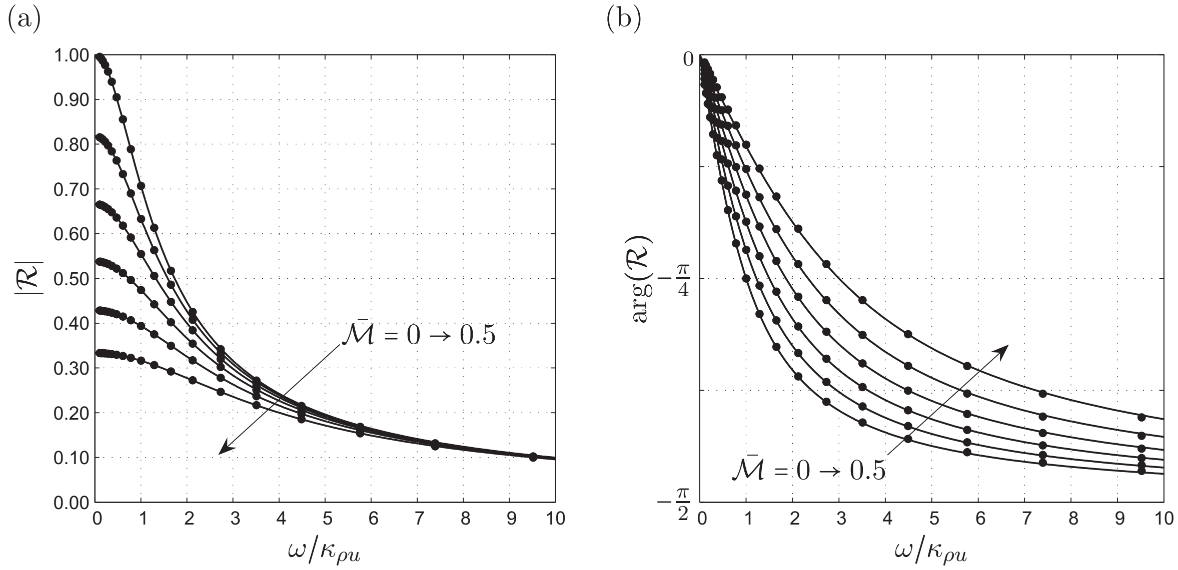

Figure 5.3 - *Reflection coefficient of the inlet boundary condition with relaxation of the mass-flow rate, with (a) the modulus and (b) the argument, for different steady Mach numbers $\bar{\mathcal{M}}$ ranging from 0 up to 0.5 with steps of 0.1. Theoretical results (—); Numerical calculations with AVBP (•).*

with six different steady Mach number $\bar{\mathcal{M}}$ ranging from 0 up to 0.5: the modulus of the reflection coefficient decreases as the Mach number $\bar{\mathcal{M}}$ increases. For non-zero Mach numbers, the modulus is less than one when the angular frequency goes to zero, which may seem strange in a first approach, since one can think that the system is losing acoustic energy when the frequency is asymptotically zero (steady state). However, the physical interpretation of the acoustic impedance provided in Sec. 5.2.1 is based on a flow at rest. Since the Mach number is important, the explanations on the properties of the reflection coefficient related to acoustic energy are no longer valid. Therefore, the general expression of the normal component of the steady acoustic energy flux $\mathscr{F}_n$ of Eq. (5.21) must be considered. The acoustic flux can be rewritten as a function of the pressure fluctuations $\hat{p}$ and the acoustic admittance $\mathcal{Y}$ instead of the velocity fluctuations and the impedance:

$$\mathscr{F}_n = \frac{1}{2\bar{\rho}\bar{c}}|\hat{p}|^2 \left[\Re\{\mathcal{Y}(i\omega)\}(1+\bar{\mathcal{M}}^2) + \bar{\mathcal{M}}(1+|\mathcal{Y}(i\omega)|^2)\right] \tag{5.47}$$

The admittance for this boundary condition can be calculated from Eq. (5.46), and when the angular frequency is zero, it is simply equal to the opposite of the steady Mach number:

$$\mathcal{Y}(\omega = 0) = -\bar{\mathcal{M}} \tag{5.48}$$

Substituting this expression into Eq. 5.47 shows that there is no flux of acoustic energy crossing this boundary condition when the frequency tends to zero, even if the amplitude of the reflected wave is lower than the incident one.

For the boundary conditions with relaxation on the pressure or the velocity, the reflection coefficient is asymptotically equal to one when the frequency is low, but the acoustic energy

Boundary condition	Reflection coeffcient	Angle when $\omega/\kappa \to 0$	Angle when $\omega/\kappa \to \infty$
Relaxation p	$-\dfrac{1}{1 - i\omega/\kappa_p}$	π	$+\dfrac{\pi}{2}$
Relaxation u	$+\dfrac{1}{1 - i\omega/\kappa_u}$	0	$-\dfrac{\pi}{2}$
Relaxation ρu	$\frac{1-\bar{\mathcal{M}}}{1+\bar{\mathcal{M}}}\dfrac{1}{1 - (i\omega/\kappa_{\rho u})\frac{1-\bar{\mathcal{M}}}{1+\bar{\mathcal{M}}}}$	0	$-\dfrac{\pi}{2}$

Table 5.3 - *Reflection coefficients of the boundary conditions used in this thesis.*

flux must also be evaluated. However, for these two boundary conditions, the demonstration is obvious since the variation of the pressure $\hat{p}$ or the velocity $\hat{u}$ tends to zero when relaxation coefficient κ is high (that is to say when the reduced angular frequency is low). Using Eqs. (5.47) and (5.21) also shows that there is no flux of acoustic energy crossing these two boundaries in this case.

5.2.4 Summary of the acoustic behavior of the main boundary conditions

The boundary conditions studied in the previous section have similar behaviors. The reflection coefficients of these boundaries are first-order low-pass filters (the power rolloff tends to 20 dB per decade for high frequencies), with cut-off angular frequencies proportional to the relaxation coefficients κ. The main properties of the acoustic behavior of these boundary conditions are summarized in Table 5.3.

Nevertheless, these boundary conditions have not been initially designed to reproduce specific impedances, but just to avoid numerical problems due to acoustics. The relaxation coefficients are generally simply chosen to impose the desired target values, and not to define some specific acoustic properties. For aeroacoustic applications, it seems obvious that the acoustic impedances have to be well-defined and that the boundaries often play an important role. The capabilities of a first-order system to stand for a *real* one are of course limited. In the numerical calculations of Part II these *classical* boundary conditions have been used, but a specific effort has been made on the choice of the different parameters in order to match the *real* acoustic properties, when they were available. To finish, one should note that acoustically-designed boundary conditions also exist. The next section briefly presents the main issues related to such boundary conditions and why they were not used here.

5.3 About time-domain impedance boundary conditions

The hard point in the acoustic-design of a boundary condition in a time-domain simulation, is due to the fact that impedances are defined in the frequency-domain. Therefore, computational problem appears when the variables of the flow have to be transposed to the temporal domain. Indeed, algebraic product in the frequency-domain is equivalent to convolution product in the time-domain. If one considers as an example the acoustic admittance from Eq. (5.22), the velocity can be written in both time- and frequency-domain as follows:

$$\hat{u} = \bar{\rho}\bar{c}\hat{p}\mathcal{Y}(i\omega) \Leftrightarrow u(t) = \bar{\rho}\bar{c}\int_0^t u(t-\tau)y(\tau)d\tau \tag{5.49}$$

where y is the acoustic impedance in the time-domain (inverse-Fourier-transform of the admittance $\mathcal{Y}$). First of all, the direct calculation of integral in Eq. (5.49) involves the storage of the entire history of the velocity at the boundary. This storage can be a limiting factor depending on the computation case and resources. Secondly, the calculation of this convolution product must be performed for each time with the whole history. This last point definitively excludes such a kind of direct approach.

However, several techniques have been developed to deal with time-domain impedances. One can for instance mention the work of Reymen *et al.* [96] who propose a method to calculate recursively the integral term of Eq. (5.49), thus minimizing both the storage and the computational cost. Authors have used the Tam and Auriault three parameters impedance model [115] with a set of well-chosen functions making the recursive calculation of this integral possible. The works of Özyörük *et al.* [83], Rienstra [97] and Cotté *et al.* [30] can also be cited. Time-domain impedance boundary conditions have also been extensively addressed by Nottin during his PhD thesis[**?**]. All these techniques allow a better representation of the acoustic behaviour of the boundary condition in comparison with the first-order one presented previously, but they require a specific implementation in the CFD code and a significant development and validation effort. Therefore, these boundary conditions are not used hereafter.

Part II

Theoretical and numerical investigations of combustion noise

Table of Contents

Chapter 6

Combustion noise theory

6.1 Introduction on combustion noise

Over the last five decades, jet and external aerodynamic noises of aircraft have been substantially reduced. Further developments will be needed for modern aircraft design in order to meet the increasingly restrictive rules about noise reduction. While drastic reductions have already been achieved on fan and jet noise, the relative importance of other noise sources has increased and the contribution of these sources must be controlled if further global noise reduction is to be achieved. Among these sources, the noise created by the turbulent flame within the combustor is already identified as non-negligible at take-off, especially in the mid-frequency range (see Sec. 1.2 and 1.3). Two main mechanisms have been identified in the seventies regarding noise propagation and generation from the combustion chamber to the far field (Fig. 6.1):

- **direct combustion noise:** acoustic perturbations generated by the unsteady heat release from the turbulent flame propagate either upstream or downstream through the turbomachinery stages where they are distorted by the mean flow, diffracted and reflected by the solid walls within the diffuser, the distributer and the turbine and compressor blades.
- **indirect combustion noise:** entropy fluctuations generated within the combustion chambers (hot spots, imperfect mixing, etc.) propagate downstream and interact with accelerating mean flow. Subsequent acoustic waves are generated and transmitted to the far field through the turbine stages.

Direct combustion noise is typically the main source of noise of a free flame. The acoustic radiation due to a turbulent flame has been theoretically treated by Bragg [17], Strahle [112], Hassan [50] and others. More recently, Ihme [52] successfully computed the sound emitted from a turbulent diffusion flame by combining Large Eddy Simulation and computational aeroacoustic methods, providing precious informations about combustion-generated noise. Experimental and theoretical work of Candel and co-authors [22, 21] about the noise generated by unsteady

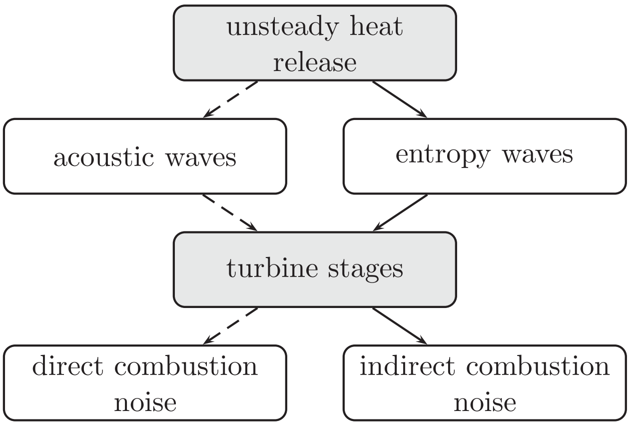

Figure 6.1 - *The two main mechanisms for noise generation from confined flames: direct (– – –) and indirect (—) noise.*

laminar flames, as well as the developments of Dowling in Crighton *et al.* [31], and experimental investigations of Lieuwen and colleagues [93, 94, 62] about combustion-generated noise of turbulent flames, are also important source of informations for direct noise comprehension.

Most of the studies performed in this field concern the flame acoustic radiation towards the free far-field, whereas in the case of confined systems like aero-engines another source of noise appears: the entropy noise. Indeed, following the work of Tsien [118] and Crocco [33] about nozzles, Candel concludes in his thesis [19] that entropy spots, inherent to the unsteady combustion process, can represent an important source of noise when considering gas expansion through the engine turbine stages. Candel considers a relative temperature fluctuation of 5%, and calculates a corresponding sound pressure level at the nozzle exhaust of about 120 dB. Marble and Candel [70] obtain solutions for planar waves within compact nozzles, and within finite length nozzles with assumed linear axial-velocity evolution. In the same period Ffowcs Williams and Howe [46] propose an extended theory for general entropy spots in low Mach number nozzle flows. Stow and Dowling [110] show that for an annular duct with a nozzle, the relations found by Marble and Candel for compact nozzles apply to first-order even when circumferential modes are present.

The compact interactions idea of Marble and Candel was extended to cylindrical 2-D flows by Cumpsty and Marble [37] and applied on commercial aero-engines [36]. Considering that the principal noise mechanism is the indirect one, Cumpsty and Marble presume the relative temperature fluctuation amplitude and spectrum, and obtain quite good results for low jet velocities: the so-called ”excess-noise”.

6.2 Theory

Dowling in [31] proposes an exact reformulation of the equations used for combustion [Eqs. (2.1) to (2.3)] in the framework of the Lighthill's analogy. This formulation aims at separating terms responsible for acoustic propagating (left-hand-side) and the sources (right-hand-side). The equation derived by Dowling is written:

$$
\begin{aligned}
\frac{1}{c_\infty^2}\frac{\partial^2 p}{\partial t^2} - \frac{\partial^2 p}{\partial x_j^2} =& \frac{\partial^2}{\partial x_i \partial x_j}(\rho u_i u_j - \tau_{ij})\ldots \\
&+\frac{1}{c_\infty^2}\frac{\partial}{\partial t}\left[\left(1-\frac{\rho_\infty c_\infty^2}{\rho c^2}\right)\frac{Dp}{Dt} - \frac{p-p_\infty}{\rho}\frac{D\rho}{dt}\right]\ldots \\
&+\frac{\partial}{\partial t}\left[\frac{\rho_\infty}{\rho}\frac{\gamma-1}{c^2}\left(\dot{\omega}_T + \frac{\partial q_j}{\partial x_j} - \sum_k c_{p,k} J_k \cdot \nabla T + \frac{\partial u_i}{\partial x_j}\tau_{ij}\right) + \rho_\infty \frac{D}{Dt}(\ln r)\right]\ldots \\
&+\frac{\partial^2}{\partial x_j \partial t}(\rho_e u_j)
\end{aligned}
\tag{6.1}
$$

where the quantities subscripted with ∞ are taken at infinity. D/Dt is the substantial derivative defined as $\partial/\partial t + u_j \partial/\partial x_j$. ρ_e is the *excess* mass density that is defined as $\rho - \rho_\infty - (p - p_\infty)/c_\infty^2$. For small perturbations, the excess mass density corresponds to the difference between the overall mass density fluctuation and the one generated by an isentropic compression (acoustics), and can thus be directly related to the entropy fluctuation. The term of the first line in the right-hand-side of Eq. (6.1) is a quadrupole source and leads to the aerodynamic noise found in the original jet-noise theory of Lighthill [63]. The second line terms are involved when the propagation medium is not uniform. According to Dowling, the term of the third line is of monopole type and is responsible for what is called the *direct* combustion noise; it is mainly caused by the variation of the heat release rate $\dot{\omega}_T$. Finally, the term of the last line is of dipole type and generates noise when mass density inhomogeneities ρ_e are accelerating. It relates to what is called here the *indirect* combustion noise or the *entropy noise*.

Recently, Bailly *et al.* [3] proposed an approximate formulation based on the Phillip's equation for low Mach numbers flows. According to Bailly *et al.* [3], the sound generation and propagation are better separated in the Phillip's approach, thus providing a better representation of the sources. If the diffusive fluxes are neglected, the so-called wave equation yields to:

$$
\begin{aligned}
\frac{1}{c_\infty^2}\frac{\partial^2 p}{\partial t^2} - \frac{\partial^2 p}{\partial x_j^2} \simeq \frac{1}{c_\infty^2}\frac{\partial}{\partial t}\left[\left(1-\frac{\rho_\infty c_\infty^2}{\rho c^2}\right)\frac{\partial p}{\partial t}\right] - \frac{\partial}{\partial x_j}\left[\left(1-\frac{\rho_\infty}{\rho}\right)\frac{\partial p}{\partial x_j}\right]\ldots \\
+\rho_\infty \frac{\partial u_i}{\partial x_j}\frac{\partial u_j}{\partial x_i} + \frac{\partial}{\partial t}\left(\frac{\rho_\infty}{\rho}\frac{\gamma-1}{c^2}\dot{\omega}_T\right) + \rho_\infty \frac{\partial^2(\ln r)}{\partial t^2}
\end{aligned}
\tag{6.2}
$$

As mentioned by Bailly *et al.* [3], the two first terms of the right-hand-side in Eq. (6.2) are the new part of the equation leading to indirect combustion noise. Nevertheless, in both formulations Eqs. (6.1) and (6.2) the direct noise is caused by the unsteady heat release rate, whereas the indirect one is related to mass density perturbation associated to non-uniform steady flow (velocity or pressure).

Solution of Eq. (6.1) or (6.2), providing the pressure fluctuation, is obtained by calculating the convolution product of the Green's function $\mathcal{G}$ relevant to the investigated system (3-D free-space, etc.), and the source terms noted $\mathcal{S}$ (left-hand-side terms). This operation writes:

$$p(x,t) = \iint \mathcal{G}(x-x',t-t')\mathcal{S}(x',t')dx'dt' \tag{6.3}$$

Studying free-space propagation is not relevant for enclosed combustion, but it can provide information on the nature of the generated sound. A 3-D free-space Green's function is considered here, noted $\mathcal{G}_{\mathrm{3D}}$. This function is defined as $\mathcal{G}_{\mathrm{3D}}(x,t) = \delta(t - x/c_\infty)/(4\pi x)$ and if one assumes that the unsteady heat release rate is the dominating term, and that the combustion is isobaric with constant specific heats, the pressure fluctuations in the far-field yield to [3]:

$$p(x,t) \simeq \frac{\gamma - 1}{4\pi c_\infty^2 x}\frac{\partial}{\partial t}\int_V \dot{\omega}_T\left(t - \frac{x-x'}{c_\infty}\right)dx' \tag{6.4}$$

The pressure fluctuations in Eq. (6.4) depend on the time derivative on the heat release rate. However, this result has to be handled with care, since it depends on the associated Green's function[1]. The statement that the direct combustion noise is caused by time derivative of the heat release rate is only true for free-space propagation and is no longer valid within combustion chambers.

Although direct and indirect combustion noise are both obtained when solving the compressible Navier-Stokes equations for reacting-flows, the underlying strategies to get one or the other are clearly different. Calculation of the direct noise requires a correct estimation of the unsteady heat release and also requires to handle well the acoustic propagation within the combustor and through the turbine. The fluctuations of entropy at the outlet of the combustor, as well as a method to evaluate their interactions with the accelerating flow within the turbine are needed for the estimation of the indirect noise. Therefore, assessing the relative importance of these two sources is required to provide an efficient method dealing with the noise caused by the combustion in aero-engines.

---

[1] The time derivative vanishes with a 1-D Green's function for example.

Chapter 7

Comparison of direct and indirect combustion noise in a model combustor

7.1 Introduction

As already mentioned in Chap. 6, the compact interactions idea of Marble and Candel [70] was extended to cylindrical 2-D flows by Cumpsty and Marble [37] and the resulting model was applied on commercial aero-engines [36]. Considering that the principal noise mechanism is the indirect one, Cumpsty and Marble presume the relative temperature fluctuation amplitude and spectrum, and obtain quite good results for low jet velocities. But Cumpsty and Marble agree to say that although the agreement of the measurements and predictions strongly supports that the indirect noise mechanism is the major core-noise generation process, this conclusion is not definitive until a clear separation of the different effects is performed. Starting from the heat release fluctuation, they provide the main ideas to do this analytically and briefly comment the expected results. The aim of the present chapter is precisely to develop this work, but in a purely one-dimensional case. It should be mentioned that Muthukrishnan *et al.* [80] experimentally investigate the core-noise sources separation and also conclude that for choked nozzles, entropy noise seems to be the main core-noise source. More recently Bake *et al.* [7, 6, 5] worked on the subject, but the separation of direct and indirect combustion noise in a real-case is still difficult to evaluate. On one hand, entropy fluctuations are controlled by complicated aerodynamical, thermal and chemical phenomena. Turbulent mixing and diffusion can also strongly affect entropy waves amplitudes at the nozzle inlet, generally speaking. On the other hand, the acoustic cavity modes of the chamber can also significantly change the acoustic levels [88, 43]. In the present study, only the most significant parameters are considered in order to establish simple analytical scaling laws for direct and indirect noise in aero-engines. To compare direct and indirect combustion noise, entropy and acoustic waves will be assumed to be directly linked to

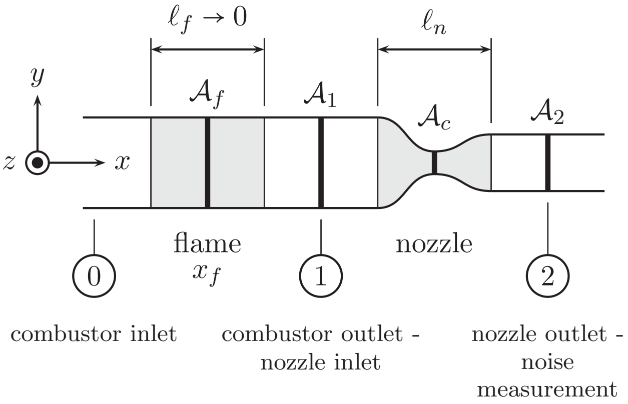

Figure 7.1 - *A generic model to evaluate direct and indirect combustion noise.*

heat release fluctuations, and a very simple case of generic combustor is considered: a combustion chamber followed by a nozzle (Fig. 7.1). The combustion chamber and the turbine stages will be represented by a quasi-1-D system. The combustion zone will be modeled by an infinitely thin heat release fluctuation in a constant section duct (generating acoustic and entropy waves) connected to a quasi-1-D nozzle representing the turbine stages (for the transmission and the generation of acoustic waves). These two elements are handled individually as shown in Fig. 7.2, and the feedback on the flame, of the acoustic waves traveling upward is not taken into account. Thus, the separation between direct and indirect noise is simple to perform since the global system is assumed to be linear. The combustion chamber creates the acoustic and entropy waves feeding the nozzle. The nozzle then generates the out-going direct or indirect noise depending on the nature of the in-going waves (acoustic or entropy respectively). The waves generated by the combustion zone are calculated analytically, considering an isolated heat release fluctuation. This model provides explicitly acoustic and entropy waves for the second part of the calculations: the transmission-generation of acoustic waves through the nozzle. The calculation of the transmission of acoustic waves through the nozzle (direct mechanism), and of the generation of acoustic waves from entropy waves within the nozzle (indirect mechanism) is performed both analytically using the results of Marble & Candel [70] for compact nozzles, and numerically by solving the Euler equations in the time-domain for a 2-D nozzle with a quasi-1-D behavior. The present method thus leads to two main approaches for the calculation of the indirect-to-direct noise ratio: a fully-analytical method and a semi-analytical method. In both cases, the calculations of the waves due to combustion and calculations of the waves transmission-generation through the nozzle are independent.

Analytical calculations of acoustic and entropy waves generated by combustion will be first reviewed in Sec. 7.2. Acoustic waves transmission and generation by the nozzle, obtained analytically and numerically, are then presented in Sec. 7.3. Finally, the ratio between direct and indirect noise is presented in Sec. 7.4.

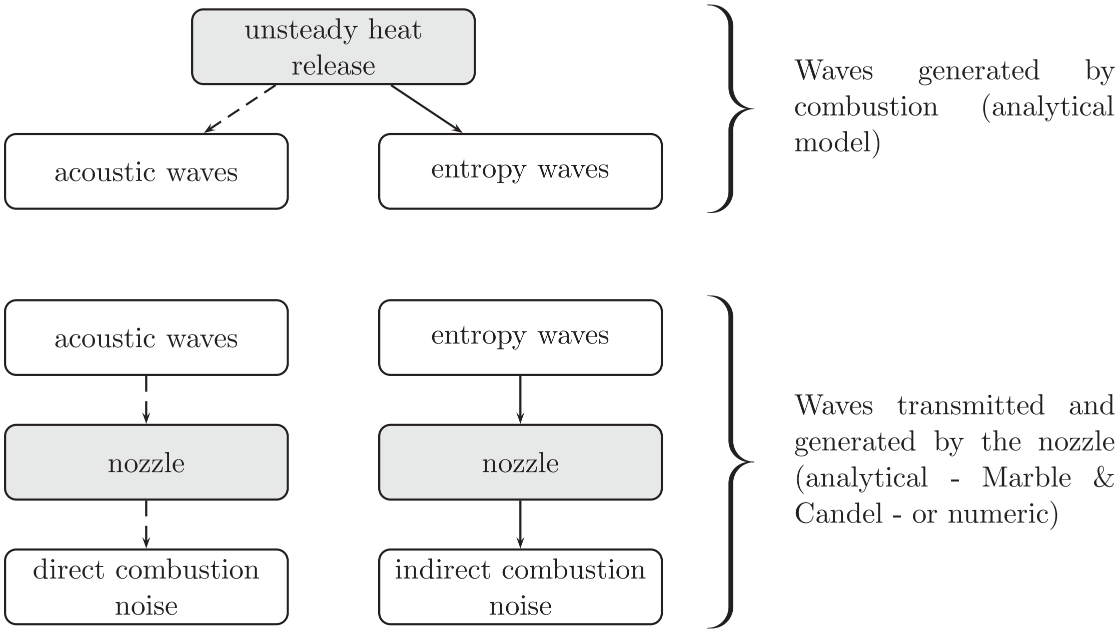

Figure 7.2 - *Strategy for the calculation of the ratio between direct and indirect noise.*

7.2 Acoustic and entropy waves generation in the combustion chamber

A subsonic flow is assumed in the combustion region. Viscous and 3-D effects are neglected and a one-dimensional heat release region is assumed to represent the combustion zone. The flow is defined with the mass density ρ, the velocity u and the heat release $\dot{Q}(t)$. The flame length ℓ_f is assumed to be small compared with the acoustic and entropy wavelengths, so that the heat release per unit volume $\dot{q}$ can be expressed as:

$$\dot{q}(x,y,z,t) = \delta(x - x_f)\dot{Q}(t)/\mathcal{A}_f \tag{7.1}$$

where δ is the Dirac distribution and $\mathcal{A}_f$ the cross-section area of the combustion chamber. The heat release $\dot{Q}(t)$ results from the following space integration of $\dot{q}(x,y,z,t)$:

$$\dot{Q}(t) = \iiint_{-\infty}^{+\infty} \dot{q}(x,y,z,t)dxdydz \tag{7.2}$$

The steady heat release of the flame model is considered negligible (*cold flame*) so that the mean flow is assumed isentropic. The *cold flame* assumption has been used by many authors to obtain analytical scaling regarding thermoacoustic instabilities [71], but it can have a non-negligible effect as shown by Dowling [40] which is ignored here. The flow is caracterised by the mass flow $\dot{m}$, the total enthalpy h_t and the entropy s. The mass flow $\dot{m}$ and the entropy s can be written as follows:

$$\dot{m} = \rho u \mathcal{A} \tag{7.3}$$

$$s = c_v \ln\left(\frac{p}{\rho^\gamma}\right) \tag{7.4}$$

or for small temporal perturbations:

$$\frac{\dot{m}'}{\bar{\dot{m}}} = \frac{1}{\bar{\mathcal{M}}}\frac{u'}{\bar{c}} + \frac{p'}{\gamma\bar{p}} - \frac{s'}{c_p} \quad \text{and} \tag{7.5}$$

$$\frac{s'}{c_p} = \frac{p'}{\gamma\bar{p}} - \frac{\rho'}{\bar{\rho}} \tag{7.6}$$

The specific heats and the composition of the gas are assumed to be constant, so that the total enthalpy is defined by $h_t = c_p T_t$, where T_t is the total temperature:

$$T_t = T\left(1 + \frac{\gamma-1}{2}\mathcal{M}^2\right) \tag{7.7}$$

The fluctuation of the Mach number $\mathcal{M}$ is:

$$\frac{\mathcal{M}'}{\bar{\mathcal{M}}} = \frac{1}{\bar{\mathcal{M}}}\frac{u'}{\bar{c}} - \frac{\gamma-1}{2}\frac{p'}{\gamma\bar{p}} - \frac{1}{2}\frac{s'}{c_p}, \tag{7.8}$$

The fluctuations of total temperature as a function of velocity, pressure and entropy perturbations can be written using Eq. (7.6, 7.8) and the state equation for small perturbations:

$$\frac{T_t'}{\bar{T}_t} = \frac{1}{1+\frac{\gamma-1}{2}\bar{\mathcal{M}}^2}\left((\gamma-1)\bar{\mathcal{M}}\frac{u'}{\bar{c}} + (\gamma-1)\frac{p'}{\gamma\bar{p}} + \frac{s'}{c_p}\right) \tag{7.9}$$

To scale direct and indirect combustion noise, the dimensionless acoustic (w^+ and w^-) and entropy (w^{S}) waves created by the compact flame of the combustion chamber must be assessed. These waves are defined as follows:

$$w^+ = \frac{p'}{\gamma\bar{p}} + \frac{u'}{\bar{c}} \tag{7.10}$$

$$w^- = \frac{p'}{\gamma\bar{p}} - \frac{u'}{\bar{c}} \tag{7.11}$$

$$w^{\mathrm{S}} = \frac{p'}{\gamma\bar{p}} - \frac{\rho'}{\bar{\rho}} \tag{7.12}$$

The wave w^+ is related to the propagation speed $u + c$, while the wave w^- is related to the propagation speed $u - c$. The wave w^{S} propagates at the convective speed u and transports entropy.

$$\begin{array}{cc||cc} w_0^+ & \rightarrow & \rightarrow & w_1^+ \\ w_0^- & \leftarrow & \leftarrow & w_1^- \\ w_0^{\mathrm{S}} & \rightarrow & \rightarrow & w_1^{\mathrm{S}} \\ & \multicolumn{2}{c}{\Lsh} & \dot{Q}' \end{array} \quad \Rightarrow$$

w_0^+	in-going	w_1^+	out-going
w_0^-	out-going	w_1^-	in-going
w_0^{S}	in-going	w_1^{S}	out-going

Table 7.1 - *In-going and out-going waves for the compact flame.*

Considering the heat release $\dot{Q}$ through the heating region according to Fig. 7.3, the balance equations of mass flow, total enthalpy and entropy at the flame front yield:

$$(\dot{m})_0 = (\dot{m})_1 \tag{7.13}$$

$$(\dot{m}h_t)_0 + \dot{Q} = (\dot{m}h_t)_1 \tag{7.14}$$

$$(\dot{m}s)_0 + \frac{\dot{Q}}{T} = (\dot{m}s)_1 \tag{7.15}$$

where the subscripts (0) and (1) correspond respectively to the quantities upstream and downstream from the flame. The mean heat release is zero, so that the mean temperature $\bar{T}$, Mach number $\bar{\mathcal{M}}$, total temperature $\bar{T}_t$ and entropy $\bar{s}$ do not change through the flame model. For small temporal perturbations and using mass flow balance Eq. (7.13), the entropy balance Eq. (7.15) leads to:

$$\left(\frac{s'}{c_p}\right)_0 + \frac{\dot{Q}'}{\bar{\dot{m}}c_p\bar{T}} = \left(\frac{s'}{c_p}\right)_1 \tag{7.16}$$

Equation (7.14) can be modified in the same way, and using the expression of the fluctuations of the total temperature Eq. (7.9), the total enthalpy balance Eq. (7.14) for small temporal perturbations leads to:

$$\begin{aligned} (\gamma-1)\bar{\mathcal{M}}\left(\frac{u'}{\bar{c}}\right)_0 + (\gamma-1)\left(\frac{p'}{\gamma\bar{p}}\right)_0 + \left(\frac{s'}{c_p}\right)_0 \quad + \quad \frac{\dot{Q}'}{\bar{\dot{m}}c_p\bar{T}} = \\ (\gamma-1)\bar{\mathcal{M}}\left(\frac{u'}{\bar{c}}\right)_1 \quad + \quad (\gamma-1)\left(\frac{p'}{\gamma\bar{p}}\right)_1 + \left(\frac{s'}{c_p}\right)_1 \end{aligned} \tag{7.17}$$

The heat release is supposed to be known, and the three in-going waves have to be imposed in order to obtain the out-going waves w_1^+, w_1^{S} and w_0^- using the three balance equations Eq. (7.13, 7.14, 7.15) as a function of the heat release. Except for the heat release, the combustor is assumed to be isolated, that is to say that the in-going acoustic waves w_0^+ and w_1^- are equal to zero, as well as the in-going entropy wave w_0^{S}. Considering the last assumption ($w_0^{\mathrm{S}} = 0$) and using Eq. (7.16), the out-going entropy w_1^{S} can be expressed as:

$$w_1^{\mathrm{S}} = \frac{\dot{Q}'}{\bar{\dot{m}}c_p\bar{T}} \tag{7.18}$$

The fluctuation of the mass flow Eq. (7.5) can be written upstream (0) and downstream (1) from the flame and expressed as a function of waves, instead of the fluctuations of velocity, pressure and entropy. Then, Eq. (7.17) related to the fluctuations of total enthalpy can also be written as a function of waves. Using Eq. (7.18) and the assumption that the flame is isolated ($w_0^+ = 0$, $w_1^- = 0$ and $w_0^S = 0$) one can show that the expression of the out-going acoustic wave w_1^+ generated by the heat release fluctuation is:

$$w_1^+ = \frac{\bar{\mathcal{M}}}{1+\bar{\mathcal{M}}} \frac{\dot{Q}'}{\bar{\dot{m}} c_p \bar{T}} \tag{7.19}$$

Finally, Eq. (7.18, 7.19) lead to the ratio between the acoustic wave w_1^+ and the entropy wave w_1^S generated by the combustion zone and propagating downstream the combustion chamber:

$$\frac{w_1^+}{w_1^S}[\mathrm{CC}] = \frac{\bar{\mathcal{M}}}{1+\bar{\mathcal{M}}} \tag{7.20}$$

where $[\mathrm{CC}]$ refers to waves produced in the combustion chamber. Equation (7.20) shows that, for a compact flame, the ratio between acoustic and entropy waves depends only on the Mach number in the flame zone $\bar{\mathcal{M}}$ and no more on the heat release fluctuations. This result allows studying the ratio between indirect and direct combustion noise mechanisms independently of the exact nature of heat release fluctuations, which are the sources of each mechanism.

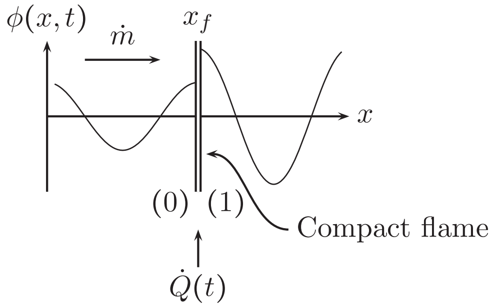

Figure 7.3 - *Compact flame illustration regarding a quantity ϕ upstream (0) and downstream (1) from the heating region.*

7.3 Waves transmission and generation through a nozzle

The transmission and the generation of acoustic and entropy waves through the nozzle are obtained using two different methods. The first one is based on the analytical development of Marble and Candel [70] assuming that the nozzle is compact (frequency is low). In their work, the authors assume a quasi-1-D nozzle flow and quasi-steady perturbations of mass flow, energy and entropy, leading to relations between the different waves that depend on the inlet and outlet Mach numbers. This approach is similar to the one used for the compact flame of Sec. 7.2, and the relations between waves for the nozzle are reviewed in the first part of this section. The second method to obtain the acoustic response of the nozzle is based on a numerical simulation of the quasi-1-D nozzle flow, by solving the Euler equations [74]. This second method is valid for all frequencies as long as the waves remain one-dimensional, and will be used here to evaluate the compact nozzle assumption of the analytical approach in the low frequency limit. The numerical approach is presented in the second part of this section.

7.3.1 Analytical approach

Following the analysis of Marble and Candel, the flow is supposed to be one-dimensional. Similarly to Sec. 7.2, u stands for the axial velocity, ρ for the mass density and $\mathcal{A}$ for the nozzle cross-section area. The mass flow $\dot{m}$ and the entropy s are defined by Eq. (7.3, 7.4). Assuming that the nozzle is isolated, the total enthalpy is conserved and thus the total temperature too. Note that the total temperature T_t is in this case always conserved, even for a non-isentropic mean flow in the nozzle (that is to say through a shock for instance). The total temperature is defined by Eq. (7.7) and the expression of the fluctuations of total temperature entering the nozzle as a function of speed, pressure and entropy perturbations is the same as in Sec. 7.2 - Eq. (7.9). Under the assumption of compact nozzle (long wavelengths compared with the nozzle length ℓ_n - see Fig. 7.4), there is no delay or distortion between the inlet and the outlet of the nozzle. As a result, mass flow, total temperature and entropy are conserved through the nozzle. The quantities upstream and downstream from the nozzle are respectively subscripted (1) and (2). The conservation equations Eq. (7.5, 7.6, 7.9) can be written as a system of equations, function only of upstream and downstream Mach numbers and waves (acoustic and entropy). This system is composed of three equations involving six waves, thus the in-going waves have to be imposed. In the case of an unchoked nozzle, the flow is totally subsonic and the w_2^- wave is in-going, so that waves w_1^+, w_1^S et w_2^- can be imposed. Finally, the system is composed of three equations and three unknown waves. Since the system is linear, mechanisms can be separated by setting $w_1^+ \neq 0$, $w_1^S = 0$ and $w_2^- = 0$ in a first step to study only the ”acoustic” response of the nozzle to an ”acoustic” perturbation. This case is called [AA]. It is also possible to set $w_1^+ = 0$, $w_1^S \neq 0$ and $w_2^- = 0$ in order to study the ”acoustic” response of the nozzle to an ”entropy” perturbation, and this case is called [SA]. Using Eq. (7.5, 7.6, 7.9) at the inlet and the outlet of

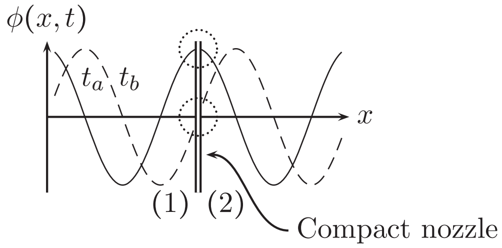

Figure 7.4 - *Compact nozzle illustration: The quantity ϕ, conserved throughout the nozzle, is the same upstream (1) and downstream (2) at each instant.*

$$\begin{array}{ccc|cc} w_1^+ & \rightarrow & \rightarrow & w_2^+ \\ w_1^- & \leftarrow & \leftarrow & w_2^- \\ w_1^S & \rightarrow & \rightarrow & w_2^S \end{array} \quad \Rightarrow$$

w_1^+	in-going	w_2^+	out-going
w_1^-	out-going	w_2^-	in-going
w_1^S	in-going	w_2^S	out-going

Table 7.2 - *In-going and out-going waves for the unchoked nozzle case.*

$$\begin{array}{ccc|cc} w_1^+ & \rightarrow & \rightarrow & w_2^+ \\ w_1^- & \leftarrow & \rightarrow & w_2^- \\ w_1^S & \rightarrow & \rightarrow & w_2^S \end{array} \quad \Rightarrow$$

w_1^+	in-going	w_2^+	out-going
w_1^-	out-going	w_2^-	out-going
w_1^S	in-going	w_2^S	out-going

Table 7.3 - *In-going and out-going waves for the choked nozzle case.*

the nozzle for the cases [AA] and [SA] gives:

$$\frac{w_2^+}{w_1^+}[\mathrm{AA}] = \left(\frac{2\bar{\mathcal{M}}_2}{1+\bar{\mathcal{M}}_2}\right)\left(\frac{1+\bar{\mathcal{M}}_1}{\bar{\mathcal{M}}_1+\bar{\mathcal{M}}_2}\right)\left(\frac{1+\frac{1}{2}(\gamma-1)\bar{\mathcal{M}}_2^2}{1+\frac{1}{2}(\gamma-1)\bar{\mathcal{M}}_1\bar{\mathcal{M}}_2}\right) \tag{7.21}$$

$$\frac{w_2^+}{w_1^S}[\mathrm{SA}] = \left(\frac{\bar{\mathcal{M}}_2-\bar{\mathcal{M}}_1}{1+\bar{\mathcal{M}}_2}\right)\left(\frac{\bar{\mathcal{M}}_2}{1+\frac{1}{2}(\gamma-1)\bar{\mathcal{M}}_1\bar{\mathcal{M}}_2}\right) \tag{7.22}$$

In the case of an isentropic choked nozzle, the flow is subsonic in the convergent part of the nozzle and totally supersonic in the divergent part and wave w_2^- cannot be imposed, since it is out-going. In the case of an isentropic choked nozzle, only two waves can be imposed so that the system is composed of four unknown waves for three equations only. The missing equation is obtained by stating that the flow at the nozzle throat is sonic so that the relation between the Mach number $\mathcal{M}$ and the cross-section area ratio can be written as follows:

$$\frac{\mathcal{A}}{\mathcal{A}_c} = \frac{1}{\mathcal{M}}\left[\frac{2}{\gamma+1}\left(1+\frac{\gamma-1}{2}\mathcal{M}^2\right)\right]^{\frac{1}{2}\frac{\gamma+1}{\gamma-1}} \tag{7.23}$$

where $\mathcal{A}_c$ is the cross-section area at the nozzle throat. One can easily show from Eq. (7.23) that for the choked nozzle case, the temporal fluctuation of the Mach number $\mathcal{M}'/\bar{\mathcal{M}}$ is zero. Then, using the expression of the fluctuation of the Mach Eq. (7.8):

$$\frac{1}{\bar{\mathcal{M}}}\frac{u'}{\bar{c}} - \frac{\gamma-1}{2}\frac{p'}{\gamma\bar{p}} - \frac{1}{2}\frac{s'}{c_p} = 0 \tag{7.24}$$

The entropy s and the total temperature T_t are constant through the nozzle, so that the total pressure p_t is also. The total pressure can be expressed as follows:

$$p_t = p\left(1+\frac{\gamma-1}{2}\mathcal{M}^2\right)^{\frac{\gamma}{\gamma-1}} \tag{7.25}$$

The temporal fluctuation of total pressure of Eq. (7.25) can be written:

$$\frac{p_t'}{\bar{p}_t} = \frac{p'}{\bar{p}} + \frac{\gamma\bar{\mathcal{M}}^2}{1+\frac{\gamma-1}{2}\bar{\mathcal{M}}^2}\frac{\mathcal{M}'}{\bar{\mathcal{M}}} \tag{7.26}$$

and shows that the fluctuations $p'/(\gamma\bar{p})$ are the same on both sides of the nozzle since the Mach number fluctuation is zero:

$$\left(\frac{p'}{\gamma\bar{p}}\right)_1 = \left(\frac{p'}{\gamma\bar{p}}\right)_2 \tag{7.27}$$

Finally, Eq. (7.6, 7.24, 7.27) used at the inlet and the outlet of the nozzle, yield:

$$\frac{w_2^+}{w_1^+}[\mathrm{AA}] = \frac{1+\frac{1}{2}(\gamma-1)\bar{\mathcal{M}}_2}{1+\frac{1}{2}(\gamma-1)\bar{\mathcal{M}}_1} \tag{7.28}$$

$$\frac{w_2^+}{w_1^{\mathrm{S}}}[\mathrm{SA}] = \frac{\frac{1}{2}(\bar{\mathcal{M}}_2-\bar{\mathcal{M}}_1)}{1+\frac{1}{2}(\gamma-1)\bar{\mathcal{M}}_1} \tag{7.29}$$

The set of equations Eq. (7.21, 7.22, 7.28, 7.29) provides analytical expressions for the out-going waves w_2^+ as a function of the in-going ones (w_1^+ and w_1^{S}) and the mean inlet ($\bar{\mathcal{M}}_1$) and outlet ($\bar{\mathcal{M}}_2$) Mach numbers for the compact nozzle.

7.3.2 Numerical approach

The previous analytical relations are based on the nozzle compactness assumption and are valid only for the low frequency limit. In order to validate this assumption and extend the model for the nozzle to a larger range of frequencies, an unsteady simulation based on Euler equations of the flow within the nozzle has been performed. Acoustic and entropy perturbations are generated at the inlet of the computational domain in a simple one-dimensional isentropic nozzle flow, and out-going noise is directly measured in the simulation.

Numerical method

The numerical tool used to solve the flow within the nozzle is the AVBP [102, 87] code. AVBP is a finite-volume cell-vertex code which can solve 3-D compressible Navier-Stokes equations on unstructured meshes, but it is used here on a 2-D regular mesh without viscous terms. The mesh is two-dimensional (476 × 5 with 320 nodes in the nozzle - Fig. 7.5), and the evolution of the transversal coordinate is small enough to assume that the flow in the nozzle is quasi-one-dimensional. There is about 320 nodes in the axial direction of the nozzle. The numerical computations have been performed with the Lax-Wendroff scheme which is second-order in space and time accurate, with a Courant-Friedrichs-Lewy number of 0.5. Preliminary tests performed with the same solver on acoustic and entropy waves propagation were used to verify that the results were independent of the mesh and that dispersion and dissipation errors were very small.

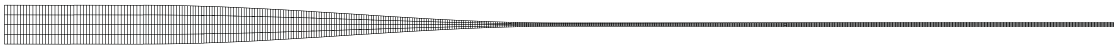

Figure 7.5 - *Mesh of the nozzle corresponding to the case with* $\mathcal{M}_1 = 0.050$ *and* $\mathcal{M}_2 = 1.600$.

		Unchoked cases		Choked cases	
		$\bar{\mathcal{M}}_2 = 0.400$	$\bar{\mathcal{M}}_2 = 0.800$	$\bar{\mathcal{M}}_2 = 1.200$	$\bar{\mathcal{M}}_2 = 1.600$
$\bar{\mathcal{M}}_1 = 0.025$,	$\mathcal{A}_1/\mathcal{A}_c$	14.604	22.482	23.365	23.365
	$\mathcal{A}_2/\mathcal{A}_c$	1.000	1.000	1.032	1.267
$\bar{\mathcal{M}}_1 = 0.050$,	$\mathcal{A}_1/\mathcal{A}_c$	7.310	11.253	11.695	11.695
	$\mathcal{A}_2/\mathcal{A}_c$	1.000	1.000	1.032	1.267
$\bar{\mathcal{M}}_1 = 0.100$,	$\mathcal{A}_1/\mathcal{A}_c$	3.671	5.651	5.873	5.873
	$\mathcal{A}_2/\mathcal{A}_c$	1.000	1.000	1.032	1.267

Table 7.4 - *Geometric cross-section area-ratio values for the different Mach number cases.*

Nozzle geometry and flow parameters

Since an inviscid, one-dimensional and compressible flow is also considered in the simulation, the mean Mach numbers $\bar{\mathcal{M}}_1$ and $\bar{\mathcal{M}}_2$ only depend on the cross-section area ratio $\mathcal{A}_1/\mathcal{A}_2$ for the unchoked nozzle case, and of the cross-section area ratios $\mathcal{A}_1/\mathcal{A}_c$ and $\mathcal{A}_2/\mathcal{A}_c$ for the isentropic choked nozzle case - Eq. (7.23). For the choked nozzle case, the nozzle is convergent and divergent, whereas it is simply convergent for the unchoked nozzle case. To calculate the section area ratio $\mathcal{A}_1/\mathcal{A}_2$ for the unchoked case, the following relation is used:

$$\frac{\mathcal{A}_1}{\mathcal{A}_2} = \frac{\bar{\mathcal{M}}_2}{\bar{\mathcal{M}}_1} \left[\frac{1 + \frac{\gamma-1}{2} \bar{\mathcal{M}}_1^2}{1 + \frac{\gamma-1}{2} \bar{\mathcal{M}}_2^2} \right]^{\frac{1}{2}\frac{\gamma+1}{\gamma-1}} \tag{7.30}$$

The different values of cross-section area ratios used in the present work are presented in Tab. 7.4 as a function of inlet Mach number $\bar{\mathcal{M}}_1$ and outlet Mach number $\bar{\mathcal{M}}_2$ for a specific heat capacities ratio γ of 1.32. The static pressure and temperature are imposed at the inlet of the nozzle ($p_1 = 800.0$ kPa, $T_1 = 1300$ K), and are the same for all cases. The static pressure p_2 is also imposed at the outlet and is chosen to obtain an isentropic flow and thus the correct target Mach numbers.

Numerical boundary conditions and computations

Like for the analytical approach, the acoustic response of the nozzle at the outlet is computed for a case where the in-going waves imposed at the nozzle inlet are entropy (case [SA]), and for a case where these waves are acoustic (case [AA]). In this numerical computation, totally non-reflecting boundary conditions are imposed, (w_1^+ independent of w_1^- at the nozzle inlet, and $w_2^- = 0$ for the subsonic nozzle outlet case), and the desired in-going perturbation added [75, 87]. The in-going waves at the nozzle inlet are imposed as follows:

$$\begin{cases} w_1^S(t) & = & n(t) \\ w_1^+(t) & = & 0 \end{cases} \text{for the case [SA]}$$

and

$$\begin{cases} w_1^S(t) & = & 0 \\ w_1^+(t) & = & n(t) \end{cases} \text{for the case [AA]}$$

$$\begin{array}{c||ccc||cc} \dot{Q}' & \rightarrow & w_1^+[\mathrm{CC}] & \rightarrow & \rightarrow & w^+_{2,\mathrm{dir}} \\ & \rightarrow & w_1^{\mathrm{S}}[\mathrm{CC}] & \rightarrow & \rightarrow & w^+_{2,\mathrm{ind}} \\ \text{flame} & & & \multicolumn{2}{c}{\text{nozzle}} & \end{array}$$

Table 7.5 - *Definition of the direct and indirect acoustic waves.*

where $n(t)$ is a filtered white noise signal. The perturbations $n(t)$ are small enough to neglect non-linear effects. As a result, one single computation with a filtered white noise signal imposed at the inlet can be performed to obtain the acoustic response of the nozzle to a large range of frequencies. The cut-off frequency of the filtered white noise signal and the size of the biggest cell are chosen in order to solve the smallest wavelength over 20 nodes in the most unfavorable case, that is to say the case of entropy waves forcing at low Mach numbers. The smallest acoustic wave length taken into account here is of the order of half the nozzle length (this corresponds to about 1/16 of the nozzle length for the entropy wave in the most unfavorable case). However, to avoid border-effects in the frequency-domain due to the low-pass filter, and to have a better numerical precision in the range of interest, the results presented in the next section are given for a reduced frequency range. The upper frequency limit of the presented results corresponds to a grid resolution of 50 nodes for the smallest entropy wavelength.

Temporal evolutions of the different waves are recorded at the nozzle inlet and outlet, and the Welch's method [26] is used to compute the spectral power density of the waves' signals and thus establish the desired spectral transfer functions. A first computation (case [SA]) provides the transfer function

$$\sqrt{\mathrm{PW}\{w_2^+\}/\mathrm{PW}\{w_1^{\mathrm{S}}\}}$$

relevant of the indirect mechanism, whereas a second computation (case [AA]) provides the transfer function

$$\sqrt{\mathrm{PW}\{w_2^+\}/\mathrm{PW}\{w_1^+\}}$$

relevant of the direct mechanism. These numerical transfer functions of the nozzle, in combination with the analytical results for waves generated by the combustion zone, are then used to calculate the semi-analytic indirect-to-direct ratio.

7.4 Results

Results of Sec. 7.2 and Sec. 7.3 are used to calculate the ratio η between amplitude $w^+_{2,\mathrm{ind}}$ of the acoustic wave generated indirectly and the amplitude $w^+_{2,\mathrm{dir}}$ of the acoustic wave generated directly as described in Tab. 7.5. The acoustic wave $w^+_{2,\mathrm{ind}}$ generated by the indirect mechanism is expressed using the entropy wave $w_1^{\mathrm{S}}[\mathrm{CC}]$ produced by the flame, and the transfer function of the nozzle of the case [SA]. The acoustic wave $w^+_{2,\mathrm{dir}}$ generated by the direct mechanism is however expressed using the acoustic wave $w_1^+[\mathrm{CC}]$ produced by the flame, and the transfer function of the nozzle of the case [AA]. The ratio η is defined as follows:

$$\eta = \frac{w^+_{2,\text{ind}}}{w^+_{2,\text{dir}}} \tag{7.31}$$

where:

$$w^+_{2,\text{dir}} = \frac{w^+_2}{w^+_1}[\text{AA}] \cdot w^+_1[\text{CC}] \quad \text{and} \quad w^+_{2,\text{ind}} = \frac{w^+_2}{w^S_1}[\text{SA}] \cdot w^S_1[\text{CC}] \tag{7.32}$$

The ratio η can be calculated, as mentioned previously, either in a fully-analytic way (using the analytical relations of Marble & Candel for the transmission and generation of waves through a compact nozzle, and the analytic relation for waves generated by combustion - Sec. 7.3-7.3.1), or in a semi-analytic manner (using the numerical calculations for the transmission and generation of waves through 1-D nozzle flow, and the same analytical relation for waves generated by combustion - Sec. 7.3-7.3.2):

$$\eta = \underbrace{\frac{w^+_2}{w^S_1}[\text{SA}]}_{\text{analytic or numeric}} \; \underbrace{\frac{w^S_1}{w^+_1}[\text{CC}]}_{\text{analytic}} \; \underbrace{\frac{w^+_1}{w^+_2}[\text{AA}]}_{\text{analytic or numeric}} \tag{7.33}$$

The fully-analytic expression of the ratio η is established using Eq. (7.20) giving the ratio between acoustic and entropy waves produced by the combustion chamber (case [CC]), and Eq. (7.21, 7.22, 7.28, 7.29) giving the transmitted and generated waves by a compact nozzle. For this approach, the expression of η is:

$$\eta = \frac{1}{\bar{\mathcal{M}}_1} \frac{(\bar{\mathcal{M}}_2 - \bar{\mathcal{M}}_1)(\bar{\mathcal{M}}_2 + \bar{\mathcal{M}}_1)}{2\left(1 + \frac{1}{2}(\gamma - 1)\bar{\mathcal{M}}_2^2\right)} \quad \text{for the unchoked nozzle} \tag{7.34}$$

$$\eta = \frac{1 + \bar{\mathcal{M}}_1}{\bar{\mathcal{M}}_1} \frac{\bar{\mathcal{M}}_2 - \bar{\mathcal{M}}_1}{2\left(1 + \frac{1}{2}(\gamma - 1)\bar{\mathcal{M}}_2\right)} \quad \text{for the choked nozzle} \tag{7.35}$$

The ratios between indirect and direct noise η, calculated with the fully-analytic and semi-analytic approaches, are plotted hereafter for the Mach numbers defined previously, as a function of reduced pulsation $\Omega = \omega \ell_n / \bar{c}_1$ related to the pulsation ω, the speed of sound at the nozzle inlet $\bar{c}_1$ and the nozzle length ℓ_n. Figure 7.6 shows that for this simple case, the indirect combustion noise is globally in the same range of magnitude as the direct one; it can be even ten times greater in the most unfavorable case (low inlet Mach number and high outlet Mach number). The ratio between indirect and direct noise in Fig. 7.6 is plotted versus the dimension-less pulsation Ω. The parameter Ω ($\omega \ell_n / \bar{c}_1$) corresponds to the "acoustically" reduced pulsation and quantifies the "acoustic" compactness of the nozzle. To be representative of the "entropy" compactness of the nozzle, this dimensionless pulsation simply needs to be divided by the Mach number at the nozzle inlet. That is to say that the nozzle is ten (inlet Mach number 0.1) to forty (inlet Mach number 0.025) times less compact from an entropy point of view than acoustically. For reduced pulsations going to zero (compact nozzle assumption), the numerical computations converge to the ratio η calculated with the analytical relations for the nozzle established by Marble & Candel. Figure 7.6 shows that the slope of η for $\Omega = 0$ is close to zero, so that the analytical expression

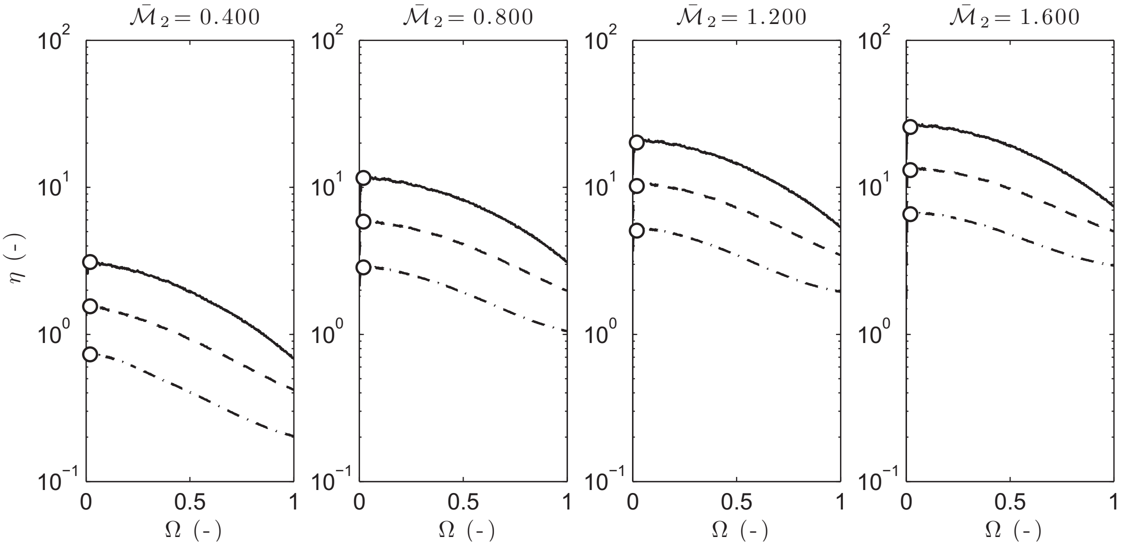

Figure 7.6 - *Estimation of the ratio η between indirect and direct noise. Chain dotted line* $\cdot - \cdot - \cdot$ *Mach number* $\bar{\mathcal{M}}_1 = 0.100$*, dotted line* $- - -$ *Mach number* $\bar{\mathcal{M}}_1 = 0.050$ *and solid line* —— *Mach number* $\bar{\mathcal{M}}_1 = 0.025$*. All curves correspond to the semi-analytic method. Circles* $\circ$ *give the analytic solution for low frequencies Eq. (7.34, 7.35).*

remains valid (less than 20% error) up to $\Omega = 0.2$ in most cases, that is to say even when the entropy wavelength is of the order of the nozzle length. The fully-analytic approach provides thus a good idea of what the indirect-to-direct ratio can be. This ratio calculated with the fully-analytic approach is plotted versus the nozzle inlet and outlet Mach numbers in Fig. 7.7. Nowadays, the overall pressure ratio at takeoff for commercial aero-engines ranges from about 30 to 40, which is equivalent to an acceleration leading to an outlet Mach number of about 2.0. This graph shows that for an outlet Mach number between unity and two and an inlet Mach number close to 0.05 (condition which can be found in aero-engines) the indirect combustion noise can be more than ten times as important as the direct one. Equation (7.35) shows that when the outlet Mach number $\bar{\mathcal{M}}_2$ is high, the ratio η depends only of the inlet Mach number $\bar{\mathcal{M}}_1$ and tends to $(1 + \bar{\mathcal{M}}_1)/\bar{\mathcal{M}}_1(\gamma - 1)$. With the previous value of the inlet Mach number of 0.05, the maximum ratio η is then greater than sixty. Of course the present estimation is quite oversimplified, since in a real engine, the strong azimuthal deviation of flow within the turbine stages have to be taken into account, as well as the blade loading and blade rows spacing. This approach has been followed by Cumpsty and Marble [37, 36], but the number of parameters involved in such a method is important and the results are engine-dependent (even if general designs can be used to perform such a calculation). The present approach provides a simple method for the estimation of the indirect-to-direct noise ratio, and confirms the importance of indirect noise.

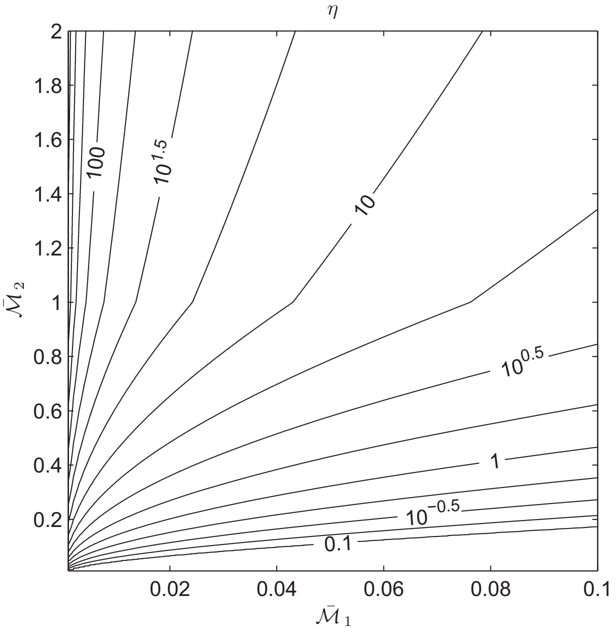

Figure 7.7 - *Estimation of the ratio η between indirect and direct noise by the fully-analytic approach. The ratio η is plotted here as a function of the Mach number $\bar{\mathcal{M}}_1$ representing the Mach number in the combustion chamber and at the nozzle inlet, and of the Mach number $\bar{\mathcal{M}}_2$ representing the outlet nozzle Mach number.*

7.5 Conclusion

The noise produced by an aero-engine is generated either by the acoustic waves created by unsteady combustion (direct noise) or by the entropy waves created by combustion and convected through the turbine stages where they create noise (indirect noise). A simple quasi-1-D combustor model, based on a combustion chamber terminated by a nozzle has been used to evaluate all waves (acoustic and entropy) created by an unsteady flame zone and to quantify direct and indirect noise. Wave propagation in this model can be determined in the low frequency limit using fully analytical methods as suggested by Marble and Candel or for all frequencies using a semi analytical-numerical technique where the wave propagation through the nozzle is solved using the Euler equations while the rest of the problem is handled analytically. Results demonstrate that the analytical approximation remains valid up to "acoustically" reduced pulsations of order of 0.2, that is to say even when the entropy wavelength is of the order of the nozzle length, for the given range of inlet Mach numbers (0.025-0.100). They also show that the ratio of indirect to direct noise depends on two Mach numbers: the Mach number in the flame zone and the Mach number at the nozzle outlet. This ratio should be small for laboratory experiments but large in most real aero-engines.

Chapter 8

Analytical and numerical investigation of indirect noise in a nozzle

8.1 Introduction

The results obtained in Chap. 7 show that indirect combustion noise is the prevalent source of noise when considering a one-dimensional model combustor. The generation of the entropy noise needs thus to be investigated for a more realistic case to confirm this observation. In the 1970's, a significant experimental and modeling effort of engine core noise was undertaken [111, 19, 70, 85, 37, 36, 13, 80, 112]. In these experiments, however, the amplitude of the induced temperature fluctuation (about 1 K) was too low to clearly measure and characterize the indirect noise. Yet no actual dedicated experimental validation of those theoretical and numerical results with significant entropy waves generated were achieved until the recent Entropy Wave Generator (EWG) experiment at DLR by Bake *et al.* [7, 6, 5, 4, 8]. In this experiment, a perturbation on the temperature in generated by means of an electrical device and the pressure signal resulting from the interaction of the entropy fluctuation with a nozzle flow is measured at the outlet. To start from a *model* experiment such as the DLR EWG set-up is a logical first step. The corresponding experimental setup and the major measurements are summarized in Sec. 8.2. In this framework, the objectives of this study are threefold:

First, the capability the code ABVP to reproduce the entropy/acoustic interaction in the presence of a strong mean velocity gradient is assessed. The associated computational domain and simulations are discussed in Sec. 8.3.1. The numerical results are then compared to the measurements from the EWG experiment and to the recent URANS computations achieved by Mühlbauer *et al.* [76].

Secondly, the first-order physical mechanisms that drive the pressure signal measured in the

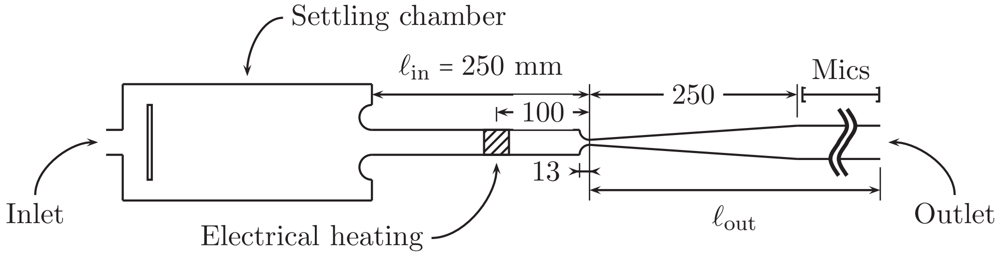

Figure 8.1 - *Sketch of the Entropy Wave Generator experimental set-up (lengths are given in mm). Short configuration:* $\ell_{out} = 500$ *mm; Long configuration:* $\ell_{out} = 2100$ *mm*

experiment are explored. Notably the effects of (a) the entropy fluctuations shape and size, and (b) the boundary conditions are assessed.

Finally, the application range of the analytical approach based on the compact nozzle approximation [70] is investigated in Sec. 8.4. The analytical relationships that can be derived for unchoked and choked nozzles are first presented and applied to the EWG configuration and flow conditions. The analytical results are then compared with both the experimental data of Bake *et al.* [8] and the present unsteady simulations.

8.2 DLR experimental set-up and measurements

All computations presented in this chapter are related to the DLR experimental setup studied by Bake *et al.* [6, 5, 4, 8]. A sketch of the so-called Entropy Wave Generator (EWG) experiment is displayed in Fig. 8.1. It consists of a tube fed by entropy waves generated by an electric heating device located between the upstream plenum and the nozzle. The main geometrical parameters of the experiment are summarized in Table 8.1. The operating conditions were varied from unchoked conditions (nozzle Mach numbers, M_{nozzle}, from 0.15 to 0.9) to choked flows ($M_{\mathrm{nozzle}} = 1$) with various exit Mach numbers, M_{exit}. The averaged amplitude of the temperature fluctuations was also varied.

The present numerical simulations are restricted to the conditions termed reference test case 1 by Bake *et al.* [8]. The nozzle is choked but not adapted so that a normal shock takes place just after the throat, within the divergent section. When accelerated through the nozzle, the small amplitude entropy fluctuations (in the order of 10 K) produce backward and forward propagating acoustic waves. The forward part of the generated noise is measured by microphones located downstream of the nozzle. The main physical parameters defining the operating conditions are presented in Table 8.2. It should be stressed that the heating duration is 100 ms which, with a bulk velocity in the order of 12 m/s, leads to an entropy perturbation longer than the nozzle (1200 mm against 263 mm). The present entropy spot (s') is made of a "raising", a "constant" and a "falling" fluctuation superimposed on the steady flow which all participate to the sound generation. Indeed, according to Marble and Candel [70], the pressure fluctuation (p') coming

Convergent length	Divergent length	Throat diameter	Inlet diameter	Exit diameter
13 mm	250 mm	7.5 mm	30 mm	40 mm

Table 8.1 - *Main geometrical characteristics of the DLR experimental nozzle*

Plenum pressure	Outlet pressure	Inlet Mach
117000 Pa	100800 Pa	0.037
Outlet Mach	Pulse duration, τ	Pulse amplitude
0.023	100 ms	9 K

Table 8.2 - *Main physical parameters of the DLR Entropy Wave Generator experiment*

from the linearized Euler equations is directly related to the entropy one, when considering indirect noise generation. It should also be stressed that in the so-called analytical approach, the entropy noise is not caused by the time-derivative of the entropy fluctuation: if there are no reflections, a Heaviside step function on the entropy perturbation produces the same result on the acoustic pressure. Therefore, the relevant length scale is believed to be the full pulse and not only its edges. Further details of the experiment and the associated measurements can be found in Bake *et al.* [5, 4].

8.3 Numerical simulation of indirect noise

8.3.1 Numerical set-ups and parameters

The numerical code used in this study is AVBP. This tool solves the complete three-dimensional compressible Navier-Stokes equations, therefore, it integrates all possible non-linear effects involved in the entropy noise generation and contained in the these equations. The unstructured approach allows meshing and computing not only the nozzle but also the whole air feeding line as well as the exhaust system. This formulation then naturally accounts for the energy transfer between the entropy and the acoustic modes, and for the actual, possibly non-compact, nozzle geometry. The numerical method used in AVBP is based on a weighted residual, Taylor-Galerkin discretization which is third-order in both space and time [28] in order to minimize the dispersion and dissipation numerical errors.

All simulations termed "2D" correspond to 3-D calculations in an axisymmetric configuration on a slice with periodic boundary conditions. Only the simulation termed "3D" refers to the full cylindrical geometry. The main characteristics of the simulations are presented in Table 8.3. The entries "short" and "long" refer to the two types of computational domain depicted in Fig. 8.1. They both include the upstream plenum and the heating section but the "short" one extends only 500 mm downstream of the nozzle throat (length ℓ_{out}) while the "long" contains the exhaust duct up to the inlet of the anechoic section, viz. approx. 2100 mm downstream of the nozzle. The "long" configuration is meant to apply realistic impedance (especially the phase of the reflection coefficient) at the duct exit. In Table 8.3, "BC" refers to the boundary condition prescribed at the outlet of the computational domain which can be either non-reflecting, fully reflecting or corresponds to a finite (neither zero nor infinite) acoustic impedance. The "heating" entries correspond to the shape of the temperature pulse: it is 1-D in most cases (viz. uniform in the plane normal to the duct) expected for case 2D-2 where it depends on the distance r to the axis (viz. non-uniform in the cross-section; in the present case, the heating source term is proportional to $\cos[(r/R)(\pi/2)]$, with R the radius of the upstream duct). The uniform and non-uniform heating cases correspond to the same overall power in the cross-section so that the comparison between runs 2D-1 and 2D-2 can provide relevant information on the effects of the inhomogeneity of the entropy perturbation. In the same way, comparing runs 2D-1 and 2D-3 will provide information about the sensitivity of the results to the outlet boundary condition while comparing 3D-1 and 2D-1 will be relevant to quantify 3-D effects. Finally, run 2D-4 is designed to mimic, as much as possible, the experimental downstream acoustic impedance which was evaluated by DLR. In all cases, the mesh resolution is enough to represent the propagation of the entropy and acoustic waves in the duct without significant dissipative and dispersive errors. The mesh size is in the order of 1 mm and allows a sufficient resolution of the perturbation size (of the order of 1200 mm, see Sec.8.2), including its sharp raising and falling edges (in the order of 100 mm). The 3-D mesh contains 1.2 million tetraedras, corresponding to approximately 15 cells in a cross-section. The mesh density is equivalent for all 2-D axisymmetric cases. As the present simulations are not meant to resolve the boundary layer and vortex dynamics, the grid resolution is limited and slip boundary conditions are imposed on the walls.

In order to mimic the experimental heating device, a source term is added to the energy equation. It reads:

$$\Phi(x,t) = \Phi_0 \frac{1}{2}\left[\tanh\left(\frac{x - x_0 + \ell_h/2}{d}\right)\tanh\left(-\frac{x - x_0 - \ell_h/2}{d}\right) + 1\right]\phi(t)$$

where $\ell_h = 30$ mm is representative of the length of the experimental heating zone and $d = 3$ mm enables to sufficiently smooth the source term to avoid numerical issues. The average location x_0 of the source term has been consistently chosen at the location of the electrical device in the experiment (100 mm upstream of the nozzle throat). The temporal evolution $\phi(t)$ is defined as the following:

$$\phi(t) = \begin{cases} 1 - e^{-\frac{t-t_0}{\tau}} & \text{if } t \in [t_0, t_0 + T_p] \\ \phi(t_0 + T_p)e^{-\frac{t-t_0}{\tau}} & \text{if } t > t_0 + T_p \end{cases}$$

where t_0 is the time when the electrical device is triggered, T_p is the pulse duration set to 100 ms and τ is a relaxation time of the pulse set to 8 ms. As shown in Fig. 8.2, these numerical parameters allow a fair representation of the temperature fluctuation produced in the DLR experiment. This temperature perturbation passes through the nozzle, gets distorted and yields pressure fluctuations which are analysed in the next section.

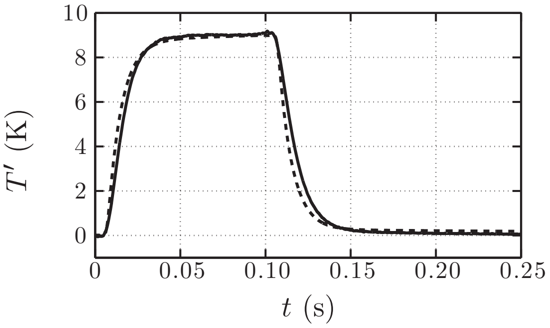

Figure 8.2 - *Time traces of the experimental (—) and numerical (– – –) temperature downstream of the heating location.*

Run	Geometry	Length	BC	Heating
3D-1	3D	short	non-reflecting	uniform
2D-1	2D axi	short	non-reflecting	uniform
2D-2	2D axi	short	non-reflecting	non-uniform
2D-3	2D axi	short	reflecting	uniform
2D-4	2D axi	long	finite impedance	uniform

Table 8.3 - *Main characteristics of the small-scale simulations.*

8.3.2 Numerical results

The time traces of the pressure computed 350 mm downstream of the throat (solid lines) are displayed in Fig. 8.3 for runs 2D-1 (top left), 2D-2 (top right), 2D-3 (bottom left) and 3D-1 (bottom right). They are compared to the experimental signal (dashed lines). Clearly enough, these simulations do not reproduce the experimental data, neither in terms of amplitude, nor in terms of signal shape. For runs 2D-1 and 3D-1, the numerical pressure trace has a top-hat behavior similar to the temperature upstream fluctuation, while the experiment shows a wavy behavior at a frequency close to 30 Hz. Figure 8.3 also indicates that 3D-1 leads to results very similar to 2D-1, indicating that the disagreement between the 2D-1 computation and the experimental data cannot be attributed to three-dimensional effects. The same conclusion can be drawn by comparing 2D-1 and 2D-2 for the temperature inhomogeneity which appears to have no effect, at least for this configuration. On the other hand, Fig. 8.3 illustrates how large the effects of the downstream acoustic boundary condition can be. When a fully reflecting condition (2D-3),which imposes pressure is used instead of a non-reflecting one (2D-1), which essentially sets the incoming acoustic wave to zero at the outlet, the amplitude decreases drastically. More importantly, the shape of the signal is also strongly modified by the superposition of the downward and backward pressure waves. A wavy behavior is also obtained in run 2D-3, although with a characteristic amplitude and a frequency in quantitative disagreement with the experiment and the simulations reported by Mühlbauer *et al.* [76, 77] (Fig. 10 in this reference). The amplitude is all the more reduced as the computational exit duct is shortened.

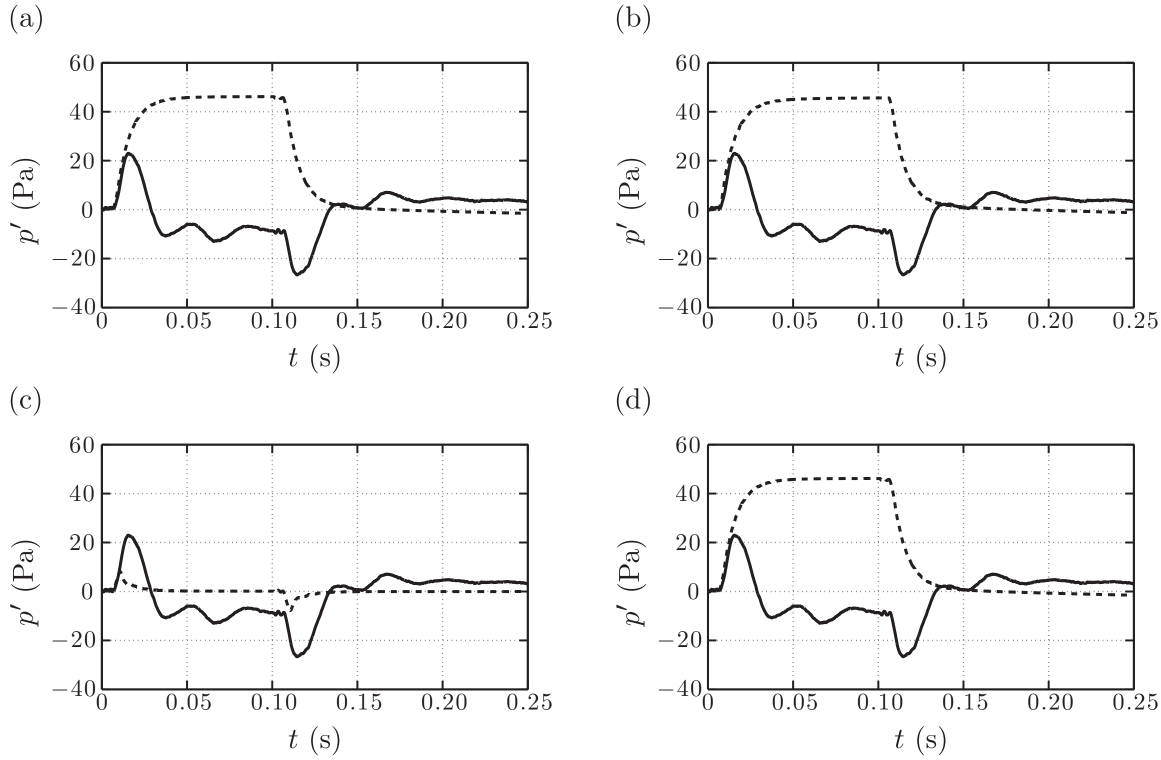

Figure 8.3 - *Time traces of the fluctuating pressure* 350 *mm downstream of the nozzle. Experimental data:* —*; Numerical result:* − − −*. (a) Run 2D-1; (b) Run 2D-2; (c) Run 2D-3; (d) Run 3D-1.*

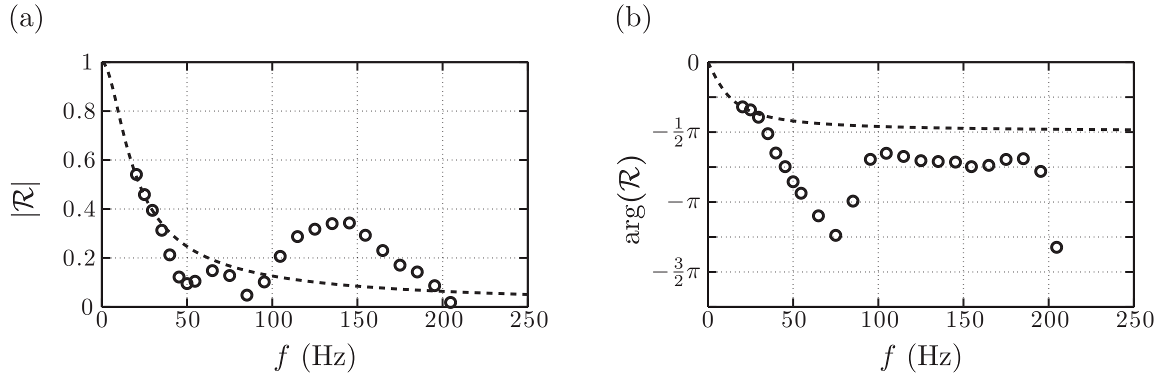

Figure 8.4 - *Experimental reflection coefficient shifted* 2100 *mm downstream of the nozzle throat and numerical reflection coefficient. Shifted experimental data: •; Tuned relaxation coefficient: − − −. (a) Modulus; (b) Argument.*

The previous results suggest that the discrepancies observed in Fig. 8.3 might be related to an incorrect downstream acoustic impedance as already suggested by Mühlbauer *et al.* [76, 77]. Indeed, the short computational domain and non-reflecting BC used in runs 2D-1, 2D-2 and 3D-1 would only be representative of the actual experimental conditions if a perfect anechoic system would have been used by Bake *et al.* [8]. It should also be noted that a slight reflectivity of the outlet boundary condition in the simulation distorts the pressure responses that get damped around 0.1 s as in the URANS simulation by Mühlbauer *et al.* [77] (Fig. 11 in this reference), which stresses the high sensitivity of the simulations to the exit flow condition. Actually, Fig. 8.4 demonstrates that substantial reflection occured in the experiment, especially in the low-frequency range: the modulus of the reflection coefficient, defined as the ratio of the backward wave to forward wave at the outlet, is as large as 0.5 at 30 Hz, the typical frequency of the reflections observed in the experimental signal (see Fig. 8.3). Accounting for frequency-dependent reflection coefficient in a CFD code solving the flow equations in the time-domain is feasible. For example, the boundary condition proposed by Reymen *et al.*can be used. However, all these models have parameters that need to be fitted over a large frequency range on the actual experimental impedance, and a specific implementation in the CFD code is required. Similarly to what was proposed by Mühlbauer *et al.* [76, 77], a simpler approach has been followed in the present study. Instead of using a non-reflecting outlet boundary condition with zero entering wave ∂w^-, it is common use to write the latter as a pressure difference times a relaxation coefficient κ_p [86], viz. $\partial w^- = 2\kappa_p \Delta t(p_{\text{ref}} - p_B)/(\rho c)$, with Δt the time step, p_B the nodal pressure at the outlet boundary and p_{ref} the reference pressure. In doing so, the outlet condition acts as a first-order low pass filter [104] whose cut-off frequency is proportional to κ and the acoustic reflection coefficient $\mathcal{R}_{\text{out}}$ reads (see Chap. 5):

$$\mathcal{R}_{\text{out}} = -\frac{1}{i\omega/\kappa_p + 1} \tag{8.1}$$

It is thus possible to tune the relaxation coefficient κ_p in order to reproduce the amplitude of the experimental reflection coefficient, at least in the low-frequency range. The length ℓ_{out} of the

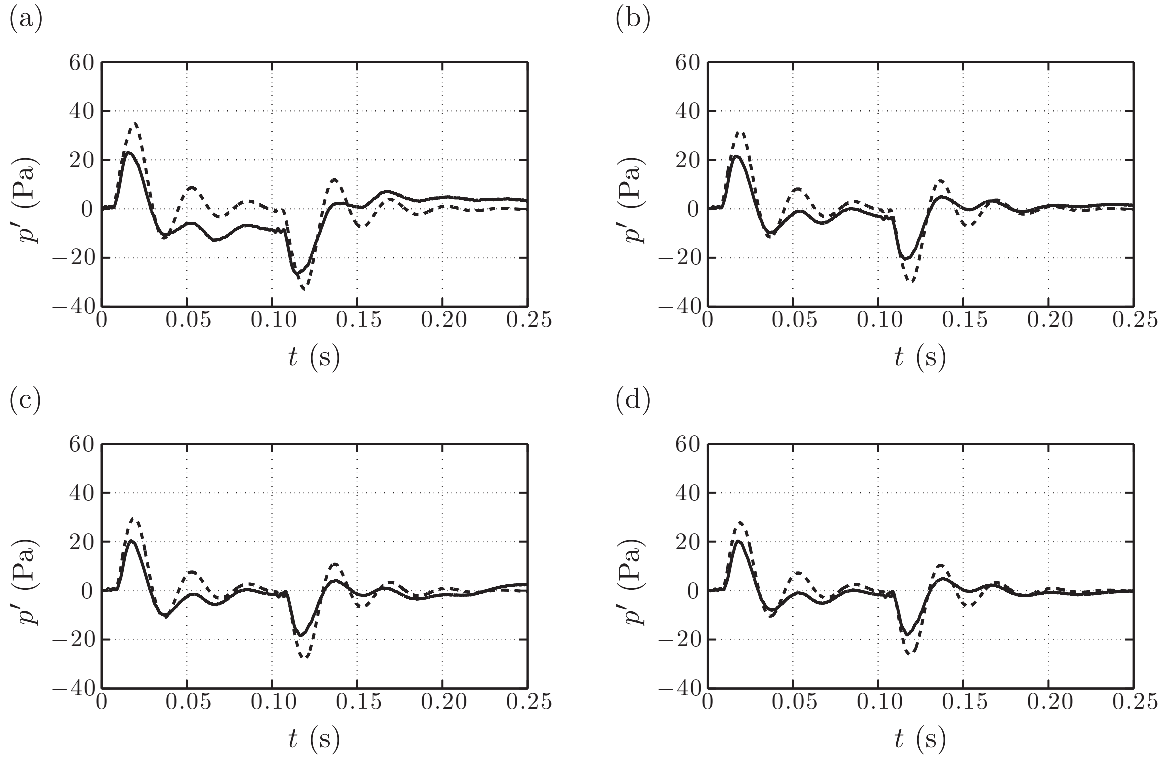

Figure 8.5 - *Time traces of the fluctuating pressure downstream of the nozzle. Experimental data: —; Run 2D-4: – – –. Distance downstream of the nozzle: (a)* 350 *mm; (b)* 730 *mm; (c)* 975 *mm; (d)* 1150 *mm.*

downstream duct is then tuned to mimic the experimental time delay as well as to compensate for the phase of the relaxation-based outlet partially reflecting condition. The experimental reflection coefficient is expressed here at the nozzle throat ($x = 0$) while the reflection coefficient of the numerical boundary condition, Eq. (8.1), is given at the end of the computational domain ($x = \ell_{\mathrm{out}}$). Assuming the Mach number to be small in the outlet duct, the experimental reflection coefficient can be multiplied by $\exp(-2\imath\ell_{\mathrm{out}}\omega/c)$ in order to shift it to the same position, at the end of the numerical domain ($x = \ell_{\mathrm{out}}$). The experimental reflection coefficient obtained in this way is depicted in Fig. 8.4 where a fair agreement with the numerical one is apparent in the frequency range 20-40 Hz. For higher frequencies the general trend is kept and the experimental peak at about 140 Hz cannot be captured, since the present reflection coefficient behaves like a first-order filter only. The best-fit relaxation coefficient κ_p and length ℓ_{out} are close to 160 s^{-1} and 2100 mm respectively. As soon as this corrected impedance is used at the outlet, results (run 2D-4) improve drastically: Fig. 8.5 indicates that the numerical pressure signal is in better agreement with the measured one when accounting for the effective downstream boundary condition, and so for all positions of the pressure sensor downstream of the nozzle.

8.4 An analytical method for indirect noise computation

The analytical approach proposed by Marble and Candel [70] is followed here to evaluate the indirect combustion noise. Their developments are extended to the case of a shock in a nozzle to obtain an analytical tool which completely describes the DLR experiment and can replace the numerical simulation. The extended analytical results, giving relations between waves in all possible cases (unchoked insentropic nozzle, choked insentropic nozzle and shock in nozzle), are then used to obtain the pressure fluctuations in the EWG experiments. Partially reflective boundary conditions identical to those used in the LES cases are also introduced in the model both at the inlet and outlet of the domain. By comparing with the above simulations using the same inlet and outlet acoustic impedances for both numerical and theoretical calculations, the domain of validity of the compact nozzle assumption and the linear regime inherent to the analytical approach can be assessed.

8.4.1 Isentropic nozzle

As already presented in Chap. 7, an isentropic flow of a homogeneous gas of density ρ, velocity u, pressure p, constant specific heat c_p and $c_v = c_p/\gamma$ is assumed in a quasi-1-D adiabatic duct of cross-section area $\mathcal{A}(x)$. The mass flow rate $\dot{m}$, the stagnation temperature T_t and the specific entropy s are defined according to Eqs. (7.3, 7.7, 7.4). These quantities are constant throughout the duct and can be differentiated to yield the corresponding fluctuations.

Unchoked nozzle

By writing equality of the fluctuations of the mass-flow rate Eq. (7.5), the stagnation temperature Eq. (7.9) and the entropy Eq. (7.6) upstream and downstream of the nozzle (compact nozzle), and introducing the waves of Eqs. (7.10, 7.11, 7.12), the following general set of equations can be obtained:

$$
\begin{aligned}
&\left(1+\frac{1}{\bar{\mathcal{M}}_a}\right)w_a^+ + \left(1-\frac{1}{\bar{\mathcal{M}}_a}\right)w_a^- - 2w_a^{\mathrm{S}} = \ldots \\
&\qquad\qquad \left(1+\frac{1}{\bar{\mathcal{M}}_b}\right)w_b^+ + \left(1-\frac{1}{\bar{\mathcal{M}}_b}\right)w_b^- - 2w_b^{\mathrm{S}} \\
&\frac{(\gamma-1)(1+\bar{\mathcal{M}}_a)}{1+\frac{\gamma-1}{2}\bar{\mathcal{M}}_a^2}w_a^+ + \frac{(\gamma-1)(1-\bar{\mathcal{M}}_a)}{1+\frac{\gamma-1}{2}\bar{\mathcal{M}}_a^2}w_a^- + \frac{2}{1+\frac{\gamma-1}{2}\bar{\mathcal{M}}_a^2}w_a^{\mathrm{S}} = \ldots \\
&\qquad\qquad \frac{(\gamma-1)(1+\bar{\mathcal{M}}_b)}{1+\frac{\gamma-1}{2}\bar{\mathcal{M}}_b^2}w_b^+ + \frac{(\gamma-1)(1-\bar{\mathcal{M}}_b)}{1+\frac{\gamma-1}{2}\bar{\mathcal{M}}_b^2}w_b^- + \frac{2}{1+\frac{\gamma-1}{2}\bar{\mathcal{M}}_b^2}w_b^{\mathrm{S}} \\
&\qquad\qquad w_a^{\mathrm{S}} = w_b^{\mathrm{S}}
\end{aligned}
\tag{8.2}
$$

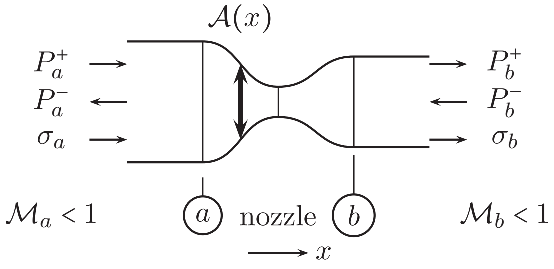

Figure 8.6 - *Sketch of the unchoked nozzle case.*

In each of the previous equations, the left-hand-side involves the three waves (w_a^+, w_a^-, w_a^{S}) upstream of the nozzle at the inlet and the right-hand-side the three waves (w_b^+, w_b^-, w_b^{S}) downstream of the nozzle at the outlet. As shown in Fig. 8.6, these waves propagate either outward or inward (toward the nozzle) depending on the flow-characteristic directions at these subsonic boundaries. In the particular case where $w_a^+ \neq 0$, $w_a^{\mathrm{S}} = 0$ and $w_b^- = 0$ (the ingoing waves can be fixed freely), Eqs. (8.2) allow recovering the expression given in [70] and Chap. 7 for the acoustic response of the unchoked nozzle to an acoustic excitation [AA]:

$$\frac{w_b^+}{w_a^+}[\mathrm{AA}] = \frac{2\bar{\mathcal{M}}_b}{1+\bar{\mathcal{M}}_b}\,\frac{1+\bar{\mathcal{M}}_a}{\bar{\mathcal{M}}_a+\bar{\mathcal{M}}_b}\,\frac{1+\frac{1}{2}(\gamma-1)\bar{\mathcal{M}}_b^2}{1+\frac{1}{2}(\gamma-1)\bar{\mathcal{M}}_a\bar{\mathcal{M}}_b} \tag{8.3}$$

In the same way, if $w_a^+ = 0$, $w_a^{\mathrm{S}} \neq 0$ and $w_b^- = 0$ are assumed, the acoustic response to an entropy perturbation [SA] is recovered as in [70] and Chap. 7, viz.:

$$\frac{w_b^+}{w_a^{\mathrm{S}}}[\mathrm{SA}] = \frac{\bar{\mathcal{M}}_b-\bar{\mathcal{M}}_a}{1+\bar{\mathcal{M}}_b}\,\frac{\bar{\mathcal{M}}_b}{1+\frac{1}{2}(\gamma-1)\bar{\mathcal{M}}_a\bar{\mathcal{M}}_b} \tag{8.4}$$

Isentropic choked nozzle

In the case of an isentropic choked nozzle, the flow is subsonic in the convergent nozzle part and supersonic in the divergent nozzle part. In this case, the acoustic wave w_b^- leaves the domain and cannot be imposed anymore (see Fig. 8.7). Two waves enter the domain, namely w_a^+ and w_a^{S}, and four must be determined, namely three transmitted/generated waves (w_b^+, w_b^- and w_b^{S}) and one reflected/generated wave (w_a^-). The cross-section area ratio equation for a choked nozzle is then introduced in order to close the problem as already mentioned in Chap. 7. In Sec. 7.3.1), by differentiating this ratio one have easily obtained that there is no fluctuation of the Mach number in this case [Eq. (7.24)]. Then, it has also been showed the static pressure is the same upstream and downstream of the nozzle [Eq. (7.27)]. Using the conservation of the entropy and

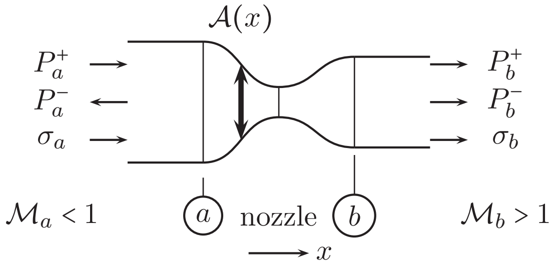

Figure 8.7 - *Sketch of the isentropic choked nozzle case.*

Eqs. (7.24,7.27), the following expressions for the four outgoing waves can be obtained:

$$\begin{aligned}
\left(1-\frac{\gamma-1}{2}\bar{\mathcal{M}}_a\right)w_a^+ - \left(1+\frac{\gamma-1}{2}\bar{\mathcal{M}}_a\right)w_a^- - \bar{\mathcal{M}}_a w_a^{\mathrm{S}} &= 0\\
\left(1-\frac{\gamma-1}{2}\bar{\mathcal{M}}_b\right)w_b^+ - \left(1+\frac{\gamma-1}{2}\bar{\mathcal{M}}_b\right)w_b^- - \bar{\mathcal{M}}_b w_a^{\mathrm{S}} &= 0\\
w_a^+ + w_a^- &= w_b^+ + w_b^-\\
w_a^{\mathrm{S}} &= w_b^{\mathrm{S}}
\end{aligned} \tag{8.5}$$

Once again, in the particular case where $w_a^+ \neq 0$ and $w_a^{\mathrm{S}} = 0$, Eqs. (8.5) allow recovering the expression given in [70] for the acoustic response of the choked nozzle to an acoustic excitation [AA]:

$$\frac{w_b^+}{w_a^+}[\mathrm{AA}] = \frac{1+\frac{\gamma-1}{2}\bar{\mathcal{M}}_2}{1+\frac{\gamma-1}{2}\bar{\mathcal{M}}_1} \tag{8.6}$$

In the same way, if $w_a^+ = 0$ and $w_a^{\mathrm{S}} \neq 0$ are assumed, the acoustic response to an entropy perturbation [SA] is recovered as in [70], viz.:

$$\frac{w_b^+}{w_a^{\mathrm{S}}}[\mathrm{SA}] = \frac{\bar{\mathcal{M}}_2 - \bar{\mathcal{M}}_1}{2}\frac{1}{1+\frac{\gamma-1}{2}\bar{\mathcal{M}}_1} \tag{8.7}$$

Yet, for all cases where the back-pressure is below the critical pressure yielding the sonic throat, a shock stands in the diverging section of the choked nozzle, the mean flow is no longer isentropic and the interaction of the waves with the shock must be accounted for as shown in the next section.

8.4.2 Waves for a shock

Even though the detailed interaction of acoustic, entropy or vorticity waves with a shock wave is a complex flow phenomenon [68, 69], the wave propagation can be fully described analytically in a

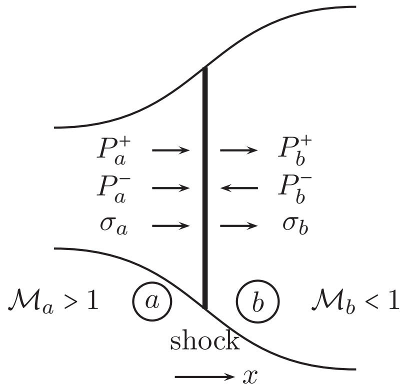

Figure 8.8 - *Sketch of the supersonic flow with normal shock case.*

simplified quasi-one-dimensional situation [74]. By construction the flow immediately upstream and downstream of a normal shock is supersonic and subsonic, respectively. Four waves are ingoing in this case (Fig. 8.8), namely w_a^+, w_a^-, w_a^{S} and w_b^-, while only two propagate in the outward direction, viz. w_b^+ and w_b^{S}. The derivation of the outgoing waves as a function of the ingoing ones builds upon the classical jump relations through a normal shock which only depend on the upstream Mach number $\mathcal{M}_a$:

$$\begin{aligned}\frac{p_b}{p_a} &= \frac{\gamma\mathcal{M}_a^2 - \frac{\gamma-1}{2}}{\frac{\gamma-1}{2}}\\ \frac{\rho_b}{\rho_a} &= \frac{\frac{\gamma-1}{2}\mathcal{M}_a^2}{1+\frac{\gamma-1}{2}\mathcal{M}_a^2}\end{aligned} \tag{8.8}$$

For small perturbations, and noting that $\mathcal{M}_a'/\bar{\mathcal{M}}_a$ is related to shock speed motion $-u_s'/\bar{u}_a$ since the Mach number depends of the cross-section area ratio only in the supersonic part, Eqs. (8.8) yield:

$$\begin{aligned}\left(\frac{p'}{\gamma\bar{p}}\right)_b - \left(\frac{p'}{\gamma\bar{p}}\right)_a &= -\frac{2\bar{\mathcal{M}}_a^2}{\gamma\bar{\mathcal{M}}_a^2 - \frac{\gamma-1}{2}}\left(\frac{u_s'}{\bar{u}_a}\right)\\ \left(\frac{\rho'}{\bar{\rho}}\right)_b - \left(\frac{\rho'}{\bar{\rho}}\right)_a &= -\frac{2}{1+\frac{\gamma-1}{2}\bar{\mathcal{M}}_a^2}\left(\frac{u_s'}{\bar{u}_a}\right)\end{aligned} \tag{8.9}$$

The conservation of the mass-flow in the frames of reference of the moving shock leads, for small perturbations, to:

$$\left(\frac{\rho'}{\bar{\rho}}\right)_a + \frac{1}{\bar{\mathcal{M}}_a}\left(\frac{u'}{\bar{c}}\right)_a = \left(\frac{\rho'}{\bar{\rho}}\right)_b + \frac{1}{\bar{\mathcal{M}}_b}\left(\frac{u'}{\bar{c}}\right)_b + \frac{1-\bar{\mathcal{M}}_a^2}{1+\frac{\gamma-1}{2}\bar{\mathcal{M}}_a^2}\left(\frac{u_s'}{\bar{u}_a}\right) \tag{8.10}$$

Equations (8.9,8.10) are first combined to eliminate $u_s'/\bar{u}_a$, noting that $[(\gamma+1)\bar{\mathcal{M}}_a^2]/[(\gamma-1)\bar{\mathcal{M}}_a^2 + 2] = \bar{\mathcal{M}}_b^2$. Then, the pressure, mass-density and velocity perturbations in the two resulting

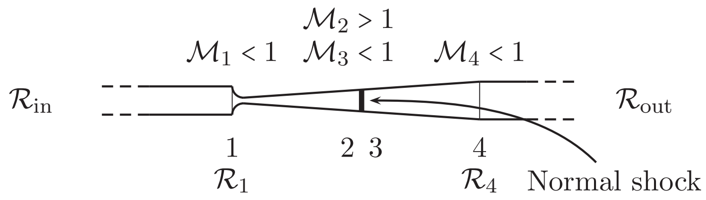

Figure 8.9 - *Notations for the analytic approach*

equations are replaced by the waves defined in Eqs. (7.10, 7.11, 7.12), and the following relations for the shock are finally obtained:

$$\begin{aligned}
\left(1+\bar{\mathcal{M}}_a^2+2\bar{\mathcal{M}}_a^2\bar{\mathcal{M}}_b\right) w_b^+ + \left(1+\bar{\mathcal{M}}_a^2-2\bar{\mathcal{M}}_a^2\bar{\mathcal{M}}_b\right) w_b^- &= \dots \\
&\left(1+\bar{\mathcal{M}}_a^2+2\bar{\mathcal{M}}_a\bar{\mathcal{M}}_b^2\right) w_a^+ + \left(1+\bar{\mathcal{M}}_a^2-2\bar{\mathcal{M}}_a\bar{\mathcal{M}}_b^2\right) w_a^- \\
\left(w_b^+ + w_b^- - w_a^+ - w_a^-\right)\frac{\gamma-1}{2}\frac{\left(\bar{\mathcal{M}}_a^2-1\right)^2}{\left[(\gamma-1)\bar{\mathcal{M}}_a^2+2\right]\bar{\mathcal{M}}_a^2} &= w_b^S - w_a^S
\end{aligned} \tag{8.11}$$

Equations (8.11) generalize the result given in [70] to the case where w_b^- is not zero and indicate that entropy fluctuations can be generated by the interaction between an acoustic wave and a shock. In the case of a perfectly reflecting outlet, a cycle of acoustic and entropic waves can be produced, which may yield an entropic-acoustic instability as described by Foglizzo and Tagger [47] in shocked accretion flows.

8.4.3 Application to the DLR configuration

Having derived the general transfer functions for the different types of flows in a compact converging-diverging nozzle, the relationships mimicking the EWG experiment can be derived based on the notations of Fig. 8.9. As mentioned above, the present focus is on the reference test case 1 in Bake *et al.* [8] of a choked nozzle with a maximum exit Mach number of 1.32. The supercritical nozzle starts at point 1 at the nozzle inlet and finishes at point 2 in the divergent section where the normal shock takes place. The normal shock relations are defined between point 2 and 3 and finally the subcritical nozzle starts at point 3, downstream of the shock, and finishes at point 4 at the end of the divergent region. Only the entropy wave generated by the electrical device, w_1^S, is taken into account at the inlet. The upstream part of the nozzle with the large settling chamber is represented in a general manner by the reflection coefficient $\mathcal{R}_1 = w_1^+/w_1^-$. The subsonic nozzle outlet is also represented by the reflection coefficient $\mathcal{R}_4 = w_4^-/w_4^+$.

For the supercritical nozzle upstream [Eqs. (8.5)], the in-going and out-going acoustic waves w_2^+ and w_2^- are given by

$$\begin{aligned} w_2^+ &= \xi_2^+ w_1^S \\ w_2^- &= \xi_2^- w_1^S \end{aligned}$$

with:

$$\xi_2^+ = \frac{1}{2}\,\frac{\bar{\mathcal{M}}_2 - \bar{\mathcal{M}}_1 - \mathcal{R}_1(\bar{\mathcal{M}}_2 + \bar{\mathcal{M}}_1)}{1 + \frac{\gamma-1}{2}\bar{\mathcal{M}}_1 - \mathcal{R}_1(1 - \frac{\gamma-1}{2}\bar{\mathcal{M}}_1)} \tag{8.12}$$

$$\xi_2^- = -\frac{1}{2}\,\frac{\bar{\mathcal{M}}_2 + \bar{\mathcal{M}}_1 - \mathcal{R}_1(\bar{\mathcal{M}}_2 - \bar{\mathcal{M}}_1)}{1 + \frac{\gamma-1}{2}\bar{\mathcal{M}}_1 - \mathcal{R}_1(1 - \frac{\gamma-1}{2}\bar{\mathcal{M}}_1)} \tag{8.13}$$

For the particular case where no reflection is considered at the inlet ($\mathcal{R}_1 = 0$) Eqs. (8.12) and (8.13) reduce to relations that can be found in [70]

$$\begin{aligned} \xi_2^+ &= \frac{\bar{\mathcal{M}}_2 - \bar{\mathcal{M}}_1}{2}\,\frac{1}{1 + \frac{\gamma-1}{2}\bar{\mathcal{M}}_1} \\ \xi_2^- &= -\frac{\bar{\mathcal{M}}_2 + \bar{\mathcal{M}}_1}{2}\,\frac{1}{1 + \frac{\gamma-1}{2}\bar{\mathcal{M}}_1} \end{aligned}$$

With the notations:

$$\begin{aligned} \alpha_3^\pm &= 1 + \bar{\mathcal{M}}_2^2 \pm 2\bar{\mathcal{M}}_2^2\bar{\mathcal{M}}_3 \\ \alpha_2^\pm &= 1 + \bar{\mathcal{M}}_2^2 \pm 2\bar{\mathcal{M}}_2\bar{\mathcal{M}}_3^2 \end{aligned}$$

and

$$\Sigma = \frac{\gamma - 1}{2}\,\frac{\left(\bar{\mathcal{M}}_2^2 - 1\right)^2}{\left[(\gamma-1)\bar{\mathcal{M}}_2^2 + 2\right]\bar{\mathcal{M}}_2^2}$$

at the normal shock [Eqs. (8.11)], the following relationships hold

$$\alpha_3^+ w_3^+ + \alpha_3^- w_3^- = \alpha_2^+ w_2^+ + \alpha_2^- w_2^- \tag{8.14}$$

and

$$(w_3^+ + w_3^- - w_2^+ - w_2^-)\,\Sigma = w_3^S - w_1^S \tag{8.15}$$

For the subcritical nozzle downstream [Eq. (8.2)], the in-going and out-going acoustic waves w_3^+, w_3^-, w_4^+ and w_4^- are given by

$$\begin{aligned} \beta_3^+ w_3^+ + \beta_3^- w_3^- &= \beta_4^+ w_4^+ + \beta_4^- w_4^- \\ \delta_3^+ w_3^+ + \delta_3^- w_3^- &= \delta_4^+ w_4^+ + \delta_4^- w_4^- + (\zeta_3 - \zeta_4)\; w_3^S \end{aligned} \tag{8.16}$$

with

$$\beta^\pm = 1 \pm \frac{1}{\bar{\mathcal{M}}}; \qquad \delta^\pm = \frac{(\gamma-1)\;(1 \pm \bar{\mathcal{M}})}{1 + \frac{\gamma-1}{2}\;\bar{\mathcal{M}}^2}; \qquad \zeta = \frac{2}{1 + \frac{\gamma-1}{2}\;\bar{\mathcal{M}}^2}$$

Eqs. (8.14) and (8.15) combined with Eqs. (8.16) yield the following coupled system of equations

$$\begin{bmatrix} \alpha_3^+ & \alpha_3^- & 0 & 0 \\ \Sigma & \Sigma & -1 & 0 \\ \beta_3^+ & \beta_3^- & 0 & -\left(\beta_4^+\mathcal{R}_4 + \beta_4^-\right) \\ \delta_3^+ & \delta_3^- & \zeta_4 - \zeta_3 & -\left(\delta_4^+\mathcal{R}_4 + \delta_4^-\right) \end{bmatrix} \begin{bmatrix} w_3^+ \\ w_3^- \\ w_3^{\mathrm{S}} \\ w_4^- \end{bmatrix} = \begin{bmatrix} \alpha_2^+\xi_2^+ + \alpha_2^-\xi_2^- \\ \Sigma\left(\xi_2^+ + \xi_2^-\right) - 1 \\ 0 \\ 0 \end{bmatrix} w_1^{\mathrm{S}} \qquad (8.17)$$

which provide the remaining four unknowns.

8.4.4 Analytical results

Solving for the equations in Sec. 8.4.3 yields the time traces of the pressure fluctuations downstream of the throat. The acoustic waves in the duct upstream of the nozzle are assumed to propagate at the speed of sound since the Mach number is small, so that one can write $\mathcal{R}_1 = \mathcal{R}_{\mathrm{in}} \exp(-2\imath\ell_{\mathrm{in}}\omega/c)$, where $\mathcal{R}_{\mathrm{in}}$ is the reflection coefficient at the duct inlet. The cross-section area of the settling chamber being large compared to the cross-section area of the duct, the pressure fluctuations can be assumed negligible for low-frequencies and thus one can write $\mathcal{R}_{\mathrm{in}} = -1$. For a more general model, the plenum could also be considered as an extended Helmholtz resonator as described in Bake *et al.* [4]. Similarly, the reflection coefficient of the subsonic nozzle outlet can be defined with the outlet reflection coefficient of the numerical simulation as $\mathcal{R}_4 = \mathcal{R}_{\mathrm{out}} \exp(-2\imath\ell_{\mathrm{out}}\omega/c)$ to match the condition used in the computation. The time evolution of the entropy wave is proportional to the one imposed in the source term of the energy equation in the numerical computation. The discrete Fourier transform of this signal $w_1^{\mathrm{S}}(\omega_k)$ is used for the analytical calculations.

Calculations [solving Eq. (8.17)] are performed for each frequency in order to take into account the frequency-dependence of the inlet and outlet boundary conditions, but the different nozzle elements are still assumed to be compact. Since a shock is present in the divergent part of the nozzle, the supercritical section (from 1 to 2) can be treated independently of the downstream elements, and provide explicitly the waves w_2^+, w_2^- and w_2^{S} entering the downstream elements. The shock (from 2 to 3) and the subcritical nozzle with the outlet BC (from 3 to 4) have to be treated together since most waves are coupled to yield the full system shown in Eq. (8.17). Finally, the reduced pressure fluctuation $[p'/\gamma\bar{p}(\omega_k)]_4$ is obtained in the frequency domain as a function of the four Mach numbers $\bar{\mathcal{M}}_1$, $\bar{\mathcal{M}}_2$, $\bar{\mathcal{M}}_3$ and $\bar{\mathcal{M}}_4$ ($\bar{\mathcal{M}}_3$ and $\bar{\mathcal{M}}_4$ are actually linked by the shock relations), the reflection coefficients $\mathcal{R}_{\mathrm{in}}(\omega_k)$, $\mathcal{R}_{\mathrm{out}}(\omega_k)$ and the reduced entropy fluctuation $w_1^{\mathrm{S}}(\omega_k)$.

The time evolutions of the pressure fluctuations reconstructed from the analytical calculations (inverse discrete Fourier transform) are compared to the numerical computations in two cases at the outlet: the non-reflecting case on the one hand (run 2D-1), and the *real* reflecting case

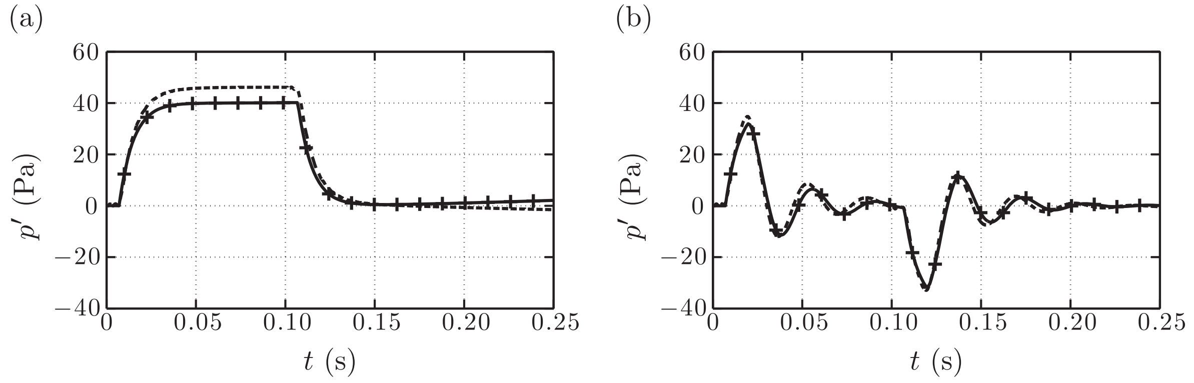

Figure 8.10 - *Time traces of the fluctuating pressure 350 mm downstream of the nozzle. Numerical results: $---$; Analytical results without reflections at the inlet and $\ell_{out} = 2100$ mm: $-+-$. (a) Non-reflecting case (Analytic compared to Run 2D-1); (b) Finite impedance case (Analytic compared to Run 2D-4).*

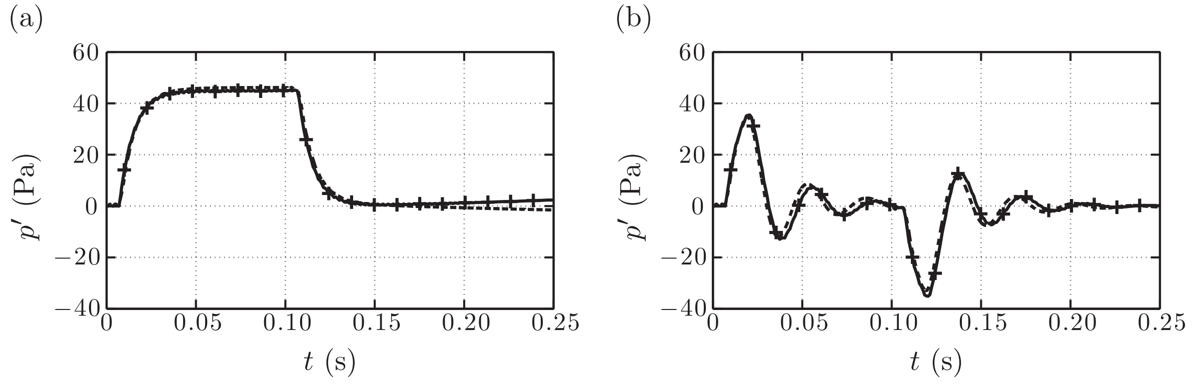

Figure 8.11 - *Time traces of the fluctuating pressure 350 mm downstream of the nozzle. Numerical results: $---$; Analytical results with reflections at the inlet and $\ell_{out} = 2100$ mm: $-+-$. (a) Non-reflecting case (Analytic compared to Run 2D-1); (b) Finite impedance case (Analytic compared to Run 2D-4).*

with the set of parameters of the tuned reflection coefficient (κ and ℓ_{out}) on the other hand (run 2D-4). Figure 8.10 shows these comparisons when no reflection is considered at the inlet. A good agreement is found which shows that the EWG experiment (for this regime) is essentially driven by linear quasi-1-D acoustics. Yet, the levels of the analytical calculation are slightly under-predicted. When considering a more realistic impedance at the inlet [$\mathcal{R}_1 = -\exp(-2\imath\ell_{\text{in}}\omega/c)$], Fig. 8.11 shows that the levels are now well recovered for both calculations with the two different outlet boundary conditions.

Finally, the analytical method can also be used to suggest improvements to the experimental set-up which would allow a clear separation of the indirect noise pressure signal and of acoustic reflection. An obvious solution would be to make the inlet and outlet termination fully anechoic to attenuate the reflections. This is difficult to achieve in practice, and a simpler solution is to

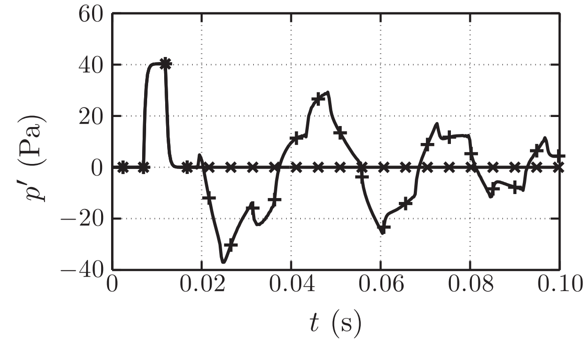

Figure 8.12 - *Analytical time traces of the fluctuating pressure downstream of the nozzle with shorter pulse duration. Totally non-reflecting at inlet and outlet:* $-\times-$*; Reflections at inlet and outlet:* $-+-$.

perform the split between generated and reflected waves by either changing the duration of the temperature pulse upstream or modifying the length of the upstream and downstream ducts to increase the waves travel times. If one considers the original pulse duration T_p of 100 ms, the length of the ducts upstream and downstream of the nozzle would have to be of the order of 35 m to avoid interaction with the reflected waves before 200 ms. This is probably difficult to establish on the real experimental set-up. But, if shorter pulses are generated ($T_p = 5$ ms and to preserve the signal shape $\tau = 0.4$ ms) and if the inlet duct length is of the order of the outlet one ($\ell_{\text{in}} = 2100$ mm), the two emitted acoustic waves (upstream and downstream) can be separated from the reflected waves if one considers only the waves travel durations. For this last case, the analytical calculations show that the duration between two pulses has to be increased until about 10 s if one wants the cycle of reflections, to be sufficiently attenuated to avoid perturbation of the theoretical pressure signal. One can see Fig. 8.12 the temporal evolution of the pressure fluctuation with the previous parameters. These analytical calculations were performed with and without reflections at the inlet and outlet. The pressure signal is not perturbed until the noise generation is finished ($t \simeq 20$ ms) so that the true indirect noise could be investigated in the absence of interference from reflected waves.

8.5 Conclusions

The DLR EWG experiment of Bake *et al.* [8] has been studied numerically and analytically. Simulations have been performed both in an axisymmetric and a fully three-dimensional configuration with various duct lengths and boundary conditions accounting for acoustic reflections. In parallel, an analytical model of the full experiment, based on an extension of the theory for compact nozzles originally derived by Marble and Candel [70], has been constructed: it takes into account the general acoustic impedances both at the inlet and outlet of the experimental set-up. The numerical and analytical analysis performed in this study demonstrate that the pressure signals obtained in the EWG experiment by Bake *et al.* [8] result from two main mechanisms: the entropy-to-acoustic conversion due the strong mean velocity gradient in the nozzle, including the normal shock that stands just downstream of the throat on the one hand; the acoustic reflection within the exhaust system downstream of the nozzle and test section on the other hand. The first mechanism is the indirect noise source and was the objective of the experiment. The second mechanism, however, is an undesired perturbation due to the non perfectly anechoic termination of the outlet, as well as the reflective inlet, which both must be understood to extract indirect noise signal from the measurements. The analysis also shows that, in the low-frequency range investigated, only 1-D planar waves are present and the compact nozzle approximation is valid, even for the entropy perturbations. As a result, the pressure signals observed experimentally and numerically can be nicely reproduced by a simple quasi-1-D analytical model derived in the low-frequency limit for the nozzle. This simpler model can also provide some guidance on how to re-design the experiment to remove or minimize the acoustic reflections in the measured pressure signals.

Chapter 9

Simulation and modelling of the waves transmission and generation in a blade row

9.1 Introduction

The scaling laws obtained for a one-dimensional (1-D) model combustor in Chap. 7 confirm that indirect combustion noise can be very important in comparison with the direct one. Both can be taken into account in practice with a minimal additional modelling effort, since the theory is based on linearized equations: entropy and acoustic waves can be extracted independently from a combustor and used as inputs of a model to get the indirect and direct noise at the outlet of the turbine stages. However, in an actual engine the waves generation and propagation through several blade rows is involved, and are strongly affected by the deviation of the flow, which occurs in the circumferential direction. The two-dimensional (2-D) configuration has an important influence on the transmission and generation of waves in comparison to the 1-D cases treated with the model of Marble and Candel in Chap. 7 and 8 (see Fig. 9.1). Moreover, the coupling within all the turbine stages should be taken into account in an ideal approach, as well as the loading of the rotor blades.

Several analytical and semi-analytical approaches have been proposed for 2-D flows to deal with the propagation of acoustic waves and vortices through turbo-machinery stages. Muir [78, 79] has treated the case of the actuator disk theory which assumes a 2-D configuration with an infinitely thin blade row, and uses classical conservation laws to establish relations between upstream and downstream flow. Kaji and Okazaki [55, 56] proposed the semi-disk actuator theory assuming in a first step that the spacing between the blades is infinitely thin but the chord-length is finite. A second step [55, 56] proposed a model with a finite chord-length and a finite spacing between blades. For both cases, the equations are solved numerically. Many other models are available for such 2-D problems. Recently Posson and Roger [91] have proposed a

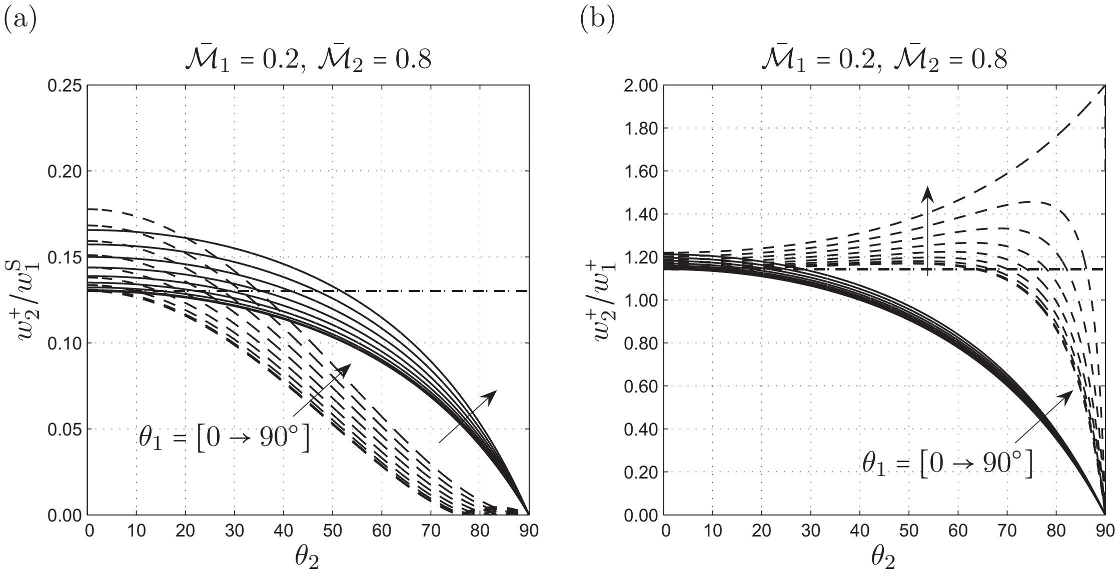

Figure 9.1 - *Acoustic response of a blade row at the outlet (2) to a perturbation at the inlet (1) for different flow orientations θ (in degree). Perturbation at the inlet: (a) Entropy; (b) Acoustic. 2-D compact model of Cumpsty and Marble (—); 1-D compact model Marble and Candel with Mach number based on the overall velocity magnitude (− · −), or on the axial velocity component (− − −).*

three-dimension cascade model both for generation and transmission losses which also accounts for cascade effects and finite chord, but neglects flow deviation (flat plates at zero incidence angle).

Literature is clearly less abundant when entropy waves are involved. Pickett [85] proposes relations based on linearized equations of continuity, momentum, energy, state and second law of thermodynamics to treat entropy waves to handle turbine blade rows. Stow and Dowling [110] have studied circumferential modes in choked nozzles. Following the approach of Marble and Candel [70], Cumpsty and Marble [37] have proposed a model to deal with waves transmission and generation through an axially compact blade row in a 2-D periodic and uniform flow based on the conservation of mass and total enthalpy (for the stator). The former model is investigated here because of the similarity with the work of Marble and Candel [70] already addressed in this thesis.

Bake *et al.* [8] have investigated experimentally the indirect noise for a 1-D nozzle flow, using the Entropy Wave Generator (EWG). These results have been numerically and analytically recovered in Chap. 8, showing that indirect noise can be well-predicted by such analytical approaches. However, no experimental or numerical study has been performed to investigate indirect noise for a 2-D flow with a blade row. What is proposed in the following study is to look at the theoretical aspects of this model and to asses its validity in a combustion noise framework by comparison with dedicated numerical results.

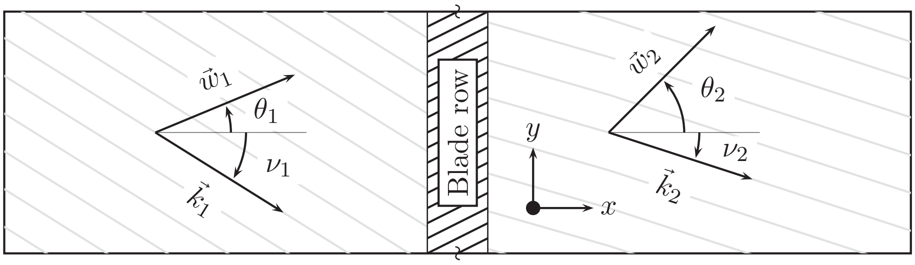

Figure 9.2 - *Schematic diagram of the flow upstream (1) and downstream (2) of the blade row in the model [37]. $\vec{w}$ is the velocity vector and $\vec{k}$ is the wave vector.*

The theoretical aspects of the model of Cumpsty and Marble [37] are first presented in Sec. 9.2, whereas the propagation of entropy, vorticity (because if the 2-D flow) and acoustic waves through an isolated blade is addressed with a CFD code in Sec. 9.3. Finally, the results are presented in Sec. 9.4 and conclusions are provided in Sec. 9.5 about the validity of the model.

9.2 Theory

The model of Cumpsty and Marble [37] is based on the same principles as the compact nozzle of Marble and Candel [70], but it assumes a 2-D configuration to take into account the circumferential component of the turbo machinery (the radial component of the flow is neglected). It can be shown that the equations derived in Chap. 7 and 8 can be recovered from the present model when the deviation is neglected and plane waves are considered (see Fig. 9.1). The model assumes that the blade row is axially compact and that the blades spacing is small compared with the chord. The steady flows on both sides of the blade row are assumed to be different, but uniform, so that the former is treated as a planar interface. Assuming that the perturbations within the flow are small, one can write first-order balance equations related to the fluctuations on both sides of the blade row, and evaluate the outgoing waves as a function of the ingoing ones and of the main characteristics of the flow (Mach number, deviation angle, etc.). In a first step, the relationships connecting the primitive flow variations upstream and downstream of the blade row are presented in Sec. 9.2.1. Secondly, the relations between the primitive flow variations (pressure, velocity, etc.) and the waves are provided in Sec. 9.2.2. Finally, using the results of Sec. 9.2.2 and Sec. 9.2.1, one writes outgoing waves as a function of the ingoing ones in Sec. 9.2.3

9.2.1 Primitive variables fluctuations at inlet and outlet

Since the blade row is assumed to be compact, fluctuations of entropy, mass-flow and energy are the same on both sides, like in [70]. The only difference is that the flow is two-dimensional, especially leading to consider an additional wave based on vorticity fluctuations (thus convected by the flow), as it will be seen hereafter. The primitive variables considered here are the pressure p, the mass-density ρ, the velocity magnitude w and the flow orientation angle θ. Therefore, in addition to the two-dimensional aspects, the underlying relations differs from those of Chap. 7 and Chap. 8 because of the choice of the mass-density instead of the entropy. For small perturbations, the conservation of the entropy betwen the inlet and the outlet of the blade row leads to:

$$\left(\frac{p'}{\gamma\bar{p}}\right)_1 - \left(\frac{\rho'}{\bar{\rho}}\right)_1 = \left(\frac{p'}{\gamma\bar{p}}\right)_2 - \left(\frac{\rho'}{\bar{\rho}}\right)_2 \tag{9.1}$$

where (1) relates to the inlet of the blade row and (2) to its outlet. Mass-flow $\dot{m}$ is also defined like in Chap. 7 and Chap. 8, however the flow deviation has to be taken into account in the 2-D case. Therefore $\dot{m} = \rho w \cos\theta \mathcal{A}$, where w is the magnitude of the flow velocity vector $\vec{w}$ and θ the deviation angle (see Fig. 9.2). For small perturbations, the mass-flow rate conservation can be expressed as:

$$\left(\frac{\rho'}{\bar{\rho}}\right)_1 + \frac{1}{\bar{\mathcal{M}}_1}\left(\frac{w'}{\bar{c}}\right)_1 - \theta_1' \tan\bar{\theta}_1 = \left(\frac{\rho'}{\bar{\rho}}\right)_2 + \frac{1}{\bar{\mathcal{M}}_2}\left(\frac{w'}{\bar{c}}\right)_2 - \theta_2' \tan\bar{\theta}_2 \tag{9.2}$$

where $\bar{\mathcal{M}}$ is the steady Mach number based on the steady velocity magnitude $\bar{w}$ and the steady speed of sound $\bar{c}$. The total temperature T_t (representing the total fluid energy) is based here on the velocity magnitude w. Therefore, considering that T_t is conserved through a static blade row, one obtains for small perturbations:

$$\begin{aligned}\frac{1}{1+\frac{1}{2}(\gamma-1)\bar{\mathcal{M}}_1^2}\left[\frac{\gamma}{\gamma-1}\left(\frac{p'}{\gamma\bar{p}}\right)_1 - \frac{1}{\gamma-1}\left(\frac{\rho'}{\bar{\rho}}\right)_1 + \bar{\mathcal{M}}_1\left(\frac{w'}{\bar{c}}\right)_1\right] = \dots \\ \frac{1}{1+\frac{1}{2}(\gamma-1)\bar{\mathcal{M}}_2^2}\left[\frac{\gamma}{\gamma-1}\left(\frac{p'}{\gamma\bar{p}}\right)_2 - \frac{1}{\gamma-1}\left(\frac{\rho'}{\bar{\rho}}\right)_2 + \bar{\mathcal{M}}_2\left(\frac{w'}{\bar{c}}\right)_2\right]\end{aligned} \tag{9.3}$$

The axial flow upstream and downstream of the blade row is here considered to be always subsonic (like in aero-engines), therefore there are always three downward traveling waves (acoustic, entropy and vorticity) and one traveling upward (acoustic). Four waves are entering the blade row (three at the inlet and one at the outlet) and four are also outgoing (one at the inlet and three at the outlet). However, the flow can be supersonic (the two upstream propagating waves at the inlet and the outlet are independent in this case because of the choked blade row). Here it is understood that the flow based on the velocity magnitude w is supersonic, but that the axial one, based on axial component u of the velocity, remains subsonic. As a consequence, four equations are required whatever the flow is (the four entering waves have to be imposed to find the outgoing ones). For the subsonic flow case, Cumpsty and Marble [37] propose to use the Kutta condition for the last equation:

$$\theta_2' = 0 \tag{9.4}$$

This assumption (the flow is perfectly aligned with the blades at the outlet) is in agreement with the infinitely small blade spacing hypothesis, but a more general form is mentionned by the authors, which is retained for this study:

$$\theta_2' = \beta\theta_1' \tag{9.5}$$

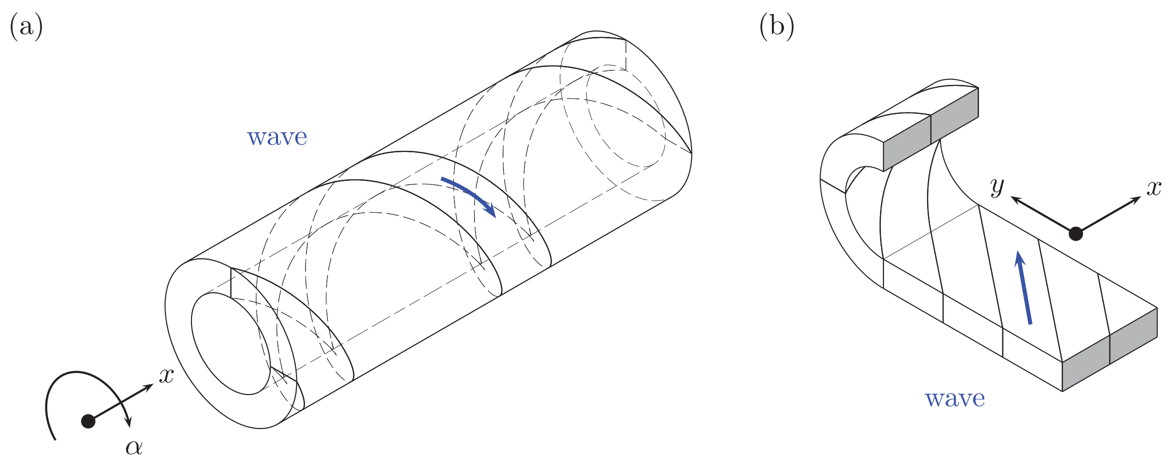

Figure 9.3 - *(a) Spiraling waves in an annular duct, (b) cylindrical to rectangular transformation.*

where β is a constant real number defined experimentally. Finally, Eqs. (9.1), (9.2), (9.3) and (9.5) can be written with the matrix $[\mathbf{E}_p^e]$ that relates the primitive variables fluctuations at the inlet and the outlet of the blade row:

$$[\mathbf{E}_p^e]_1 \cdot \begin{Bmatrix} p'/\gamma\bar{p} \\ \rho'/\bar{\rho} \\ w'/\bar{c} \\ \theta' \end{Bmatrix}_1 = [\mathbf{E}_p^e]_2 \cdot \begin{Bmatrix} p'/\gamma\bar{p} \\ \rho'/\bar{\rho} \\ w'/\bar{c} \\ \theta' \end{Bmatrix}_2 \tag{9.6}$$

with:

$$[\mathbf{E}_p^e]_1 = \begin{bmatrix} 1 & -1 & 0 & 0 \\ 0 & 1 & \frac{1}{\mathcal{M}_1} & -\tan\theta_1 \\ \mu_1\frac{\gamma}{\gamma-1} & -\mu_1\frac{1}{\gamma-1} & \mu_1\mathcal{M}_1 & 0 \\ 0 & 0 & 0 & \beta \end{bmatrix} \tag{9.7}$$

and:

$$[\mathbf{E}_p^e]_2 = \begin{bmatrix} 1 & -1 & 0 & 0 \\ 0 & 1 & \frac{1}{\mathcal{M}_2} & -\tan\theta_2 \\ \mu_2\frac{\gamma}{\gamma-1} & -\mu_2\frac{1}{\gamma-1} & \mu_2\mathcal{M}_2 & 0 \\ 0 & 0 & 0 & 1 \end{bmatrix} \tag{9.8}$$

where $\mu = 1/[1+(\gamma-1)\bar{\mathcal{M}}^2/2]$. The first line in Eqs. (9.7) and (9.8) corresponds to entropy, the second to mass-flow, the third to energy, and the last to the Kutta condition. The experimental value of β was not available for this thesis, so that it should be taken as zero. This parameter as been kept in the equations for sake of generality, but $\beta = 0$ leads to a singular matrix in Sec. 9.2.3. Therefore, β has been set here to 10^{-6}.

9.2.2 Primitive variables fluctuations and waves

The steady flows upstream and downstream of the blade row are assumed to be uniform, so that harmonic form fluctuations (in time and space) are solutions of the underlying linearized equations (mass, momentum and entropy). The general form of a perturbation ϕ' can be written $\phi \exp\left\{-i(\omega t - \vec{k}\cdot\vec{x})\right\}$ where ω is the angular frequency and t the time. $\vec{x}$ is the position vector (x, y) and $\vec{k}$ is the wave vector which is associated with the propagation of these perturbations. This vector has an axial (k_x) and a circumferential (k_y) component defining the angle ν (see Fig 9.2), therefore, the different fluctuations have a spiralling propagation, since the configuration is actually cylindrical (Fig. 9.3). At this point, one must highlight the difference between azimuthal acoustic modes of annular combustors mentioned in the combustion community [109], and the spiraling waves (sometimes also called *modes* in the acoustics community, which can be very confusing). Indeed, the azimuthal acoustic modes are made of waves that do not propagate axially ($k_x = 0$), contrarily to the so-called spiraling ones. The previously mentioned linearized equations are:

$$\frac{D}{Dt}\left(\rho'\right) = -\bar{\rho}\left(\frac{\partial u'}{\partial x} + \frac{\partial v'}{\partial y}\right) \tag{9.9}$$

$$\frac{D}{Dt}\left(u'\right) = -\frac{1}{\bar{\rho}}\frac{\partial p'}{\partial x} \tag{9.10}$$

$$\frac{D}{Dt}\left(v'\right) = -\frac{1}{\bar{\rho}}\frac{\partial p'}{\partial y} \tag{9.11}$$

$$\frac{D}{Dt}\left(s'\right) = 0 \tag{9.12}$$

where Eq. (9.9) is related to mass, Eqs. (9.10) and (9.11) to momentum and Eq. (9.12) to entropy balance equations written for small perturbations. The operator D/Dt is the substantial derivative after linearization and can be written as follows:

$$\frac{D}{Dt} = \frac{\partial}{\partial t} + \bar{u}\frac{\partial}{\partial x} + \bar{v}\frac{\partial}{\partial y} = i\omega - \bar{u}ik_x - \bar{v}ik_y \tag{9.13}$$

with:

$$\bar{u} = \bar{w}\cos\bar{\theta} \quad \text{and} \quad \bar{v} = \bar{w}\sin\bar{\theta} \tag{9.14}$$

Entropy wave

The entropy wave w^{S} is directly related to the dimensionless entropy fluctuation s'/c_p, and can be written as:

$$w^{\mathrm{S}} = \frac{s'}{c_p} = A_s \exp\left\{-i(\omega t - \vec{k}_s\cdot\vec{x})\right\} \tag{9.15}$$

where s' is the entropy fluctuation, c_p the specific heat at constant pressure. The subscript (s) stands for quantites related to entropy perturbations. The scalar product between the wave vector $\vec{k}_s$ and the position vector $\vec{x}$ verifies the following relation:

$$\vec{k}_s \cdot \vec{x} = k_{x,s} x + k_{y,s} y \tag{9.16}$$

with:

$$k_{x,s} = k_s \cos \nu_s \quad \text{and} \quad k_{y,s} = k_s \sin \nu_s \tag{9.17}$$

where $k_s = ||\vec{k}_s||$ and ν_s is the propagation angle of the entropy wave. One can notice that a local entropy perturbation is convected by the steady flow, so that its propagation is related to the velocity vector. However, the spatial pattern created by these fluctuations is related to the wave vector $\vec{k}_s$, which is different from the velocity vector generally speaking. For entropy, the relationship between $\vec{k}_s$, $\vec{w}$ and ω (the dispersion equation) is deduced from Eqs. (9.12), (9.13) and (9.14). Introducing the non-dimensionnal wave number $K_s = k_s \bar{c}/\omega$, where $\bar{c}$ is the steady speed of sound, this dispersion equation can be written as:

$$K_s \bar{\mathcal{M}} \cos(\nu_s - \bar{\theta}) = 1 \tag{9.18}$$

The entropy wave w^{S}, by definition, does not generate any velocity or pressure fluctuation. Since $s'/c_p = p'/\gamma\bar{p} - \rho'/\bar{\rho}$, the related fluctuations of primitive variables are:

$$\left| \begin{array}{rcl} (p'/\gamma\bar{p})_s & = & 0 \\ (\rho'/\bar{\rho})_s & = & -w^{\mathrm{S}} \\ (w'/\bar{c})_s & = & 0 \\ (\theta')_s & = & 0 \end{array} \right. \tag{9.19}$$

Vorticity wave

The vorticity perturbation is defined as $\xi' = \partial v'/\partial x - \partial u'/\partial y$. No pressure or mass-density fluctuation is related to the vorticity at first-order [57]. The associated wave w^{V} is written as follows:

$$w^{\mathrm{V}} = \frac{\xi'}{\omega} = A_v \exp\left\{-i(\omega t - \vec{k}_v \cdot \vec{x})\right\} \tag{9.20}$$

where the subscript (v) stands for quantites related to vorticity:

$$\vec{k}_v \cdot \vec{x} = k_{x,v} x + k_{y,v} y \tag{9.21}$$

and:

$$k_{x,v} = k_v \cos \nu_v \quad \text{and} \quad k_{y,v} = k_v \sin \nu_v \tag{9.22}$$

with $k_v = ||\vec{k}_v||$. Taking the derivative over x of Eq. (9.11) and subtracting the derivative over y of Eq. (9.10) leads to the vorticity perturbation governing equation:

$$\frac{D}{Dt}\left(\xi'\right) = 0 \tag{9.23}$$

Therefore, the dispersion relation can be written in the same manner as for the entropy, $K_v = k_v \bar{c}/\omega$ being the non-dimensionnal wave number:

$$K_v \bar{\mathcal{M}} \cos(\nu_v - \bar{\theta}) = 1 \tag{9.24}$$

To find the relationship between the vorticity and the primitive variable fluctuations, one considers in a first step that the vorticity wave is divergence free, therefore one can write:

$$\frac{\partial u'}{\partial x} + \frac{\partial v'}{\partial y} = 0 \tag{9.25}$$

which leads to:

$$v' = -u' k_{x,v}/k_{y,v} \tag{9.26}$$

In a second step, one writes the vorticity fluctuations as a function of the wave vector components:

$$\xi' = -i k_{x,v} v' + i k_{y,v} u' \tag{9.27}$$

Combining Eqs. (9.26) and (9.27) yield:

$$\begin{aligned} \frac{u'}{\bar{c}} &= -i \frac{\xi'}{\omega} \frac{\sin \nu_v}{K_v} \\ \frac{v'}{\bar{c}} &= i \frac{\xi'}{\omega} \frac{\cos \nu_v}{K_v} \end{aligned} \tag{9.28}$$

Now, one needs to express the fluctuations of velocity compoments u' and v' in terms of the fluctuations of the velocity magnitude w' and flow orientation angle θ'. Since $u = w \cos \theta$ and $v = w \sin \theta$, one can write for small perturbations:

$$\begin{aligned} \frac{u'}{\bar{u}} &= \frac{w'}{\bar{w}} - \theta' \tan \bar{\theta} \\ \frac{v'}{\bar{v}} &= \frac{w'}{\bar{w}} + \theta' \frac{1}{\tan \bar{\theta}} \end{aligned} \tag{9.29}$$

Equation (9.29) can be rearranged to get θ' and w' as a function of u' and v':

$$\begin{aligned} w' &= u' \cos \theta + v' \sin \theta \\ \theta' &= (-u' \cos \theta + v' \sin \theta)/\bar{w} \end{aligned} \tag{9.30}$$

Finally, replacing u' and v' in Eq. (9.30) by those defined in Eq. (9.28) provides the fluctuations of primitives variables related to the vorticity wave w^{V}:

$$\left| \begin{array}{rcl} (p'/\gamma \bar{p})_v &=& 0 \\ (\rho'/\bar{\rho})_v &=& 0 \\ (w'/\bar{c})_v &=& -i \sin(\nu_v - \bar{\theta})/K_v \; w^{\mathrm{V}} \\ (\theta')_v &=& i \cos(\nu_v - \bar{\theta})/(K_v \bar{\mathcal{M}}) \; w^{\mathrm{V}} \end{array} \right. \tag{9.31}$$

Acoustic waves

Two independent waves can be associated to acoustic perturbations. The acoustic wave propagating downward is noted w^+ and the upward propagating one w^-. These waves are defined with respect to the related non-dimensonal pressure fluctuation $(p'/\gamma\bar{p})_\pm$ as:

$$w^\pm = \left(\frac{p'}{\gamma\bar{p}}\right)_\pm = A_\pm \exp\left\{-i(\omega t - \vec{k}_\pm \cdot \vec{x})\right\} \tag{9.32}$$

where the subscript ($\pm$) stands for quantities related to acoustic perturbations, propagating downward (+) or upward (−). The definition of the acoustic waves in this chapter is based on the pressure caused by the upstream, or downstream, wave and not on the combination of the overall pressure and velocity like in Chap. 7 and 8. The following relationship can be written for the acoustic wave vector:

$$\vec{k}_\pm \cdot \vec{x} = k_{x,\pm}x + k_{y,\pm}y \tag{9.33}$$

with:

$$k_{x,\pm} = k_\pm \cos\nu_\pm \quad \text{and} \quad k_{y,\pm} = k_\pm \sin\nu_\pm \tag{9.34}$$

where $k_\pm = \|\vec{k}_\pm\|$. The governing equation for acoustic pressure fluctuations can be obtained by taking the derivative over x of Eq. (9.10) and over y for Eq. (9.11), and multiplying both by $\bar{\rho}$. The results are used to replace right-hand-side terms of the substantial derivative D/Dt of Eq. (9.9). Since acoustic pertubations are by definition isentropic, ρ' can be replaced by $p'/\bar{c}^2$ and it finally leads to:

$$\left(\frac{D}{Dt}\right)^2 (p') - \bar{c}^2 \left(\frac{\partial^2}{\partial x^2} + \frac{\partial^2}{\partial y^2}\right)(p') = 0 \tag{9.35}$$

Considering the non-dimensional wave vector $K_\pm = k_\pm \bar{c}/\omega$, the underlying dispersion equation can be written as:

$$\left(1 - K_\pm \bar{\mathcal{M}} \cos(\nu_\pm - \bar{\theta})\right)^2 - K_\pm^2 = 0 \tag{9.36}$$

Two wave vectors $\vec{k}_+$ and $\vec{k}_-$ satisfy Eq. (9.36). The circumferential components $k_{y,\pm}$ have a real representation since the domain is periodic along the turbine periphery. The axial components $k_{x,+}$ and $k_{x,-}$ are deduced from Eq. (9.36) and correspond to the two possible solutions:

$$K_{x,\pm} = \frac{-\bar{\mathcal{M}}\cos\bar{\theta}(1 - K_{y,\pm}\bar{\mathcal{M}}\sin\bar{\theta})}{1 - \bar{\mathcal{M}}^2\cos^2\bar{\theta}} \pm \ldots$$
$$\left(\frac{(1 - K_{y,\pm}\bar{\mathcal{M}}\sin\bar{\theta})^2 - (1 - \bar{\mathcal{M}}^2\cos^2\bar{\theta})K_{y,\pm}^2}{(1 - \bar{\mathcal{M}}^2\cos^2\bar{\theta})^2}\right)^{\frac{1}{2}} \tag{9.37}$$

The relationship between the fluctuations of the velocity magnitude w' and the flow orientation θ' is obtained, in a first step, by expressing u' and v' from the momentum relations Eqs. (9.10) and (9.11):

$$\begin{aligned} \frac{u'}{\bar{c}} &= -\frac{K_\pm \cos\nu_\pm}{1 - K_\pm \bar{\mathcal{M}}\cos(\nu_\pm - \bar{\theta})}\frac{p'}{\gamma\bar{p}} \\ \frac{v'}{\bar{c}} &= -\frac{K_\pm \sin\nu_\pm}{1 - K_\pm \bar{\mathcal{M}}\cos(\nu_\pm - \bar{\theta})}\frac{p'}{\gamma\bar{p}} \end{aligned} \tag{9.38}$$

Then, replacing u' and v' in Eq.(9.28) by those in Eq. (9.38) provides the fluctuations w' and θ' related to the acoustic perturbation. Since $\rho'/\bar{\rho} = p'/\gamma\bar{p}$ when considering acoustics only, one finally obtains:

$$\left|\begin{array}{rcl} (p'/\gamma\bar{p})_{\pm} & = & w^{\pm} \\ (\rho'/\bar{\rho})_{\pm} & = & w^{\pm} \\ (w'/\bar{c})_{\pm} & = & K_{\pm}\cos(\nu_{\pm}-\bar{\theta})/\left\{1-K_{\pm}\bar{\mathcal{M}}\cos(\nu_{\pm}-\bar{\theta})\right\}\ w^{\pm} \\ (\theta')_{\pm} & = & K_{\pm}\cos(\nu_{\pm}-\bar{\theta})/\left\{\bar{\mathcal{M}}\left(1-K_{\pm}\bar{\mathcal{M}}\sin(\nu_{\pm}-\bar{\theta})\right)\right\}\ w^{\pm} \end{array}\right. \tag{9.39}$$

Transformation matrix

The contribution of all waves (s, v and ±) are summed to yield the total fluctuations of the primitive variables, since the so-called waves are independent at the first-order. Equations (9.19), (9.31) and (9.39) are used to build the transformation matrix $[\mathbf{M}_w^p]$, which serves to express the fluctuations of the primitive variables as a function of the waves:

$$\left\{\begin{array}{c} p'/\gamma\bar{p} \\ \rho'/\bar{\rho} \\ w'/\bar{c} \\ \theta' \end{array}\right\} = [\mathbf{M}_w^p]\cdot\left\{\begin{array}{c} w^{\mathrm{S}} \\ w^{\mathrm{V}} \\ w^{+} \\ w^{-} \end{array}\right\} \tag{9.40}$$

with:

$$[\mathbf{M}_w^p] = \begin{bmatrix} 0 & 0 & 1 & 1 \\ 1 & 0 & 1 & 1 \\ 0 & -i\frac{\sin(\nu_v-\bar{\theta})}{K_v} & \frac{K_+\cos(\nu_+-\bar{\theta})}{1-K_+\bar{\mathcal{M}}\cos(\nu_+-\bar{\theta})} & \frac{K_-\cos(\nu_--\bar{\theta})}{1-K_-\bar{\mathcal{M}}\cos(\nu_--\bar{\theta})} \\ 0 & i\frac{\cos(\nu_v-\bar{\theta})}{K_v\bar{\mathcal{M}}} & \frac{K_+\sin(\nu_+-\bar{\theta})}{\bar{\mathcal{M}}\{1-K_+\bar{\mathcal{M}}\cos(\nu_+-\bar{\theta})\}} & \frac{K_-\sin(\nu_--\bar{\theta})}{\bar{\mathcal{M}}\{1-K_-\bar{\mathcal{M}}\cos(\nu_--\bar{\theta})\}} \end{bmatrix} \tag{9.41}$$

9.2.3 Ingoing and outgoing waves

Using Eq. (9.40) in Eq. (9.6), the problem can be expressed in terms of the waves upstream (1) and downstream (2) of the blade row as follows:

$$\underbrace{[\mathbf{E}_p^e]_1\cdot[\mathbf{M}_w^p]_1}_{[\mathbf{B}]_1}\cdot\left\{\begin{array}{c} w^{\mathrm{S}} \\ w^{\mathrm{V}} \\ w^{+} \\ w^{-} \end{array}\right\}_1 = \underbrace{[\mathbf{E}_p^e]_2\cdot[\mathbf{M}_w^p]_2}_{[\mathbf{B}]_2}\cdot\left\{\begin{array}{c} w^{\mathrm{S}} \\ w^{\mathrm{V}} \\ w^{+} \\ w^{-} \end{array}\right\}_2 \tag{9.42}$$

In Eq. (9.42), the left-hand-side term contains the wave w_1^- that is traveling upward from the blade row and which has to be found, whereas the other waves have to be imposed. The situation is reversed in the right-hand-side term, where the wave w_2^- has to be imposed, and the other ones have to be found. In the case of an isolated blade row, it is simply necessary to permute the terms of the last column of the matrices $[\mathbf{B}]_1$ and $[\mathbf{B}]_2$ from left-to-right to yield the matrices

$[\mathbf{A}]_I$ and $[\mathbf{A}]_O$, which relate to the ingoing and outgoing waves respectively. Finally, the linear problem to be solved is the following:

$$\left\{ \begin{array}{c} w_2^{\mathrm{S}} \\ w_2^{\mathrm{V}} \\ w_2^{+} \\ w_1^{-} \end{array} \right\} = \underbrace{[\mathbf{A}]_O^{-1} \cdot [\mathbf{A}]_I}_{\mathbf{M}_{\mathrm{in}}^{\mathrm{out}}} \left\{ \begin{array}{c} w_1^{\mathrm{S}} \\ w_1^{\mathrm{V}} \\ w_1^{+} \\ w_2^{-} \end{array} \right\} \tag{9.43}$$

The literal expression of the outgoing waves is rather cumbersome in a general case and thus it is not presented here. However, the simulations handled in Sec. 9.3 are performed for waves travelling axially only ($k_y = 0$), so that the outgoing waves of the relation Eq. (9.43) can be expressed in a quite simpler form in this situation. Three different cases are treated hereafter where entropy, vorticity or acoustics are perturbed at the inlet of the blade row; the relating analytical solutions are provided in App. A.

9.3 Numerical simulations

The aim of the numerical simulations presented in this section is to calculate realistic transfer functions of a blade row to different perturbations, in order to evaluate the error made when using the model of Cumpsty and Marble [37]. However, computing the complete blade row, even for a 2-D case, is beyond the scope of the present work. Validating the model involves a very large range of characteristic times (ratio in the order of 10^7 in this case). On one hand, wavelengths of the imposed perturbations have to be sufficiently large to be able to verify the compact blade row assumption. On the other hand, the time-step of the computation has to be sufficiently small to solve the flow correctly for the small geometrical details, such as the trailing-edge for instance. Therefore, the present simulations are performed in a 2-D case with a single blade limiting thus the study to longitudinal waves only: circumferential waves associated to this single blade are non-evanescent from 16 kHz which is out interest for this study. Periodical boundary conditions are used at the top and the bottom of the computational domain (see Fig. 9.4). Note that the origin of the reference frame is located at the blade trailing edge. The blade used for these simulations comes from the High-Pressure Turbine of the engine computed in Chap. 10.1 and the corresponding mesh contains 115000 triangles.

The 2-D flow is simulated using the unsteady and compressible solver AVBP. The laminar and turbulent Prandtl numbers (Pr and Pr_t respectively) are chosen large enough to minimize heat diffusion within the flow ($Pr_t = 100$), and thus avoid dissipation of the entropy waves in the long inlet and outlet regions. The 2-D simulations are performed using the Smagorinsky Large-Eddy Simulation (LES) sub-grid scale model, but only to avoid numerical issues, and not for turbulence modelling. The numerical method used for the simulations is TTG4A scheme which is third-order in space and fourth-order in time (see Sec. 4.2), and which exhibits quite good dispersion properties.

The transfer functions are obtained according to Table 9.1. Three different simulations are performed where the entropy (simulation S-1), the vorticity (simulation V-1) and the ingoing

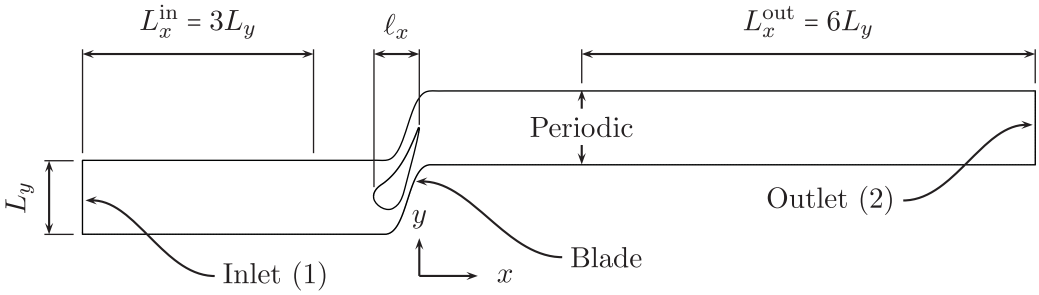

Figure 9.4 - *Description of the computational case.*

acoustic wave (simulation A-1) are separately perturbed at the inlet of the computational domain. A fourth simulation is performed where no ingoing wave is disturbed (N-0), and it is used as the reference case. During these simulations, the amplitudes of the non-perturbed ingoing waves are forced to be zero. Like in Chap. 7, NSCBC is used to impose the wave levels, and only planar ones are considered, with a purely axial wave vector ($k_y = 0$). The pulsed waves are imposed in the following way:

$$f(t) = \sum_{k=1}^{N_k} \sin(2\pi k f_0 t) \tag{9.44}$$

where N_k is the number of frequencies which are pulsed (50 in this study) and where f_0 is the fundamental frequency of the excitation (f_0 = 100 Hz). The signal $f(t)$ plotted versus the non-dimensional time t/τ_0, where $\tau_0 = 1/f_0$, is shown in Fig. 9.5. This signal is made up of N_k harmonics based on the frequency f_0 and of the same magnitude (in the order of 0.001). All the simulations presented in Table 9.1 are performed starting from a satistically converged unperturbed flow. The three simulations S-1, V-1 and A-1 are performed to evaluate the acoustic outgoing waves comparatively to the ingoing ones, and thus obtain the acoustic transfer functions of the blade row. The simulation N-0 is performed to evaluate the global sound level of the unsteady unperturbed flow, and verify whether it is lower (or not) than the one produced by the interaction between the ingoing waves and the blade row. The flow studied here is subsonic and the operating conditions were: $\bar{\mathcal{M}}_1 = 0.12$, $\bar{\theta}_1 = 0^o$ and $\bar{\mathcal{M}}_2 = 0.66$, $\bar{\theta}_2 = 76^o$.

9.4 Results

The transfer functions computed numerically are compared in this section with the analytical relations presented in Sec. 9.2 (see appendix A for more details). The field of the entropy perturbation s'/c_p at three different times is shown in Fig. 9.6. It can be observed that the entropy wave remains planar before the blade row (there is no injection of vortical perturbations) and that it is rather perturbed after the interaction with the blade row (Reynolds number based on the chord length $Re_c \approx 10^6$). Therefore, the post-processing of the waves is performed by

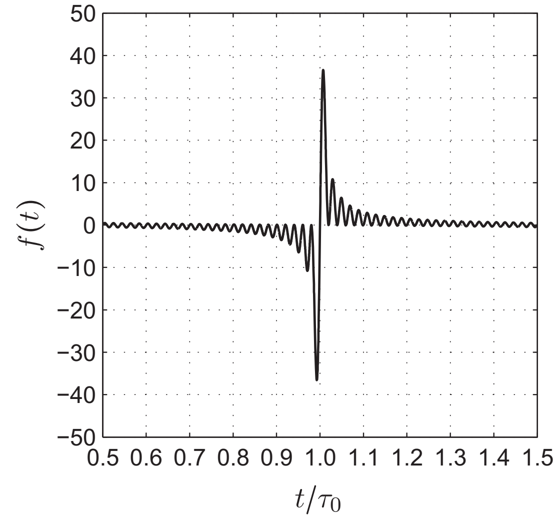

Figure 9.5 - *Temporal evolution of the pertubation imposed on acoustic or entropy waves at the computational domain inlet.*

	Perturbed waves				
Name	w_1^{S} (entropy)	w_1^{V} (vorticity)	w_1^{+} (acoustic)	w_2^{-} (acoustic)	Duration
S-1	●	○	○	○	66 τ_0
V-1	○	●	○	○	66 τ_0
A-1	○	○	●	○	66 τ_0
N-0	○	○	○	○	18 τ_0

Table 9.1 - *Description of the different simulations for the subsonic case ($\bar{\mathcal{M}}_1 = 0.12$, $\bar{\theta}_1 = 0^o$ and $\bar{\mathcal{M}}_2 = 0.66$, $\bar{\theta}_2 = 76^o$). Wave amplitude forced to zero (○), wave amplitude imposed according to $f(t)$ signal (●).*

(a) $t/\tau_0 = 0.1$

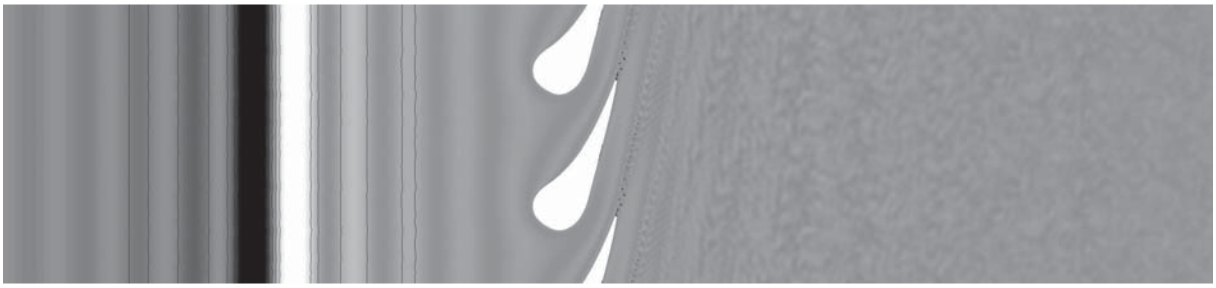

(b) $t/\tau_0 = 0.2$

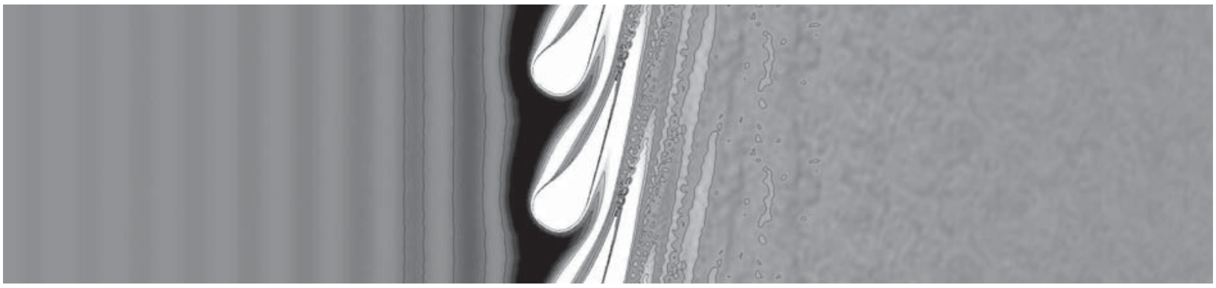

(c) $t/\tau_0 = 0.3$

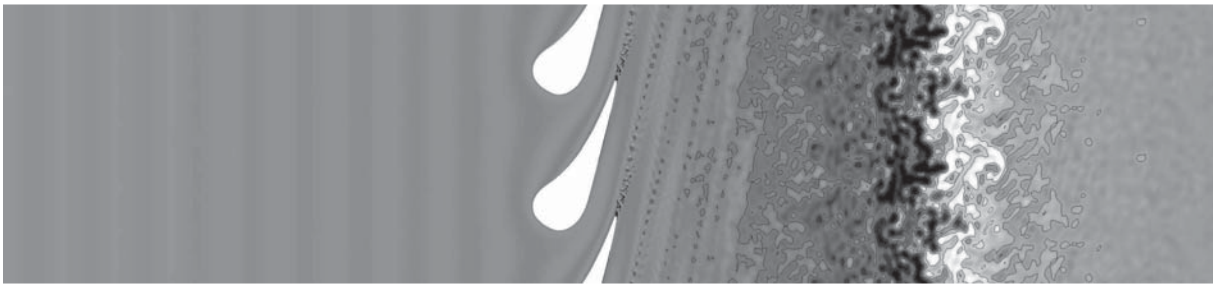

Figure 9.6 - *Instantaneous field of the entropy wave at different times for the case where entropy is pulsed at the inlet. (a)* $t/\tau_0 = 0.1$*, (b)* $t/\tau_0 = 0.2$*, (c)* $t/\tau_0 = 0.3$.

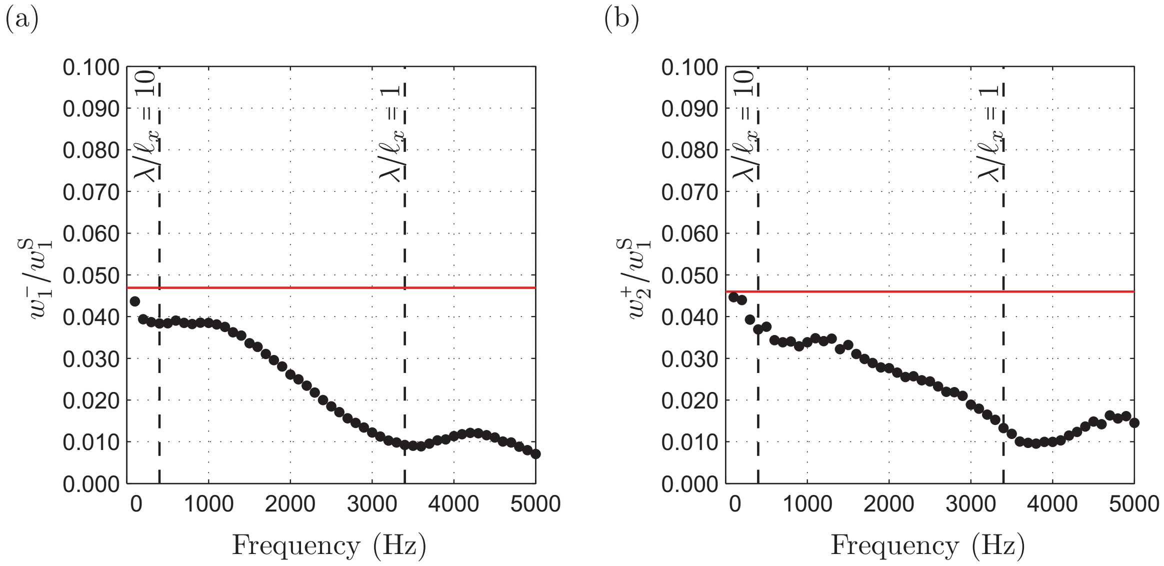

Figure 9.7 - *Acoustic response of the blade row to an entropy perturbation at the inlet (S-1). (a) Upstream propagating waves; (b) Downstream propagating waves. Model (—), simulation (•).*

integration of the required quantities along the transversal direction, since the waves of interest are axially oriented ($k_y = 0$). Afterwards, quadratic averaging of the waves Fourier-transform modulus is performed along the axial direction. The local 1-D waves w_x^j, where the superscript j stands for (S), (V), (+) or (−), are calculated as follows:

$$w_x^j(x,k) = \left| \frac{1}{N_t\tau_0} \int_0^{N_t\tau_0} \left\{ \frac{1}{L_y} \int_0^{L_y} w^j(x,y,t)dy \right\} \exp(i2\pi f_0 kt)dt \right| \tag{9.45}$$

where N_t is the number of computed periods τ_0[1] and L_y is the height of the inter-blade channel (see Fig. 9.4). The global 1-D waves w^j are obtained using the following relation:

$$w^j(k) = \sqrt{\frac{1}{L_x} \int_0^{L_x} \left\{ w_x^j(x,k) \right\}^2 dx} \tag{9.46}$$

where L_x corresponds to $3L_y$ for the waves at the inlet (subscripted 1) and $6L_y$ for the waves at the outlet (subscripted 2) as depicted in Fig 9.4. The acoustic response of the blade row [acoustic waves propagating upstream (a) and downstream (b)] to an entropy perturbation plotted as a function of the frequency (simulation S-1) is shown in Fig. 9.7. Two values of the non-dimensionalised entropy wavelength λ/ℓ_x based on the inlet quantities are also depicted to provide an idea of the compactness of the blade row for the perturbed frequency range. The transfer function obtained from the simulation S-1 tends to the model for the low-frequencies, and decreases rapidly for higher frequencies. Figure 9.8 shows the acoustic response of the

---

[1] $\tau_0 = 1/f_0$ where f_0=100 Hz.

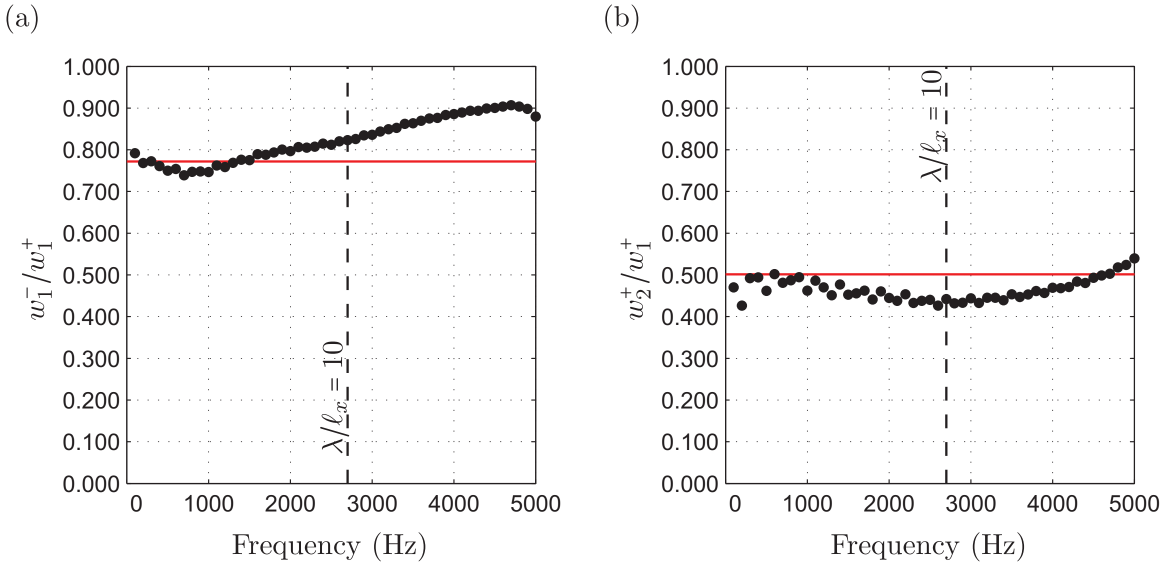

Figure 9.8 - *Acoustic response of the blade row to an acoustic perturbation at the inlet (A-1). (a) Upstream propagating waves; (b) Downstream propagating waves. Model (—), simulation (•).*

blade row to a downward propagating acoustic wave (simulation A-1) perturbation. The non-dimensional acoustic wavelength λ/ℓ_x is also depicted. The transfer function obtained from the simulation A-1 is thus very close to the model value since the perturbed wavelengths λ are large compared with the blade axial length ℓ_x. Finally, Fig. 9.9 shows the acoustic response of the blade to a vorticity perturbation (simulation V-1). Since the flow is axially oriented at the blade row entrance ($\bar{\theta}_1 = 0$), the model predicts that the vorticity does not generate acoustic waves [Eqs. (A.14) and (A.15) in App. A]. Therefore, the comparison is not really relevant for this case (the theoretical result is exactly zero).

As seen in Section 9.2, the model of Cumpsty and Marble [37] assumes that the entropy is conserved. The verification of this statement can be interesting if the model is used for more than one blade row. The turbulent mixing in the flow downstream of the blade row strongly affects the structure of the wave and the initial planar coherence of the entropy perturbation is lost for higher frequencies as shown in Fig. 9.10-a. The global entropy wave, as defined as the axially averaged wave (Eq. 9.46), is not representative in this case, since the mixing process takes place after the blade row. The evolution along the axial direction of the entropy wave is more relevant of its attenuation, described by the ratio $w_{x,2}^{\mathrm{S}}/w_1^{\mathrm{S}}$, and is shown in Fig. 9.10-b for different frequencies. Lower frequencies (larger wavelengths) are almost not affected by the mixing which occurs at the scales of the blade dimension, and levels remain the same until the outlet. The intensity of small wavelengths not only decreases more rapidly, but mostly the waves are already attenuated at the very beginning of the downstream section ($x/l_x = 0$). Since the spacing between the stator and the rotor Δx is generally very small ($\Delta x/l_x < 0.5$), it is interesting to understand the reasons of such a phenomenon. The attenuation in the channel between blades

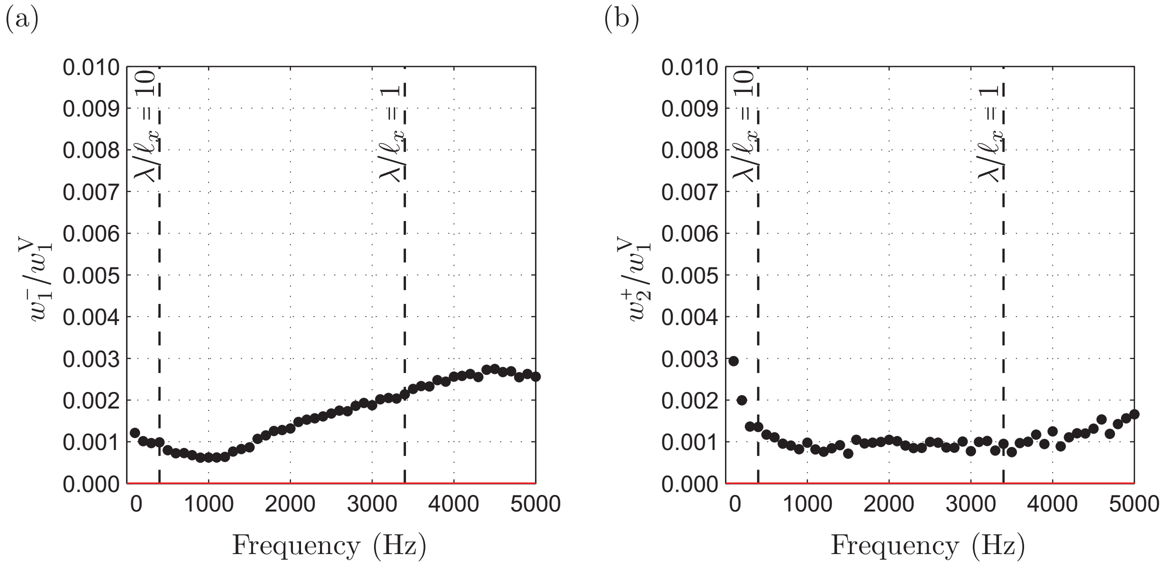

Figure 9.9 - *Acoustic response of the blade row to a vorticity perturbation at the inlet (V-1). (a) Upstream propagating waves; (b) Downstream propagating waves. Model (—), simulation (•).*

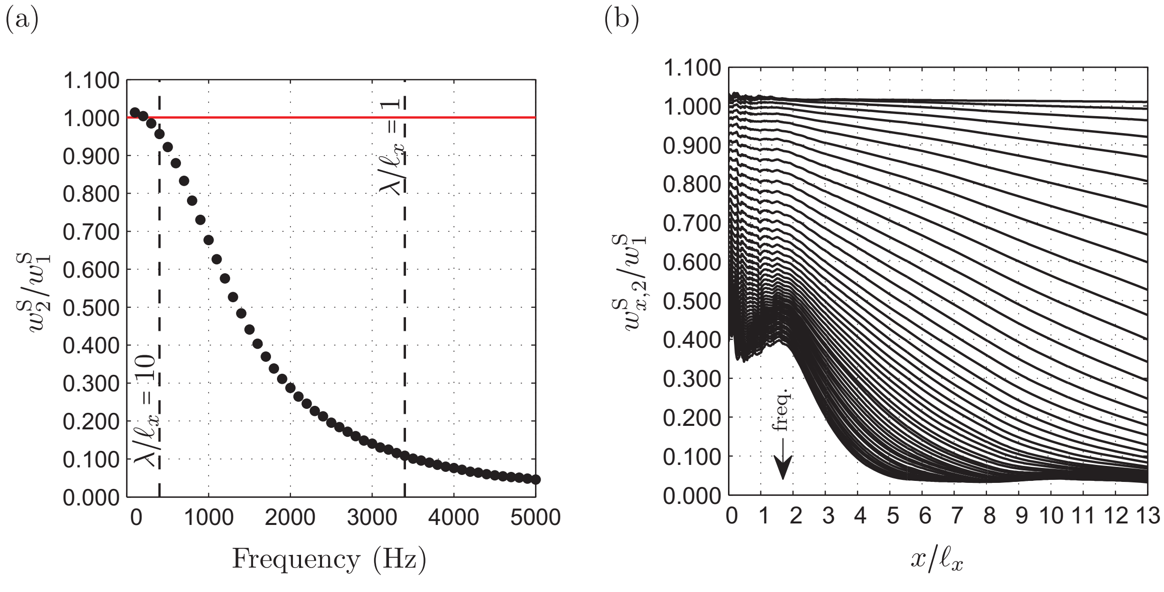

Figure 9.10 - *Entropy response of the blade row at the outlet to an entropy perturbation at the inlet. (a) Global entropy wave, where (—) stands for the model, and (•) for the simulation; (b) Local entropy wave at the outlet, where the different curves represent different frequencies.*

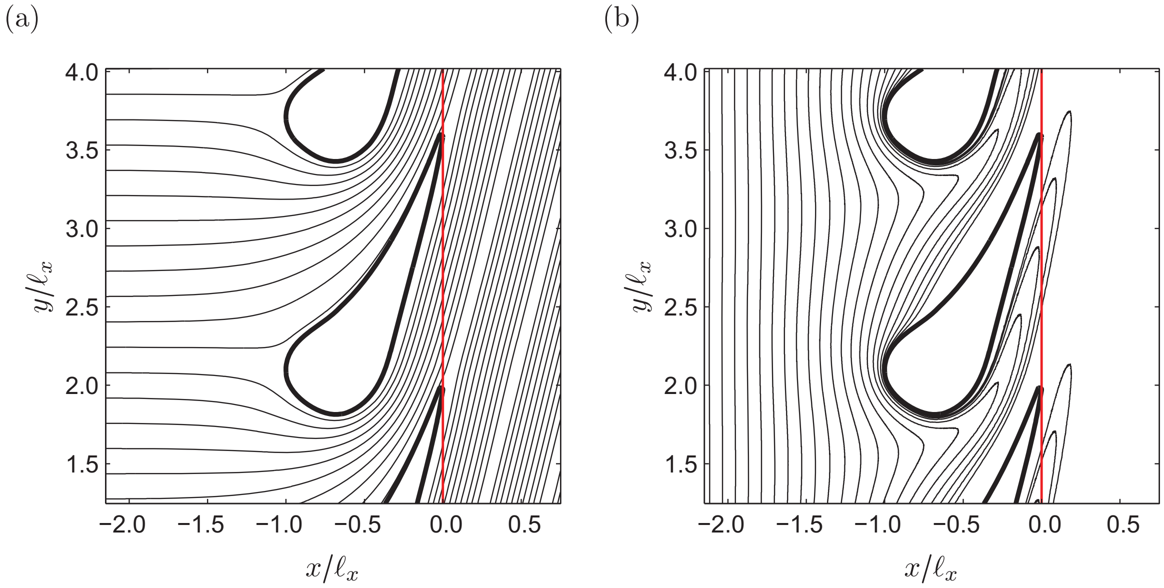

Figure 9.11 - *Mean flow characteristics. (a) Path-lines calculated from the mean flow; (b) Particules-lines seeded from the inlet and calculated from the mean flow.*

can be explained by the distortion of the planar waves by the steady flow, and can be calculated from the related 2-D velocity field. The distortion of the waves at the outlet of the blade row is here evaluated using lagrangian tracking of particles seeded at the inlet (post-processing of the steady flow). Figure 9.11-a shows the path-lines of the particles computed from the steady flow (the flow is quasi-steady in channel between blades), whereas Fig. 9.11-b shows particle-lines seeded at the same time. Both graphs show that the flow between the blades is not uniform. As a consequence, initially axially co-current particles have a different time of arrival at the blade row outlet plane ($x/l_x = 0$). Figure 9.11-b clearly reveals the deformation of the initially planar waves. The delay in the arrival of particles at the outlet $t_d(y)$ is plotted in Fig. 9.13-a versus the transversal direction y non-dimensionalised by the pitch length L_y ($y/L_y = 0$ and $y/L_y = 1$ correspond to the blade trailing-edges). These quantity is obtained by calculating the duration required by a particle to reach the outlet plane $x/\ell_x = 0$ when following a given path-line. The particles passing by the trailing-edges should theoretically have an infinite time of arrival, but have a finite value here because of the finite number of path-lines used to evaluate the function $t_d(y)$. This function can be directly used to calculate the *attenuation* of the entropy waves, which no longer appear as planar at the outlet of the blade row (see example in Fig.9.12). Indeed, each serie of particles can be associated to a sinusoidal level of amplitude. As a consequence, the 1-D temporal fluctuations (average along the transversal direction y) at the blade row outlet $d_0(t,k)$ can be simply expressed as follows:

$$d_0(t,k) = \frac{1}{L_y}\int_0^{L_y} \exp\left\{i2\pi k f_0\left[t + t_d(y)\right]\right\} dy \tag{9.47}$$

The local entropy fluctuations are actually not decreased, but simply redistributed in space.

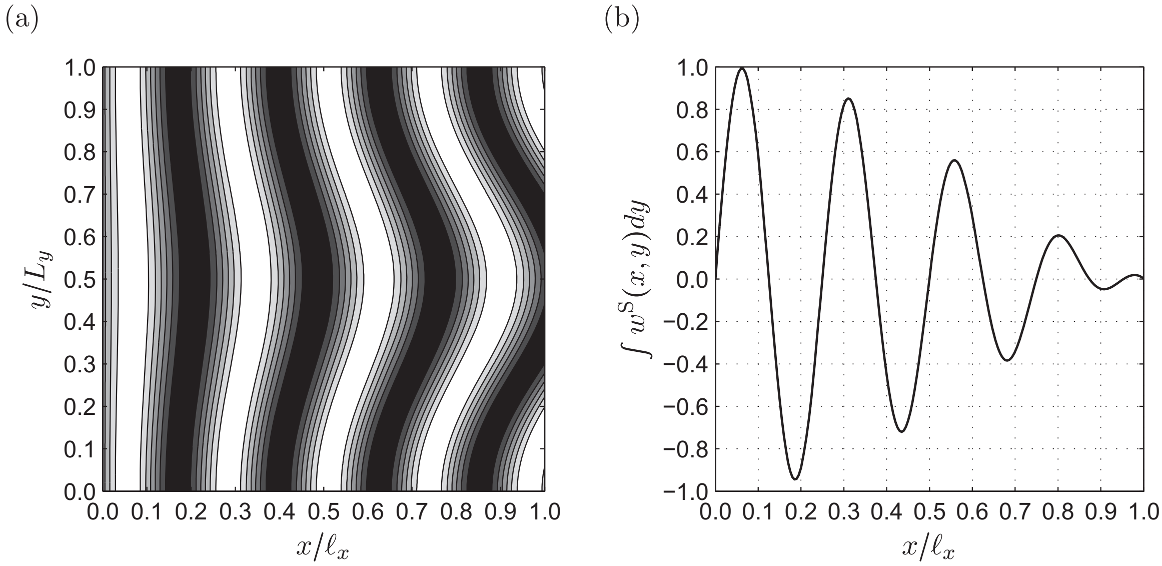

Figure 9.12 - *Example of entropy wave distortion. (a) 2-D field of entropy wave* $w^S(x,y)$ *with faster mean flow in the middle; (b) Integral of the entropy wave over the transversal direction* y.

Using Eq. 9.47, the attenuation of the longitudinal waves $D_0(k)$ for the frequency k is:

$$D_0(k) = \left| \frac{1}{L_y} \int_0^{L_y} \exp\left\{ i2\pi k f_0 t_d(y) \right\} dy \right| \tag{9.48}$$

which only depends on the function $t_d(y)$ and on k. In Fig. 9.13-b (for $n = 0$), the attenuation measured in the simulation, and the one computed using the mean flow distortion, are in a quite good agreement for almost the whole spectrum. This point strongly supports that the attenuation for small convective wavelength at the beginning of the downstream section is caused by the distortion of initially planar waves by the mean flow. It is interesting to remark that this phenomenon will of course produce non-planar waves at the outlet. A more general expression for Eq. (9.48) can be:

$$D_n(k) = \left| \frac{1}{L_y} \int_0^{L_y} \exp\left\{ i2\pi \left[k f_0 t_d(y) + n(y/L_y) \right] \right\} dy \right| \tag{9.49}$$

where the integer n corresponds to the n-th transversal wave vector component related to the propagation of the entropy wave. This function is also plotted in Fig. 9.13 for different values of n ($n = [-3:3]$). One can see that when the frequency tends to zero, only planar waves ($n = 0$) are observed and without attenuation. When the wavelength diminishes (higher frequency) the transversal waves appear whereas the longitudinal wave strongly decreases (for wavelengths in the order of the blade dimension, or rather the blade spacing). These observations suggest that, to study the non-compact aspects of the propagation of entropy waves, not only planar waves should be looked at, even if the excitation is planar. This redistribution of the entropy fluctuations can have an influence when several blade rows are involved.

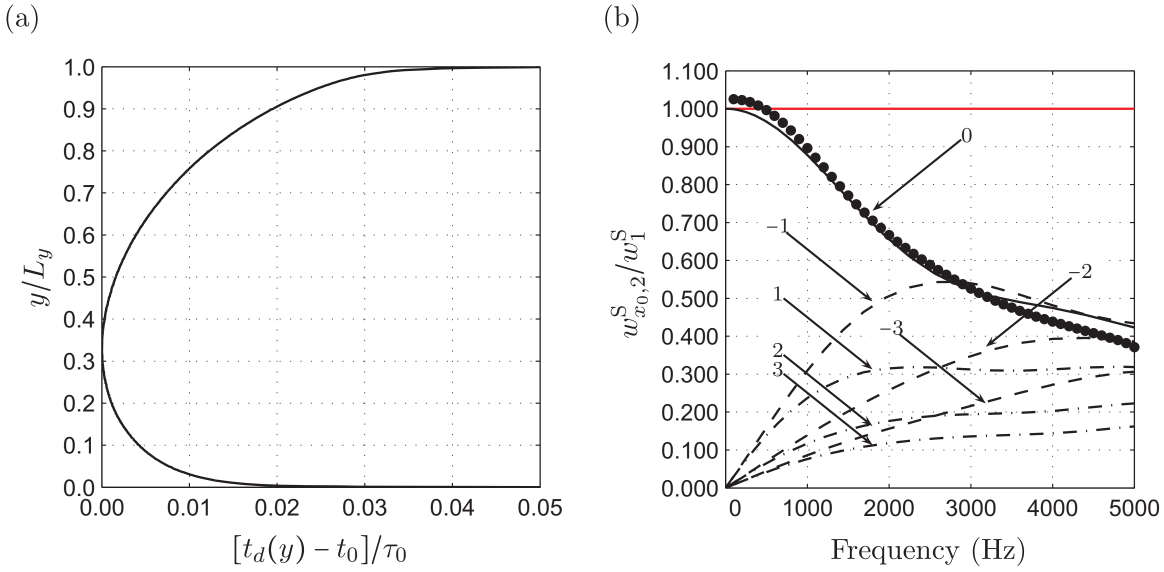

Figure 9.13 - *(a) Difference in time for a particle to reach the blade row outlet x_0 on a given path-line. (b) Attenuation $D_n(k)$ of the entropy wave through the blade row: calculated from the steady flow (—), simulated (•) for $n = 0$. From the post-processing with $n < 0$ (– – –) and $n > 0$ (– · –).*

The model of Cumpsty and Marble [37] also predicts the generation of vorticity waves. It can be interesting to look at this aspect in the scope of the coupling between different blade rows, even if it has been seen that there is no noise caused theoretically by the vorticity in the investigated case. Figure. 9.14 shows the response of the blade row in terms of vorticity to either an entropy (a), or an acoustic perturbation (b). The vorticity induced by the entropy perturbations in simulation S-1 seems to be negligible in comparison to the vorticity caused by trailing-edge wake, and thus the model seems to under-predict the vorticity response of the blade row. This statement is confirmed by Fig. 9.15 that shows the vorticity levels at the inlet and the outlet of the blade row for all simulations. Concluding about the validity of the model for the induced vorticity in simulation S-1 is thus not possible since the magnitude of the imposed entropy perturbations is too small. However for the simulation A-1 (Fig. 9.14-b), which seems to exhibit more vorticity because of the acoustic perturbation (see Fig. 9.15), the model works well in the low frequency range.

9.5 Conclusion

Numerical unsteady simulations of the response of an isolated blade row have been performed in a 2-D configuration to evaluate the validity of the analytical model of Cumpsty and Marble [37], which assumes a compact blade row. The acoustic transmission and reflection is well predicted

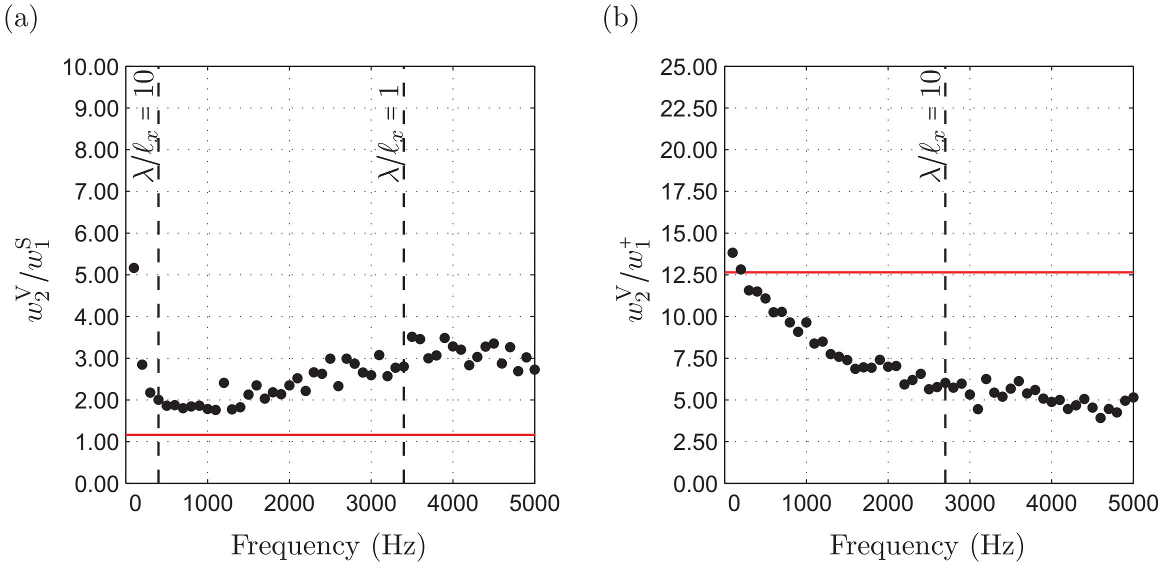

Figure 9.14 - *Vorticity response of the blade row to an entropy or acoustic perturbation at the inlet (case S-1 and A-1). (a) Entropy; (b) Acoustic. Model (—), simulation (•).*

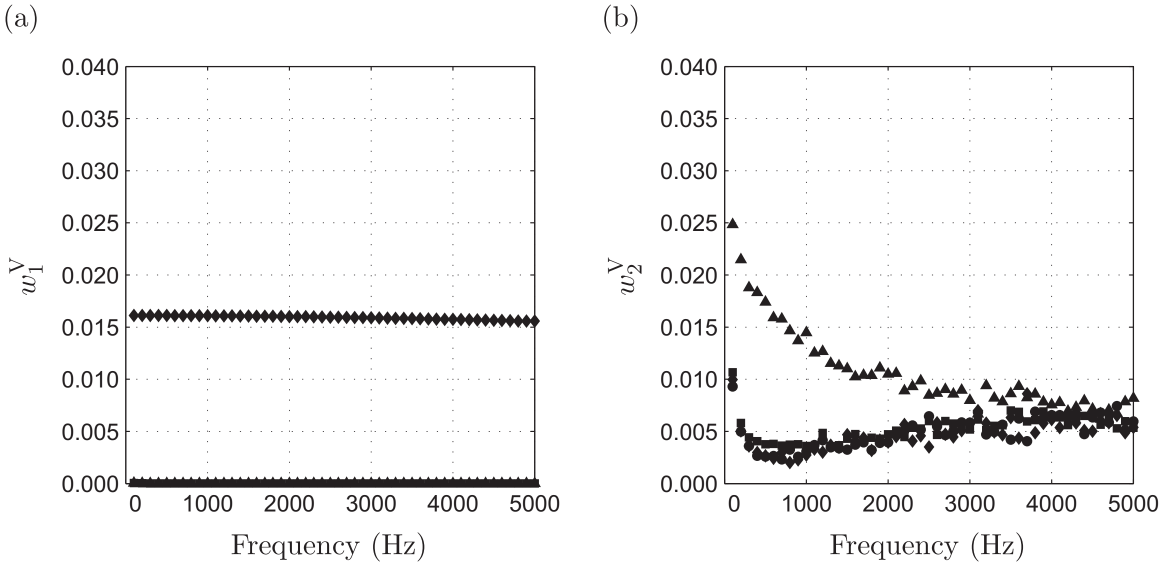

Figure 9.15 - *Vorticity at the inlet (a) and outlet (b) for the four different simulations. Simulation N-0 (•), S-1 (▪), V-1 (◆) and A-1 (▲).*

by the model in the investigated frequency range (100-5000 Hz). The acoustic waves generated by entropy disturbances impinging on the blade row is also well predicted at low-frequencies (100-500 Hz or for $\lambda/\ell_x > 10$), but the theoretical results rapidly depart from the numerical ones for higher frequencies. Moreover, a proper post-processing of the steady flow has shown that the initially planar entropy waves are also strongly distorted by the inter-blade non-uniform steady flow at high-frequencies. This last point can lead to additional disagreement when considering coupling between blade rows. However, entropy perturbations within an aeronautical combustion chamber are expected to be in the low-frequency range. Therefore the so-called transfer functions should be considered taking into account more realistic inputs. The calculation of the errors made on the noise prediction at the outlet of the blade handled in this Chapter shows that an error of 0.6 dB is done on the direct noise, and 2.0 dB on the entropy one (see App. C), when using the model with disturbances spectra from an actual combustor LES (see Sec. 12.2). The entropy fluctuations obtained in Sec. 12.2 are in the low-frequency range, therefore the overall indirect noises calculated analytically and numerically are in the same range of magnitude. The results provided by this first-order approach are globally quite good and make it suitable as part of the core-noise evaluation tool.

Part III

Application of AVBP and CHORUS to an aero-engine combustion chamber

Table of Contents

Chapter 10

Numerical set-up of the SNECMA combustion chamber

This part gathers all the methods investigated in the first sections of the thesis (extraction of waves and transmission models) in a tool called CHORUS. Chapters 10 to 12 describes the computation of the noise at the outlet of the turbine nozzle of an actual combustor (SNECMA). LES (described in part I) is used to calculated the flow within a single burner and then to extract the outgoing waves using CHORUS. The model of Cumpsty and Marble (described in part II) is used to evaluate the noise at the outlet of the turbo-machinery. In this chapter, the description of the geometry is first provided (Sec. 10.1) and then the related numerical set-up (Sec. 10.2). Almost no experimental data was available for this chamber and the objective was not to validate LES but to demonstrate how LES and CHORUS can be coupled. Appendix B presents a comparison of the LES and experimental results for the only available measurements: microphone probes but this was done in addition to the main task of the thesis which was the construction of CHORUS.

10.1 Geometry, boundary conditions and mesh

The combustor of the engine demonstrator DEM21 is investigated here. The engine has been used in 2004 at SNECMA to assess numerous technological improvements. This test engine is made only of the high-pressure core (high-pressure compressor, combustor and high-pressure turbine - see Fig. 1.4), and thus it is fed with pressurized and preheated air to replace the low-pressure compressor. The domain chosen for the combustion chamber simulation is located between the planes 300 and 410 (see Fig. 10.1): all elements of the combustor are taken into account, including the diffuser, the swirler, the outer and inner annulus, as well as the High-Pressure Turbine Nozzle (HPTN). The different cavities surrounding the flame tube are also included in the computational domain, because of their large volumes that can act on the acoustics of the combustor. Only one of the 18 burners is studied here, and the associated

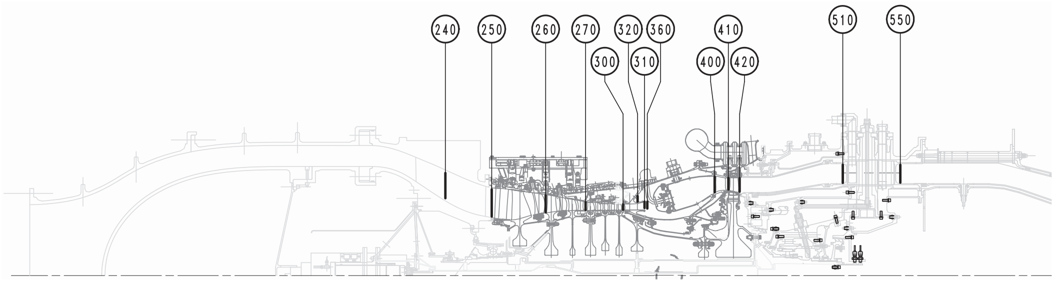

Figure 10.1 - *Sketch of the experimental set-up of the High-Pressure Core.*

computational domain is depicted in Fig. 10.2. The main air inlet is placed at the diffuser entrance, but additional air is injected to model cooling films which represent about 5% of the overall air. The burned gases are outgoing by the HPTN, but 20% of the fresh air is derivated through the outer and inner annulus (main part of this air is used for the cooling of the turbine blades on the real engine). The outer-inner casing, the diffuser and the swirler solid boundaries are represented by no-slip adiabatic walls, and the HPTN is modelled with a slip adiabatic wall. The flame tube and surrounding annuli are separated by multi-perforated plates (solid walls with milli-metric holes) that improve the cooling in the actual combustor. These boundaries are taken into account here using a model proposed by Mendez *et al.* [72] that is available in AVBP. The outer side sucks up fresh air (suction side), whereas the inner side blows the same mass-flow rate of air within the flame tube (blowing side). The mass-flow rates passing through these multi-perforated walls (as well as the cooling films) are here imposed in a hard way according to data provide by SNECMA. Such walls can have an influence on the acoustics (see [117] for example), but this phenomenon is not taken into account here.

The actual burners are fueled with liquid kerosene, but a purely gaseous computation is performed here. Therefore some simplifications have been done concerning the injection of fuel. Indeed, as illustrated in Fig. 10.3, the spray generated from the bottom of the swirler is expected to impact on the Venturi that separates the outer and inner vane air. As a consequence, a film of liquid kerosene is expected to be formed at the end of the venturi. The two co-rotating inner and outer air from the guide vanes induce a strong shear of the flow (different vane orientation) at the liquid film position. The liquid breakup is expected to take place between the inner and outer air. For these reasons, the gaseous fuel is injected along the venturi in the simulation. Figure 10.3 describes the impact region where pure fuel ($Y_F = 1$) is injected from the wall. It is important to keep in mind that assuming a purely gaseous flow for the computation involves many uncertainties about the combustion process, because of fluid-mechanics (gaseous fuel distribution) and thermodynamics (evaporation and heat transfer) issues. However, it reduces the complexity of the numerical configuration, which is already very important.

The mesh used for the simulation contains 5.9 million of tetrahedrons (Fig. 10.4). Refinement can be observed close to the swirler, the primary and dilution air holes. The smallest grid element is located at the trailing edge of the HPTN. The grid resolution can appear to be insufficient for

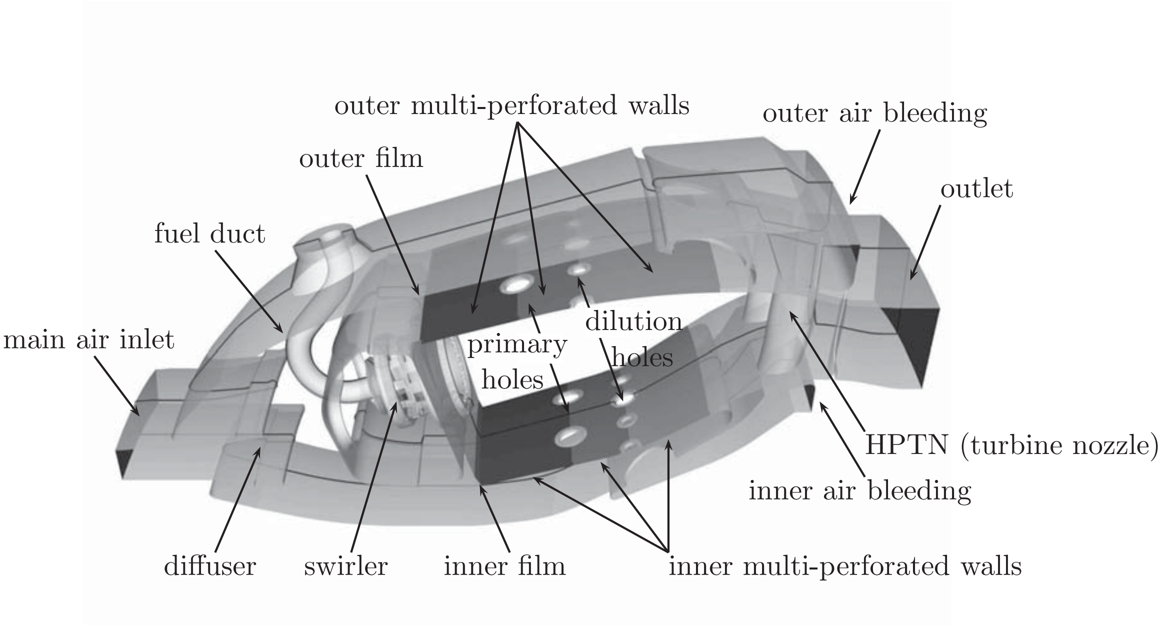

Figure 10.2 - *Description of the different elements composing the combustor (one sector).*

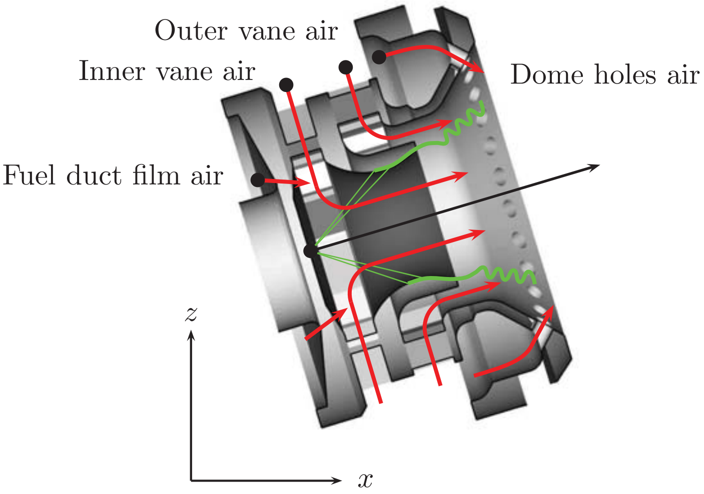

Figure 10.3 - *Description of the swirler. Part of the spray (in green) impacts on the Venturi walls, and it is expected to generate a liquid film which atomises and vaporises at the lips of the injector.*

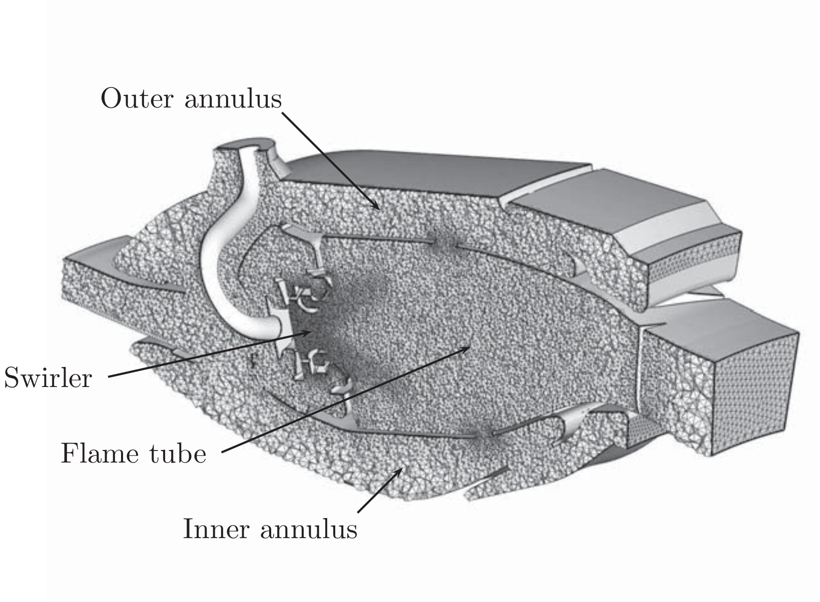

Figure 10.4 - *Cutaway of the mesh used for the simulation.*

an aeroacoustic computation in comparison with what is done for jet noise where shear layers must be resolved (see [12] for example). In the combustor, noise is mainly produced by the unsteady reaction zones in which the resolution constraints are weaker.

10.2 Operating conditions and numerical parameters

The investigated operating conditions correspond to a fully-loaded engine (take-off) since the relative importance of the combustion noise has been identified to be the most for this regime (see Fig. 1.3). The total temperature of the fresh air coming from the compressor $T_{t,300}$ is 795 K and it is imposed at the main inlet of the computational domain with the mass-flow rate (about 2 kg/s for one burner) using relaxation on both (see Chap. 5). Table 10.1 summarizes the boundary conditions used for the LES. The flow within the HPTN is choked on the real engine for these conditions. Therefore, the pressure at the outlet of the HPTN p_{410} is imposed in the LES as 50% (to be sure that the HTPN is choked) of the sonic static pressure related to $p_{t,300}$:

$$p_{410}^{\mathrm{LES}} = 0.5 \times p_{t,300} \left(\frac{\gamma + 1}{2} \right)^{-\frac{\gamma}{\gamma - 1}}, \tag{10.1}$$

where $p_{t,300}$ is the total pressure within the actual combustor, and it equals 2.2 MPa. However, the overall pressure in the combustion chamber depends directly on the imposed mass-flow rate, and on the total temperature at the outlet of the flame tube that is simulated ($p_{t,300} \equiv \dot{m}\sqrt{T_{t,300}}$ since the HPTN is choked). As a consequence, this pressure is not exactly equal to the reference one (1.9 MPa in the simulation), since the air re-injected in the HTPN for cooling (milimetric

BC	Type	$\dot{m}$ (kg.s^{-1})	T (K)	p (kPa)	$\kappa_{\rho u}$ (s^{-1})	κ_T (s^{-1})	κ_p (s^{-1})	$\mathscr{P}$ (-)
Main air inlet	`INLET_RELAX_RHOUN_T_Y`	1.9079	795	-	2000	100	-	-
Film air up	`INLET_FILM`	0.0603	795	-	-	-	-	-
Film air down	`INLET_FILM`	0.0476	795	-	-	-	-	-
Fuel duct film air	`INLET_FILM`	0.0209	795	-	-	-	-	-
Blowing side inner MPW 1	`WALL_LAW_MULTIPERF_QDM`	0.0444	795	-	-	-	-	0.0308
Blowing side inner MPW 2	`WALL_LAW_MULTIPERF_QDM`	0.0277	795	-	-	-	-	0.0280
Blowing side inner MPW 3	`WALL_LAW_MULTIPERF_QDM`	0.0831	795	-	-	-	-	0.0343
Blowing side outer MPW 1	`WALL_LAW_MULTIPERF_QDM`	0.0513	795	-	-	-	-	0.0360
Blowing side outer MPW 2	`WALL_LAW_MULTIPERF_QDM`	0.0316	795	-	-	-	-	0.0327
Blowing side outer MPW 3	`WALL_LAW_MULTIPERF_QDM`	0.1042	795	-	-	-	-	0.0343
Suction side inner MPW 1	`WALL_LAW_MULTIPERF_S`	-0.0444	-	-	-	-	-	0.0308
Suction side inner MPW 2	`WALL_LAW_MULTIPERF_S`	-0.0277	-	-	-	-	-	0.0280
Suction side inner MPW 3	`WALL_LAW_MULTIPERF_S`	-0.0831	-	-	-	-	-	0.0343
Suction side outer MPW 1	`WALL_LAW_MULTIPERF_S`	-0.0513	-	-	-	-	-	0.0360
Suction side outer MPW 2	`WALL_LAW_MULTIPERF_S`	-0.0316	-	-	-	-	-	0.0327
Suction side outer MPW 3	`WALL_LAW_MULTIPERF_S`	-0.1042	-	-	-	-	-	0.0343
Fuel inlet	`INLET_FILM`	0.0422	795	-	-	-	-	-
Main outlet	`OUTLET_RELAX_P_3D`	-	-	610	-	-	1000	-
Outer air bleeding	`WALL_LAW_MULTIPERF_S`	-0.1856	-	-	-	-	-	1.0000
Inner air bleeding	`WALL_LAW_MULTIPERF_S`	-0.2767	-	-	-	-	-	1.0000

Table 10.1 - *Boundary conditions used for the DEM21 LES. Refers to Fig. 10.2 and 10.3 for BC location. κ is the relaxation coefficient and $\mathscr{P}$ is the Multi-Perforate Wall (MPW) porosity.*

holes that create a film of fresh air on the blades) is not taken into account here. Moreover, the sonic surface within the HPTN flow is probably smaller than on the real configuration because of the slip-walls used for these element, and thus it also influences the pressure inside the combustor. A strong relaxation coefficient κ_p (see Sec. 5.2.2) is required on the outlet pressure p_{410} to keep the HPTN choked (the flow after the HPTN is globally supersonic, but axially subsonic: acoustic waves can go up the flow). Therefore, direct acoustic analysis downstream from the HPTN is not possible. The acoustic waves propagating between the HPTN trailing-edge and the outlet are perturbed because of the important reflections generated by this boundary condition. The estimation of the noise caused by the combustor at this position would thus be erroneous. To use the model of Cumpsty and Marble, the waves amplitudes are evaluated upstream of the HTPN choked section where the signals are isolated from the effects of the outlet condition by the sonic flow.

The simulation is done using the Lax-Wendroff numerical scheme with a CFL number of 0.7. Artificial viscosity is used to handle the strong velocity gradient in the swirler and in the HPTN region. The classical model of Smagorinsky is used to deal with sub-grid scale effects, and the

TFLES combustion model is applied to the reaction rates. The chemistry associated to the combustion of the kerosene in the framework of the TFLES combustion model is presented in the next section.

Chapter 11

Kerosene-type fuel chemistry

The combustor used for the LES of this PhD is operated at high pressure (2.2 MPa) and high inlet temperature (795 K). AVBP contains a standard scheme for kerosene/air flames called 2S-KERO-BFER [48] which has been validated extensively and coupled to the TFLES model but only from 0.1 up to 1.2 MPa and fresh gas temperature up to 700 K. Therefore, a verification of this standard kerosene/air scheme is required (Sec. 11.1 and 11.2) and of the TFLES model (Sec. 11.3) in there conditions.

11.1 Two-step chemistry for kerosene

The aeronautical burner studied here is fueled with liquid kerosene. The combustion process takes place in the gaseous phase (even with a liquid fuel, but extra burning regimes can be defined in this case [95]), so that the properties of the chemistry of the gaseous kerosene need to be established for elementary flames required by the TF-LES model. Kerosene is a mixture of hydrocarbons with a high specific energy and specific properties according to aviation and security requirements (low freezing point, high flash point, etc.) whose composition may vary depending on the application. It is mainly made of alkanes ranging from $C_{10}H_{22}$ up to $C_{14}H_{30}$, but can contain additives (antistatic agents, etc.). It also contains aromatic and naphthenic compounds, that will finally lead to a rather complex chemical scheme of reactions.

Therefore the composition, as well as the chemistry, needs to be modelled to deal with the combustion of kerosene. The chosen surrogate kerosene is based on the work of Franzelli *et al.* [48] who have developed a model working for a large range of pressures, temperatures and equivalence ratios in the framework of TF-LES combustion model. It is called 2S-KERO-BFER and it is based on the following two-reaction scheme:

$$F + 10O_2 \quad \rightarrow \quad 10CO + 10H_2O \tag{11.1}$$

$$CO + \frac{1}{2}O_2 \quad \leftrightarrow \quad CO_2 \tag{11.2}$$

Reaction i	$\phi_{0,i}$	$\sigma_{0,i}$	B_i	$\phi_{1,i}$	$\sigma_{1,i}$	C_i	$\phi_{2,i}$	$\sigma_{2,i}$	$\phi_{3,i}$	$\sigma_{3,i}$
1	1,173	0,04	0,29	1,200	0,02	7,10	1,800	0,18	-	-
2	1,146	0,045	0,00015	1,200	0,040	0,03500	1,215	0,030	1,320	0,090

Table 11.1 - *Coefficient for the functions f_1 and f_2 for the chemical scheme 2S-KERO-BFER.*

where F is the surrogate fuel and is equivalent to $C_{10}H_{20}$. Reaction (11.1) is irreversible and strongly exothermic, whereas reaction (11.2) is an equilibrium reaction and is needed for getting correct adiabatic temperatures for rich flames. Entropy fluctuations, and therefore indirect noise, are directly related to this temperature. The key point of the 2S-KERO-BFER chemical scheme model is the expression of the two forward reaction rates $k_{f,1}$ and $k_{f,2}$ which are expressed as follows:

$$k_{f,1} = f_1(\phi)A_1 e^{(-E_{a,1}/RT)}[F]^{n_F}[O_2]^{n_{O_2,1}} \tag{11.3}$$

$$k_{f,2} = f_2(\phi)A_2 e^{(-E_{a,2}/RT)}[CO]^{n_{CO}}[O_2]^{n_{O_2,2}} \tag{11.4}$$

Equations (11.3) and (11.4) are classical Arrhenius laws that are corrected with the terms f_1 and f_2 which depend on the local equivalence ratio ϕ. The adjustment of the first pre-exponentional constant A_1 is a usual technique to obtain the correct laminar flame speed for one-step chemistry [60, 45, 16]. It is extended here for two-step chemical schemes to obtain a correct flame structure for rich mixtures. The two correction functions are defined as follows:

$$f_1(\phi) = 2\left[\left\{1 + \tanh\left(-\frac{\phi - \phi_{0,1}}{\sigma_{0,1}}\right)\right\}\ldots\right.$$
$$\left. + B_1\left\{1 + \tanh\left(\frac{\phi - \phi_{1,1}}{\sigma_{1,1}}\right)\right\} + C_1\left\{1 + \tanh\left(\frac{\phi - \phi_{2,1}}{\sigma_{2,1}}\right)\right\}\right]^{-1} \tag{11.5}$$

$$f_2(\phi) = \frac{1}{2}\left\{1 + \tanh\left(-\frac{\phi - \phi_{0,2}}{\sigma_{0,2}}\right)\right\} + \frac{B_2}{2}\left\{1 + \tanh\left(\frac{\phi - \phi_{1,2}}{\sigma_{1,2}}\right)\right\}\ldots$$
$$+ \frac{C_2}{2}\left\{1 + \tanh\left(\frac{\phi - \phi_{2,2}}{\sigma_{2,2}}\right)\right\}\left\{1 + \tanh\left(\frac{\phi - \phi_{3,2}}{\sigma_{3,2}}\right)\right\} \tag{11.6}$$

where the constants ($\phi_{0,1}$, $\sigma_{0,1}$, $\ldots$) are defined in Table 11.1, and the parameters for the Arrhenius law (Activation energy, pre-exponential factor ...) can be found in Table 11.2.

The model developed by Franzelli *et al.* [48] has been validated for pressures ranging from 0.1 up to 1.2 MPa. Therefore, an evaluation of the model is required for the operating pressure of the combustion chamber (take-off conditions at 2.2 MPa). The 2S-KERO-BFER chemical scheme is compared in the next sections with the detailed mechanism developed during the PhD thesis of Luche [65] using the Open Source CANTERA software [1]. Laminar premixed flame speeds are investigated as well as adiabatic flame temperature.

Reaction i	Activation energy $E_{a,i}$ (cal/mol)	Pre-exponential factor A_i (cgs)	Exponents
1	4.15×10^4	8.00×10^{11}	$n_F = 0.55$, $n_{O_2,1} = 0.90$
2	2.00×10^4	4.50×10^{10}	$n_{CO} = 1.00$, $n_{O_2,2} = 0.50$

Table 11.2 - *Arrhenius law parameters for the chemical scheme 2S-KERO-BFER.*

11.2 Laminar flame speed and adiabatic temperature

The TFLES combustion model assumes that the flame is premixed or partially premixed. Therefore, elementary laminar premixed flames are studied to validate the simplified chemical scheme, as well as the adiabatic temperature. The reference case is based on the detailed chemistry of Luche [65], and calculated using CANTERA with detailed thermodynamic and transport properties. The mechanism of Luche involves 91 species and 991 reactions. It has been validated for pressure between 0.1 and 1.0 MPa and initial temperature between 300 and 700 K, but it is extrapolated here to 2.2 MPa and 795 K, since the experimental measurements for these particular thermodynamic conditions are not available because of the obvious difficulties involved by such measurements. [1]

Computations of the two-step chemical scheme 2S-KERO-BFER are also performed with CANTERA but with the transport properties of AVBP (constant and equal Schmidt numbers for all species). Calculations provide the laminar flame speeds that are plotted versus equivalence ratio ϕ in Fig. 11.1 (a), whereas equilibrium calculations yield the adiabatic temperature (b). The results for a chemical scheme involving 5 species (one-step) are also shown, and one can notice the important improvement of the results for the adiabatic temperature because of the addition of the CO species and the corresponding reversible reaction. This one-step chemistry is simply written:

$$F + 15O_2 \rightarrow 10CO_2 + 10H_2O \tag{11.7}$$

Indeed, the dissociation of CO_2 and oxidation of CO due to reaction 11.1 that occurs for rich mixtures, involve important formation enthalpies, and thus influence at first-order the temperature of burned gases. One can also see that even though 2S-KERO-BFER is used here beyond the range where it was constructed, it gives very good results. The laminar flame speed is well-reproduced in Fig. 11.1-a, since the usual errors in the measurements of flame speed are in the order of 5%, and that for kerosene-type fuels at high pressure and temperature, it can rise up to 20%. The important point is simply to avoid very fast flames on the rich side, as is the case for non-corrected one- and two-step chemical schemes. To conclude, the 2S-KERO-BFER scheme was used without modification in this PhD.

---

[1] More generally, even complex chemical schemes such as Luche's scheme and transport models used in CHEMKIN or COSILAB are not validated beyond 1.5 MPa. Verifying the qualities of a scheme at 2.2 MPa is therefore a difficult exercise because the *exact* value of the flame speed are complex to obtain experimentally or numerically. Here, the Luche mechanism is assumed to be valid and could be used as a reference.

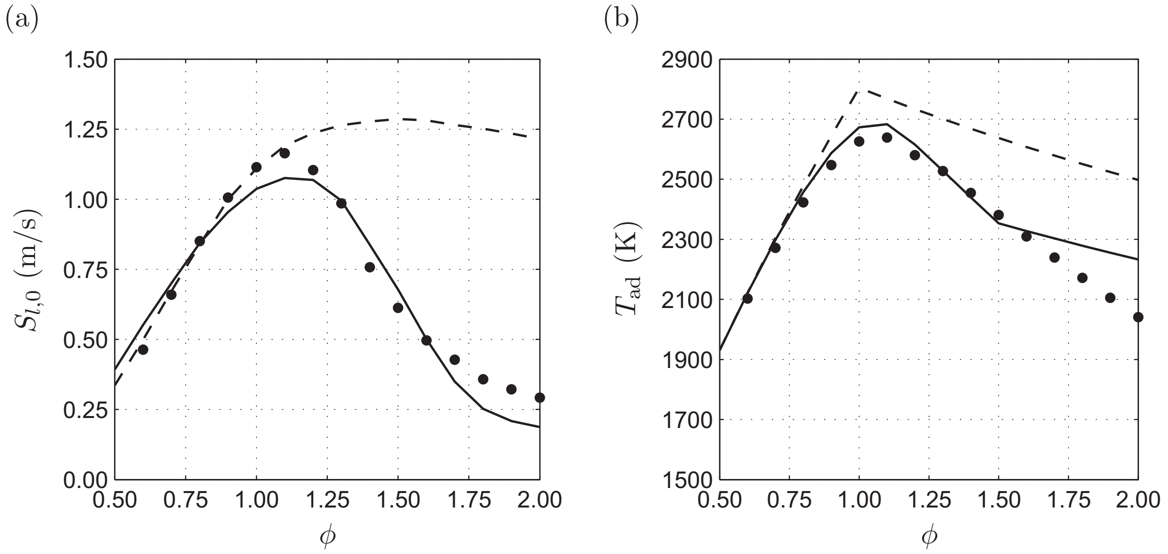

Figure 11.1 - *CANTERA calculations at* 2.2 *MPa and inlet temperature of* 795 *K: Laminar flame speed (a) and adiabatic temperature (b) plotted versus equivalence ratio. Two-steps with 6 species 2S-KERO-BFER chemistry (—); Detailed chemistry of Luche* et al. *(•); One-step with 5 species irreversible chemistry (– – –).*

11.3 Dynamic thickening and chemistry

As mentioned in Sec. 3.4, the flame needs to be thickened dynamically (that is to say locally) in order to avoid modifying mixing in the fresh or burned gases, and thus get the correct entropy waves at the combustor outlet. Thickening is triggered using a flame sensor $\mathcal{S}$ that is written as:

$$\mathcal{S} = \tanh\left(\beta' \frac{\Omega}{\Omega_0}\right) \tag{11.8}$$

where β' is a constant, as well as Ω_0. The pseudo-reaction rate Ω is based on an Arrhenius-type law function:

$$\Omega = Y_F^{n_F} Y_{O_2}^{n_{O_2,1}} \exp\left(-\Gamma \frac{E_{a,1}}{RT}\right) \tag{11.9}$$

The constant Γ in Eq. 11.9 is smaller than one in order to trigger thickening before the actual flame front, and it is usually equal to 0.5. The parameter Ω_0 is the maximum $\Omega_{\max}$ of the function $\Omega(x)$ for the 1-D flame with stoichiometric conditions:

$$\Omega_{\max} = \max\left\{\Omega(x, \phi = 1.0)\right\} \tag{11.10}$$

These constants have to be chosen to get $\mathcal{S} = 0$ outside the flame, and $\mathcal{S} = 1$ within. Figure. 11.2 shows the sensor $\mathcal{S}$ for 1-D flame computations with the usual values of these parameters. It is plotted versus non-dimensionalized coordinate based on the flame thickness δ_L^0, that is defined

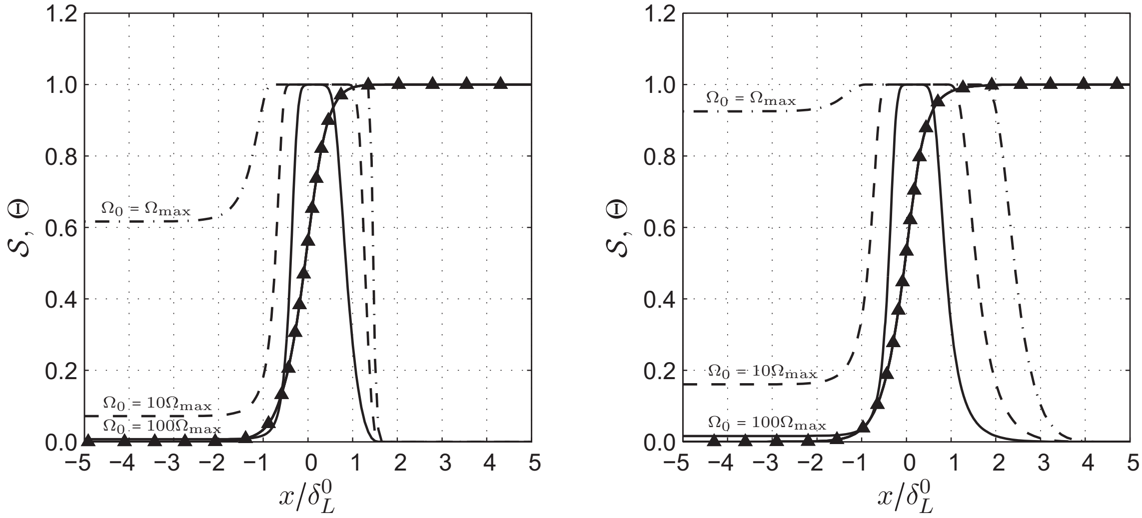
(a) $\phi = 1.0$ (b) $\phi = 1.5$

Figure 11.2 - *CANTERA calculations of 1-D premix flame for equivalence ratio* $\phi = 1.0$ *(a) and* $\phi = 1.5$ *(b). Reduced temperature* Θ *(▲) and post-processed thickening sensor* $\mathcal{S}$ *with* $\Omega = \Omega_{max}$ *(−·−),* $\Omega = 10\Omega_{max}$ *(− − −) and* $\Omega = 100\Omega_{max}$ *(—).*

by Poinsot and Veynante in [87] as:

$$\delta_L^0 = \max\left\{\frac{T_b - T_f}{\left|\frac{dT}{dx}\right|}\right\} \tag{11.11}$$

where T_f and T_b are respectively the temperatures of the fresh and burned gases. The sensor $\mathcal{S}$ clearly fails to frame correctly the flame which is represented here by the reduced temperature $\Theta = (T - T_f)/(T_b - T_f)$: thickening also takes place in the fresh gases, something which must be avoided because it would modify mixing. Even taking greater values of Ω_0 (10 and 100 times $\Omega_{\max}$), does not change the fact that fresh gases are thickened (especially for the rich mixture - in Fig. 11.2 - b).

This abnormal behavior of the flame sensor is due to the high initial temperature of the present computational case (795 K). A simple way to fix this problem is to adjust Γ in Eq.(11.9). Indeed when $\Gamma = 0.5$, this leads here to an equivalent temperature of 1590 K in the fresh gases relatively to the sensor $\mathcal{S}$. This temperature is greater than the autoignition temperature and thus the sensor is triggered before the flame as seen in Fig. 11.2. Figure 11.3 shows post-processed thickening sensor $\mathcal{S}$ with greater values of Γ (0.7 and 0.9) for two different equivalence ratios: (a) $\phi = 1.0$ and (b) $\phi = 1.5$. This time the resulting sensor is correct for $\Gamma = 0.9$ and ensures that $\mathcal{S} = 0$ outside the reacting region. This value of Γ has been selected for the simulations of the combustor. However, the sensor is in this case slightly not enough sensitive for very lean and rich flame as seen in Fig. 11.4. The net reaction rates of the two reactions $\mathcal{Q}_1$ and $\mathcal{Q}_2$ are plotted, as well as the mass-fractions Y_k of the species involved in the reduced scheme. Clearly, the sensor used here is not perfect. However, it provides the best compromise to identify the flame front

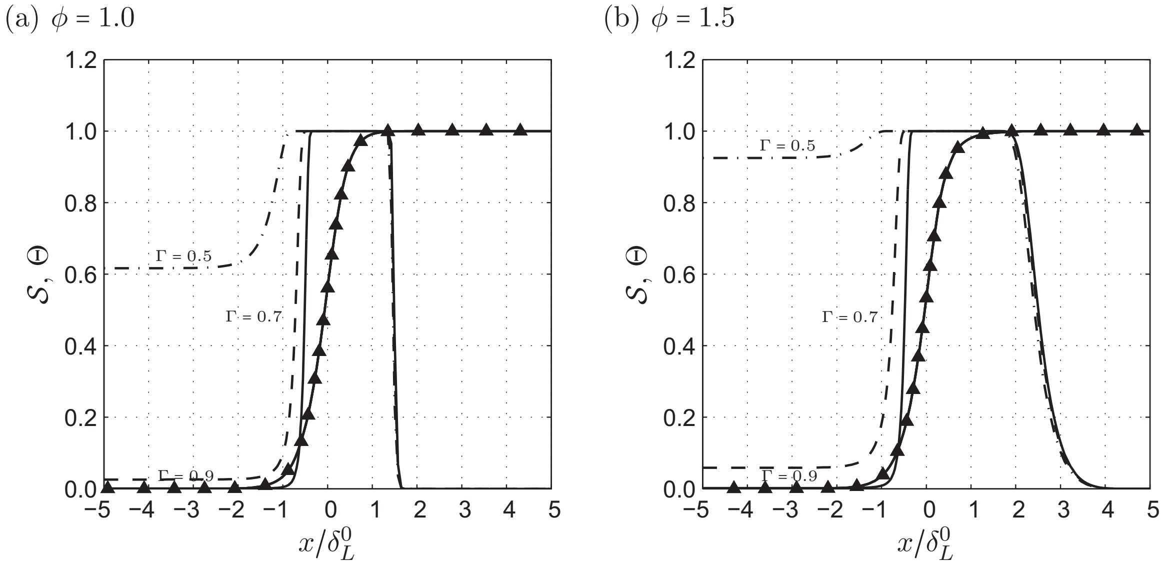

Figure 11.3 - *CANTERA calculations of 1-D premix flame for equivalence ratio* $\phi = 1.0$ *(a) and* $\phi = 1.5$ *(b). Reduced temperature* Θ *(▲) and post-processed thickening sensor* $\mathcal{S}$ *with* $\Gamma = 0.5$ *(−·−),* $\Gamma = 0.7$ *(−−−) and* $\Gamma = 0.9$ *(—).*

in a correct way, and to be set off outside the reacting region. 1-D premixed flames calculated with this sensor in AVBP (on a LES resolution 1-D mesh with thickening) provide quite similar results for laminar flame speeds. Finally, only the usual value of Γ has been modified in the TFLES combustion model ($\Gamma = 0.9$ instead of $\Gamma = 0.5$).

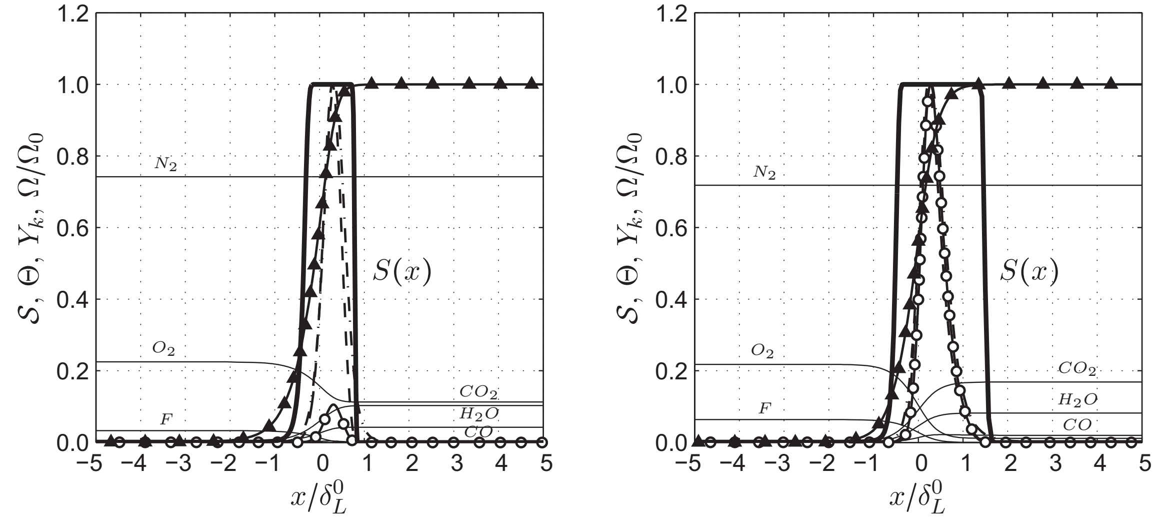

(a) $\phi = 0.5$ (b) $\phi = 1.0$

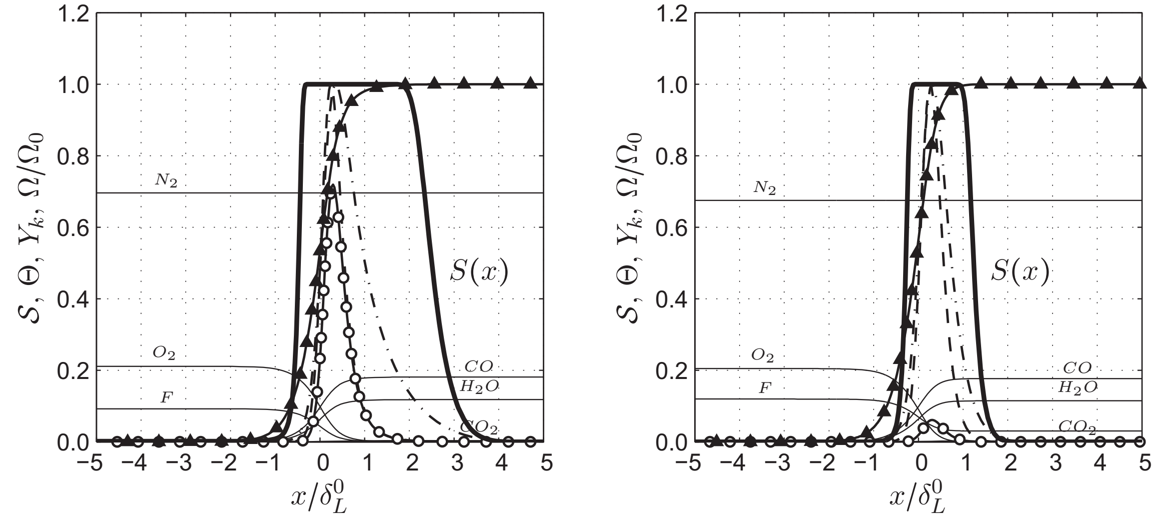

(c) $\phi = 1.5$ (d) $\phi = 2.0$

Figure 11.4 - *CANTERA calculations of 1-D premix flame for equivalence ratio* $\phi = 0.5$ *(a)*, $\phi = 1.0$ *(b)*, $\phi = 1.5$ *(c) and* $\phi = 2.0$ *(d). Reduced temperature* Θ *(*▲*) and post-processed thickening sensor* $\mathcal{S}$ *with* $\Gamma = 0.9$ *and* $\Omega_0 = \Omega_{max}$. Ω/Ω_0 *(*○*), reaction rate* $\mathcal{Q}_1/max(\mathcal{Q}_1)$ *(− − −) and* $\mathcal{Q}_2/max(\mathcal{Q}_2)$ *(− · −).*

Chapter 12

Combustion noise computation

The LES results of the DEM21 combustor are presented in this chapter, as well as the method to extract wave amplitudes and to compute the noise at the turbine outlet. First, a description of the flow within the DEM21 burner is provided in Sec. 12.1. In a second step, the calculation of the waves leaving the combustor is explained in Sec. 12.2. Finally, the model of Cumpsty and Marble [37] is used in Sec. 12.3 to compute the overall noise caused by the combustion and conclusion is provided in Sec. 12.4.

12.1 Description of the flow

The present LES of the DEM21 configuration does not have the objective of being quantitative when compared to the (limited) set of measurements performed on the real engine. In the real engine only a limited set of pressure measurements have been performed and these are much too limited to really validate a LES. Furthermore the LES is performed on a single sector without compressor while the experiment was performed on a full annular chamber feeding a real turbine so that azimuthal modes (due to the full annular geometry) as well as tonal modes of the compressor are expected in the experimental data while they are obviously not present in the LES. A comparison between LES and the available experimental measurements is provided in appendix B, but it is not discussed here since our only objective in this chapter is to show how LES can be coupled with a wave analysis technique to extract the amplitude of acoustic and entropy waves hitting the turbine. These amplitudes will then be post processed using the Marble and Cumpsty [37] model to predict their transmission through the turbine. No comparison with experimental data noise outside the engine will be performed, and we are only looking for a proof of concept.

A description of the flow is presented here providing an order of magnitude of the pressure and temperature fluctuations within the combustor. The associated topology is also given. The burner investigated here generates a Central Recirculating Zone (CRZ) because of the strongly

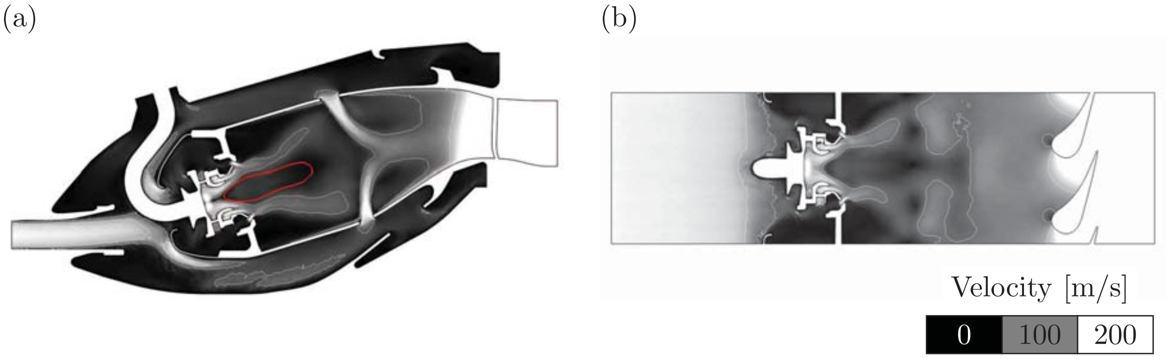

Figure 12.1 - *Mean fields of the velocity magnitude. Cutaway in* $y = 0$ *(a), and in the developed surfaces defined by the mean radius* $R(x)$ *(b). In (a) the contour in red shows the recirculation region defined by a null axial velocity with regards to the swirler axis*

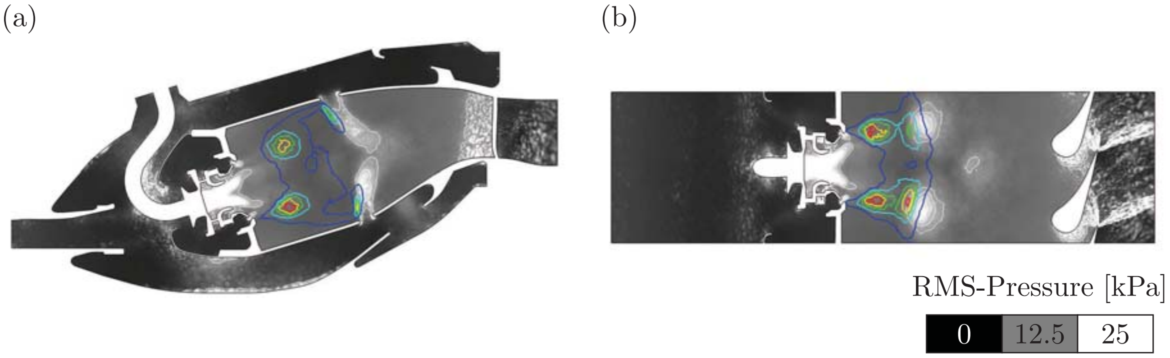

Figure 12.2 - *Fields of RMS of the pressure fluctuations. Cutaway in* $y = 0$ *(a), and in the developed surfaces defined by the mean radius* $R(x)$ *(b). The colored isolines are related to the mean heat release.*

swirled flow. This region can be seen in Fig. 12.1 where contour in red stands for a zero axial velocity component related to the swirler axis. The flow inside this region contains recirculating burned gases. Therefore, the CRZ participates in pre-heating the fresh mixture, and thus improves the stabilisation of the flame. The strongly swirled flow leads in the present burner to the formation of a hydrodynamic instability called Precessing Vortex Core (PVC) [114], which generates large pressure fluctuations (over 25 kPa) as observed in Fig. 12.2 showing the related Root Mean Square (RMS) fields. The center of the low pressure core generated by the vortex is rotating over the swirler axis (precession) and produces high RMS pressure levels. It should be noticed that, although these pressure fluctuations are purely hydrodynamic, and do not propagate at the speed of sound, the PVC may excite the flame, and then generate acoustics. The jets feeding the flame tube also produce strong hydrodynamic pressure fluctuations (about 20 kPa according to Fig. 12.2). It is clear from these fields that the evaluation of the direct combustion noise must be performed very close to HPTN to avoid erroneous estimation of the acoustic waves. The same conclusion can be obtained about temperature fluctuations: the secondary air (dilution jets) leads to intense mixing close the to HPTN inlet. The resulting mean temperature (Fig. 12.3) field is quite uniform (as required to improve turbines lifetimes), but entropy fluctuations also need to be measured at the very end of the burner. The RMS

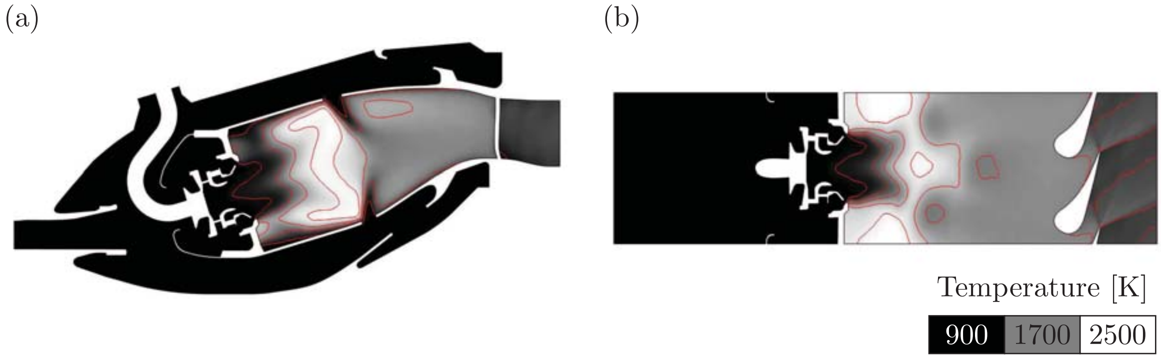

Figure 12.3 - *Mean fields of the temperature. Cutaway in $y = 0$ (a), and in the developed surfaces defined by the mean radius $R(x)$ (b).*

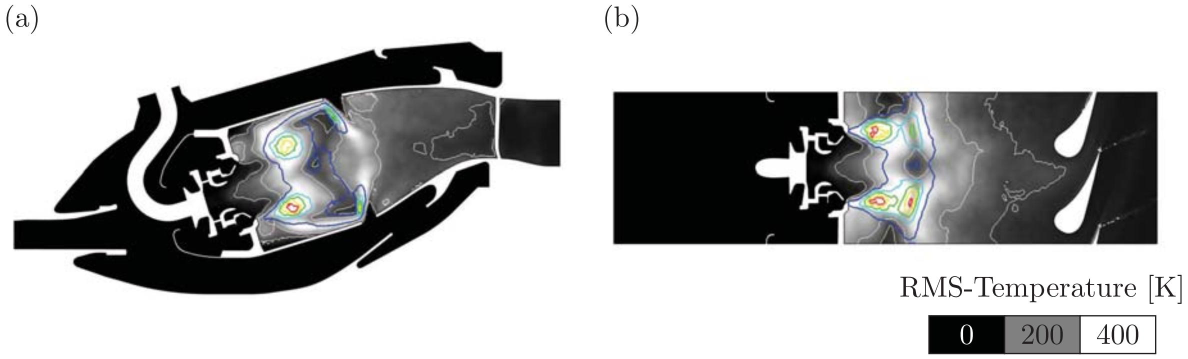

Figure 12.4 - *Fields of RMS of the temperature fluctuations. Cutaway in $y = 0$ (a), and in the developed surfaces defined by the mean radius $R(x)$ (b). The colored isolines are related to the mean heat release.*

fields of temperature are depicted in Figure. 12.4-b: although the largest values are obviously found close to the flame region, the HPTN inlet section exhibits important variations of about 100 K. However, it must be noticed that these values are related to the temporal fluctuations only, without information on the spatial coherence of the hot spots. Therefore, these values cannot be used as they are in order to extrapolate the indirect noise at the HPTN outlet. This point is addressed in the next section.

12.2 Calculation of waves

The calculation of the entire engine noise created by combustion requires the calculation of the transmission and the generation of acoustic waves through the static and rotating blade rows of the turbine. In Chap. 9 it has been shown that the model of Cumpsty and Marble [37] can provide a good first-order estimation of this noise in the limit of low frequency waves. Therefore, the LES results of the combustor are used in this section to calculate the *waves* at the inlet of the turbine, which will be used as inputs of the Cumpsty and Marble model in Sec. 12.3.

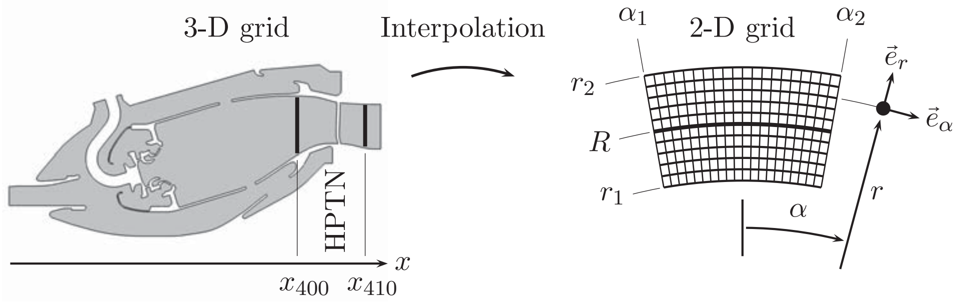

Figure 12.5 - *Positions x_{400} and x_{410} of the planes used for the calculation of waves. The fields interpolated on a 2-D structured grid are projected on the basis ($\vec{e}_x$,$\vec{e}_r$,$\vec{e}_\alpha$).*

Cumpsty and Marble in [37] assume that the flow is inviscid, 2-D, cylindrical and uniform, in order to obtain a well-defined set of waves. Two acoustic waves appear from the decomposition, as well as one entropy wave and one vorticity wave. By definition, the acoustic waves are related to perturbations of velocity, mass-density and pressure which are isentropic. Conversely, the entropy wave is related to a perturbation of pure entropy, that is to say without pressure or velocity fluctuations. The vorticity wave is related to velocity fluctuations only, without fluctuation of entropy, mass-density or pressure. Indeed, these waves are derived from linearized Euler equations where only the first order terms are kept. As shown by Kovasznay [57], the pressure generated by vorticity is a second-order term and the former vanishes in this first-order linearized form. These pressure fluctuations are not taken into account here, that is to say that no special operation has been performed to separate acoustic and hydrodynamic pressure contribution. However, this term may be very large, and an important error may be done for a 3-D flow. Nevertheless, the fluctuations are here radially averaged, which reduces the effect of turbulence on the pressure field.

The waves are calculated inverting the relations (9.40) on the radially averaged fluctuations of the LES. Averaging is performed in the plane $x = x_{400}$ at the inlet of the HPTN as defined in Fig. 12.5. The global procedure performing these operations is called CHORUS and is coded in MATLAB as a post-processing tool of AVBP snapshots. The different steps for the calculation of these waves are the following:

- Interpolation of the 3-D instantaneous fields of the LES on a 2-D structured grid. The plane x_{400} defining the interpolation grid is located about one blade chord before the inlet of the high-pressure turbine stator (Fig. 12.5). A structured grid is used to perform easier spatial integrals.
- Projection of the primitive variables $\mathrm{P} = \{p, \rho, u_x, u_y, u_z\}$ into the polar coordinates system based on the motor axis, where it reads $\mathrm{P} = \{p, \rho, u_x, u_\alpha, u_r\}$. It is equivalent to unroll the annulus sector defined by the 2-D structured grid.
- The primitive variables $\mathrm{P}(x, \alpha, r, t)$ are averaged along the radial coordinate r, to comply with the 2-D model of Cumpsty and Marble. The averaged fluctuations $\mathrm{P} = \{p'/\gamma\bar{p}, \rho'/\bar{\rho}, w'/\bar{c}, \theta'\}$ depend only on angle α and time t.

Total samples	Total time	Samples in a portion	Portion duration	Samples portion shift	Number of portions (N_p)	Sampling frequency
8192	164 ms	1024	20.5 ms	4	1793	50 kHz

Table 12.1 - *Parameters used in CHORUS.*

- Double Fourier-transform in space, along the angular coordinate α, and time t, to agree with the temporal and circumferential harmonic perturbations assumption.
- Calculation of the waves $\mathrm{W} = \left\{w^{\mathrm{S}}, w^{\mathrm{V}}, w^{+}, w^{-}\right\}$ using the transformation matrices given by the Cumpsty and Marble model and defined in Eq. (9.40). These matrices depend on the frequency and the circumferential wavelength, so that this operation has to be performed after the Fourier-transforms.

The following text describes these operations more in details. The primitive variables in the polar basis are defined as:

$$\left\{\langle \mathrm{P}_{400}\rangle_r(\alpha,t)\right\} = \frac{2}{r_2^2 - r_1^2}\int_{r_1}^{r_2}\left\{\mathrm{P}_{400}(r,\alpha,t)\right\} r dr \tag{12.1}$$

where $\langle\cdot\rangle_r$ stands for radial average. The calculation of the Fourier-transforms is performed in three steps: (a) a first Fourier-transform over the angular coordinate α is performed, where the index defining the circumferential component of the wave vector is m. This integration is written:

$$\left\{\langle \hat{\mathrm{P}}_{400}\rangle_r(m,t)\right\} = \frac{1}{\alpha_2 - \alpha_1}\int_{\alpha_1}^{\alpha_2}\left\{\langle \mathrm{P}_{400}\rangle_r(\alpha,t)\right\} e^{im\alpha} d\alpha \tag{12.2}$$

The result still depends on time t and (b) it is split into N_P overlapping temporal portions (superscripted by j). The splitting operation is performed in order to smooth the spectral density in the last step, as done in the Welch's method for example. Afterwards, (c) Fourier-transform over time t is performed for each temporal portion j. This temporal integration is defined as:

$$\left\{\langle \hat{\hat{\mathrm{P}}}_{400}\rangle_r^j(m,\omega)\right\} = \frac{1}{t_2^j - t_1^j}\int_{t_1^j}^{t_2^j}\left\{\langle \hat{\mathrm{P}}_{400}\rangle_r^j(m,t)\right\} e^{-i\omega t} dt \tag{12.3}$$

The waves are calculated for each portion j using the transformation matrix $[\mathbf{M}_w^p]$, defined in Eq (9.41) and that depends on m and ω:

$$\left\{\mathrm{W}_{400}^j(m,\omega)\right\} = [\mathbf{M}_w^p]^{-1}\left\{\langle \hat{\hat{\mathrm{P}}}_{400}\rangle_r^j(m,\omega)\right\} \tag{12.4}$$

Finally, the wave moduli related to portions j are averaged in a mean-square sense (summation over j) to smooth the spectra. The phasing between the primitive variable is involved in the definition of the waves, therefore this operation can be done only after applying the transformation matrix. The phase information is lost on the resulting waves. The smoothing operation writes:

$$\left|\left\{\mathrm{W}_{400}(m,\omega)\right\}\right| = \sqrt{\sum_{j=1}^{N_P}\left|\left\{\mathrm{W}_{400}^j(m,\omega)\right\}\right|^2} \tag{12.5}$$

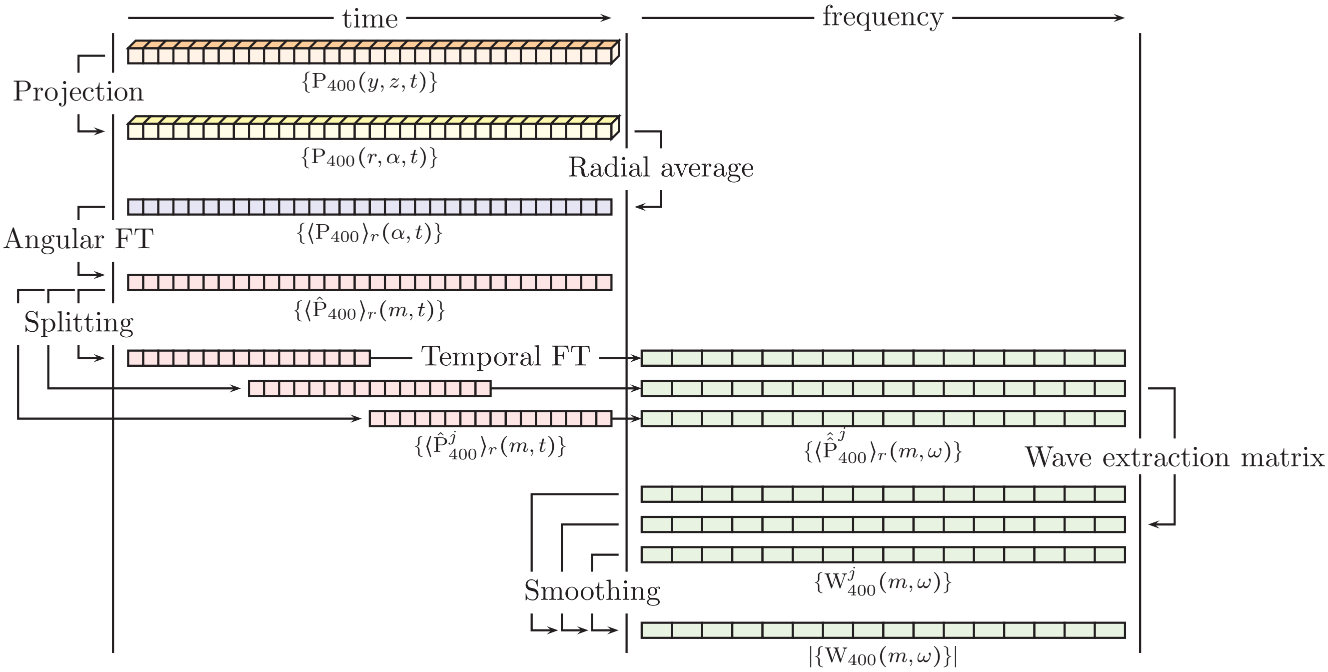

Figure 12.6 - *CHORUS procedure for the extraction of waves at the combustor outlet (x_{400}).*

The parameter m is related to the circumferential component of the wave vector of the complete annular combustor. Since the investigated case is made of only one burner, m is a multiple of the number of burners ($N_B = 18$). Therefore, the number $n = m/N_B$ is introduced. Results are depicted in Fig. 12.7 where the spectra of the waves for different circumferential wave numbers index n ranging from 0 up to 5 can be seen. The circumferential deviation of the steady flow within the combustion chamber is small (the angle θ_{400} between the steady flow and the chamber axis is close to $10°$), so that spectra are rather symmetric with regards to $n = 0$ (positive and negative values of n are plotted but the same symbol is used for both). It can be seen that the acoustic waves (Fig. 12.7-a,b) are mainly longitudinal ones ($n = 0$). The difference between the spiralling waves ($n \neq 0$) and the longitudinal ones is important here because only one burner is computed in the LES. The first circumferential wave in the simulation $n = 1$ is equivalent to $m = 18$ on the actual combustor. The cutoff frequency for this wave is close to 8 kHz ($\Im\{k_{x,\pm}\} \neq 0$ in Eq. (9.37)), so that, according to the investigated frequency range, the acoustic waves propagating without attenuation within the combustion chamber are only the longitudinal ones. Figure 12.7-c shows that the entropy waves spectrum is broadband, with a linear slope for high-frequencies. The two first circumferential waves contain most of the energy, and the magnitudes of the fluctuations decrease for higher n in the low-frequency range. Finally, the vorticity waves spectra can be seen in Figure 12.7-d. Parameters used for the calculations of these waves can be found in Table 12.1. The non-dimensionalized pressure fluctuation related

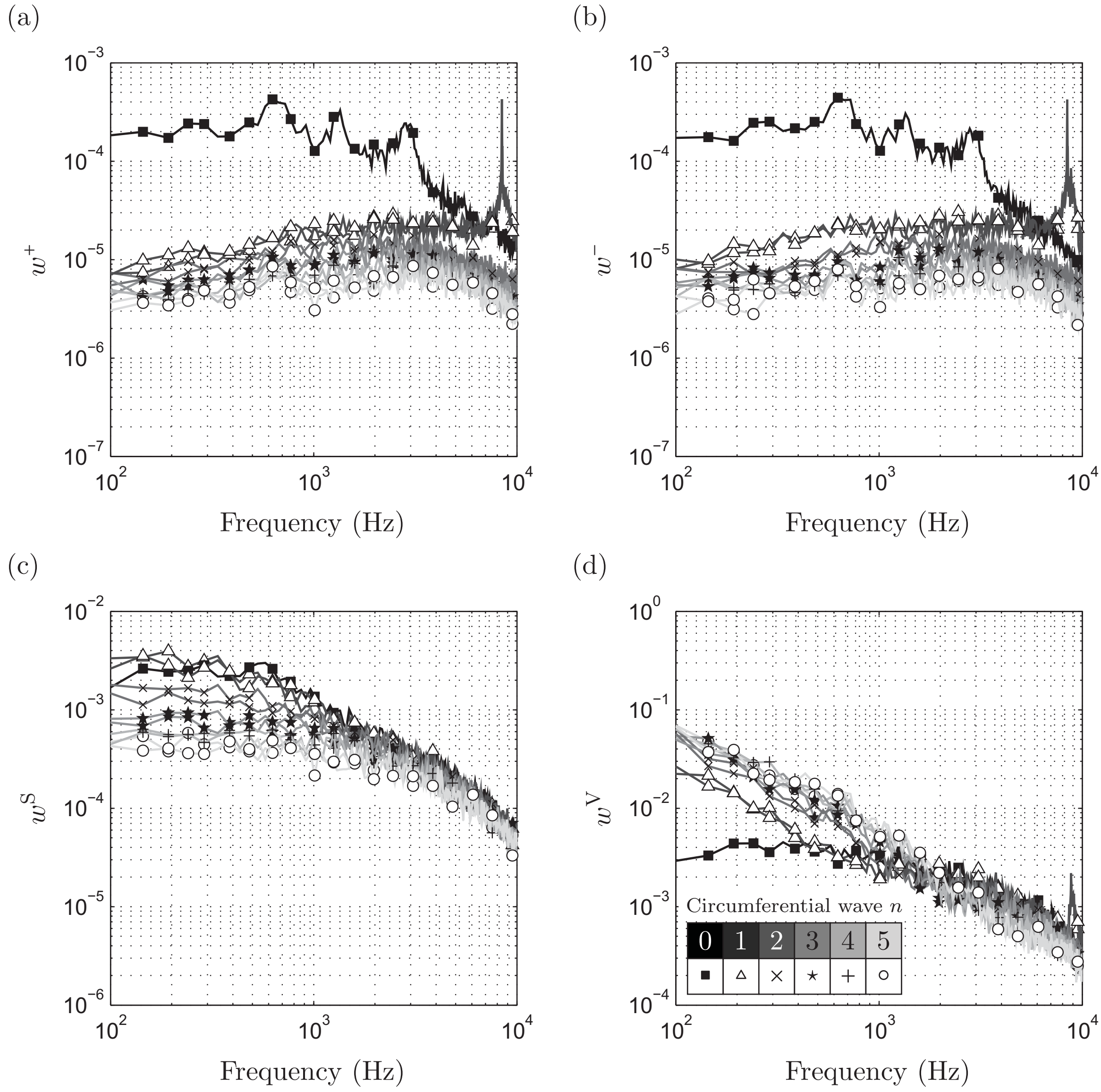

Figure 12.7 - *Spectra of the waves calculated at the outlet of the combustor* $x = x_{400}$ *for different circumferential waves* n*. (a) Downstream propagating acoustic wave* w^+*; (b) upstream propagating acoustic wave* w^-*; (c) entropy wave* w^S*, (d) vorticity wave* w^V*.*

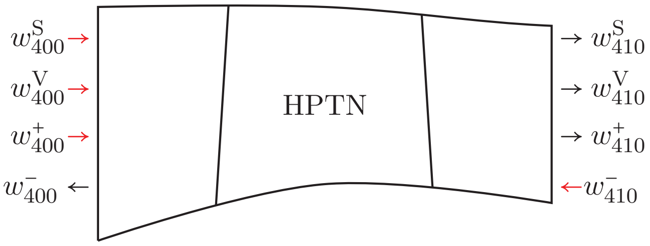

Figure 12.8 - *Waves ingoing and outgoing the HPTN.*

to all the calculated waves is in the order of 0.3% whereas it is about 3% for the entropy.

It confirms the fact that entropy noise can be important since the conversion coefficient from entropy to acoustics is about 10%, and in the order of 50% for acoustic transmission when one considers one stator only (see Sec. 9.4). However, one should keep in mind that the sound within the combustion chamber is not only direct noise. Anyway, this entropy-induced noise inside the combustion chamber is directly computed in the LES and simply appears as acoustics at the inlet of the turbine. This noise is associated with the direct one thereafter, that is to say that one calls direct noise all acoustic waves entering the turbine, whatever the sources are. The acoustic, vorticity and entropy waves calculated here are used to evaluate the global noise in the next section.

12.3 Core-noise evaluation

A method to evaluate the waves (acoustic, entropy and vorticity) leaving the combustor at x_{400} (see Fig. 12.5) has been provided in Sec. 12.2. The present section shows how these waves are transmitted through the turbine to evaluate noise at the outlet of the HPTN [1].

The waves ingoing the HPTN obtained from the LES are used to compute the outgoing waves (see Fig. 12.8) using the model of Cumpsty and Marble [37] . The waves used here are related to the temporal portions j (already presented in Sec. 12.2) and the outgoing ones are calculated as follows:

$$\left\{\mathrm{W}^{j}_{\mathrm{out}}(m,\omega)\right\} = [\mathbf{M}^{\mathrm{out}}_{\mathrm{in}}]\left\{\mathrm{W}^{j}_{\mathrm{in}}(m,\omega)\right\} \tag{12.6}$$

where $[\mathbf{M}^{\mathrm{out}}_{\mathrm{in}}]$ is the transfer matrix defined in Eq. (9.43). The effect of the mean flow variations is taken into account through this matrix. The four different sets of ingoing waves considered in

---

[1] The comparison between the measured pressure fluctuations within the flame tube, and the simulated ones (see App. B), show that although the spectra do not agree because of the azimuthal acoustic eigenmodes, the magnitude of the fluctuations is predicted correctly by the 3-D LES. Therefore, one assumes that the waves extracted from the LES provide the correct magnitude of the fluctuations, and thus can be used as inputs for the model of Cumpsty and Marble [37].

	Considered ingoing waves $\mathrm{W}_{\mathrm{in}}^{j}$			
Case	$w_{j,400}^{\mathrm{S}}$ (entropy)	$w_{j,400}^{\mathrm{V}}$ (vorticity)	$w_{j,400}^{+}$ (down. ac.)	$w_{j,410}^{-}$ (up. ac.)
Total	●	●	●	○
Entropy	●	○	○	○
Vorticity	○	●	○	○
Acoustic	○	○	●	○

Table 12.2 - *Description of the different cases for the calculation of the noise at the HPTN outlet. Ingoing wave amplitude forced to zero (○), ingoing wave from LES (●).*

this study are described in Table 12.2. The first case is representative of the total noise at the HPTN outlet that is caused by combustion, whereas the other cases are presented to show the contribution of each type of downstream propagating wave (entropy, vorticity or acoustic). Note that $\mathrm{W}_{\mathrm{in}}^{j}$ could also contains w_{410}^{-} (last term of the vector), corresponding to an acoustic wave propagating from right to left and coming from downstream elements of the turbine. This case is not studied here: only the noise coming from the combustor is investigated and the HPTN outlet is assumed to be non-reflective. One can mention that the acoustic power calculated with all waves is not necessary equal to the summation of the acoustic powers generated by each type of wave, because of the phasing of the acoustic waves at the HPTN outlet. The smoothing operation of these outgoing waves is defined as:

$$\left|\left\{\mathrm{W}_{\mathrm{out}}(m,\omega)\right\}\right| = \sqrt{\sum_{i=1}^{N_P}\left|\left\{\mathrm{W}_{\mathrm{out}}^{i}(m,\omega)\right\}\right|^{2}} \tag{12.7}$$

Finally, the acoustic power A_{410} at the outlet of the HPTN is calculated according to the relation provide by Cumpsty and Marble [36] (Eq. 41 in the reference), that is based on the approach of Bretherton and Garrett [18]:

$$\mathrm{A}_{410}(m,\omega) = \left[(\bar{\mathcal{M}}\cos\bar{\theta} + \cos\nu)(1 + \bar{\mathcal{M}}\cos(\bar{\theta} - \nu))\right]_{410} \left|w_{410}^{+}\right|^{2} (\gamma\bar{c}\bar{p}\mathcal{A})_{410} \tag{12.8}$$

where w_{410}^{+} is the downstream acoustic wave obtained from the outgoing set of waves. The reader can refer to Fig. 12.9 for the complete CHORUS calculation flowchart.

The spectra of the acoustic power downstream from the choked stator using Eq. (12.8) are plotted in Fig. 12.10. One can see that the entropy noise is more important than the direct one in the low-frequency range. The noise caused by the vorticity is negligible for this case, but this observation is not expected to be a general statement when all the turbine stages are involved. The acoustic power caused by the circumferential waves is not depicted here, since the acoustics do not propagate in the range of frequencies presented here (they are evanescent under 8 kHz for $n = 1$). The overall acoustic power associated to the longitudinal waves for the four different cases (total, acoustic, entropy and vorticity), can be observed in Fig. 12.11. It appears that, although entropy represents the most important source of noise, the direct one is not negligible. The present evaluation of the core-noise is limited to the high-pressure turbine

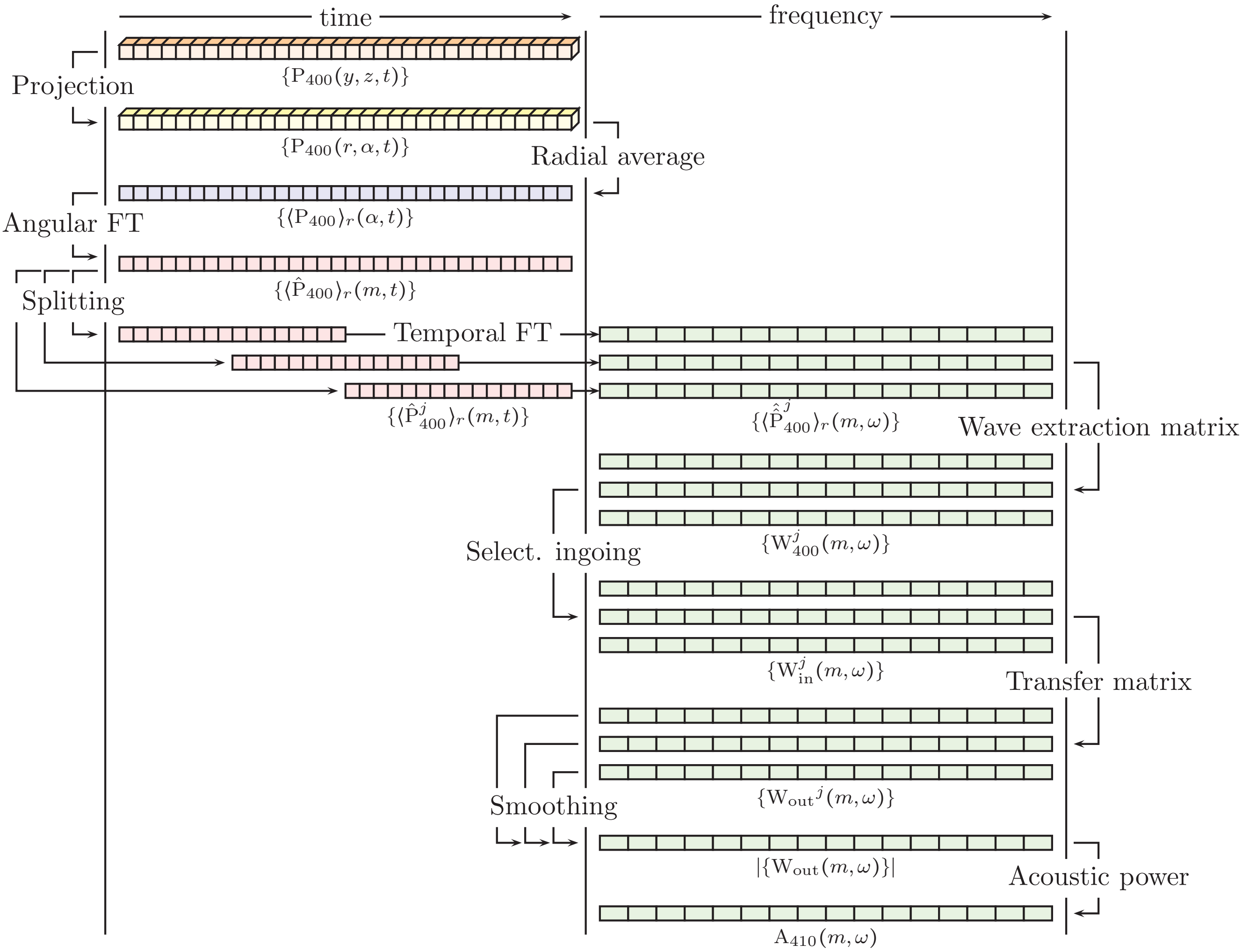

Figure 12.9 - *CHORUS procedure for the calculation of the overall noise caused by the combustion at the outlet of the HPTN (x_{410}).*

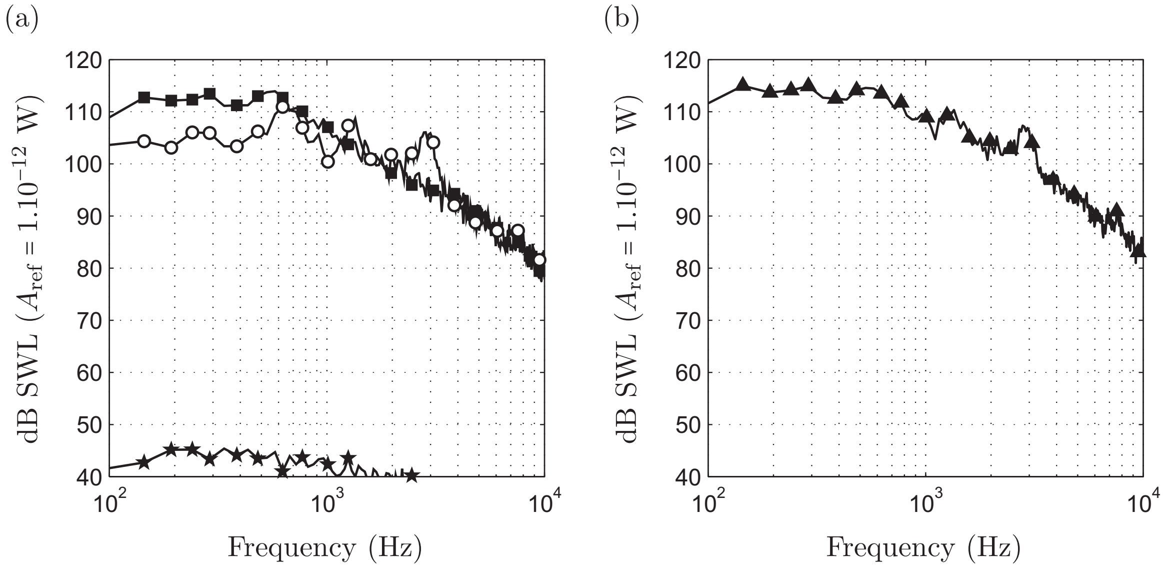

Figure 12.10 - *Spectral acoustic power at the HPTN outlet obtained using LES and CHORUS. (a) Noise from entropy (○), acoustics (▪) and vorticity (⋆). (b) Total spectral acoustic power including entropy, acoustics and vorticity.*

nozzle, and one can expect the indirect noise to be greater and the direct one to be smaller when all turbine stages are involved[2]. One can imagine that each blade row produces entropy noise, and attenuates the direct one. In practice however, the overall indirect sound (for the whole turbine stages) is probably smaller than the one predicted by the theoretical approach because of the entropy wave dissipation and the non-compact effects. Moreover, the rotor case has not been investigated here and one cannot really conclude about the overall combustion-generated core-noise. Nevertheless, it has been shown here that indirect noise is important at the outlet of the first turbine stator, following a more precise approach than in Chap. 7.

---

[2] CHORUS can handle all turbine stages but this was not done here since it was not validated for mobile blade rows

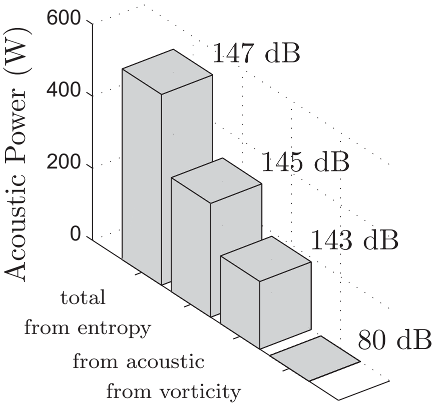

Figure 12.11 - *Overall acoustic power at the HPTN outlet obtained with theoretical transfer functions when considering the four different cases: entropy, acoustic, vorticity or all ingoing waves.*

12.4 Conclusion

The Large-Eddy-Simulation of an actual combustor has been performed and a method called CHORUS has also been proposed to calculate the overall noise caused by combustion based on this simulation. All possible interactions with the turbine (entropy, vorticity and acoustics) are taken into account by CHORUS using the analytical model of Cumpsty and Marble [37]. On one hand waves are extracted from the LES, and on the other hand they are used as inputs for the model. Spectra of acoustic power are obtained depending on the circumferential waves, which can be used in the most general case, that is to say the whole annular combustor, even if only one burner has been computed here. The present method shows that in this case the indirect combustion noise is greater than the direct one, and thus confirms the conclusion of Chap. 7 in a more realistic framework.

General conclusion

The difficulty of evaluating the noise caused by the combustion in aero-engines can be incriminated to two majors points: the complexity of the combustion process itself and the numerous interactions with external elements. These two points have not been extensively investigated during this thesis but have been treated together to propose a method to handle technological effects of aero-engine combustors. The direct and indirect mechanisms identified from the literature that generate noise in aero-engines have been first numerically and analytically compared in a well-defined theoretical framework. This study proves the importance of the indirect combustion noise and also shows the ability of analytical approaches to capture such phenomena. This last conclusion has also been confirmed by using these approaches (numerical and analytical) on the experimental set-up operated at the DLR. These academic cases (1-D) allow to highlight the indirect noise, however it is required to go to more realistic ones (2-D) to deal with actual aero-engines. Therefore, simulations of an isolated blade have been performed to get realistic transfer functions and they have been compared with a 2-D analytical model. Although for high frequencies differences are important, the global theoretical results are good given the compact nozzle assumption. The former model has been used with fluctuations provided by the LES of one burner of an actual combustor to calculate the total noise at the outlet of the first turbine nozzle, including both direct and indirect ones. The method proposed here clearly shows the necessity of taking into account the entropy within the core-noise evaluation method, and the main steps to do this for an actual aero-engine are provided. The majors design modifications are generally made on the combustor, and the former is handled here with a high-fidelity method (LES), so that it allows to deal with different combustor designs in a realistic manner. In a first approach, the transmission of the direct noise and the generation of the indirect one can be assumed not to be caused by design effects of the turbine, but only to its operating condition. Therefore the former can be handled with a simplified model even if it is one of the most important element to evaluate the noise at the engine outlet.

This method aims to provide absolute noise levels at the outlet of an engine-core and then discriminates combustors of an acoustic point of view. However, many points need to be investigated more in details to achieve this objective. First of all, the LES results of one burner combustor should be compared with experiments. This point, as itself, already is a big matter of interest. The combustion modelling, the two phase flow and acoustics simulation for instance are indeed already huge research subjects that couldn't be addressed during this PhD thesis. Moreover, the experiments should provide the entropy fluctuations at the combustor outlet, in addition to the aerodynamic fields and the acoustic pressure, to validate numerical calculations in a reduction noise framework of combustors. Now, even if the LES of one burner is assumed to provide correct results for acoustics, aerodynamics and entropy, the multi-burner configuration of an actual combustor, which has not been investigated here, is intended to have a huge effect. The few experimental data available for the engine combustor investigated in the present thesis seems to exhibit strong circumferential acoustic eigenmodes which are not handled with a single burner. The direct noise appears to be smaller than the indirect one, so that the influence of the acoustic eigenmodes within the combustor are probably less important. However, the multi-burner set-up may also produce circumferential entropy waves, and thus circumferential acoustic waves at the turbine outlet. The computation of the whole combustor is rapidly becoming possible [14, 109] and obviously accurate noise computation using CHORUS will not be possible before they are coupled to an LES of the full combustor (360°). This is not done yet but this work has provided the basis and the tools to do this in the next years.

Bibliography

[1] Cantera software. `http://code.google.com/p/cantera/`. 142

[2] Angelberger, C., Veynante, D., Egolfopoulos, F., and Poinsot, T. Large eddy simulations of combustion instabilities in premixed flames. In *Proc. of the Summer Program* (Center for Turbulence Research, NASA AMES, Stanford University, USA, 1998), pp. 61–82. 42

[3] Bailly, C., Bogey, C., and Candel, S. Modelling of sound generation by turbulent flows. *International Journal of Aeroacoustics (to appear)* (2010). 75, 76

[4] Bake, F., Kings, N., Fischer, A., and Röhle, I. Experimental investigation of the entropy noise mechanism in aero-engines. *International Journal of Aeroacoustics 8*, 1-2 (2009), 125–142. 91, 92, 93, 105

[5] Bake, F., Kings, N., and Röhle, I. Fundamental mechanism of entropy noise in aero-engines: Experimental investigation. *Journal of Engineering for Gas Turbines and Power 130*, 1 (2008). 77, 91, 92, 93

[6] Bake, F., Michel, U., and Röhle, I. Investigation of entropy noise in aero-engine combustors. *Journal of Engineering for Gas Turbines and Power 129*, 2 (2007), 370–376. 77, 91, 92

[7] Bake, F., Michel, U., Röhle, I., Richter, C., Thiele, F., Liu, M., and Noll., B. Indirect combustion noise generation in gas turbines. In *11th AIAA/CEAS Aeroacoustics Conference* (Monterey, CA, May 2005), vol. Paper AIAA-2005-2830. 77, 91

[8] Bake, F., Richter, C., Mühlbauer, B., Kings, N., Röhle, I., Thiele, F., and Noll, B. The Entropy Wave Generator (EWG): A reference case on entropy noise. *Journal of Sound and Vibration 326* (2009), 574–598. 91, 92, 97, 103, 107, 110

[9] Baum, M., Poinsot, T. J., and Thévenin, D. Accurate boundary conditions for multicomponent reactive flows. *Journal of Computational Physics 116* (1994), 247–261. 56

[10] Benoit, L. *Prédiction des instabilités thermo-acoustiques dans les turbines à gaz.* Phd thesis, University Montpellier II, 2005. 185

[11] Bird, R. B., Stewart, W. E., and Lighfoot, E. N. *Transport phenomena.* John Wiley, New York, 1960. 33

[12] Bogey, C., Barré, S., Juvé, D., and Bailly, C. Simulation of a hot coaxial jet: Direct noise prediction and flow-acoustics correlations. *Physics Of Fluids 21*, 3 (2009), 035105. 138

[13] Bohn, M. Response of a subsonic nozzle to acoustic and entropy disturbances. *Journal of Sound and Vibration 52*, 2 (1977), 283–297. 91

[14] Boileau, M., Staffelbach, G., Cuenot, B., Poinsot, T., and Bérat, C. LES of an ignition sequence in a gas turbine engine. *Combustion and Flame 154*, 1-2 (2008), 2–22. 164

[15] Boineau, P. *Modélisation et étude expérimentale des sources acoustiques entropiques en combustion turbulente : Application au calcul de l'emission sonore d'une flamme turbulente non prémélangée.* PhD thesis, UFR Ecole Supérieur d'Ingénieur de Poitiers, 1997. 193

[16] Boudier, G., Gicquel, L. Y. M., Poinsot, T., Bissières, D., and Bérat, C. Effect of mesh resolution on large eddy simulation of reacting flows in complex geometry combustors. *Combustion and Flame 155*, 1-2 (2008), 196–214. 142

[17] Bragg, S. Combustion noise. *Journal of Institute of Fuel 36* (1963), 12–16. 73

[18] Bretherton, F. P., and Garrett, C. J. R. Wavetrains in inhomogeneous moving media. *Proceedings of the Royal Society of London A 302*, 1471 (1968), 529–554. 157

[19] Candel, S. *Analytical studies of some acoustic problems of jet engines.* PhD thesis, California Institute of Technology, Pasadena, California, 1972. 20, 74, 91

[20] Candel, S. Acoustic conservation principles, application to plane and modal propagation in nozzles and diffusers. *Journal of Sound and Vibration 41* (1975), 207–232. 61

[21] Candel, S., Durox, D., Ducruix, S., Birbaud, A.-L., Noiray, N., and Schuller, T. Flame dynamics and combustion noise: Progress and challenges. In *11th CEAS-ASC Workshop of X3-Noise* (Lisbon, Portugal, 2007). 73

[22] Candel, S., Durox, D., and Schuller, T. Flame interactions as a source of noise and combustion instabilities. In *10th AIAA/CEAS Aeroacoustics Conference - AIAA 2004-2928* (2004). 73

[23] Charlette, F., Veynante, D., and Meneveau, C. A power-law wrinkling model for LES of premixed turbulent combustion: Part I - Non-dynamic formulation and initial tests. *Combustion and Flame 131* (2002), 159–180. 44

[24] Charlette, F., Veynante, D., and Meneveau, C. A power-law wrinkling model for LES of premixed turbulent combustion: Part II - Dynamic formulation. *Combustion and Flame 131* (2002), 181–197. 44

[25] Chassaing, P. *Turbulence en mécanique des fluides, analyse du phénomène en vue de sa modélisation à l'usage de l'ingénieur.* Cépaduès-éditions, Toulouse, France, 2000. 37

[26] Childers, D. G. *Modern Spectrum Analysis.* IEEE Press, USA, 1978. 87

[27] Colin, O., Ducros, F., Veynante, D., and Poinsot, T. A thickened flame model for large eddy simulations of turbulent premixed combustion. *Physics Of Fluids 12*, 7 (2003), 1843–1863. 42, 43, 44

[28] Colin, O., and Rudgyard, M. Development of high-order Taylor-Galerkin schemes for unsteady calculations. *Journal of Computational Physics 162*, 2 (2000), 338–371. 53, 93

[29] Cordier, L., and Bergmann, M. Proper orthogonal decomposition: An overview. *Von Karman Institute for Fluid Dynamics, Lecture Series 2003-04 on post-processing of experimental and numerical data* (2003). 189

[30] Cotté, B., Blanc-Benon, P., Bogey, C., and Poisson, F. Time-domain impedance boundary conditions for simulations of outdoor sound propagation. *AIAA Journal 47*, 10 (2009), 2391–2403. 68

[31] Crighton, D. G., Dowling, A. P., Williams, J. E. F., Heckl, M., and Leppington, F. *Modern methods in analytical acoustics.* Lecture Notes. Springer Verlag, New-York, 1992. 74, 75

[32] Crocco, L. Aspects of combustion instability in liquid propellant rocket motors. Part I. *J. American Rocket Society 21* (1951), 163–178. 185

[33] Crocco, L. Supercritical gaseaous discharge with high frequency oscillations. *Aerotechnica 33*, 1 (1953), 46–53. 74

[34] Crumpton, P. I. An efficient cell vertex method for unstructured tetrahedral grids. Tech. Rep. 95/19, Oxford University Computing Laboratory, 1995. 49

[35] Crumpton, P. I., Mackenzie, J. A., and Morton, K. W. Cell vertex algorithms for the compressible navier-stokes equations. *Journal of Computational Physics 109* (1993), 1–15. 49

[36] Cumpsty, N., and Marble, F. Core noise from gas turbine exhausts. *Journal of Sound and Vibration 54* (1977), 297–309. 74, 77, 89, 91, 157

[37] Cumpsty, N. A., and Marble, F. E. The interaction of entropy fluctuations with turbine blade rows; a mechanism of turbojet engine noise. *Proceedings of the Royal Society of London A 357* (1977), 323–344. 20, 22, 23, 74, 77, 89, 91, 110, 111, 112, 119, 124, 128, 149, 151, 152, 156, 161, 177, 185, 202

[38] Donea, J. Taylor-Galerkin method for convective transport problems. *Int. J. Numer. Meth. in Eng. 20*, 1 (1984), 101–119. 53

[39] Donea, J., Quartapelle, L., and Selmin, V. An analysis of time discretization in the finite element solution of hyperbolic problems. *Journal of Computational Physics 70*, 2 (1987), 463–499. 53

[40] Dowling, A. P. The calculation of thermoacoustic oscillations. *Journal of Sound and Vibration 180*, 4 (1995), 557–581. 79

[41] Dunn-Rankin, D. *Lean Combustion: Technology and Control*. Elsevier, 2007. 21

[42] Dutt, P. Stable boundary conditions and difference schemes for Navier-Stokes equations. *J. Numer. Anal. 25* (1988), 245–267. 55

[43] Eckstein, J., Freitag, E., Hirsch, C., and Sattelmayer, T. Experimental study on the role of entropy waves in low-frequency oscillations for a diffusion burner. In *ASME Turbo Expo: Power for Land, Sea and Air* (Vienna, Austria, 2004), vol. Paper ASME-GT2004-54163. 77

[44] Evans, G. W., and Maxwell, L. Chronic noise exposure and reading deficits: The mediating effects of language acquisition. *Environment and Behavior 29*, 5 (1997), 638–656. 17

[45] Fernandez-Tarrazo, E., Sanchez, A., Linan, A., and Williams, F. A simple one-step chemistry model for partially premixed hydrocarbon combustion. *Combustion and Flame 147*, 1-2 (2006), 32–38. 142

[46] Ffowcs Williams, J. E., and Howe, M. S. The generation of sound by density inhomogeneities in low mach number nozzle flows. *J. Fluid Mech. 70* (1975), 605–622. 74

[47] Foglizzo, T., and Tagger, M. Entropic-acoustic instability in shocked accretion flows. *Astrnomy and Astrophysics 363* (2000), 174–183. 103

[48] Franzelli, B., Riber, E., Sanjosé, M., and Poinsot, T. A two-step chemical scheme for kerosene-air premixed flames. *Combustion and Flame (in press)* (2010). 141, 142

[49] Gliebe, P., Mani, R., Shin, H., Mitchell, B., Ashford, G., Salamah, S., and Connell, S. Aeroacoustic prediction codes. Tech. Rep. CR-2000-210244, NASA, 2000. 20, 21

[50] Hassan, H. A. Scaling of combustion-generated noise. *J. Fluid Mech. 66*, 3 (1974), 445–453. 73

[51] Hirschfelder, J., Curtiss, C., and Bird, B. *Molecular Theory of Gases and Liquids*, 1954 ed. John Wiley & Sons, 1954. 33

[52] Ihme, M., Pitsch, H., and Bodony, D. Radiation of noise in turbulent non-premixed flames. *Proceedings of the Combustion Institute 32*, 1 (2009), 1545–1553. 73

[53] International Civil Aviation Organization. Growth in air traffic projected to continue to 2025. `http://www.icao.int/icao/en/nr/2007/pio200708_e.pdf`, 2007. 17

[54] Julliard, J. Problématique des matériaux absorbants sonores pour applications sur turboréacteur. `http://www.onera.fr/congres/jso2003mat-bruit/pdfs/SNECMA-Julliard.pdf`, 2003. 20

[55] Kaji, S., and Okazaki, T. Propagation of sound waves through a blade row: I. Analysis based on the semi-actuator disk theory. *Journal of Sound and Vibration 11*, 3 (1970), 339–353. 109

[56] Kaji, S., and Okazaki, T. Propagation of sound waves through a blade row: II. Analysis based on acceleration potential method. *Journal of Sound and Vibration 11*, 3 (1970), 355–375. 109

[57] Kovasznay, L. S. G. Turbulence in supersonic flow. *Journal of the Aeronautical Sciences 20*, 10 (1953), 657–674. 115, 152

[58] Lamarque, N. *Schémas numériques et conditions limites pour la simulation aux grandes échelles de la combustion diphasique dans les foyers d'hélicoptère.* Phd thesis, INP Toulouse, 2007. 49, 53

[59] Lax, P. D., and Wendroff, B. Difference schemes for hyperbolic equations with high order of accuracy. *Commun. Pure Appl. Math. 17* (1964), 381–398. 52

[60] Légier, J.-P. *Simulations numériques des instabilités de combustion dans les foyers aéronautiques.* Phd thesis, INP Toulouse, 2001. 142

[61] Légier, J.-P., Poinsot, T., and Veynante, D. Dynamically thickened flame LES model for premixed and non-premixed turbulent combustion. In *Proc. of the Summer Program* (2000), Center for Turbulence Research, NASA Ames/Stanford Univ., pp. 157–168. 45

[62] Lieuwen, T., Mohan, S., Rajaram, R., and Preetham. Acoustic radiation from weakly wrinkled premixed flames. *Combustion and Flame 144*, 1-2 (2006), 360–369. 74

[63] Lighthill, M. J. On sound generated aerodynamically. I. General theory. *Proceedings of the Royal Society of London A , Mathematical and Physical Sciences 211*, 1107 (1952), 564–587. 75

[64] Lodato, G., Domingo, P., and Vervisch, L. Three-dimensional boundary condtions for direct and large-eddy simulation of compressible viscous flow. *Journal of Computational Physics* (2008). 56

[65] Luche, J. *Obtention de modèles cinétiques réduits de combustion. Application à un mécanisme du kérosène.* PhD thesis, LCSR Orleans, 2003. 142, 143

[66] Lumley, J. The structure of inhomogeneous turbulent flows. *Atmospheric Turbulence and Radio Wave Propagation 166–178*, ed. A. Yaglom and V. Tatarski. (Nauka, Moscow) (1967). 189

[67] Mackenzie, J. A. *Cell vertex finite volume methods for the solution of the compressible Navier-Stokes equations.* Phd thesis, Oxford University Computing Laboratory, 1991. 49

[68] Mahesh, K., Lee, S., Lele, S., and Moin, P. The interaction of an isotropic field of acoustic waves with a shock wave. *Journal of Fluid Mechanics 300* (1995), 383–407. 101

[69] Mahesh, K., Lele, S., and Moin, P. The influence of entropy fluctuations on the interaction of turbulence with a shock. *Journal of Fluid Mechanics 334* (1997), 353–379. 101

[70] Marble, F. E., and Candel, S. Acoustic disturbances from gas nonuniformities convected through a nozzle. *Journal of Sound and Vibration 55* (1977), 225–243. 22, 74, 77, 78, 82, 91, 92, 99, 100, 101, 103, 104, 107, 110, 111

[71] McManus, K., Poinsot, T., and Candel, S. A review of active control of combustion instabilities. *Progress in Energy and Combustion Science 19* (1993), 1–29. 79

[72] Mendez, S., and Nicoud, F. Adiabatic homogeneous model for flow around a multi-perforated plate. *AIAA Journal 46*, 10 (2008), 2623–2633. 136

[73] Meneveau, C., and Poinsot, T. Stretching and quenching of flamelets in premixed turbulent combustion. *Combustion and Flame 86* (1991), 311–332. 43

[74] Moase, W., Brear, M., and Manzie, C. The forced response of choked nozzles and supersonic diffusers. *Journal of Fluid Mechanics 585* (2007), 281–304. 83, 102

[75] Moureau, V., Lartigue, G., Sommerer, Y., Angelberger, C., Colin, O., and Poinsot, T. Numerical methods for unsteady compressible multi-component reacting flows on fixed and moving grids. *Journal of Computational Physics 202*, 2 (2005), 710–736. 56, 86

[76] Mühlbauer, B., Noll, B., and Aigner, M. Numerical investigation of entropy noise and its acoustic sources in aero-engines. In *ASME Turbo Expo 2008* (Berlin, Germany, June 2008), vol. GT2008-50321. 91, 95, 97

[77] Mühlbauer, B., Noll, B., and Aigner, M. Numerical investigation of the fundamental mechanism for entropy noise generation in aero-engines. *Acta Acustica united with Acustica 95*, 3 (2009), 470–478. 95, 97

[78] Muir, R. S. The application of a semi-actuator disk model to sound transmission calculations in turbomachinery, part I: The single blade row. *Journal of Sound and Vibration 54*, 3 (October 1977), 393–408. 109

[79] Muir, R. S. The application of a semi-actuator disk model to sound transmission calculations in turbomachinery, part II: Multiple blade rows. *Journal of Sound and Vibration 55*, 3 (Decembre 1977), 335–349. 109

[80] Muthukrishnan, M., Strahle, W., and Neale, D. Separation of hydrodynamic, entropy, and combustion noise in a gas turbine combustor. *AIAA Journal 16*, 4 (1978), 320–327. 77, 91

[81] Nottin, C. *Simulation numérique des instabilités de combustion.* Phd thesis, Ecole Centrale Paris, 2002. 185

[82] Oliger, J., and Sundstrom, A. Theoretical and practical aspects of some initial boundary value problems in fluid dynamics. *SIAM J. Appl. Math. 35* (1978), 419–446. 55

[83] Özyörük, Y., Long, L., and Jones, M. G. Time-domain numerical simulation of a flow-impedance tube. *Journal of Computational Physics 146* (1998), 29–57. 68

[84] Paisley, M. F. *Finite Volume Method for the Steady Euler Equations.* PhD thesis, Oxford University Computing Laboratory, 1986. 49

[85] Pickett, G. F. Core engine noise due to temperature fluctuations convecting through turbine blade rows. In *2nd AIAA Aeroacoustics Conference* (1975), vol. Paper AIAA-1975-528. 20, 91, 110

[86] Poinsot, T., and Lele, S. Boundary conditions for direct simulations of compressible viscous flows. *Journal of Computational Physics 101*, 1 (1992), 104–129. 56, 62, 97

[87] Poinsot, T., and Veynante, D. *Theoretical and Numerical Combustion.* R.T. Edwards, 2nd edition, 2005. 38, 39, 42, 61, 85, 86, 145

[88] Polifke, W., Paschereit, C., and Doebbeling, K. Constructive and destructive interference of acoustic and entropy waves in a premixed combustor with a choked exit. *International Journal of Acoustics and Vibration 6*, 3 (2001), 135–146. 77

[89] Pope, S. B. *Turbulent flows.* Cambridge University Press, 2000. 37

[90] Porta, M. *Développement, vérification et validation des outils LES pour l'étude du bruit de combustion et de l'interaction combustion/acoustique/turbulence - TH/CFD/07/46.* PhD thesis, INP Toulouse, France - Dynamique des Fluides, 2007. 57

[91] Posson, H., and Roger, M. Parametric study of gust scattering and sound transmission through a blade row. In *13th AIAA/CEAS Aeroacoustics Conference* (2007), vol. AIAA-2007-3690. 109

[92] Quartapelle, L. *Numerical solution of the incompressible Navier-Stokes equations.* Birkhäuser Verlag, 1993. 53

[93] Rajaram, R., and Lieuwen, T. Parametric studies of acoustic radiation from turbulent premixed flames. *Com. Sci. Tech. 175*, 12 (2003), 2269–2298. 74

[94] Rajaram, R., and Lieuwen, T. Effect of approach flow turbulence characteristics on sound generation from premixed flames. In *42nd AIAA Aerospace Sci. Meet. and Ex. - AIAA 2004-0461* (2004). 74

[95] Réveillon, J., and Vervisch, L. Analysis of weakly turbulent diluted-spray flames and spray combustion regimes. *J. Fluid Mech. 537* (2005), 317–347. 141

[96] Reymen, Y., Baelmans, M., and W., D. Efficient implementation of tam and auriault's time-domain impedance boundary condition. *AIAA Journal 46*, 9 (2008), 2368–2376. 68

[97] Rienstra, S. Impedance models in time domain including the extended helmholtz resonator model. In *12$^{\text{th}}$ AIAA/CEAS Aeroacoustics Conference* (Cambridge, MA, May 2006), vol. Paper AIAA-2006-2686. 68

[98] Rudgyard, M. A. *Cell Vertex methods for compressible gas flows.* Phd thesis, Oxford University Computing Laboratory, 1990. 49

[99] Rudy, D. H., and Strikwerda, J. C. A non-reflecting outflow boundary condition for subsonic navier stokes calculations. *Journal of Computational Physics 36* (1980), 55–70. 62

[100] Sagaut, P. *Large Eddy Simulation for Incompressible Flows*, 3rd ed. Scientific computation series. Springer-Verlag, Berlin, Germany, 2005. 37, 41

[101] Sataloff, R. T., and Sataloff, J. *Hearing Loss*, 4th ed. Marcel Dekker Inc, 2005. 17

[102] Schmitt, P., Poinsot, T., Schuermans, B., and Geigle, K. P. Large-eddy simulation and experimental study of heat transfer, nitric oxide emissions and combustion instability in a swirled turbulent high-pressure burner. *J. Fluid Mech. 570* (2007), 17–46. 85

[103] Schönfeld, T., and Rudgyard, M. Steady and unsteady flow simulations using the hybrid flow solver avbp. *AIAA Journal 37*, 11 (1999), 1378–1385. 49

[104] Selle, L., Nicoud, F., and Poinsot, T. The actual impedance of non-reflecting boundary conditions: Implications for the computation of resonators. *AIAA Journal 42*, 5 (2004), 958–964. 62, 63, 64, 97

[105] Selmin, V. Third-order finite element schemes for the solution of hyperbolic problems. Tech. Rep. 707, INRIA, Sophia Antipolis, France, 1987. 53

[106] Sensiau, C. *Simulations numériques des instabilités thermoacoustiques dans les chambres de combustion aéronautiques - TH/CFD/08/127.* PhD thesis, Université de Montpellier II, - Institut de Mathématiques et de Modélisation de Montpellier, France, 2008. 186

[107] Sirovich, L. Turbulence and the dynamics of coherent structures. part I: Coherent structures. *Quarterly of Applied Mathematics 45*, 3 (1987), 561–571. 192

[108] Smagorinsky, J. General circulation experiments with the primitive equations: 1. the basic experiment. *Mon. Weather Rev. 91* (1963), 99–164. 41

[109] Staffelbach, G., Gicquel, L., Boudier, G., and Poinsot, T. Large eddy simulation of self-excited azimuthal modes in annular combustors. *Proc. Combust. Inst. 32*, 2 (2009), 2909–2916. 49, 114, 164

[110] Stow, S. R., Dowling, A. P., and Hynes, T. P. Reflection of circumferential modes in a choked nozzle. *J. Fluid Mech. 467* (2002), 215–239. 74, 110

[111] Strahle, W. On combustion generated noise. *Journal of Fluid Mechanics 49*, 2 (1971), 399–414. 91

[112] Strahle, W. Combustion noise. *Progress in Energy and Combustion Science 4* (1978), 157–176. 73, 91

[113] Strikwerda, J. C. Initial boundary value problem for incompletely parabolic systems. *Commun. Pure Appl. Math. 30* (1977), 797. 55

[114] Syred, N. A review of oscillation mechanims and the role of the precessing vortex core in swirl combustion systems. *Progress in Energy and Combustion Science 32*, 2 (2006), 93–161. 150

[115] Tam, C., and Auriault, L. Time-domain impedance boundary conditions for computational aeroacoustics. *AIAA Journal 34*, 5 (1996), 917–923. 68

[116] Thompson, K. W. Time dependent boundary conditions for hyperbolic systems. *Journal of Computational Physics 68* (1987), 1–24. 56

[117] Tran, N., Ducruix, S., and Schuller, T. Damping combustion instabilities with perforates at the premixer inlet of a swirled burner. *Proc. Combust. Inst. 32*, 2 (2009), 2917–2924. 136

[118] Tsien, H. S. The transfer functions of rocket nozzles. *J. American Rocket Society 22* (1952), 139–143. 74

[119] Tyler, J. M., and Sofrin, T. G. Axial flow compressor noise studies. *SAE Transactions 70*, 1 (1962), 309–332. 183

[120] Wagner, C., Hüttl, T., and Sagaut, P. *Large-Eddy Simulation for Acoustic.* Cambridge University Press, 2007. 17

[121] White, F. M. *Viscous fluid flow.* McGraw-Hill, New-York, 1991. 33

[122] Yoo, C., and Im, H. Characteristic boundary conditions for simulations of compressible reacting flows with multi-dimensional, viscous, and reaction effects. *Combust. Theory and Modelling 11* (2007), 259–286. 56

Appendix

Appendix A

Analytical blade row transfer functions for longitudinal waves

This appendix provides the analytical solutions of Eq. (9.43) used in Chap. 9 when perturbing axially the entropy, the vorticity or the acoustics at the inlet of a blade row [37]. When $k_y = 0$ and $\beta = 0$, Eq. (9.42) leads to following relationships:

$$w_1^{\mathrm{S}} = w_2^{\mathrm{S}} \tag{A.1}$$

$$-w_1^{\mathrm{S}} + w_1^{+}\left(1 + \frac{1}{\bar{\mathcal{M}}_1 \cos\bar{\theta}_1}\right) + w_1^{-}\left(1 - \frac{1}{\bar{\mathcal{M}}_1 \cos\bar{\theta}_1}\right) = \dots$$

$$-w_2^{\mathrm{S}} + w_2^{+}\left(1 + \frac{1}{\bar{\mathcal{M}}_2 \cos\bar{\theta}_2}\right) + w_2^{-}\left(1 - \frac{1}{\bar{\mathcal{M}}_2 \cos\bar{\theta}_2}\right) \tag{A.2}$$

$$\mu_1\left[\frac{1}{\gamma - 1} w_1^{\mathrm{S}} + w_1^{\mathrm{V}}(i\bar{\mathcal{M}}_1^2 \cos\bar{\theta}_1 \sin\bar{\theta}_1) + w_1^{+}(1 + \bar{\mathcal{M}}_1 \cos\theta_1) + w_1^{+}(1 - \bar{\mathcal{M}}_1 \cos\theta_1)\right] = \dots$$

$$\mu_2\left[\frac{1}{\gamma - 1} w_2^{\mathrm{S}} + w_2^{\mathrm{V}}(i\bar{\mathcal{M}}_2^2 \cos\bar{\theta}_2 \sin\bar{\theta}_2) + w_2^{+}(1 + \bar{\mathcal{M}}_2 \cos\theta_2) + w_2^{+}(1 - \bar{\mathcal{M}}_2 \cos\theta_2)\right] \tag{A.3}$$

$$i\cos^2\bar{\theta}_2 w_2^{\mathrm{V}} + \frac{\sin\bar{\theta}_2}{\bar{\mathcal{M}}_2}(w_2^{-} - w_2^{+}) = 0 \tag{A.4}$$

where

$$\mu = \frac{1}{1 + \frac{1}{2}(\gamma - 1)\bar{\mathcal{M}}^2} \tag{A.5}$$

For ingoing wave $w_1^{\mathrm{S}} \neq 0$ (other ingoing waves are equal to zero):

$$\frac{w_1^-}{w_1^{\mathrm{S}}} = \frac{\left(\dfrac{\mu_1}{\mu_2} - 1\right)/(\gamma - 1)}{\left(\bar{\mathcal{M}}_1 \cos\bar{\theta}_1 - 1\right)\left(\dfrac{\cos\bar{\theta}_2 + \bar{\mathcal{M}}_2}{(\cos\bar{\theta}_2 + 1/\bar{\mathcal{M}}_2)\bar{\mathcal{M}}_1 \cos\bar{\theta}_1} + \dfrac{\mu_1}{\mu_2}\right)} \tag{A.6}$$

$$\frac{w_2^+}{w_1^{\mathrm{S}}} = \frac{1 - \dfrac{1}{\bar{\mathcal{M}}_1 \cos\bar{\theta}_1}}{1 + \dfrac{1}{\bar{\mathcal{M}}_2 \cos\bar{\theta}_2}} \frac{w_1^-}{w_1^{\mathrm{S}}} \tag{A.7}$$

$$\frac{w_2^{\mathrm{V}}}{w_1^{\mathrm{S}}} = -i \frac{\sin\bar{\theta}_2}{\cos^2\bar{\theta}_2} \frac{1}{\bar{\mathcal{M}}_2} \frac{w_2^+}{w_1^{\mathrm{S}}} \tag{A.8}$$

$$\frac{w_2^{\mathrm{S}}}{w_1^{\mathrm{S}}} = 1 \tag{A.9}$$

For ingoing wave $w_1^+ \neq 0$ (other ingoing waves are equal to zero):

$$\frac{w_1^-}{w_1^+} = -\frac{1 + \dfrac{1}{\bar{\mathcal{M}}_1 \cos\bar{\theta}_1} - \dfrac{\mu_1}{\mu_2} \dfrac{(1 + \bar{\mathcal{M}}_1 \cos\bar{\theta}_1)(\bar{\mathcal{M}}_2 \cos\bar{\theta}_2 + 1)}{\bar{\mathcal{M}}_2(\cos\bar{\theta}_2 + \bar{\mathcal{M}}_2)}}{1 - \dfrac{1}{\bar{\mathcal{M}}_1 \cos\bar{\theta}_1} - \dfrac{\mu_1}{\mu_2} \dfrac{(1 - \bar{\mathcal{M}}_1 \cos\bar{\theta}_1)(\bar{\mathcal{M}}_2 \cos\bar{\theta}_2 + 1)}{\bar{\mathcal{M}}_2(\cos\bar{\theta}_2 + \bar{\mathcal{M}}_2)}} \tag{A.10}$$

$$\frac{w_2^+}{w_1^+} = \frac{\mu_1}{\mu_2} \frac{1 + \bar{\mathcal{M}}_1 \cos\bar{\theta}_1 + \dfrac{w_1^-}{w_1^+}}{1 + \dfrac{\bar{\mathcal{M}}_2}{\cos\bar{\theta}_2}} \tag{A.11}$$

$$\frac{w_2^{\mathrm{V}}}{w_1^+} = -i \frac{\sin\bar{\theta}_2}{\cos^2\bar{\theta}_2} \frac{1}{\bar{\mathcal{M}}_2} \frac{w_2^+}{w_1^+} \tag{A.12}$$

$$\frac{w_2^{\mathrm{S}}}{w_1^+} = 0 \tag{A.13}$$

For ingoing wave $w_1^{\mathrm{V}} \neq 0$ (other ingoing waves are equal to zero):

$$\frac{w_1^-}{w_1^{\mathrm{V}}} = i \frac{\cos\bar{\theta}_1 \sin\bar{\theta}_1 \bar{\mathcal{M}}_1^2}{\bar{\mathcal{M}}_1 \cos\bar{\theta}_1 - 1 + \dfrac{\mu_2}{\mu_1}\left(1 + \dfrac{\bar{\mathcal{M}}_2}{\cos\bar{\theta}_2}\right)\dfrac{1 - 1/\bar{\mathcal{M}}_1 \cos\bar{\theta}_1}{1 + 1/\bar{\mathcal{M}}_1 \cos\bar{\theta}_1}} \tag{A.14}$$

$$\frac{w_2^+}{w_1^{\mathrm{V}}} = \frac{1 - \dfrac{1}{\bar{\mathcal{M}}_1 \cos\bar{\theta}_1}}{1 + \dfrac{1}{\bar{\mathcal{M}}_2 \cos\bar{\theta}_2}} \frac{w_1^-}{w_1^{\mathrm{V}}} \tag{A.15}$$

$$\frac{w_2^{\mathrm{V}}}{w_1^{\mathrm{V}}} = -i \frac{\sin\bar{\theta}_2}{\cos^2\bar{\theta}_2} \frac{1}{\bar{\mathcal{M}}_2} \frac{w_2^+}{w_1^{\mathrm{V}}} \tag{A.16}$$

$$\frac{w_2^{\mathrm{S}}}{w_1^{\mathrm{V}}} = 0 \tag{A.17}$$

Appendix B

Comparison of LES with DEM21 measurements

The objective of this work was not to compare extensively LES and experimental data. Only unsteady pressure probes data was available in the experiment, so that only these data have been compared with LES, which is insufficient for a real validation.

B.1 Test-rig instrumentation, measurements and calculations

The unsteady pressure signals investigated here were obtained during the measurement campaign of 2004 (DEM21 2B - May to October). Three different unsteady pressure probes are considered: one placed in the spark plug well, that measures the unsteady pressure within the flame tube (PFT); and two placed on the outer casing and diametrically opposite, that measure the unsteady pressure within the outer annulus (POA1 and POA2). The positions of these probes are depicted in Fig. B.1. The same radial and axial positions have been retained for comparison with LES, but obviously not the azimuthal one. The equivalent probes in the LES are located at $\alpha = 0°$, so that only one probe in the outer annulus is considered in the LES. The pressure signals of the test-rig are sampled at 50 kHz and are 120 s long, whereas they are 200 ms long in the LES. The pressure fluctuations levels at the different probes can be found in table B.1 (root mean square in dB SPL with $p_{\text{ref}} = 20.10^{-6}$ Pa). The global levels of pressure variations in LES are in

Location	Probe name	Measurements	LES
Flame tube	PFT	171.8	173.2
Outer annulus (140°)	POA1	166.8	165.8
Outer annulus (320°)	POA2	167.0	-

Table B.1 - *Pressure levels for the different probes for the measurements and in the LES (in dB SPL).*

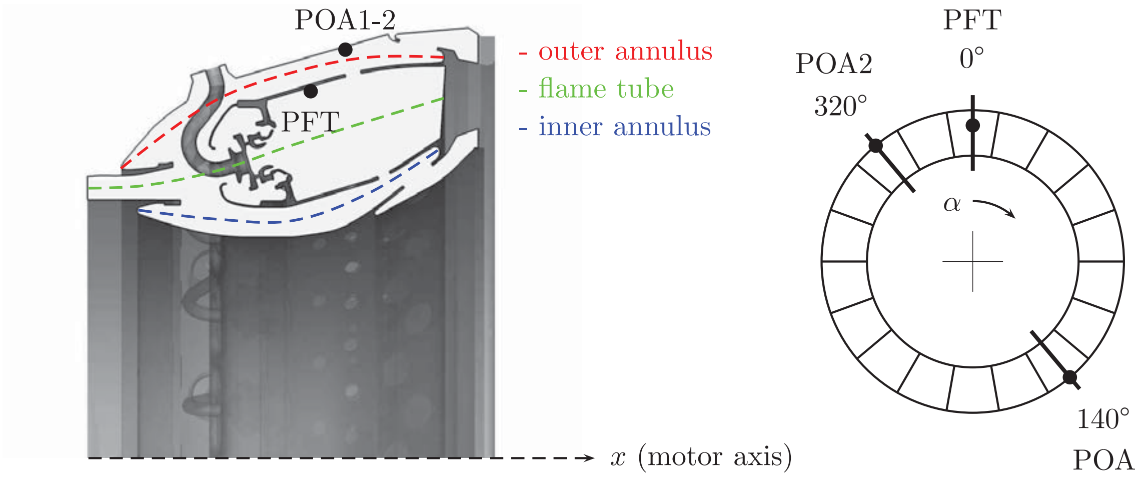

Figure B.1 - *Positions of the pressure probes within the combustor, and definitions of the revolution surfaces for the developing of the acoustic pressure fields from AVSP calculations.*

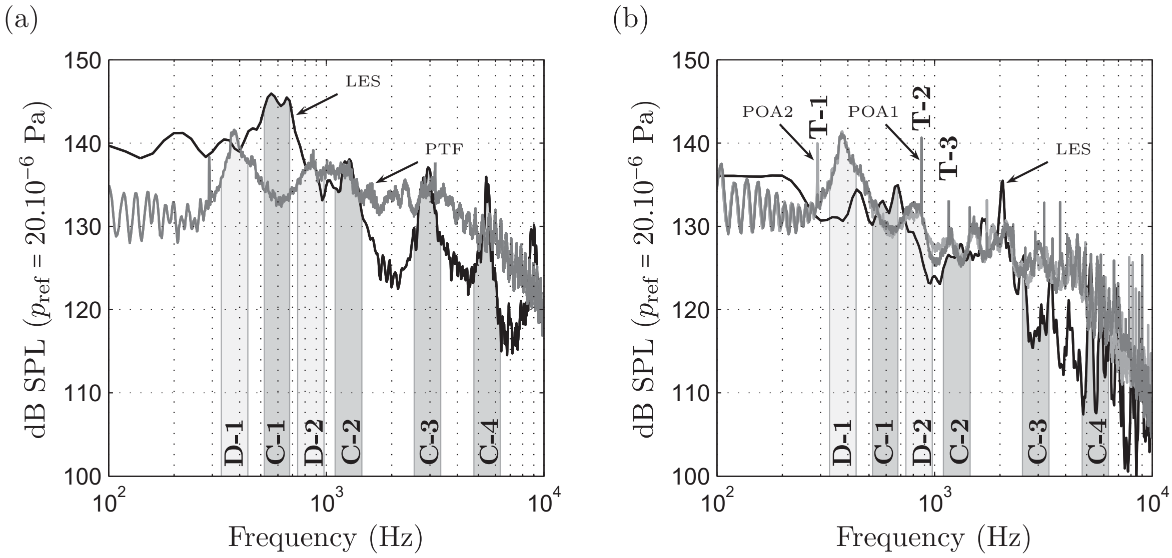

Figure B.2 - *Power spectral density of pressure fluctuations, in the flame tube (a), in the outer annulus (b). Numerical calculations : (—); Measurements PFT and POA1 (—); POA2 (—).*

good agreement with the measurements, but one can observe that the fluctuations within the flame tube (PFT) are stronger in the calculations than on the test-rig, whereas it is the contrary within the outer annulus (POA1-2).

Power density spectra of these fluctuations are plotted in Fig. B.2. The spectra in the flame tube (a) and the outer annulus (b) are plotted versus frequency in a log-scale. Numerous differences between the LES and the measurements are observed:

- A strong tonal noise is present on the test-rig (290, 872, 1162 Hz, ...) whereas no spectral line of this nature is recovered in the LES. It can be seen that this extra noise is important mainly in the outer annulus (POA1 and POA2). The different lines in the spectra are noted T-1, T-2, etc. according to ascending frequency. These modes are caused by the compressor and the related explanations are provided in Sec. B.2.
- Two main ranges of frequencies D-1 and D-2 can be identified in the measurements, where stronger power density levels appear. Similar ones can also be found in the LES but in a different range of frequencies noted C-1, C-2, C-3 and C-4. It is shown in Sec. B.3 and B.4 that C-1 and C-2 are related to hydrodynamic perturbations of the flame, and that D-1, D-2, C-3 and C-4 correspond to excited acoustic eigenmodes. Only one burner is computed here and important differences are observed because of the azimuthal acoustic eigenmodes found in the actual combustor.

B.2 Tonal noise

The test engine is made of the whole high-pressure core, that is to say operating with the high-pressure compressor, combustor (with all 18 burners) and high-pressure turbine. The strong tonal noise (T-1, T-2, etc.) which is present both in the flame tube and the outer annulus is presumably due to the turbo-machinery acoustic modes. The turbine nozzle is choked for this regime, so that the peaks in the spectra can be only due to the compressor. Moreover, this noise is much higher in the outer annulus than in the flame tube, that also supports the hypothesis related to the compressor. Following the theory of Tyler and Sofrin [119], the ratio between the eigenfrequencies of the axial compressor flow f_c and the rotation frequency f_r can be written:

$$\frac{f_c}{f_r} = qB + rV \tag{B.1}$$

where q and r are integers. B and V are the number of blades of the rows involved in the interaction. The rotation speed of the HPC is 17000 rpm. One can consider the interaction with consecutive rows as well as with non-consecutive ones. Table B.2 shows the frequencies obtained with q ranging from 0 up to 25, and with r ranging from -25 up to 0. The number of blades of the different rows ranges from 36 up to 126 for the present compressor. The results are sorted in table B.2 from the lowest frequency to the highest depending on the type of interaction (the i-th stator with the i-th rotor, etc.). It can be observed that all frequencies found experimentally in Fig. B.2 are recovered with an error of less than 1%, which strongly supports the idea that these modes are caused by the compressor. This explains why the lines in the spectra from measured signals cannot be found in the LES, which is performed without the compressor.

B.3 Combustor acoustic modes

The levels of pressure fluctuations of the test-rig in the frequency range D-1 and D-2 are the same within the flame tube and the outer annulus. This trend is not recovered in the simulation

Name	Measurements (Fig. B.2-b POA1-2)	Rotor i - Sator i and Stator i - Rotor $i+1$
T-1	290	291
T-2	872	872
T-3	1162	1163
T-4	1742	1744
T-5	2904	2907
T-6	3196	3197
T-7	3486	3488
T-8	3776	3779
T-9	4066	4069
T-10	4648	4651
T-11	4938	4941
T-12	5230	5232
T-13	5810	5813
T-14	6100	6104
T-15	6682	6685
T-16	6972	6976
T-17	7262	7267
T-18	8134	8139
T-19	8424	8429
T-20	8714	8720
T-21	9006	9011
T-22	9586	9592
T-23	10168	10173
T-24	10458	10464

Table B.2 - *Eigenfrequencies of the compressor in Hertz.*

for C-1 or C-2 where the associated fluctuations seem to vanish in the outer annulus. The spectral resolution of the computation is smaller than for the measurements and interpretation of the low-frequency range is hazardous, but nothing seems to emerge for the frequency range of D-1, or D-2, in the numerical calculations. LES doesn't recover correctly the fluctuations for these frequencies because of they corresponds to azimuthal acoustic eigenmodes that cannot be represented in the LES of only one burner. Therefore, the acoustic eigenmodes of the whole multi-burner combustor are calculated with the acoustic Helmholtz-solver AVSP to support this explanation and justify the disagreement between the measurements and the simulations.

AVSP is a solver developed by Benoit [10] at CERFACS and based on the work of Nottin [81] during its PhD thesis at EM2C laboratory. It solves the Helmholtz equation, which results from the linearization of the flow perturbations around a low-Mach number mean state in the frequency domain. AVSP is mainly used to investigate acoustic eigenmodes of combustors and takes into account any speed of sound distribution. The eigenvalueproblem which is solved by AVSP is the following:

$$\left[(i\omega)^2 - \frac{\partial}{\partial x_k}\left(\bar{c}^2 \frac{\partial}{\partial x_k}\right)\right]\hat{p} = 0 \tag{B.2}$$

Equation B.2 depends on the steady speed of sound $\bar{c}$ which strongly varies in space for reacting flows, and is evaluated here averaging the LES results. Nevertheless, it can be provided by any CFD solver dealing with combustion. AVSP can also solve eigenvalueproblems taking into account the heat release fluctuations for the study of combustion instabilities:

$$\left[(i\omega)^2 - \frac{\partial}{\partial x_k}\left(\bar{c}^2 \frac{\partial}{\partial x_k}\right)\right]\hat{p} = (i\omega)(\gamma - 1)\hat{q} \tag{B.3}$$

where Fourier-transform $\hat{q}$ of the heat release is handled with the n-τ model of Crocco [32]. Only the pure eigenvalue-problem (Eq. B.2) is addressed hereafter.

Since the Helmholtz-solver is based on the low-Mach number flow assumption, its computational domain must be ended before the turbine nozzle which needs to be replaced by its equivalent admittance. The combustor is cut close to the outlet where the Mach number is less than 0.1. It has been seen in Chap. 9 that, for axially impinging acoustic waves, the reflection coefficient is close to one when the inlet Mach number is low and the nozzle is choked. Therefore, the outlet boundary condition has been modeled by $\hat{u}_{\text{out}} = 0$. The inlet impedance can ideally also be calculated using the relations of Cumpsty and Marble [37], but the data concerning the compressor were not available for this study, so that the reflection coefficient at the inlet is also set to one, that is to say that $\hat{u}_{\text{in}} = 0$, like for the outlet.

Two different calculations have been performed with AVSP: a first one with only one burner to capture specifically the longitudinal acoustic eigenmodes; and a second one with all burners to get the azimuthal acoustic eigenmodes. The eigenmodes in AVSP are calculated by ascending order of frequencies, so that an important number of frequencies has to be calculated on the multi-burner configuration before getting the longitudinal eigenmodes, which correspond to much higher frequencies. Table B.3 shows the different calculated eigenfrequencies sorted according to the eigenmode type (longitudinal L- or azimuthal A-).

Longitudinal		Azimuthal	
Name	Frequency	Name	Frequency
L-1	849	A-1a	421
L-2	966	A-1b	421
L-3	1272	A-2	810
L-4	1645	A-3	915
L-5	1810	A-4	1046
L-6	1900	A-5	1077
L-7	2303	A-6	1123
L-8	2586		
L-9	2788		
L-10	3024		
L-11	3385		

Table B.3 - *Eigen-frequencies calculated with AVSP in Hertz for the DEM21 configuration.*

The frequencies of the A-1a and A-1b modes at 421 Hz seem to be close to D-1 identified in the actual combustor. Figure B.3 displays the spatial distribution of the acoustic pressure modulus $|\hat{p}|$ for these modes. The three developed-surfaces, constructed according to Fig. B.1, correspond to the outer and inner annulus and flame tube. The two eigenmodes A1-a and A1-b, that are related to the same frequency are seen to be orthogonal, so that linear combination of both is required to recover the actual pressure fluctuations. This can easily be explained considering a purely annular problem like in Chap. 9. Let's consider a fluid at rest ($\bar{\mathcal{M}} = 0$) and waves propagating along the azimuthal direction only ($k_x = 0$). The dispersion relation leads in this case to the relationship:

$$\left(1 + \frac{k_y c}{\omega}\right)\left(1 - \frac{k_y c}{\omega}\right) = 0 \tag{B.4}$$

with $k_y = m/R$ and R the mean radius of the combustor. Therefore, two possible solutions exist for the same angular frequency ω, but with opposite number m. The resulting acoustic waves are contra-rotating and can be sum to yield the pressure fluctuation:

$$\frac{p'}{\gamma\bar{p}}(t,\theta) = \frac{p'_+}{\gamma\bar{p}} e^{i(\omega t + m\theta)} + \frac{p'_-}{\gamma\bar{p}} e^{i(\omega t - m\theta)} \tag{B.5}$$

with $\omega = mc/R$. The decomposition found by AVSP for this frequency is just one possible representation of the same problem, as shown by Sensiau [106]. A-1a et A-1b have actually sinusoidal distributions of the acoustic pressure with an angle difference of $\pi/2$ radian. The following linear combination of the simplified modes A-1a and A-1b:

$$\frac{p'}{\gamma\bar{p}}(t,\theta) = \frac{p'_+}{\gamma\bar{p}}[\underbrace{\cos(m\theta)}_{\text{A-1a}} + i\underbrace{\sin(m\theta)}_{\text{A-1b}}]e^{i\omega t} \tag{B.6}$$

leads for instance to the expression of the wave $p'_+/\gamma\bar{p}$ of Eq. (B.5) (using Euler's formula). Actually, this former combination seems to emerge in test-rig combustor, that is to say only one wave is propagating along the azimuthal direction. This can be shown by studying, in a first step, the cross power spectral density S_{xy} of the two diametrically-opposed pressure probes in the outer annulus POA1 and POA2.

S_{xy} is defined as the Fourier-transform the cross-correlation C_{xy} of signals x and y. Figure. B.4-a shows that the two signals seems to be correlated for the frequency ranges D-1 and D-2. A quantity which is more relevant of the correlation of signals x and y is the coherence function Γ_{xy}, and it is written:

$$\Gamma_{xy} = \frac{S_{xy} S^{\star}_{xy}}{S_{xx} S_{yy}} \tag{B.7}$$

where $S^{\star}_{xy}$ the complex conjugate of S_{xy}. This function is plotted in Fig. B.4-b: the two signals are correlated in the D-1 frequency range, but it is less obvious for D-2 since the measured signal is quite noisy.

This correlation does not necessary mean that the pressure fluctuations in the outer annulus is caused by the azimuthal acoustic mode, and the phase between both pressure sensors needs to be investigated in a second step. The angle resulting from S_{xy} being too noisy, the auto- and cross-correlation (C_{xx}, C_{yy} and C_{xy}) of the digitally-filtered signals are used to get the delay. Figure B.5-a, respectively -b, shows the auto-correlation, respectively cross-correlation, of POA1 and POA2 (Fig. B.5) filtered for frequencies ranging from 300 up to 500 Hz (D-1). Figures B.5-a and -b are related to frequencies ranging from 700 up to 900 Hz (D-2). One can state from the cross-correlation function that, as already seen in Fig. B.4-b, the POA1 and POA2 are well correlated for D-1. Moreover the delay found here corresponds to the half-period of the relating frequencies (C_{xy} minimum for $\tau = 0$) which shows that the first azimuthal acoustic mode (A-2 in table B.3) seems to be excited in the actual combustor. The second azimuthal mode should have in-phase pressure fluctuations POA1 and POA2 if only one rotating acoustic wave is present ($m = -2$ or $m = 2$). It does not appear clearly from Fig. B.5-a. Nevertheless, one can also suppose, with regards to the cross power spectral density, that it is related to azimuthal acoustics.

To conclude, this analysis strongly supports that the important acoustic perturbations of D-1 and D-2 are due to the first azimuthal and second modes of the complete combustor at 380 and 800 Hz, and this explains why they cannot be recovered with the mono-burner LES.

Part of the large pressure fluctuations found in the LES (especially for PFT) can also be explained using the acoustic solver. According to table B.3, the closest acoustic eigenfrequency is related to the longitudinal mode L-1. However, as seen in Fig. B.6, none of the three closest calculated longitudinal acoustic modes (L-1, L-2 and L-3) exhibits pressure fluctuation within the flame tube (FT). Only mode C-3 seems to correspond to L-11 that is related to such an observation. The mode L-11 is the half-wave mode of the flame tube, and its eigenfrequency agrees with the simplified expression $f = \bar{c}_{FT}/2\ell_{FT}$, where $\bar{c}_{FT}$ is the space average speed of sound and ℓ_{FT} axial length of this region. It may seem surprising that none of the first longitudinal eigenmodes calculated with AVSP exhibits fluctuations within the flame tube. However, the pressure fluctuations in C-1 and C-2 are here caused by the unsteady heat release. The fields of perturbations are investigated in Sec. B.4 using Proper Orthogonal Decomposition in order to

(a) A-1a: outer annulus

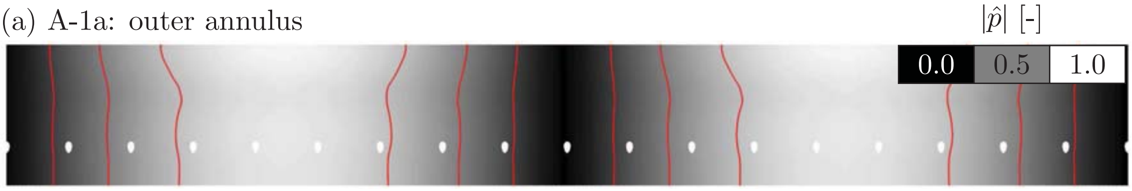

(b) A-1a: flame tube

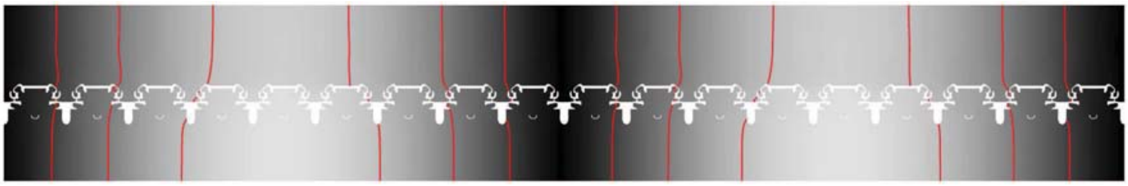

(c) A-1a: inner annulus

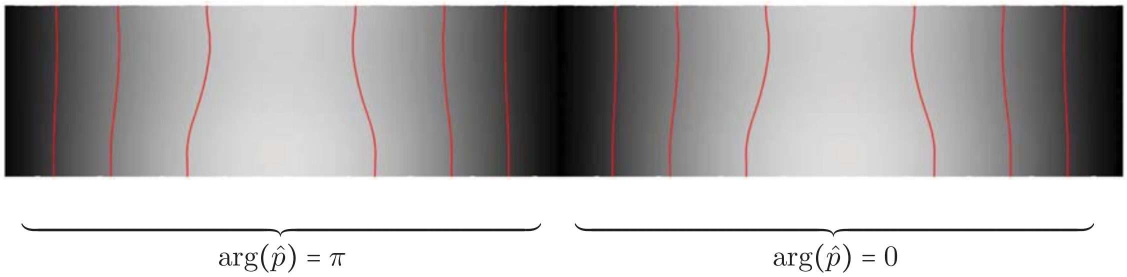

(d) A-1b: outer annulus

(e) A-1b: flame tube

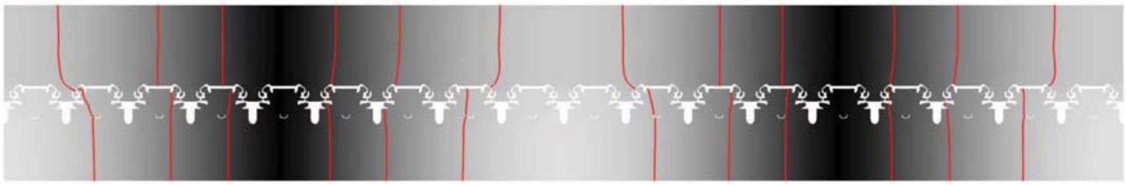

(f) A-1b: inner annulus

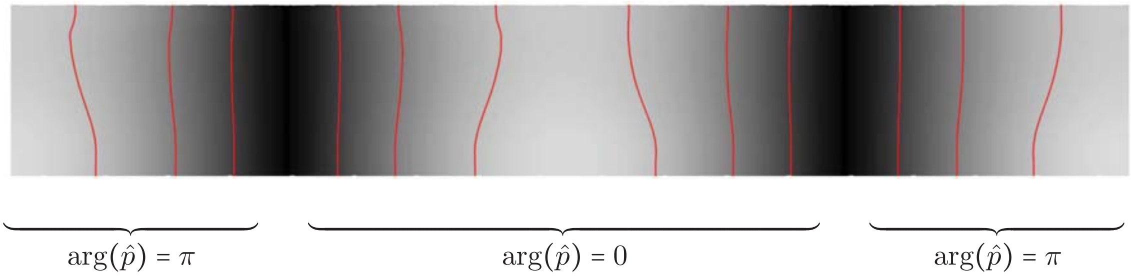

Figure B.3 - *Pressure modulus $|\hat{p}|$ of the azimuthal eigenmodes A-1a (a,b,c) and A-1b (d,e,f) computed with AVSP and depicted on developed surface of the outer annulus (a,d), the flame tube (b,e) and the inner annulus (c,f).*

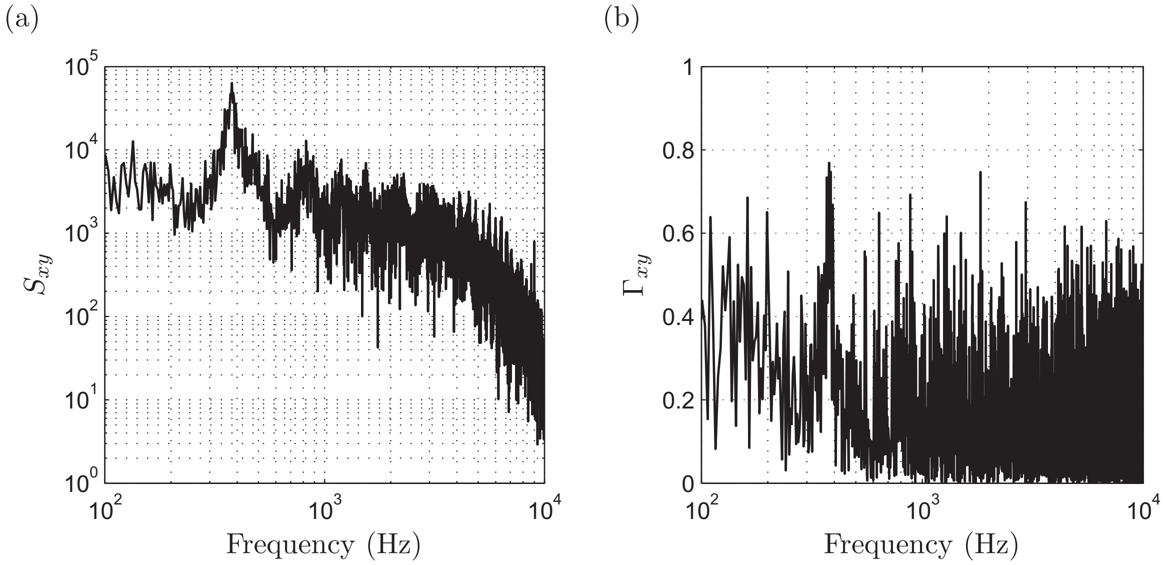

Figure B.4 - *(a) Cross power spectral density S_{xy} of signals POA1 and POA2. (b) Coherence function Γ_{xy} between POA1 and POA2 measured in the outer annulus.*

explain the mechanism leading to such pressure fluctuations.

B.4 Proper orthogonal decomposition

Dynamic systems, even as complex as the one studied here, can often be represented by a reduced number of eigenmodes, in comparison with all the degrees of freedom involved to handle the phenomenon. Proper Orthogonal Decomposition (POD) is a post-processing technique that uses instantaneous fields of the flow variables, called *snapshots*, to provide the most representative description of the temporal evolution of the structures containing the largest part of the *energy*. A description of the POD method can be found in [29], but a brief overview is given in this section. Lets $q_i(\vec{x})$ be a set of snapshots at point $\vec{x}$ of the computation domain with $i = 1, \ldots, N$. The POD aims to find functions ψ such that

$$\frac{\left\langle |(q,\psi)|^2 \right\rangle}{||\psi||^2} \tag{B.8}$$

is maximum, that is to say that q suits the best with the function ψ. The operator $\langle\cdot\rangle$ is some kind of average, $(\cdot,\cdot)$ is an inner product and $||\cdot||$ the corresponding norm. The functions ψ span the subspace of the original space of the snapshots $q_i(\vec{x})$ in order to minimize the error of the orthogonal projection. Solving the optimization problem leads to an eigenvalue problem, where the functions ψ are the eigenfunctions. The spatial POD (or classical), introduced by Lumely [66] in fluids mechanics, requires solving the eigenvalue problem based on space and with an average in time. It is not adapted for CFD where the space resolutions are often large

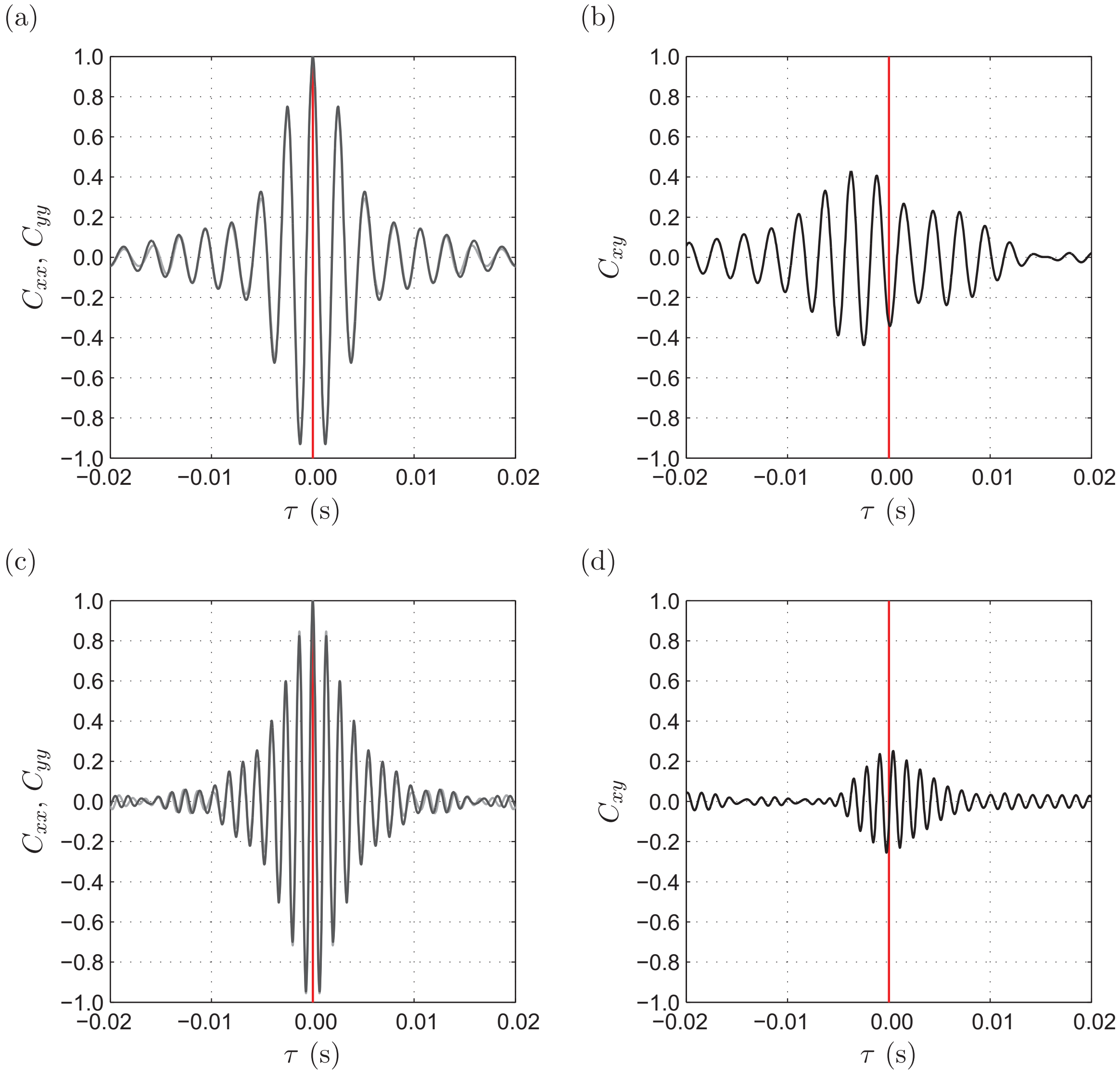

Figure B.5 - *(a,c) Auto-correlation of the filtered signals measured in POA1 (—) and POA2 (—). (b,d) Cross-correlation between the filtered signals measured in POA1 and POA2. (a,b) pass-band filter from 300 up to 500 Hz and (c,d) from 700 up to 900 Hz.*

(a) L-1, 849 Hz (b) L-2, 966 Hz

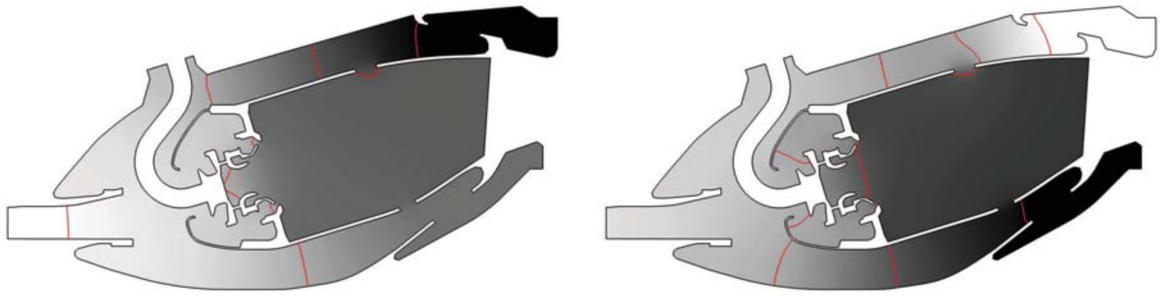

(c) L-3, 1272 Hz (d) L-6, 1900 Hz

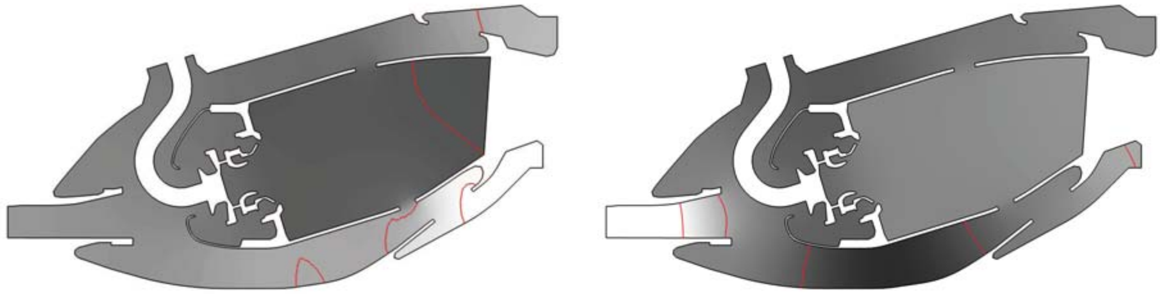

(e) L-7, 2303 Hz (f) L-11, 3385 Hz

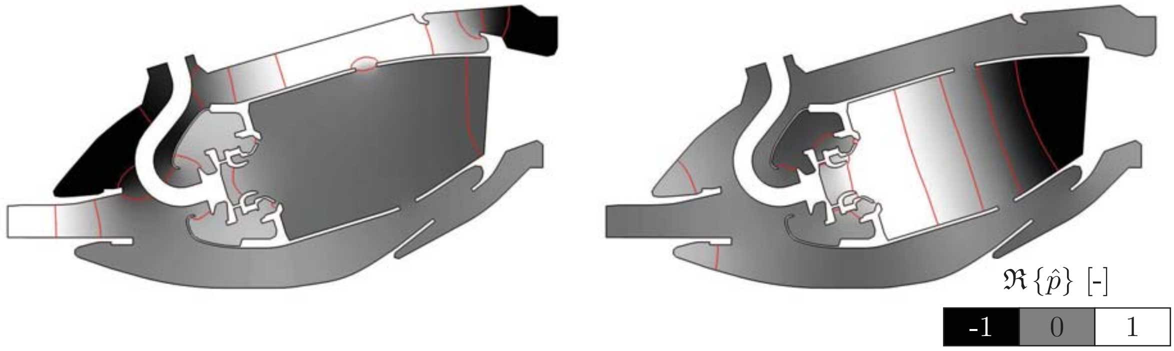

Figure B.6 - *Longitudinal modes in the DEM21 combustor calculated with AVSP: real part* $\Re\{\hat{p}\}$ *of the acoustic pressure calculated with AVSP. (a) L-1; (b) L-2; (c) L-3; (d) L-6; (e) L-7; (f) L-11.*

compared with the temporal one. Sirovich [107] has introduced the snapshot POD that avoids the direct calculation of the eigenfunctions ψ, and then the eigenvalue problem is based on time. One can show that if one considers the following eigenvalue problem:

$$r_{ij}\ a_{im} = \lambda_m\ a_{im} \quad \text{with} \quad r_{ij} = \frac{1}{N}(q_i, q_j) \tag{B.9}$$

where a_{im} is the m-th eigenvector related to the eigenvalue λ_m (representative of the energy associated to the eigenmode), then eigenfunctions are linear combinations of the snapshots:

$$\psi_m = \sum_{i=1}^{N} a_{im} q_i \tag{B.10}$$

According to the properties of the POD base, and if the eigenvalues are sorted in a descending mode, the following relationships can be written:

$$q_k = \sum_{m=1}^{N} a_{km}\psi_m \simeq \sum_{m=1}^{M<N} a_{km}\psi_m \tag{B.11}$$

The eigenfunctions ψ_m are also called POD modes, and the snapshots can be approximated by a reduced number M of these modes (the most important ones). The eigenvectors a_{im} are also called temporal eigenvectors. The inner product $(\cdot,\cdot)$ for the pressure fluctuations, $q_k = (\ p'_k\ )$, is here written as:

$$(q_i, q_j) = \int_V \frac{p'_i}{\bar{\gamma}\bar{p}}(\vec{x})\frac{p'_j}{\bar{\gamma}\bar{p}}(\vec{x})dV \tag{B.12}$$

Figure B.7 shows energy associated to the first twenty POD modes (eigenvalues λ_m), whereas the three first eigenfunctions are depicted in Fig. B.8. Let's note POD-m the m-th POD mode, then one can observe that POD-1 is related to uniform pressure fluctuations within the flame tube. The spectrum of the associated temporal eigenvector contains the frequency ranges C-1 and C-2 of the LES, since it is the most energetic. The mode POD-2 seems to be very close to the acoustic mode L-11 (Fig. B.6-f) because of both spatial et spectral aspects. Pressure fluctuations are mainly located in the outer and inner annulus, and in the diffuser for POD-3. The pressure fluctuations for the POD-2 related to frequency range C-3 in the LES can thus be associated to the longitudinal half-wave acoustic mode of the flame tube. The peaks in the higher frequencies (C-4, etc.) are probably associated with the harmonic modes of this half-wave acoustic one. It is interesting to notice that this modes do not stand out for the pressure signal measured on the test-rig. This observation can be explained considering one more time the whole annular combustor. Indeed, if one assumes that the source of the acoustic excitation is due to the global heat release of each burner (assumption that stands for both direct and indirect sound), then one should take into account the correlation between each ones. The present computation with only one burner and with periodical boundaries is equivalent to a whole combustor in which the heat releases of each sector fluctuate perfectly in phase. However, there is no reasons to have such coherence between all sectors of the combustor. Therefore, the computation of only one sector can lead to greater pressure fluctuations levels and to a strong excitation of the longitudinal acoustic eigenmodes of the combustor (peaks in the spectra).

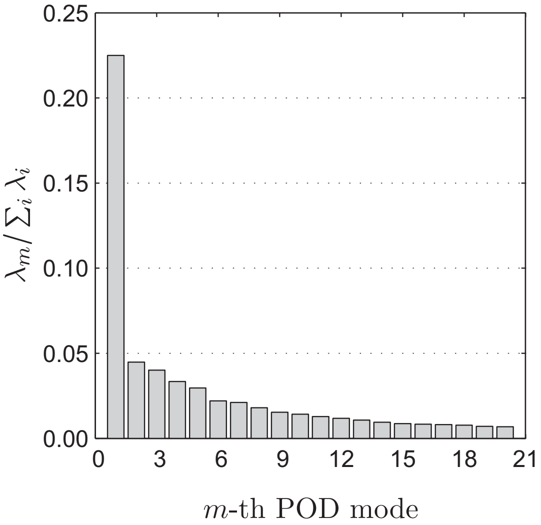

Figure B.7 - *POD of the pressure fluctuations in the LES. The twentieth firsts POD modes eigenvalues for the pressure fluctuations sorted descending*

The global heat release is investigated hereafter to understand the acoustics within the combustion chamber in the LES. One can see in Fig. B.9 the auto-correlation function and the spectrum of the global heat release that is defined as:

$$\langle \dot{\omega}_T \rangle_V = \frac{1}{V} \int_V \dot{\omega}_T(\vec{x}) dV \tag{B.13}$$

where $\langle \cdot \rangle_V$ stands for volume average. Two frequencies stand out that are related to the frequency ranges C-1 and C-2 of the pressure fluctuations in the flame tube (PTF). The correlation between the global heat release and pressure fluctuation in the LES is shown here calculating the coherence function Γ_{xy} of both, as Boineau done during his PhD thesis [15]. Figure B.10-a shows the temporal evolution of the dimensionless global heat release rate derivative and the dimensionless pressure fluctuation signal within the flame (PTF) from the LES. The related coherence function is plotted in Fig. B.10-b. It is clear that for the two frequency ranges C-1 and C-2 the correlation is very important (close to one), as well as for the frequency range C-3. For the longitudinal acoustic modes related to higher frequencies, the global heat release is no longer representative and thus the coherence decreases.

The mechanism which lead to such a behaviour of the global heat release are explained hereafter. It is shown that the two peaks in the spectra are caused by the Precessing Vortex Core (PVC). The spectra of the pressure fluctuations at two points along the swirler axis are plotted in Fig. B.11. The first point is located close to the beginning of the swirler, and the second is placed at one diameter from the end of the swirler. The pressure spectrum for the first point exhibits a clear peak at 1280 Hz that matches very well with the one found for the global heat release. For the second point, the same peak can be observed, but it is not so marked because of the overall pressure fluctuation within the flame tube. Figure B.12 shows an iso-surface of pressure (in blue) that represents the PVC. Different instants are depicted for

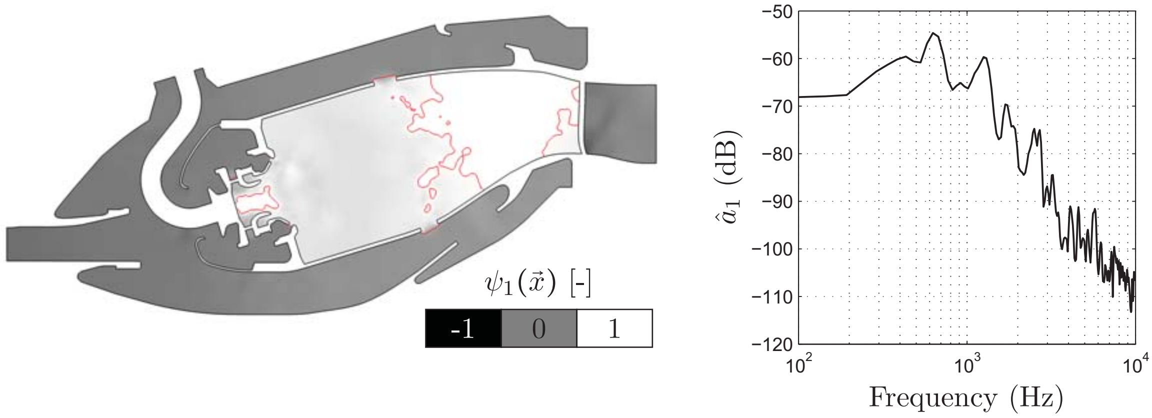
(a) POD-1 (b)

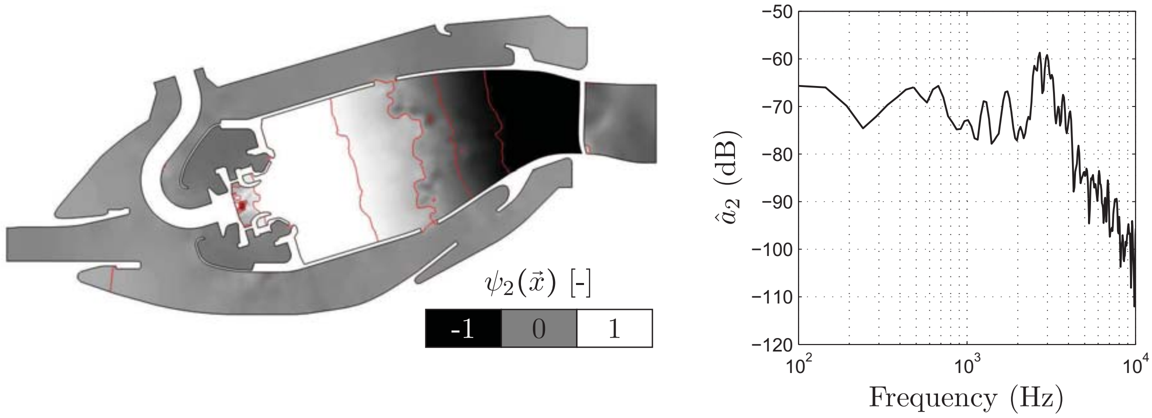
(c) POD-2 (d)

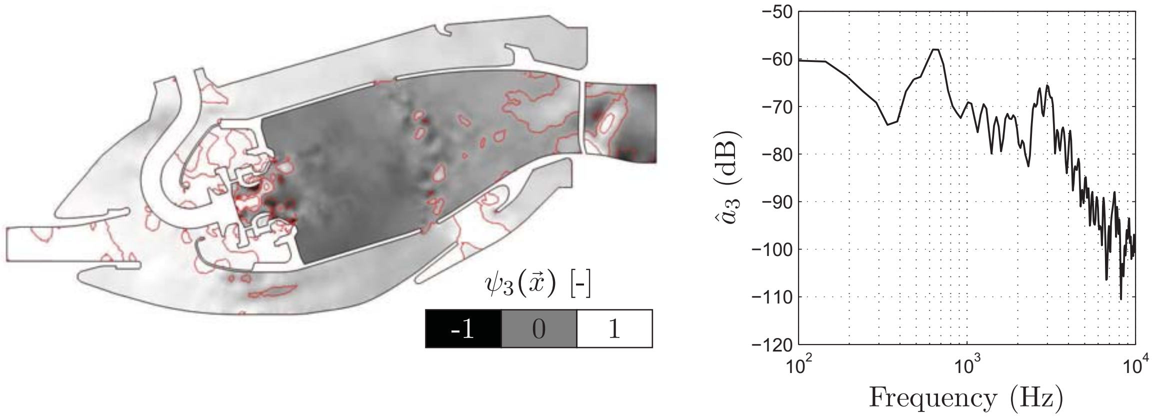
(e) POD-3 (f)

Figure B.8 - *(a, c, e) POD eigenfunctions $\psi_m(\vec{x})$ of the pressure fluctuations. (b, d, f) spectra of the temporal eigenvectors associated to the POD modes.*

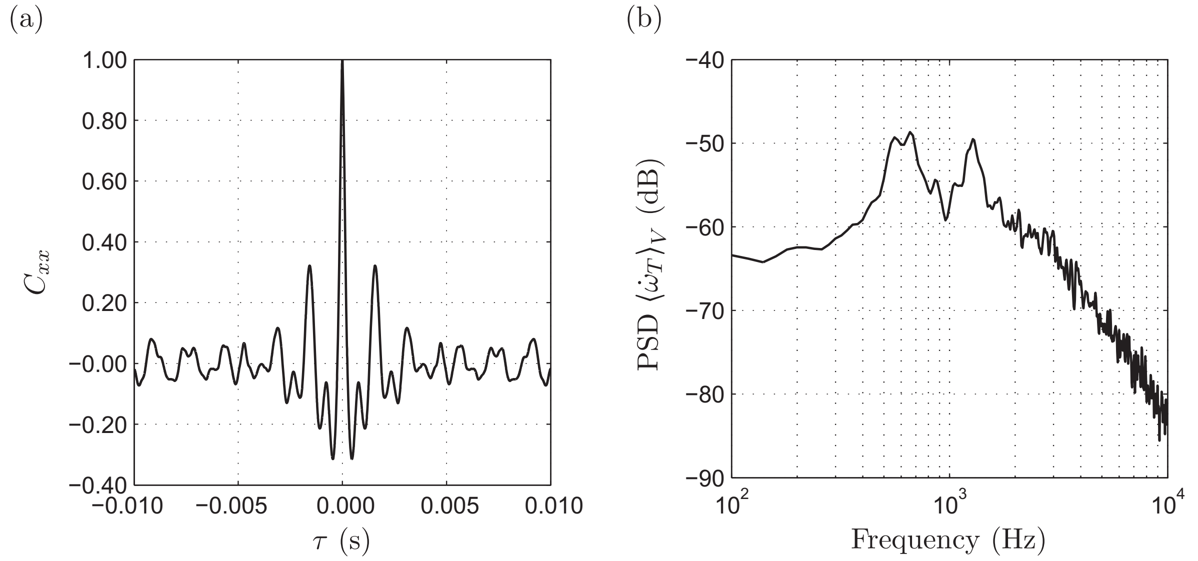

Figure B.9 - *(a) Auto-correlation C_{xx} function of $\langle\dot{\omega}_T\rangle_V(t)$. (b) Spectrum of the global heat release rate $\langle\dot{\omega}_T\rangle_V$.*

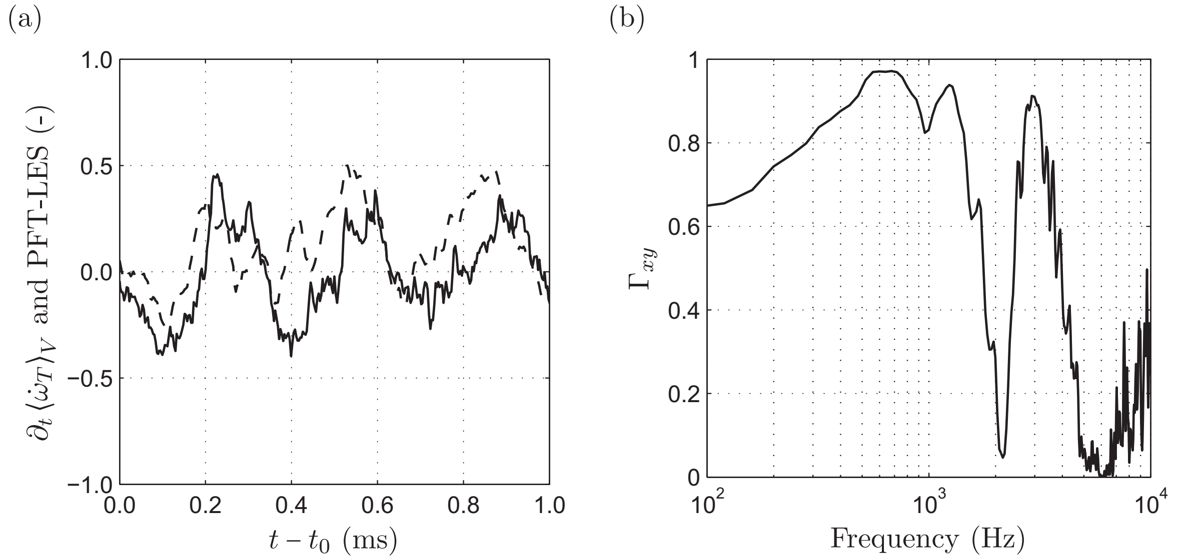

Figure B.10 - *(a) Temporal evolution of the global heat release rate derivative $\partial_t\langle\dot{\omega}_T\rangle_V$ (—) and the LES pressure fluctuation within the flame tube PTF (– – –). (b) Coherence function Γ_{xy} of $\langle\dot{\omega}_T\rangle_V$ and the pressure fluctuation PTF.*

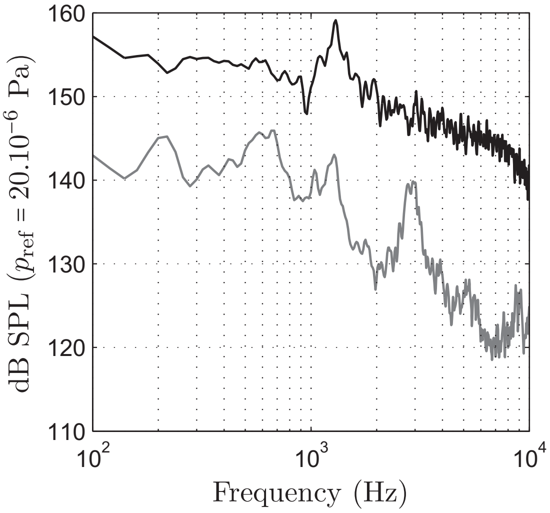

Figure B.11 - *Spectra of pressure fluctuations for two probes placed on the axis of the swirler. Probe placed at the beginning of the swirler (—), and at one diameter from the end of the swirler (—).*

one period of the main frequency (1280 Hz) and the rotation the vortex core is clearly seen. One can observe that the PVC generates ring vortices (seen $t^\star = 0.9$), that can interact with the flame. This interaction does not appear clearly on the iso-surface of the local heat release which is also depicted in Figure B.12 (in red). In order to get more information concerning the flame dynamics, a POD of the local heat release has been performed. The associated inner product $(\cdot,\cdot)$ is here simply written as $[q_k = (\ \dot{\omega}'_T\ )]$:

$$(q_i, q_j) = \int_V \dot{\omega}'_{T,i}(\vec{x})\dot{\omega}'_{T,j}(\vec{x})dV \tag{B.14}$$

The eigenvalues of this decomposition are plotted in Fig. B.13. The eigenfunctions corresponding to the three modes containing the most of energy are depicted in Fig. B.14, where one can see iso-surfaces of positive and negative values of the eigenfunctions (a,c,e). The shape of these surfaces is very close the vortices generates by the swirler (see Fig. B.12 for $t^\star = 0.9$). Moreover, the Fourier-transforms of the corresponding temporal eigenvector (Fig. B.14-b-d-f) support the explanation stating that the flame is excited by the PVC, since the same frequency stands out (1280 Hz). The spectra of the three first modes show that the heat release is also driven by the sub-harmonic frequency of the PVC (640 Hz).

To end up with the comparison between the LES and the actual combustor, one can say that the agreement on pressure fluctuations magnitudes is correct, but that the spectra are different because of the restriction to computation of only one burner.

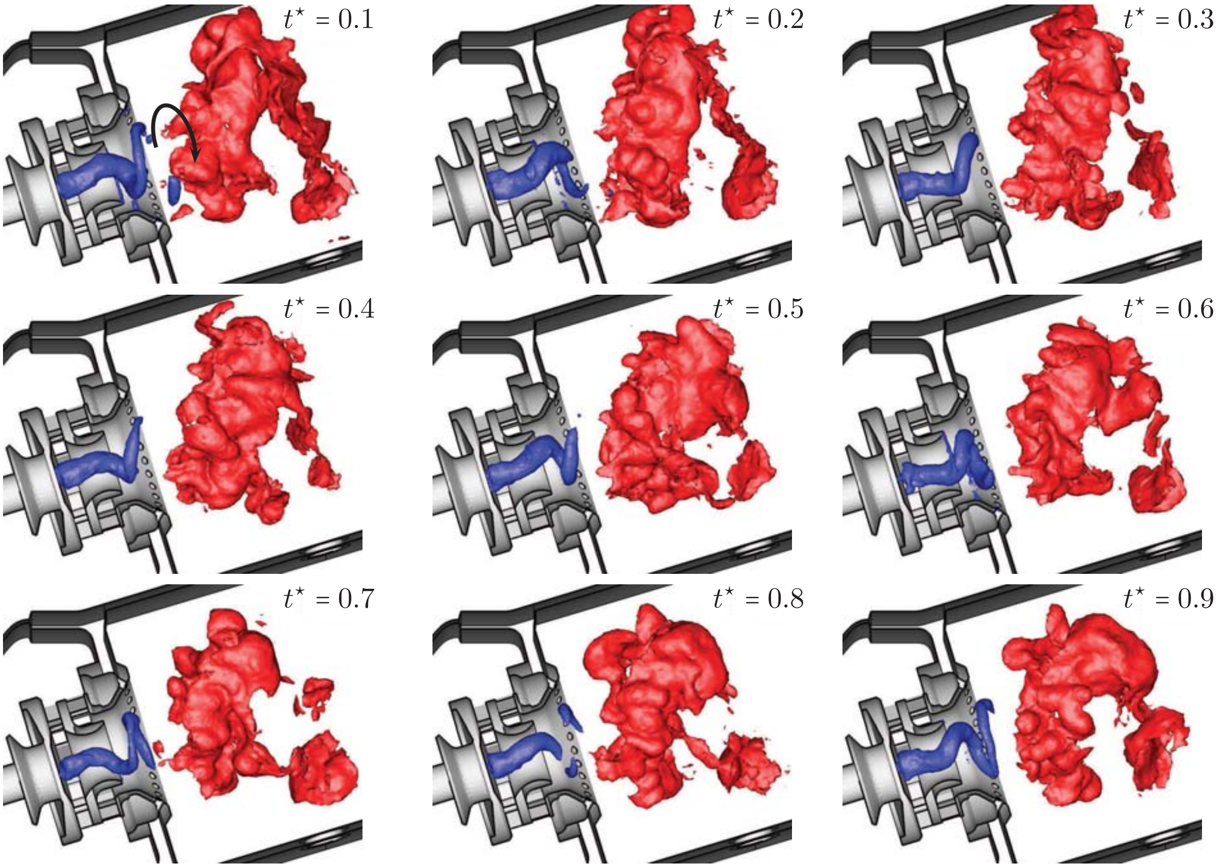

Figure B.12 - *Instantaneous fields of iso-surface of pressure (in blue) and of the heat release rate (in red). The dimensionless time* $t^\star$ *is based on the period of the PVC frequency (1280 Hz).*

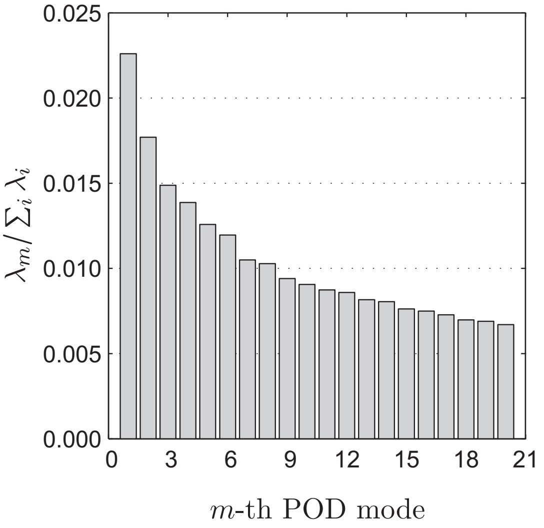

Figure B.13 - *The twentieth firsts POD modes eigenvalues for the heat release* $\dot{\omega}_T$ *sorted by decreasing eigenvalues* λ_m.

(a) POD-1 (b)

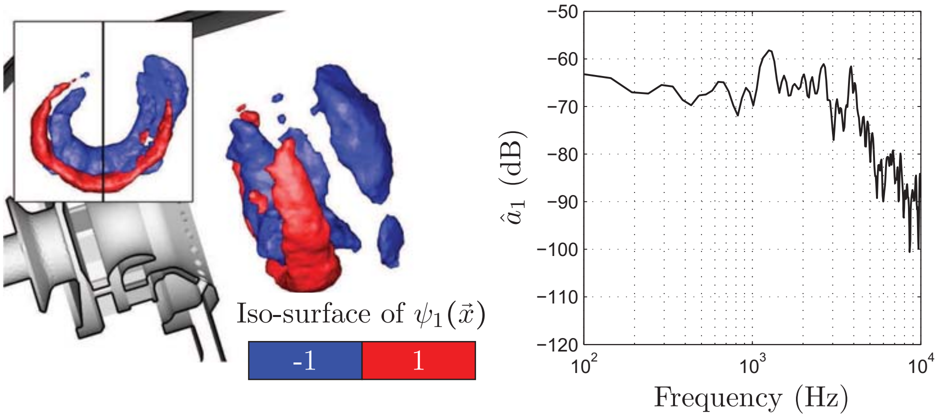

(c) POD-2 (d)

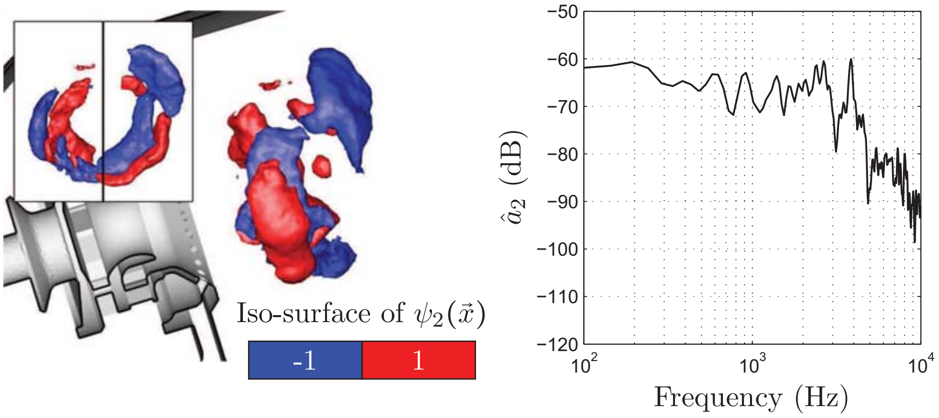

(e) POD-3 (f)

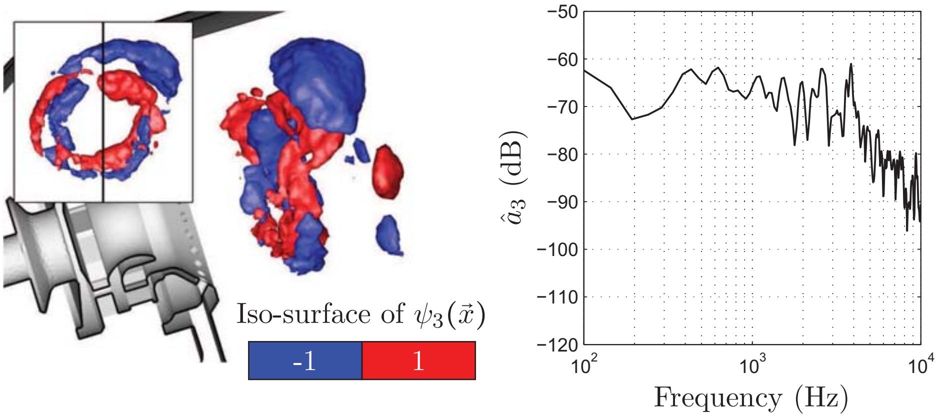

Figure B.14 - *(a, c, e) iso-surface of POD eigenfunctions $\psi_m(\vec{x})$ of the heat release fluctuations. (b, d, f) spectra of the temporal eigenvectors associated to the POD modes.*

Appendix C

Cumpsty and Marble model error estimation

This appendix aims to evaluate the error that is made on the outgoing noise when the model is used with *realistic* input spectra. The acoustic and entropy waves are used to calculate the acoustics at the outlet the stator investigated in Chap. 9. The analytical transfer functions and the simulated ones obtained in Chap. 9 are both used with the waves computed in Sec. 12.2. Only the longitudinal waves are investigated since the case $m > 0$ has not been studied numerically. Results of Chap. 9 shows that the entropy noise efficiency decreases rapidly for high frequencies. Nevertheless, the entropy has been identified in Sec. 12.2 to be a mainly low-frequency perturbation. The overall error done on the calculation of the indirect noise with the model is here calculated to show that the former provide good first-order estimation. The direct and indirect noise calculated with the transfer functions of the numerical simulations and with the model are plotted in Fig. C.1. The spectra are defined using the following relationships:

$$w_2^+ = \underbrace{\underbrace{\left[\frac{w_2^+}{w_1^S}\right]}_{\text{numeric or model}} \underbrace{w_{1,\mathrm{LES}}^S}_{\text{numeric}}}_{\text{fully-numeric or semi-numeric}} \qquad \text{for entropy} \tag{C.1}$$

$$w_2^+ = \underbrace{\underbrace{\left[\frac{w_2^+}{w_1^+}\right]}_{\text{numeric or model}} \underbrace{w_{1,\mathrm{LES}}^+}_{\text{numeric}}}_{\text{fully-numeric or semi-numeric}} \qquad \text{for acoustics} \tag{C.2}$$

Figure. C.1 shows that the model overestimates indirect noise at high-frequencies whereas it handles very well the direct one. The overall error is calculated using the overall acoustic power from Eq. (12.8). The error made on indirect noise is about 2 dB and 0.6 dB for the direct one (see Table C.1). Assuming that the numerical results are correct, the model of Cumpsty and Marble provides a very good first-order approximation of the overall noise coming from the

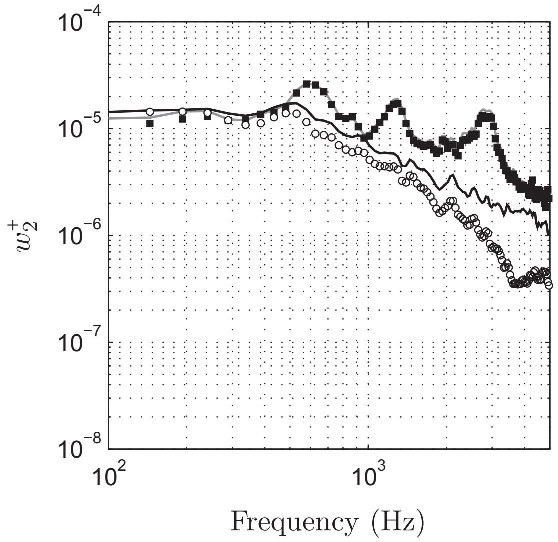

Figure C.1 - *Spectra of the acoustic waves downstream from the first turbine nozzle* w_2^+. *Outgoing waves from the LES used with theoretical (solid lines) and with numerical (symbols) transfer functions for the nozzle of Chap.* 9. *Acoustic wave caused by the entropy (○ and —), and the acoustics (■ and —).*

Source	Error (in dB)
Entropy	2.0
Acoustics	0.6

Table C.1 - *Error done on the overall acoustic power at the turbine outlet when using the model of Cumpsty and Marble [37] with LES input spectra.*

combustor in this case.

Appendix D

Articles

- *Comparison of Direct and Indirect Combustion Noise Mechanisms in a Model Combustor* published in *AIAA Journal* in 2009 (presented in Chap. 7).
- *Numerical and analytical investigation of the indirect combustion noise in a nozzle* published in *C.R. Mecanique* in 2009 (presented in Chap. 8). Study initially performed during the summer program of 2008 at the *Center for Turbulence Research* (Stanford University).
- *Numerical and analytical modelling of entropy noise in a supersonic nozzle with a shock* submitted in *Journal of Sound and Vibration* (presented in Chap. 8). Article extending the study published in *C.R. Mecanique.*
- *Assessment of combustion noise in a premixed swirled combustor via Large-eddy simulation* submitted for a special issue in *Computers and Fluids* in 2010 (co-author).

AIAA JOURNAL
Vol. 47, No. 11, November 2009

Comparison of Direct and Indirect Combustion Noise Mechanisms in a Model Combustor

M. Leyko*
Snecma Groupe SAFRAN, 77550 Moissy-Cramayel, France
F. Nicoud†
Université Montpellier II, 34095 Montpellier, France
and
T. Poinsot‡
Institut de Mécanique des Fluides de Toulouse, 31400 Toulouse, France

DOI: 10.2514/1.43729

Core noise in aeroengines is due to two main mechanisms: direct combustion noise, which is generated by the unsteady expansion of burning gases, and indirect combustion noise, which is due to the acceleration of entropy waves (temperature fluctuations generated by unsteady combustion) within the turbine stages. This paper shows how a simple burner model (a flame in a combustion chamber terminated by a nozzle) can be used to scale direct and indirect noise. An analytical formulation is used for waves generated by combustion. The transmission and generation of waves through the nozzle is calculated using both the analytical results of Marble and Candel (Marble, F. E., and Candel, S., "Acoustic Disturbances from Gas Nonuniformities Convected Through a Nozzle," ***Journal of Sound and Vibration*****, Vol. 55, 1977, pp. 225–243.) and a numerical tool. Numerical results for the nozzle verify and extend the analytical approach. The analytical relations for the combustion and the nozzle provide simple scaling laws for direct and indirect noise ratio as a function of the Mach number in the combustion chamber and at the nozzle outlet.**

Nomenclature

$\mathcal{A}$ = nozzle cross-sectional area, m^2
$\mathcal{A}_c$ = throat nozzle cross-sectional area, m^2
$\mathcal{A}_f$ = combustor cross-sectional area, m^2
c = speed of sound, m/s
c_p = massic heat capacity at constant pressure, J/K/kg
c_v = massic heat capacity at constant volume, J/K/kg
ℓ_f = flame length, m
ℓ_n = nozzle length, m
$\mathcal{M}$ = Mach number
$\dot{m}$ = mass flow rate, kg/s
PW$\{\phi\}$ = spectral power density of ϕ computed with Welch's method
p = thermodynamic pressure, Pa
$\dot{Q}$ = heat release rate, W
$\dot{q}$ = heat release rate per volume unit, W/m^3
r = massic ideal gas constant, J/K/kg
s = massic entropy, J/K/kg
T = temperature, K
t = time, s
u = gas velocity, m/s
w^S = dimensionless entropy wave
w^+ = dimensionless acoustic wave propagating downstream
w^- = dimensionless acoustic wave propagating upstream
x = x-axis value, m
y = y-axis value, m
z = z-axis value, m
γ = specific heat capacities ratio
δ = Dirac distribution
η = ratio between indirect and direct noise
ρ = mass density, kg/m^3
$\bar{\phi}$ = temporal mean value of ϕ
ϕ' = temporal fluctuation value of ϕ
Ω = reduced angular pulsation
ω = angular pulsation, rad/s

Subscripts

[AA] = acoustic response of the nozzle to an acoustic perturbation
[CC] = response of the combustion chamber to a heat release fluctuation
[SA] = acoustic response of the nozzle to an entropy perturbation
ϕ_t = total quantity of ϕ
ϕ_0 = quantity ϕ upstream from the combustor
ϕ_1 = quantity ϕ downstream from the combustor and upstream from the nozzle
ϕ_2 = quantity ϕ downstream from the nozzle

I. Introduction

OVER the last five decades, jet and external aerodynamic noises of aircraft have been substantially reduced. Further developments will be needed for modern aircraft design in order to meet the increasingly restrictive rules about noise reduction. Although drastic reductions have already been achieved on fan and jet noise, the relative importance of other noise sources has increased and the contribution of these sources must be controlled if further global noise reduction is to be achieved. Among these sources, the noise created by the turbulent flame within the combustor is already identified as nonnegligible at takeoff, especially in the midfrequency range. Two main mechanisms have been identified in the 1970s regarding noise propagation and generation from the combustion chamber to the far field (Fig. 1):

Received 10 February 2009; revision received 3 July 2009; accepted for publication 4 July 2009.

*Ph.D. Student, Centre Européen de Recherche et de Formation Avancée en Calcul Scientifique, 31057 Toulouse, France; leyko@cerfacs.fr.

†Professor.

‡Research Director, Associate Fellow AIAA.

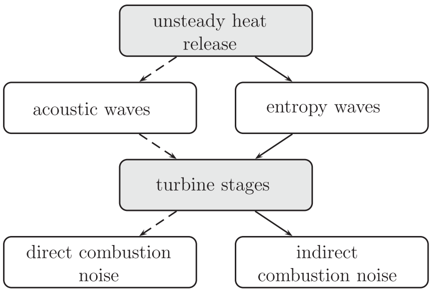

Fig. 1 The two main mechanisms for noise generation from confined flames: direct (dashed line) and indirect (solid line) noise.

1) With direct combustion noise, acoustic perturbations generated by the unsteady heat release from the turbulent flame propagate either upstream or downstream through the turbomachinery stages, where they are distorted by the mean flow, diffracted, and reflected by the solid walls within the diffuser, the distributor, and the turbine and compressor blades.

2) With indirect combustion noise, entropy fluctuations generated within the combustion chambers (hot spots, imperfect mixing, etc.) propagate downstream and interact with accelerating mean flow. The kinematic and thermodynamic variables are strongly coupled when the flow is compressible. Therefore, when there is a sharp variation of the mean flow (turbine stages), mass density fluctuations generate perturbations of the other flow variables. Subsequent acoustic waves are generated and transmitted to the far field through the turbine stages.

Direct combustion noise is typically the main source of noise of a free flame. The acoustic radiation due to a turbulent flame has been theoretically treated by Bragg [1], Strahle [2], Hassan [3], and others. More recently, Ihme et al. [4] successfully computed the sound emitted from a turbulent diffusion flame by combining a large eddy simulation and a computational aeroacoustic method, providing precious information about the combustion-generated noise. The experimental and theoretical work of Candel et al. [5,6] about the noise generated by unsteady laminar flames, as well as the developments of Crighton et al. [7] and the experimental investigations of Rajaram and Lieuwen [8,9] and Lieuwen et al. [10] about combustion-generated noise of turbulent flames, are also an important source of information for direct noise comprehension. However, several studies performed in this field concern the flame acoustic radiation toward the free far field, and in the case of confined systems like aeroengines, another source of noise appears to be relevant: the entropy noise. Indeed, following the work of Tsien [11] and Crocco [12] about nozzles, Candel [13] concludes that entropy spots, inherent to the unsteady combustion process, can represent an important source of noise when considering gas expansion through the engine turbine stages. Candel considers a relative temperature fluctuation of 5% and calculates a corresponding sound pressure level at the nozzle exhaust of about 120 dB. Marble [14] and Marble and Candel [15] obtain solutions for planar waves within compact nozzles and within finite-length nozzles with assumed linear axial-velocity evolution. In the same period, Ffowcs Williams and Howe [16] propose an extended theory for general entropy spots in low Mach number nozzle flows. Stow et al. [17] show that for an annular duct with a nozzle, the relations found by Marble and Candel [15] for compact nozzles apply to the first order even when circumferential modes are present. The compact interactions idea of Marble and Candel was extended to cylindrical 2-D flows by Cumpsty and Marble [18] and applied to commercial aeroengines [19]. Considering that the principal noise mechanism is the indirect one, Cumpsty and Marble presume the relative temperature fluctuation amplitude and spectrum and obtain quite good results for low jet velocities: the so-called excess noise. But Cumpsty and Marble agree to say that although the agreement of the measurements and predictions strongly supports that the indirect noise mechanism is the major core noise generation process, this conclusion is not definitive until a clear separation of the different effects is performed. Starting from the heat release fluctuation, they provide the main ideas to do this analytically, and they briefly comment on the expected results. The aim of the present paper is precisely to develop this work but in a purely one-dimensional (1-D) case.

It should be mentioned that Muthukrishnan et al. [20] experimentally investigated the core noise sources separation and also concluded that for choked nozzles, entropy noise seems to be the main core noise source. More recently, Bake et al. [21–24] worked on the subject, but the separation of direct and indirect combustion noise in a real case is still difficult to evaluate. On one hand, entropy fluctuations are controlled by complicated aerodynamical, thermal, and chemical phenomena. Turbulent mixing and diffusion can also strongly affect entropy wave amplitudes at the nozzle inlet, generally speaking. On the other hand, the acoustic cavity modes of the chamber can also significantly change the acoustic levels [25,26].

In the present study, only the most significant parameters are considered in order to establish simple analytical scaling laws for direct and indirect noise in aeroengines. To compare direct and indirect combustion noise, entropy and acoustic waves will be assumed to be directly linked to heat release fluctuations, and a very simple case of generic combustor is considered: a combustion chamber followed by a nozzle (Fig. 2). The combustion chamber and the turbine stages will be represented by a quasi-1-D system. The combustion zone will be modeled by an infinitely thin heat release fluctuation in a constant section duct (generating acoustic and entropy waves) connected to a quasi-1-D nozzle representing the turbine stages (for the transmission and generation of acoustic waves). These two elements are handled individually, as shown in Fig. 3, and the feedback on the flame of the acoustic waves traveling upward is not taken into account. Thus, the separation between direct and indirect noise is simple to perform because the global system is assumed to be linear. The combustion chamber creates the acoustic and entropy waves feeding the nozzle. The nozzle then generates the outgoing direct or indirect noise depending on the nature of the incoming waves (acoustic or entropy, respectively).

The waves generated by the combustion zone are calculated analytically, considering an isolated heat release fluctuation. This model provides explicitly acoustic and entropy waves for the second

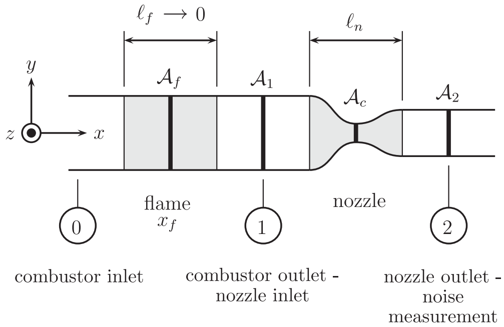

Fig. 2 A generic model to evaluate direct and indirect combustion noise.

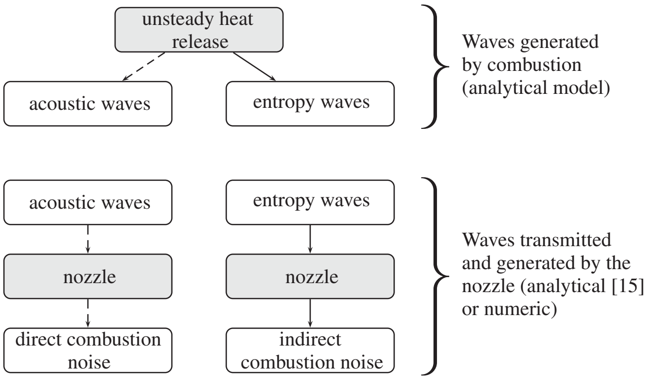

Fig. 3 Strategy for the calculation of the ratio between direct (dashed line) and indirect (solid line) noise.

part of the calculations: the transmission and generation of acoustic waves through the nozzle. The calculation of the transmission of acoustic waves through the nozzle (direct mechanism) and of the generation of acoustic waves from entropy waves within the nozzle (indirect mechanism) is performed both analytically using the results of Marble and Candel [15] for compact nozzles and numerically by solving the Euler equations in the time domain for a 2-D nozzle with a quasi-1-D behavior. The present method thus leads to two main approaches for the calculation of the indirect-to-direct noise ratio: a fully analytical method and a semi-analytical method. In both cases, the calculations of the waves due to combustion and the calculations of the wave transmission and generation through the nozzle are independent.

The analytical calculations of acoustic and entropy waves generated by combustion will be first reviewed in Sec. II. The acoustic wave transmission and generation by the nozzle, obtained analytically and numerically, are then presented in Sec. III. Finally, the ratio between direct and indirect noise is presented in Sec. IV.

II. Acoustic and Entropy Wave Generation in the Combustion Chamber

A subsonic flow is assumed in the combustion region. Viscous and three-dimensional (3-D) effects are neglected and a 1-D heat release region is assumed to represent the combustion zone. The flow is defined with the mass density ρ, the velocity u, and the heat release $\dot{Q}(t)$. The flame length ℓ_f is assumed to be small compared with the acoustic and entropy wavelengths, so that the heat release per unit volume $\dot{q}$ can be expressed as

$$\dot{q}(x,y,z,t) = \delta(x - x_f)\dot{Q}(t)/\mathcal{A}_f \tag{1}$$

where δ is the Dirac distribution and $\mathcal{A}_f$ is the cross-sectional area of the combustion chamber. The heat release $\dot{Q}(t)$ results from the following space integration of $\dot{q}(x,y,z,t)$:

$$\dot{Q}(t) = \iiint_{-\infty}^{+\infty} \dot{q}(x,y,z,t)\,\mathrm{d}x\,\mathrm{d}y\,\mathrm{d}z \tag{2}$$

The steady heat release of the flame model is considered negligible (cold flame) so that the mean flow is assumed isentropic. The cold flame assumption has been used by many authors to obtain analytical scaling regarding thermoacoustic instabilities [27], but it can have a nonnegligible effect as shown by Dowling [28], which is ignored here. The flow is characterized by the mass flow $\dot{m}$, the total enthalpy h_t, and the entropy s. The mass flow $\dot{m}$ and the entropy s can be written as follows:

$$\dot{m} = \rho u \mathcal{A} \tag{3}$$

$$s = c_v \ln\left(\frac{p}{\rho^\gamma}\right) \tag{4}$$

or for small temporal perturbations,

$$\frac{\dot{m}'}{\bar{\dot{m}}} = \frac{1}{\bar{\mathcal{M}}}\frac{u'}{\bar{c}} + \frac{p'}{\gamma\bar{p}} - \frac{s'}{c_p} \tag{5}$$

and

$$\frac{s'}{c_p} = \frac{p'}{\gamma\bar{p}} - \frac{\rho'}{\bar{\rho}} \tag{6}$$

Heat capacities and the composition of the gas are assumed to be constant, so that the total enthalpy is defined by $h_t = c_p T_t$, where T_t is the total temperature:

$$T_t = T\left(1 + \frac{\gamma - 1}{2}\mathcal{M}^2\right) \tag{7}$$

The fluctuation of the Mach number $\mathcal{M}$ is:

$$\frac{\mathcal{M}'}{\bar{\mathcal{M}}} = \frac{1}{\bar{\mathcal{M}}}\frac{u'}{\bar{c}} - \frac{\gamma - 1}{2}\frac{p'}{\gamma\bar{p}} - \frac{1}{2}\frac{s'}{c_p} \tag{8}$$

The fluctuations of total temperature as a function of velocity, pressure, and entropy perturbations can be written using Eqs. (6) and (8), and the state equation for small perturbations:

$$\frac{T_t'}{\bar{T}_t} = \frac{1}{1 + [(\gamma - 1)/2]\bar{\mathcal{M}}^2}\left[(\gamma - 1)\bar{\mathcal{M}}\frac{u'}{\bar{c}} + (\gamma - 1)\frac{p'}{\gamma\bar{p}} + \frac{s'}{c_p}\right] \tag{9}$$

To scale direct and indirect combustion noise, the dimensionless acoustic waves (w^+ and w^-) and the entropy wave (w^S) created by the compact flame of the combustion chamber must be assessed. These waves are defined as follows:

$$w^+ = \frac{p'}{\gamma\bar{p}} + \frac{u'}{\bar{c}} \tag{10}$$

$$w^- = \frac{p'}{\gamma\bar{p}} - \frac{u'}{\bar{c}} \tag{11}$$

$$w^S = \frac{p'}{\gamma\bar{p}} - \frac{\rho'}{\bar{\rho}} \tag{12}$$

The wave w^+ is related to the propagation speed $u + c$, whereas the wave w^- is related to the propagation speed $u - c$. The wave w^S propagates at the convective speed u and transports entropy.

Considering the heat release $\dot{Q}$ through the heating region according to Fig. 4, the balance equations of mass flow, total enthalpy, and entropy at the flame front yield

$$(\dot{m})_0 = (\dot{m})_1 \tag{13}$$

$$(\dot{m}h_t)_0 + \dot{Q} = (\dot{m}h_t)_1 \tag{14}$$

$$(\dot{m}s)_0 + \frac{\dot{Q}}{T} = (\dot{m}s)_1 \tag{15}$$

where the subscripts 0 and 1 correspond, respectively, to the quantities upstream and downstream from the flame. The mean heat release is zero, so that the mean temperature $\bar{T}$, Mach number $\bar{\mathcal{M}}$, total temperature $\bar{T}_t$, and entropy $\bar{s}$ do not change through the flame model. For small temporal perturbations, using the mass flow balance equation (13), the entropy balance equation (15) leads to

$$\left(\frac{s'}{c_p}\right)_0 + \frac{\dot{Q}'}{\bar{\dot{m}}c_p\bar{T}} = \left(\frac{s'}{c_p}\right)_1 \tag{16}$$

Equation (14) can be modified in the same way; using the expression of the fluctuations of the total temperature in Eq. (9), the total enthalpy balance equation (14) for small temporal perturbations leads to

$$\begin{aligned}(\gamma - 1)\bar{\mathcal{M}}\left(\frac{u'}{\bar{c}}\right)_0 + (\gamma - 1)\left(\frac{p'}{\gamma\bar{p}}\right)_0 + \left(\frac{s'}{c_p}\right)_0 + \frac{\dot{Q}'}{\bar{\dot{m}}c_p\bar{T}} \\ = (\gamma - 1)\bar{\mathcal{M}}\left(\frac{u'}{\bar{c}}\right)_1 + (\gamma - 1)\left(\frac{p'}{\gamma\bar{p}}\right)_1 + \left(\frac{s'}{c_p}\right)_1\end{aligned} \tag{17}$$

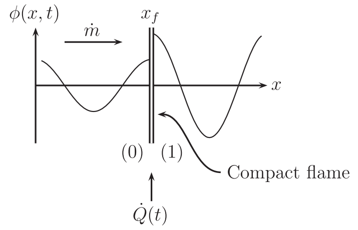

Fig. 4 Compact flame illustration regarding a quantity ϕ upstream (0) and downstream (1) from the heating region.

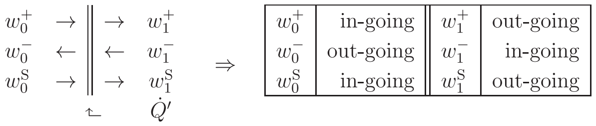

w_0^+	in-going	w_1^+	out-going
w_0^-	out-going	w_1^-	in-going
w_0^S	in-going	w_1^S	out-going

Fig. 5 Incoming and outgoing waves for the compact flame.

The heat release is supposed to be known, and the three incoming waves have to be imposed in order to obtain the outgoing waves w_1^+, w_1^S, and w_0^- using the three balance equations (13–15) as a function of the heat release (Fig. 5) . Except for the heat release, the combustor is assumed to be isolated; that is to say, the incoming acoustic waves w_0^+ and w_1^- are equal to zero as well as the incoming entropy wave w_0^S. Considering the last assumption $w_0^S = 0$ and using Eq. (16), the outgoing entropy w_1^S can be expressed as

$$w_1^S = \frac{\dot{Q}'}{\bar{\dot{m}} c_p \bar{T}} \tag{18}$$

The fluctuation of the mass flow equation (5) can be written at the upstream (0) and downstream (1) from the flame and expressed as a function of waves instead of the fluctuations of velocity, pressure, and entropy. Then, Eq. (17) (related to the fluctuations of total enthalpy) can also be written as a function of waves. Using Eq. (18) and the assumption that the flame is isolated ($w_0^+ = 0$, $w_1^- = 0$, and $w_0^S = 0$), one can show that the expression of the outgoing acoustic wave w_1^+ generated by the heat release fluctuation is

$$w_1^+ = \frac{\bar{\mathcal{M}}}{1 + \bar{\mathcal{M}}} \frac{\dot{Q}'}{\bar{\dot{m}} c_p \bar{T}} \tag{19}$$

Finally, Eqs. (18) and (19) lead to the ratio between the acoustic wave w_1^+ and the entropy wave w_1^S generated by the combustion zone and propagating downstream of the combustion chamber:

$$\frac{w_1^+}{w_1^S}[\mathrm{CC}] = \frac{\bar{\mathcal{M}}}{1 + \bar{\mathcal{M}}} \tag{20}$$

where [CC] refers to the waves produced in the combustion chamber. Equation (20) shows that, for a compact flame, the ratio between acoustic and entropy waves depends only on the Mach number in the flame zone $\bar{\mathcal{M}}$ and no more on the heat release fluctuations. This result allows study of the ratio between indirect and direct combustion noise mechanisms independently of the exact nature of heat release fluctuations, which are the sources of each mechanism.

III. Wave Transmission and Generation Through a Nozzle

The transmission and generation of acoustic and entropy waves through the nozzle are obtained using two different methods. The first one is based on the analytical development of Marble and Candel [15], assuming that the nozzle is compact (frequency is low). In their work, the authors assume a quasi-1-D nozzle flow and quasi-steady perturbations of mass flow, energy, and entropy leading to relations between the different waves that depend on the inlet and outlet Mach numbers. This approach is similar to the one used for the compact flame of Sec. II, and the relations between waves for the nozzle are reviewed in the first part of this section. The second method to obtain the acoustic response of the nozzle is based on a numerical simulation of the quasi-1-D nozzle flow by solving the Euler equations [29]. This second method is valid for all frequencies as long as the waves remain 1-D, and it will be used here to evaluate the compact nozzle assumption of the analytical approach in the low-frequency limit. The numerical approach is presented in the second part of this section.

A. Analytical Approach

Following the analysis of Marble and Candel [15], the flow is supposed to be 1-D. Similar to Sec. II, u stands for the axial velocity, ρ for the mass density, and $\mathcal{A}$ for the nozzle cross-sectional area. The mass flow $\dot{m}$ and the entropy s are defined by Eqs. (3) and (4). Assuming that the nozzle is isolated, the total enthalpy is conserved, and thus the total temperature also. Note that the total temperature T_t is, in this case, always conserved, even for a nonisentropic mean flow in the nozzle (which is to say, through a shock, for instance). The total temperature is defined by Eq. (7) and the expression of the fluctuations of total temperature entering the nozzle as a function of speed, pressure, and entropy perturbations is the same as in Sec. II [Eq. (9)]. Under the assumption of a compact nozzle [long wavelengths compared with the nozzle length ℓ_n (see Fig. 6)], there is no delay or distortion between the inlet and the outlet of the nozzle. As a result, mass flow, total temperature, and entropy are conserved through the nozzle. The quantities upstream and downstream from the nozzle are, respectively, subscripted 1 and 2. The conservation equations (5), (6), and (9) can be written as a system of equations which are functions only of the Mach numbers and the waves (acoustic and entropy) upstream and downstream of the nozzle. This system is composed of three equations involving six waves, thus the incoming waves have to be imposed. In the case of an unchoked nozzle, the flow is totally subsonic and the w_2^- wave is incoming so that waves w_1^+, w_1^S, and w_2^- can be imposed (Fig. 7). Finally, the system is composed of three equations and three unknown waves. Because the system is linear, mechanisms can be separated by setting $w_1^+ \neq 0$, $w_1^S = 0$, and $w_2^- = 0$ in a first step to study only the acoustic response of the nozzle to an acoustic perturbation. This case is called [AA]. It is also possible to set $w_1^+ = 0$, $w_1^S \neq 0$, and $w_2^- = 0$ in order to study the acoustic response of the nozzle to an entropy perturbation, and this case is called [SA]. Using Eqs. (5), (6), and (9) at the inlet and the outlet of the nozzle for the cases [AA] and [SA] gives

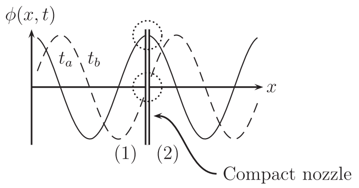

Fig. 6 Compact nozzle illustration. The quantity ϕ, conserved throughout the nozzle, is the same upstream (1) and downstream (2) at each instant.

$$\frac{w_2^+}{w_1^+}[\mathrm{AA}] = \frac{2\bar{\mathcal{M}}_2}{1 + \bar{\mathcal{M}}_2} \frac{1 + \bar{\mathcal{M}}_1}{\bar{\mathcal{M}}_1 + \bar{\mathcal{M}}_2} \frac{1 + [(1/2)(\gamma - 1)]\bar{\mathcal{M}}_2^2}{1 + [(1/2)(\gamma - 1)]\bar{\mathcal{M}}_1 \bar{\mathcal{M}}_2} \tag{21}$$

$$\frac{w_2^+}{w_1^S}[\mathrm{SA}] = \frac{\bar{\mathcal{M}}_2 - \bar{\mathcal{M}}_1}{1 + \bar{\mathcal{M}}_2} \frac{(1/2)\bar{\mathcal{M}}_2}{1 + [(1/2)(\gamma - 1)]\bar{\mathcal{M}}_1 \bar{\mathcal{M}}_2} \tag{22}$$

In the case of an isentropic choked nozzle, the flow is subsonic in the convergent part of the nozzle and totally supersonic in the divergent part, and wave w_2^- cannot be imposed because it is outgoing (Fig. 8). In the case of an isentropic choked nozzle, only two waves can be imposed so that the system is composed of four unknown waves for three equations only. The missing equation is obtained by stating that the flow at the nozzle throat is sonic so that the relation between the Mach number $\mathcal{M}$ and the cross-sectional area ratio can be written as follows:

$$\frac{\mathcal{A}}{\mathcal{A}_c} = \frac{1}{\mathcal{M}} \left[\frac{2}{\gamma + 1} \left(1 + \frac{\gamma - 1}{2} \mathcal{M}^2 \right) \right]^{(1/2)[(\gamma+1)/(\gamma-1)]} \tag{23}$$

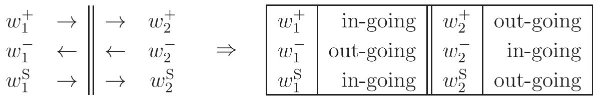

w_1^+	in-going	w_2^+	out-going
w_1^-	out-going	w_2^-	in-going
w_1^S	in-going	w_2^S	out-going

Fig. 7 Incoming and outgoing waves for the unchoked nozzle case.

$$\begin{array}{cc||cc} w_1^+ & \rightarrow & \rightarrow & w_2^+ \\ w_1^- & \leftarrow & \rightarrow & w_2^- \\ w_1^S & \rightarrow & \rightarrow & w_2^S \end{array} \quad \Rightarrow \quad \begin{array}{|c|r||c|c|}\hline w_1^+ & \text{in-going} & w_2^+ & \text{out-going} \\ w_1^- & \text{out-going} & w_2^- & \text{out-going} \\ w_1^S & \text{in-going} & w_2^S & \text{out-going} \\ \hline \end{array}$$

Fig. 8 Incoming and outgoing waves for the choked nozzle case.

where $\mathcal{A}_c$ is the cross-sectional area at the nozzle throat. One can easily show from Eq. (23) that for the choked nozzle case, the temporal fluctuation of the Mach number $\mathcal{M}'/\bar{\mathcal{M}}$ is zero. Then, using the expression of the fluctuation of the Mach equation (8),

$$\frac{1}{\bar{\mathcal{M}}}\frac{u'}{\bar{c}} - \frac{\gamma - 1}{2}\frac{p'}{\gamma\bar{p}} - \frac{1}{2}\frac{s'}{c_p} = 0 \tag{24}$$

The entropy s and the total temperature T_t are constant through the nozzle, so that the total pressure p_t is also constant. The total pressure can be expressed as follows:

$$p_t = p\left(1 + \frac{\gamma - 1}{2}\mathcal{M}^2\right)^{\gamma/(\gamma-1)} \tag{25}$$

The temporal fluctuation of total pressure of Eq. (25) can be written:

$$\frac{p_t'}{\bar{p}_t} = \frac{p'}{\bar{p}} + \frac{\gamma\bar{\mathcal{M}}^2}{1 + [(\gamma - 1)/2]\bar{\mathcal{M}}^2}\frac{\mathcal{M}'}{\bar{\mathcal{M}}} \tag{26}$$

and shows that the fluctuations $p'/(\gamma\bar{p})$ are the same on both sides of the nozzle because the Mach number fluctuation is zero:

$$\left(\frac{p'}{\gamma\bar{p}}\right)_1 = \left(\frac{p'}{\gamma\bar{p}}\right)_2 \tag{27}$$

Finally, Eqs. (6), (24), and (27) used at the inlet and outlet of the nozzle yield

$$\frac{w_2^+}{w_1^+}[\mathrm{AA}] = \frac{1 + [(1/2)(\gamma - 1)]\bar{\mathcal{M}}_2}{1 + [(1/2)(\gamma - 1)]\bar{\mathcal{M}}_1} \tag{28}$$

$$\frac{w_2^+}{w_1^S}[\mathrm{SA}] = \frac{(1/2)(\bar{\mathcal{M}}_2 - \bar{\mathcal{M}}_1)}{1 + [(1/2)(\gamma - 1)]\bar{\mathcal{M}}_1} \tag{29}$$

The set of equations (21), (22), (28), and (29) provides analytical expressions for the outgoing waves w_2^+ as a function of the incoming waves w_1^+ and w_1^S and the mean inlet $\bar{\mathcal{M}}_1$ and outlet $\bar{\mathcal{M}}_2$ Mach numbers for the compact nozzle.

B. Numerical Approach

The previous analytical relations are based on the nozzle compactness assumption and are valid only for the low-frequency limit. To validate this assumption and extend the model for the nozzle to a larger range of frequencies, an unsteady simulation based on Euler equations of the flow within the nozzle has been performed. Acoustic and entropy perturbations are generated at the inlet of the computational domain in a simple 1-D isentropic nozzle flow, and outgoing noise is directly measured in the simulation.

1. Numerical Method

The numerical tool used to solve the flow within the nozzle is the AVBP [30,31] code. AVBP is a finite volume cell-vertex code that can solve 3-D compressible Navier–Stokes equations on unstructured meshes, but it is used here on a 2-D regular mesh without viscous terms. The mesh is two-dimensional (2-D) [476×5 with 320 nodes in the nozzle (see Fig. 9)] and the evolution of the transversal coordinate is small enough to assume that the flow in the nozzle is quasi-1-D. There are about 320 nodes in the axial direction of the nozzle. The numerical computations have been performed with the Lax–Wendroff scheme, which is second-order accurate in both space and time, with a Courant–Friedrichs–Lewy number of 0.5. Preliminary tests performed with the same solver on acoustic and entropy wave propagation were used to verify that the results were independent of the mesh and that dispersion and dissipation errors were very small.

2. Nozzle Geometry and Flow Parameters

Because an inviscid 1-D and compressible flow is also considered in the simulation, the mean Mach numbers $\bar{\mathcal{M}}_1$ and $\bar{\mathcal{M}}_2$ only depend on the cross-sectional area ratio $\mathcal{A}_1/\mathcal{A}_2$ for the unchoked nozzle case, and on the cross-sectional area ratios $\mathcal{A}_1/\mathcal{A}_c$ and $\mathcal{A}_2/\mathcal{A}_c$ for the isentropic choked nozzle case [see Eq. (23)]. For the choked nozzle case, the nozzle is convergent and divergent, whereas it is simply convergent for the unchoked nozzle case. To calculate the section area ratio $\mathcal{A}_1/\mathcal{A}_2$ for the unchoked case, the following relation is used:

$$\frac{\mathcal{A}_1}{\mathcal{A}_2} = \frac{\bar{\mathcal{M}}_2}{\bar{\mathcal{M}}_1}\left[\frac{1 + [(\gamma - 1)/2]\bar{\mathcal{M}}_1^2}{1 + [(\gamma - 1)/2]\bar{\mathcal{M}}_2^2}\right]^{[(1/2)(\gamma+1)/(\gamma-1)]} \tag{30}$$

The different values of cross-sectional area ratios used in the present work are presented in Table 1 as a function of inlet Mach number $\bar{\mathcal{M}}_1$ and outlet Mach number $\bar{\mathcal{M}}_2$ for a specific heat capacities ratio γ of 1.32. The static pressure and temperature are imposed at the inlet of the nozzle ($p_1 = 800.0$ kPa, $T_1 = 1300$ K) and are the same for all cases. The static pressure p_2 is also imposed at the outlet and is chosen to obtain an isentropic flow and thus the correct target Mach numbers.

3. Numerical Boundary Conditions and Computations

Like in the analytical approach, the acoustic response of the nozzle at the outlet is computed for a case in which the incoming waves pulsed at the nozzle inlet are entropy (case [SA]) and for a case in which the waves are acoustic (case [AA]). In this numerical computation, totally nonreflecting boundary conditions are imposed (w_1^+ independent of w_1^- at the nozzle inlet and $w_2^- = 0$ for the subsonic nozzle outlet case) and the desired incoming perturbation added [31,32]. The incoming waves at the nozzle inlet are imposed as follows:

$$\begin{cases} w_1^S(t) = n(t) \\ w_1^+(t) = 0 \end{cases}$$

for the case [SA] and

$$\begin{cases} w_1^S(t) = 0 \\ w_1^+(t) = n(t) \end{cases}$$

for the case [AA], where $n(t)$ is a filtered white noise signal. The perturbations $n(t)$ are small enough to neglect nonlinear effects. As a result, one single computation with a filtered white noise signal imposed at the inlet can be performed to obtain the acoustic response of the nozzle to a large range of frequencies. The cutoff frequency of the filtered white noise signal and the size of the biggest cell are chosen in order to solve the smallest wavelength over 20 nodes in the most unfavorable case, that is to say, when the entropy waves are pulsed and when the Mach numbers are small. The smallest acoustic wave length taken into account here is of the order of half the nozzle length (this corresponds to about one-sixteenth of the nozzle length for the entropy wave in the most unfavorable case). However, to avoid border effects in the frequency domain due to the low-pass filter and to have a better numerical precision in the range of interest,

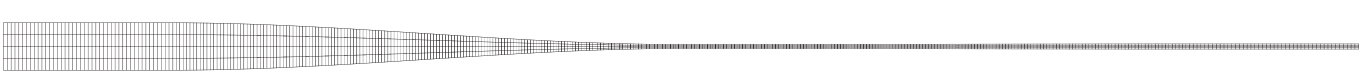

Fig. 9 Mesh of the nozzle corresponding to the case with $\mathcal{M}_1 = 0.050$ and $\mathcal{M}_2 = 1.600$.

Table 1 Geometric cross-sectional area ratio values for the different Mach number cases

	Unchoked cases		Choked cases	
	$\bar{\mathcal{M}}_2 = 0.400$	$\bar{\mathcal{M}}_2 = 0.800$	$\bar{\mathcal{M}}_2 = 1.200$	$\bar{\mathcal{M}}_2 = 1.600$
$\bar{\mathcal{M}}_1 = 0.025$				
$\mathcal{A}_1/\mathcal{A}_c$	14.604	22.482	23.365	23.365
$\mathcal{A}_2/\mathcal{A}_c$	1.000	1.000	1.032	1.267
$\bar{\mathcal{M}}_1 = 0.050$				
$\mathcal{A}_1/\mathcal{A}_c$	7.310	11.253	11.695	11.695
$\mathcal{A}_2/\mathcal{A}_c$	1.000	1.000	1.032	1.267
$\bar{\mathcal{M}}_1 = 0.100$				
$\mathcal{A}_1/\mathcal{A}_c$	3.671	5.651	5.873	5.873
$\mathcal{A}_2/\mathcal{A}_c$	1.000	1.000	1.032	1.267

the results presented in the next section are given for a reduced frequency range. The upper frequency limit of the presented results corresponds to a grid resolution of 50 nodes for the smallest entropy wavelength.

Temporal evolutions of the different waves are recorded at the nozzle inlet and outlet, and the Welch's method [33] is used to compute the spectral power density of the wave signals and thus establish the desired spectral transfer functions. A first computation (case [SA]) provides the transfer function:

$$\sqrt{\mathrm{PW}\{w_2^+\}/\mathrm{PW}\{w_1^S\}}$$

relevant of the indirect mechanism, whereas a second computation (case [AA]) provides the transfer function:

$$\sqrt{\mathrm{PW}\{w_2^+\}/\mathrm{PW}\{w_1^+\}}$$

relevant of the direct mechanism. These numerical transfer functions of the nozzle, in combination with the analytical results for waves generated by the combustion zone, are then used to calculate the semi-analytic indirect-to-direct ratio.

IV. Results

Results of Sec. II and III are used to calculate the ratio η between amplitude $w_{2,\mathrm{ind}}^+$ of the acoustic wave generated indirectly and the amplitude $w_{2,\mathrm{dir}}^+$ of the acoustic wave generated directly as described in Fig. 10. The acoustic wave $w_{2,\mathrm{ind}}^+$ generated by the indirect mechanism is expressed using the entropy wave $w_1^S[\mathrm{CC}]$ produced by the flame and the transfer function of the nozzle of the case [SA]. The acoustic wave $w_{2,\mathrm{dir}}^+$ generated by the direct mechanism is, however, expressed using the acoustic wave $w_1^+[\mathrm{CC}]$ produced by the flame and the transfer function of the nozzle of the case [AA]. The ratio η is defined as follows:

$$\eta = \frac{w_{2,\mathrm{ind}}^+}{w_{2,\mathrm{dir}}^+} \tag{31}$$

where

$$w_{2,\mathrm{dir}}^+ = \frac{w_2^+}{w_1^+}[\mathrm{AA}] \cdot w_1^+[\mathrm{CC}] \tag{32}$$

and

$$w_{2,\mathrm{ind}}^+ = \frac{w_2^+}{w_1^S}[\mathrm{SA}] \cdot w_1^S[\mathrm{CC}]$$

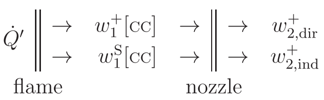

Fig. 10 Definition of the direct and indirect acoustic waves.

The ratio η can be calculated, as mentioned previously, either in a fully analytic [using the analytical relations of Marble and Candel [15] for the transmission and generation of waves through a compact nozzle and the analytic relation for waves generated by combustion (Sec. III.A)] or a semi-analytic manner [using the numerical calculations for the transmission and generation of waves through 1-D nozzle flow and the same analytical relation for waves generated by combustion (Sec. III.B)]:

$$\eta = \underbrace{\frac{w_2^+}{w_1^S}[\mathrm{SA}]}_{\text{analytic or numeric}} \; \underbrace{\frac{w_1^S}{w_1^+}[\mathrm{CC}]}_{\text{analytic}} \; \underbrace{\frac{w_1^+}{w_2^+}[\mathrm{AA}]}_{\text{analytic or numeric}} \tag{33}$$

The fully analytic expression of the ratio η is established using Eq. (20), which gives the ratio between acoustic and entropy waves produced by the combustion chamber (case [CC]), and Eqs. (21), (22), (28), and (29), which give the transmitted and generated waves by a compact nozzle (cases [SA] and [AA]. For this approach, the expression of η is

$$\eta = \frac{1}{\bar{\mathcal{M}}_1} \frac{(\bar{\mathcal{M}}_2 - \bar{\mathcal{M}}_1)(\bar{\mathcal{M}}_2 + \bar{\mathcal{M}}_1)}{2(1 + \frac{1}{2}(\gamma - 1)\bar{\mathcal{M}}_2^2)} \tag{34}$$

for the unchoked nozzle and

$$\eta = \frac{1 + \bar{\mathcal{M}}_1}{\bar{\mathcal{M}}_1} \frac{\bar{\mathcal{M}}_2 - \bar{\mathcal{M}}_1}{2(1 + \frac{1}{2}(\gamma - 1)\bar{\mathcal{M}}_2)} \tag{35}$$

for the choked nozzle.

The ratios between indirect and direct noise η calculated with the fully analytic and semi-analytic approaches are plotted hereafter for the Mach numbers defined previously, as a function of reduced pulsation $\Omega = \omega \ell_n / \bar{c}_1$ related to the pulsation ω, the speed of sound at the nozzle inlet $\bar{c}_1$, and the nozzle length ℓ_n. Figure 11 shows that for this simple case, the indirect combustion noise is globally in the same range of magnitude as the direct one; it can be even 10 times greater in the most unfavorable case (low inlet Mach number and high outlet Mach number). The ratio between indirect and direct noise in Fig. 11 is plotted versus the dimensionless pulsation Ω. The parameter $\Omega(\omega \ell_n / \bar{c}_1)$ corresponds to the acoustically reduced pulsation and quantifies the acoustic compactness of the nozzle. To be representative of the entropy compactness of the nozzle, this dimensionless pulsation simply needs to be divided by the Mach number at the nozzle inlet. That is to say, the nozzle is 10 (inlet Mach number 0.1) to 40 (inlet Mach number 0.025) times less compact from an entropy point of view than acoustically. For reduced pulsations going to zero (compact nozzle assumption), the numerical computations converge to the ratio η calculated with the analytical relations for the nozzle established by Marble and Candel [15]. Figure 11 shows that the slope of η for $\Omega = 0$ is close to zero, so that the analytical expression remains valid (less than 20% error) up to $\Omega = 0.2$ in most cases, that is to say, even when the entropy wavelength is of the order of the nozzle length. The fully analytic approach thus provides a good idea of what the indirect-to-direct ratio can be.

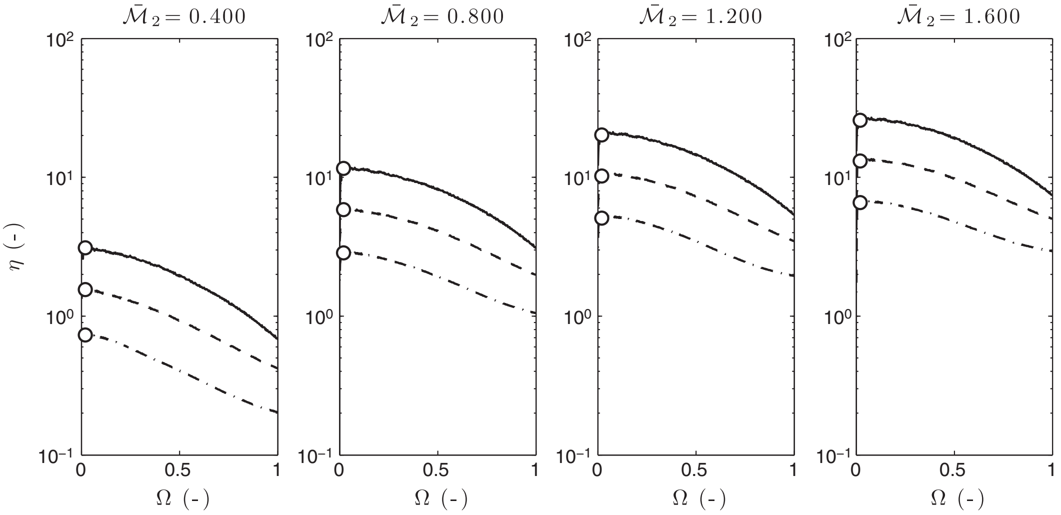

Fig. 11 Estimation of the ratio η between indirect and direct noise. Chain dotted line Mach number $\bar{\mathcal{M}}_1 = 0.100$, dotted line Mach number $\bar{\mathcal{M}}_1 = 0.050$, and solid line Mach number $\bar{\mathcal{M}}_1 = 0.025$. All curves correspond to the semi-analytic method. Circles give the analytic solution for low frequencies [Eqs. (34) and (35)].

This ratio calculated with the fully analytic approach is plotted versus the nozzle inlet and outlet Mach numbers in Fig. 12. Nowadays, the overall pressure ratio at takeoff for commercial aeroengines ranges from about 30 to 40, which is equivalent to an acceleration leading to an outlet Mach number of about 2.0. This graph shows that for an outlet Mach number between unity and two and an inlet Mach number close to 0.05 (a condition which can be found in aeroengines), the indirect combustion noise can be more than 10 times as important as the direct one. Equation (35) shows that when the outlet Mach number $\bar{\mathcal{M}}_2$ is high, the ratio η depends only on the inlet Mach number $\bar{\mathcal{M}}_1$ and tends to $(1 + \bar{\mathcal{M}}_1)/\bar{\mathcal{M}}_1(\gamma - 1)$. With the previous value of the inlet Mach number of 0.05, the maximum ratio η is then greater than 60. Of course, the present estimation is quite oversimplified because, in a real engine, the strong azimuthal deviation of flow within the turbine stages have to be taken into account as well as the blade loading and blade rows spacing. This approach has been followed by Cumpsty and Marble [18,19], but the number of parameters involved in such a method is important and the results are engine dependent (even if general designs can be used to perform such a calculation). The present approach provides a simple method for the estimation of the indirect-to-direct noise ratio and confirms the importance of indirect noise.

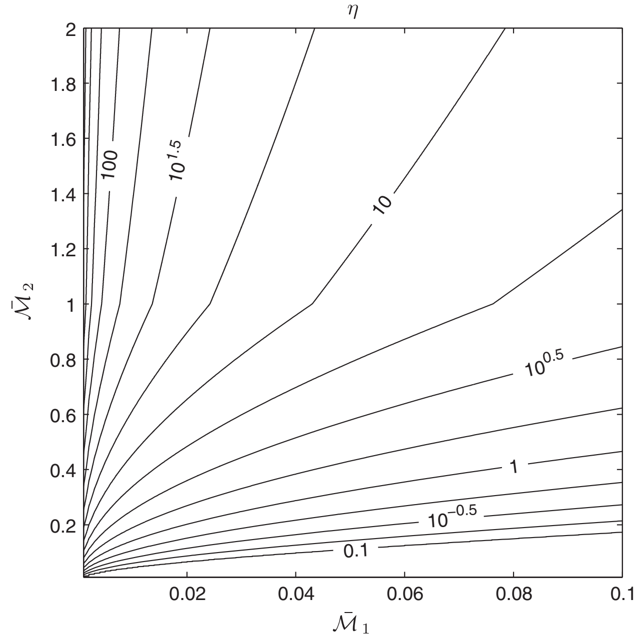

Fig. 12 Ratio η between indirect and direct noise calculated by the fully analytic approach. $\bar{\mathcal{M}}_1$ is the Mach number in the combustion chamber and at the nozzle inlet, and $\bar{\mathcal{M}}_2$ is the Mach number at the nozzle outlet.

V. Conclusions

The noise produced by an aeroengine is generated either by the acoustic waves created by unsteady combustion (direct noise) or by the entropy waves created by combustion and convected through the turbine stages, where they create noise (indirect noise). A simple quasi-1-D combustor model, based on a combustion chamber terminated by a nozzle, has been used to evaluate all waves (acoustic and entropy) created by an unsteady flame zone and to quantify direct and indirect noise. Wave propagation in this model can be determined in the low-frequency limit using fully analytical methods as suggested by Marble and Candel [15] or for all frequencies using a semi-analytical-numerical technique in which the wave propagation through the nozzle is solved using the Euler equations while the rest of the problem is handled analytically. Results demonstrate that the analytical approximation remains valid up to the acoustically reduced pulsations of order of 0.2 (that is to say, even when the entropy wavelength is of the order of the nozzle length) for the given range of inlet Mach numbers (0.025–0.100). They also show that the ratio of indirect-to-direct noise depends on two Mach numbers: the Mach number in the flame zone and the Mach number at the nozzle outlet. This ratio should be small for laboratory experiments but large in most real aeroengines, showing that research on combustion noise needs to incorporate indirect noise generation.

Acknowledgments

This work was partly funded by the Fondation de Recherche pour l'Aéronautique et l'Espace and the Direction Générale de l'Aviation Civile, within the BRUCO (bruit de combustion issu des turbines à gaz) project and the AITEC (analyse instationnaire des turbomachines en aerodynamique et acoustique) research program, respectively. The authors gratefully acknowledge support from the Centre Informatique National de l'Enseignement Supérieur for the access to computing resources. N. Lamarque is thanked for questions and discussions on theoretical backgrounds. F. Duchaine and A. Roux are thanked for their support about computational issues.

References

[1] Bragg, S., "Combustion Noise," *Journal of Institute of Fuel*, Vol. 36, No. 264, 1963, pp. 12–16.
[2] Strahle, W., "Combustion Noise," *Progress in Energy and Combustion Science*, Vol. 4, No. 3, 1978, pp. 157–176.

[3] Hassan, H. A., "Scaling of Combustion-Generated Noise," *Journal of Fluid Mechanics*, Vol. 66, No. 3, 1974, pp. 445–453. doi:10.1017/S0022112074000292

[4] Ihme, M., Pitsch, H., and Bodony, D., "Radiation of Noise in Turbulent Non-Premixed Flames," *Proceedings of the Combustion Institute*, Vol. 32, No. 1, 2009, pp. 1545–1553. doi:10.1016/j.proci.2008.06.137

[5] Candel, S., Durox, D., and Schuller, T., "Flame Interactions as a Source of Noise and Combustion Instabilities," 10th AIAA/CEAS Aeroacoustics Conference, AIAA Paper 2004-2928, 2004.

[6] Candel, S., Durox, D., Ducruix, S., Birbaud, A.-L., Noiray, N., and Schuller, T., "Flame Dynamics and Combustion Noise: Progress and Challenges," *11th CEAS-ASC Workshop and 2nd Scientific Workshop of X3-Noise: Experimental and Numerical Analysis and Prediction of Combustion Noise*, Inst. Superior Tecnico, Lisbon, 2007.

[7] Crighton, D. G., Dowling, A. P., Ffowcs Williams, J. E., Heckl, M., and Leppington, F., *Modern Methods in Analytical Acoustics: Lecture Notes*, Springer–Verlag, New York, 1992.

[8] Rajaram, R., and Lieuwen, T., "Parametric Studies of Acoustic Radiation from Turbulent Premixed Flames," *Combustion Science and Technology*, Vol. 175, No. 12, 2003, pp. 2269–2298.

[9] Rajaram, R., and Lieuwen, T., "Effect of Approach Flow Turbulence Characteristics on Sound Generation from Premixed Flames," 42nd AIAA Aerospace Sciences Meeting and Exhibit, AIAA Paper 2004-0461, 2004.

[10] Lieuwen, T., Mohan, S., Rajaram, R., and Preetham, "Acoustic Radiation from Weakly Wrinkled Premixed Flames," *Combustion and Flame*, Vol. 144, Nos. 1–2, 2006, pp. 360–369. doi:10.1016/j.combustflame.2005.08.004

[11] Tsien, H. S., "The Transfer Functions of Rocket Nozzles," *Journal of the American Rocket Society*, Vol. 22, No. 3, May–June 1952, pp. 139–143.

[12] Crocco, L., "Supercritical Gaseous Discharge with High Frequency Oscillations," *Aerotechnica*, Vol. 33, No. 1, 1953, pp. 46–53.

[13] Candel, S., "Analytical Studies of Some Acoustic Problems of Jet Engines," Ph.D. Thesis, California Inst. of Technology, Pasadena, CA, 1972.

[14] Marble, F. E., "Acoustic Disturbances from Gas Nonuniformities Convected Through a Nozzle,"*Proceedings of the Interagency Symposium on University Research in Transportation Noise*, Vol. 1, Stanford Univ., Stanford, CA, March 1973.

[15] Marble, F. E., and Candel, S., "Acoustic Disturbances from Gas Nonuniformities Convected Through a Nozzle," *Journal of Sound and Vibration*, Vol. 55, No. 2, 1977, pp. 225–243.

[16] Ffowcs Williams, J. E., and Howe, M. S., "The Generation of Sound by Density Inhomogeneities in Low Mach Number Nozzle Flows," *Journal of Fluid Mechanics*, Vol. 70, No. 3, 1975, pp. 605–622. doi:10.1017/S0022112075002224

[17] Stow, S. R., Dowling, A. P., and Hynes, T. P., "Reflection of Circumferential Modes in a Choked Nozzle," *Journal of Fluid Mechanics*, Vol. 467, No. 1, 2002, pp. 215–239. doi:10.1017/S0022112002001428

[18] Cumpsty, N. A., and Marble, F. E., "The Interaction of Entropy Fluctuations with Turbine Blade Rows: A Mechanism of Turbojet Engine Noise," *Proceedings of the Royal Society of London, Series A: Mathematical and Physical Sciences*, Vol. 357, No. 1960, 1977, pp. 323–344.

[19] Cumpsty, N., and Marble, F., "Core Noise from Gas Turbine Exhausts," *Journal of Sound and Vibration*, Vol. 54, No. 2, 1977, pp. 297–309.

[20] Muthukrishnan, M., Strahle, W., and Neale, D., "Separation of Hydrodynamic, Entropy, and Combustion Noise in a Gas Turbine Combustor," *AIAA Journal*, Vol. 16, No. 4, 1978, pp. 320–327. doi:10.2514/3.60895

[21] Bake, F., Michel, U., Rohle, I., Richter, C., Thiele, F., Liu, M., and Noll, B., "Indirect Combustion Noise Generation in Gas Turbines," 11th AIAA/CEAS Aeroacoustics Conference, AIAA Paper 2005-2830, 2005.

[22] Bake, F., Michel, U., and Röhle, I., "Investigation of Entropy Noise in Aero-Engine Combustors," *Journal of Engineering for Gas Turbines and Power*, Vol. 129, No. 2, 2007, pp. 370–376. doi:10.1115/1.2364193

[23] Bake, F., Kings, N., and Röhle, I., "Fundamental Mechanism of Entropy Noise in Aero-Engines: Experimental Investigation," *Journal of Engineering for Gas Turbines and Power*, Vol. 130, No. 1, 2008, pp. 11202–12207. doi:10.1115/1.2749286

[24] Bake, F., Richter, C., Mühlbauer, B., Kings, N., Röhle, I., Thiele, F., and Noll, B., "The Entropy Wave Generator (EWG): A Reference Case on Entropy Noise," *Journal of Sound and Vibration*, Vol. 326, No. 3–5, Oct. 2009, pp. 574–598. doi:10.1016/j.jsv.2009.05.018

[25] Polifke, W., Paschereit, C., and Doebbeling, K., "Constructive and Destructive Interference of Acoustic and Entropy Waves in a Premixed Combustor with a Choked Exit," *International Journal of Acoustics and Vibration*, Vol. 6, No. 3, 2001, pp. 135–146.

[26] Eckstein, J., Freitag, E., Hirsch, C., and Sattelmayer, T., "Experimental Study on the Role of Entropy Waves in Low-Frequency Oscillations in a RQL Combustor," *Journal of Engineering for Gas Turbines and Power*, Vol. 128, No. 2, 2006, pp. 264–270. doi:10.1115/1.2132379

[27] McManus, K., Poinsot, T., and Candel, S., "A Review of Active Control of Combustion Instabilities," *Progress in Energy and Combustion Science*, Vol. 19, No. 1, 1993, pp. 1–29. doi:10.1016/0360-1285(93)90020-F

[28] Dowling, A. P., "The Calculation of Thermoacoustic Oscillations," *Journal of Sound and Vibration*, Vol. 180, No. 4, 1995, pp. 557–581. doi:10.1006/jsvi.1995.0100

[29] Moase, W., Brear, M., and Manzie, C., "The Forced Response of Choked Nozzles and Supersonic Diffusers," *Journal of Fluid Mechanics*, Vol. 585, No. 1, 2007, pp. 281–304. doi:10.1017/S0022112007006647

[30] Schmitt, P., Poinsot, T., Schuermans, B., and Geigle, K., "Large-Eddy Simulation and Experimental Study of Heat Transfer, Nitric Oxide Emissions and Combustion Instability in a Swirled Turbulent High Pressure Burner," *Journal of Fluid Mechanics*, Vol. 570, No. 1, 2007, pp. 17–46. doi:10.1017/S0022112006003156

[31] Poinsot, T., and Veynante, D., *Theoretical and Numerical Combustion*, 2nd ed., R. T. Edwards, Philadelphia, 2005.

[32] Moureau, V., Lartigue, G., Sommerer, Y., Angelberger, C., Colin, O., and Poinsot, T., "Numerical Methods for Unsteady Compressible Multi-Component Reacting Flows on Fixed and Moving Grids," *Journal of Computational Physics*, Vol. 202, No. 2, 2005, pp. 710–736. doi:10.1016/j.jcp.2004.08.003

[33] Childers, D. G., *Modern Spectrum Analysis*, IEEE, Piscataway, NJ, 1978.

P. Givi
Associate Editor

Available online at www.sciencedirect.com
ScienceDirect

C. R. Mecanique 337 (2009) 415–425

COMPTES RENDUS
MECANIQUE

Combustion for aerospace propulsion

Numerical and analytical investigation of the indirect combustion noise in a nozzle

M. Leyko [a,b,*], F. Nicoud [c], S. Moreau [d], T. Poinsot [e]

[a] SNECMA Villaroche, 77550 Moissey-Cramayel, France
[b] CERFACS, 42, avenue Coriolis, 31057 Toulouse, France
[c] Applied mathematics, Université Montpellier II, France
[d] GAUS, Faculté de Génie, Université de Sherbrooke, Canada
[e] CNRS, Institut de mécanique des fluides, Toulouse, France

---

Abstract

Analytical and numerical assessments of the indirect noise generated through a nozzle are presented. The configuration corresponds to an experimental setup operated at DLR by Bake et al. (2008) where an entropy wave is generated upstream of the nozzle by means of an electrical heating device. Both 3-D and 2-D axisymmetric simulations are performed to demonstrate that the experiment is mostly driven by linear acoustic phenomena, including pressure wave reflection at the outlet and entropy-to-acoustic conversion in the accelerated regions. Results show that the acoustic impedance downstream of the nozzle must be accounted for appropriately in order to recover the experimental pressure signal. A good agreement is also obtained with a purely analytical assessment based on the Marble and Candel compact nozzle approximation. ***To cite this article: M. Leyko et al., C. R. Mecanique 337 (2009).***

Résumé

Étude numérique et analytique du bruit de combustion indirect dans une tuyère. L'évaluation du bruit indirect généré par une tuyère est effectuée de manière analytique et numérique. La configuration étudiée correspond à un dispositif expérimental du DLR exploité par Bake et al. (2008), dans lequel une onde d'entropie est produite en amont de la tuyère au moyen d'un dispositif de chauffage électrique. Des simulations 3-D et 2-D axisymétriques sont effectuées afin de montrer que l'expérience est principalement pilotée par des phénomènes acoustiques linéaires, comprenant les réflections acoustiques en sortie et la génération du bruit d'entropie. Les résultats montrent que l'impédance acoustique en aval de la tuyère doit être prise en compte de façon appropriée afin de retrouver le signal de pression expérimental. Un bon accord est obtenu avec un calcul purement analytique basé sur l'approximation de tuyère compacte de Marble et Candel. ***Pour citer cet article : M. Leyko et al., C. R. Mecanique 337 (2009).***

Keywords: Combustion; Thermoacoustic; Indirect combustion noise; Numerical simulations

Mots-clés : Combustion ; Thermoacoustique ; Bruit de combustion indirect ; Simulations numériques

---

[*] Corresponding author.
E-mail addresses: matthieu.leyko@cerfacs.fr (M. Leyko), franck.nicoud@univ-montp2.fr (F. Nicoud), stephane.moreau@usherbrooke.ca (S. Moreau), thierry.poinsot@imft.fr (T. Poinsot).

1631-0721/$ – see front matter © 2009 Académie des sciences. Published by Elsevier Masson SAS. All rights reserved.
doi:10.1016/j.crme.2009.06.025

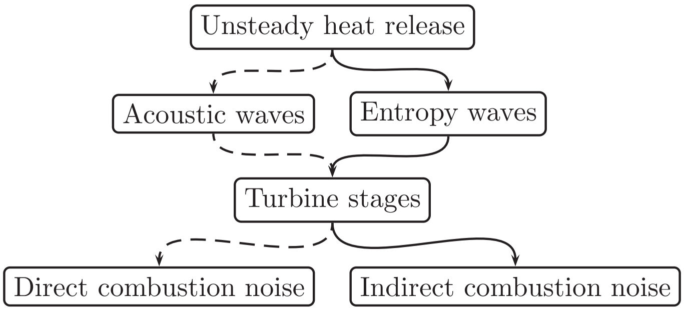

Fig. 1. The two main mechanisms for noise generation from confined flames: direct (– – –) and indirect (———) noise.

1. Introduction

Over the last five decades, jet and external aerodynamic noises of aircraft have been substantially reduced. Further developments will be needed for modern aircraft design in order to meet the increasingly restrictive rules about noise reduction; there is no doubt that Computational AeroAcoustics (CAA) will play a major role in these future developments. With the drastic jet noise reduction already achieved, the relative importance of other noise sources has increased and the contribution of these sources must be controlled if further global noise reduction is to be achieved. Among these sources, the noise stemming from the turbulent flame within the combustor is already identified as non-negligible at take-off, especially in the mid-frequency range. Two main mechanisms have been identified (Muthukrishnan et al. [1], Cumpsty and Marble [2], Pickett [3]) regarding noise propagation from the combustion chamber to the far field (see Fig. 1):

- *direct combustion noise*: acoustic perturbations generated by the unsteady heat release from the turbulent flame (Ihme et al. [4]) propagate either upstream or downstream through the turbomachinery stages and can reach the far field after it has been drastically distorted by the mean flow and also diffracted and reflected by the solid walls within the diffuser, the distributer and the turbine and compressor blades;
- *indirect combustion noise*: entropy fluctuations generated within the combustion chambers (hot spots, imperfect mixing, etc.) are propagated downstream and interact with accelerating mean flow. During this interaction, part of the energy contained in the entropy mode is transferred into the acoustic mode and the subsequent acoustic waves are transmitted to the far field through the turbine stages in a similar way as for the direct combustion noise.

From the current knowledge and expertise regarding Large Eddy Simulations (LES) of turbulent reacting flows in complex geometries and the accuracy requirements regarding noise prediction in CAA, computing the absolute level of combustion noise from a realistic combustor is certainly out of reach of the actual computing/modeling capabilities. The objectives of this study are threefold:

- to assess/establish the capability of a state-of-the-art LES tool for the computation of compressible reacting flows to reproduce the entropy/acoustic interaction in the presence of a strong mean velocity gradient. To this end, the numerical results will be compared to the measurements from the entropy wave generator experiment studied at DLR by Bake et al. [5–7];
- to gain insight into the first-order physical mechanisms that drive the pressure signal measured in the experiment. Notably the effect of (a) the entropy fluctuations shape and size and (b) the boundary conditions will be assessed;
- to investigate to what extent an analytical approach based on the compact nozzle approximation (Marble and Candel [8], Leyko et al. [9]) and valid for 1-D planar waves can reproduce the experimental data of Bake et al. [5].

The analytical relationships that can be derived under the compact assumption for plane waves are first reviewed in Section 2. The experimental setup and associated computational domain are then discussed in Section 3 where a short description of the LES solver is also provided. Finally, results are discussed in Section 4.

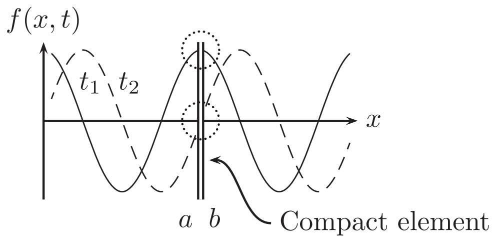

Fig. 2. Compact element illustration: the quantity f, conserved throughout the element, is the same upstream (a) and downstream (b) at each instant.

2. Theoretical background

This section builds upon the results obtained by Marble and Candel [8], who focused on the generation and the transmission of flow perturbations (acoustic and entropy) through a steady non-uniform flow. Assuming a quasi-1-D nozzle flow and quasi-steady perturbations (nozzle compactness), they established the relations linking the different perturbations using mass flow, energy and entropy conservations. These developments are reviewed here to provide a better understanding of the indirect noise-generation mechanism.

2.1. Isentropic nozzle

Consider an isentropic flow of a homogeneous gas of density ρ, velocity u, pressure p, constant heat capacity c_p and $c_v = c_p/\gamma$ within a quasi-1-D adiabatic duct of cross-section area $\mathcal{A}(x)$. In this case, the mass flow

$$\dot{m} = \rho u \mathcal{A} \tag{1}$$

the total temperature

$$T_t = T\left(1 + \frac{\gamma - 1}{2}\mathcal{M}^2\right) \tag{2}$$

and the entropy

$$s = c_v \log \frac{p}{\rho^\gamma} \tag{3}$$

are constant throughout the duct. The above relations can be differentiated to yield:

$$\frac{\mathrm{d}s}{c_p} = \frac{\mathrm{d}p}{\gamma p} - \frac{\mathrm{d}\rho}{\rho} \tag{4}$$

$$\frac{\mathrm{d}\dot{m}}{\dot{m}} = \frac{1}{\mathcal{M}}\frac{\mathrm{d}u}{c} + \frac{\mathrm{d}p}{\gamma p} - \frac{\mathrm{d}s}{c_p} \tag{5}$$

and

$$\frac{\mathrm{d}T_t}{T_t} = \frac{1}{1 + \frac{\gamma-1}{2}\mathcal{M}^2}\left((\gamma - 1)\mathcal{M}\frac{\mathrm{d}u}{c} + (\gamma - 1)\frac{\mathrm{d}p}{\gamma p} + \frac{\mathrm{d}s}{c_p}\right) \tag{6}$$

where the speed of sound $c = \sqrt{\gamma p/\rho}$ and the Mach number u/c have been introduced.

Under the compact nozzle assumption (the wavelengths of the perturbations are large compared with the axial dimension of the nozzle), there is no delay and distortion between the inlet and the outlet of the nozzle. As a result, the instantaneous values of the mass flow, the total temperature and the entropy are conserved throughout the nozzle at each instant, as displayed in Fig. 2. In other words, the compact nozzle assumption allows writing:

$$[\mathrm{d}s]_a^b = 0; \quad [\mathrm{d}\dot{m}]_a^b = 0; \quad [\mathrm{d}T_t]_a^b = 0 \tag{7}$$

where $[\ ]_a^b$ stands for the jump between downstream (index b) and upstream (index a) of the related object (subcritical nozzle, supercritical nozzle and normal shock). At this point, it proves useful to introduce the following reduced variables and acoustic waves (Marble and Candel [8]):

$$\sigma=\frac{\mathrm{d}s}{c_p};\qquad P^{+}=\frac{1}{2}\left(\frac{\mathrm{d}p}{\gamma p}+\frac{\mathrm{d}u}{c}\right);\qquad P^{-}=\frac{1}{2}\left(\frac{\mathrm{d}p}{\gamma p}-\frac{\mathrm{d}u}{c}\right) \tag{8}$$

2.1.1. *Unchoked nozzle*

Combining Eq. (7) with Eqs. (4), (5) and (6) the following set of three equations can be obtained:

$$\begin{aligned}
&-\left(1-\frac{1}{\mathcal{M}_a}\right)P_a^{-}+\left(1+\frac{1}{\mathcal{M}_b}\right)P_b^{+}-\sigma_b\\
&\quad=-\left(1-\frac{1}{\mathcal{M}_b}\right)P_b^{-}+\left(1+\frac{1}{\mathcal{M}_a}\right)P_a^{+}-\sigma_a\\
&-\frac{(\gamma-1)(1-\mathcal{M}_a)}{1+\frac{\gamma-1}{2}\mathcal{M}_a^2}P_a^{-}+\frac{(\gamma-1)(1+\mathcal{M}_b)}{1+\frac{\gamma-1}{2}\mathcal{M}_b^2}P_b^{+}-\frac{1}{1+\frac{\gamma-1}{2}\mathcal{M}_b^2}\sigma_b\\
&\quad=-\frac{(\gamma-1)(1-\mathcal{M}_b)}{1+\frac{\gamma-1}{2}\mathcal{M}_b^2}P_b^{-}+\frac{(\gamma-1)(1+\mathcal{M}_a)}{1+\frac{\gamma-1}{2}\mathcal{M}_a^2}P_a^{+}-\frac{1}{1+\frac{\gamma-1}{2}\mathcal{M}_a^2}\sigma_a\\
&\sigma_b=\sigma_a
\end{aligned} \tag{9}$$

In each of the previous equations, the l.h.s. involves the three waves propagating outward, either upstream (P_a^-) or downstream (P_b^+ and σ_b); the r.h.s. involves only (known) waves propagating inward, viz. toward the nozzle, either upstream (P_a^+, σ_a) or downstream (P_b^-). Note that in the particular case where $P_a^+\neq 0$, $\sigma_a=0$ and $P_b^-=0$ (the ingoing waves can be fixed freely), Eqs. (9) allows recovering the expression given in Marble and Candel [8] for the acoustic response of the nozzle to an acoustic excitation (AA):

$$\frac{P_b^+}{P_a^+}(\mathrm{AA})=\left(\frac{2\mathcal{M}_b}{1+\mathcal{M}_b}\right)\left(\frac{1+\mathcal{M}_a}{\mathcal{M}_a+\mathcal{M}_b}\right)\left(\frac{1+\frac{1}{2}(\gamma-1)\mathcal{M}_b^2}{1+\frac{1}{2}(\gamma-1)\mathcal{M}_a\mathcal{M}_b}\right) \tag{10}$$

In the same way, if one assumes $P_a^+=0$, $\sigma_a\neq 0$ and $P_b^-=0$, the acoustic response to an entropy perturbation (SA) is recovered as in Marble and Candel [8], viz.:

$$\frac{P_b^+}{\sigma_a}(\mathrm{SA})=\left(\frac{\mathcal{M}_b-\mathcal{M}_a}{1+\mathcal{M}_b}\right)\left(\frac{\frac{1}{2}\mathcal{M}_b}{1+\frac{1}{2}(\gamma-1)\mathcal{M}_a\mathcal{M}_b}\right) \tag{11}$$

2.1.2. *Isentropic choked nozzle*

In the case of isentropic choked nozzle, the flow is subsonic in the convergent nozzle part and totally supersonic in the divergent nozzle part. In this case, the acoustic wave P_b^- leaves the domain and cannot be imposed anymore. Two waves enter the domain, namely P_a^+ and σ_a, and four must be determined, namely three transmitted/generated waves (P_b^+, P_b^- and σ_b) and one reflected/generated wave (P_a^-). The critical mass flow equation is then introduced in order to close the problem ($\mathcal{A}^\star$ being the critical section area and $\dot{m}^\star$ being the critical mass flow):

$$\dot{m}^\star=\frac{p_{t1}}{\sqrt{\gamma r T_{t1}}}\mathcal{A}^\star\gamma\left(\frac{\gamma+1}{2}\right)^{-\frac{1}{2}\frac{\gamma+1}{\gamma-1}} \tag{12}$$

Combining the differential of Eq. (12) with Eq. (5), one obtains the following additional condition:

$$\frac{\mathrm{d}u}{c}-\frac{\gamma-1}{2}\mathcal{M}\frac{\mathrm{d}p}{\gamma p}-\frac{1}{2}\mathcal{M}\frac{\mathrm{d}s}{c_p}=0 \tag{13}$$

which can be used to complete the previous jump equations (7) and close the system. After some algebra the following expressions for the four outgoing waves can be obtained:

$$\begin{aligned}
&\left(1-\frac{\gamma-1}{2}\mathcal{M}_a\right)P_a^{+}-\left(1+\frac{\gamma-1}{2}\mathcal{M}_a\right)P_a^{-}-\frac{1}{2}\mathcal{M}_a\sigma_a=0\\
&\left(1-\frac{\gamma-1}{2}\mathcal{M}_b\right)P_b^{+}-\left(1+\frac{\gamma-1}{2}\mathcal{M}_b\right)P_b^{-}-\frac{1}{2}\mathcal{M}_b\sigma_a=0
\end{aligned}$$

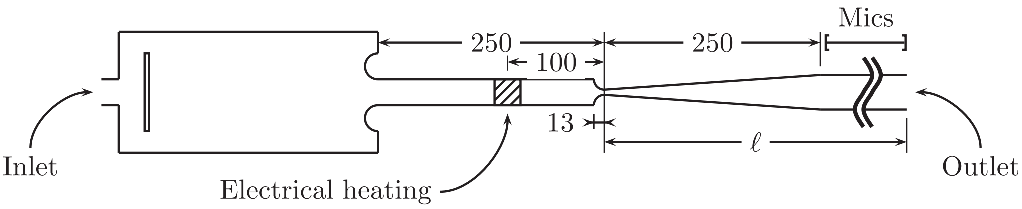

Fig. 3. Principle of the Entropy Wave Generator experiment (lengths are given in mm). Short configuration: $\ell = 500$ mm; Long configuration: $\ell = 2100$ mm.

$$\begin{aligned} &P_a^+ + P_a^- = P_b^+ + P_b^- \\ &\sigma_a = \sigma_b \end{aligned} \tag{14}$$

In many practical cases, however, a residual shock stands downstream of the throat of a choked nozzle and the mean flow is not isentropic anymore.

2.2. *Waves for a shock*

The interaction of acoustic, entropy or vorticity waves with a shock wave is a complicated problem (Mahesh et al. [10,11]), but it can be managed quite well analytically in 1-D (Moase et al. [12]). By construction the flow immediately upstream and downstream of a normal shock is supersonic and subsonic, respectively. This means that four waves are ingoing in this case, namely P_a^+, P_a^-, σ_a and P_b^-, while only two propagate in the outward direction, viz. P_b^+ and σ_b. The derivation of the outgoing waves as a function of the ingoing ones builds upon the classical jump relations trough a normal shock which only depends on the upstream Mach number. This latter quantity is modified by the shock motion induced by the in-going waves. After some algebra, one obtains:

$$\begin{aligned} &\left(1 + \mathcal{M}_a^2 + 2\mathcal{M}_a^2\mathcal{M}_b\right)P_b^+ + \left(1 + \mathcal{M}_a^2 - 2\mathcal{M}_a^2\mathcal{M}_b\right)P_b^- \\ &\quad = \left(1 + \mathcal{M}_a^2 + 2\mathcal{M}_a\mathcal{M}_b^2\right)P_a^+ + \left(1 + \mathcal{M}_a^2 - 2\mathcal{M}_a\mathcal{M}_b^2\right)P_a^- \\ &\left(P_b^+ + P_b^- - P_a^+ - P_a^-\right)(\gamma - 1)\frac{(\mathcal{M}_a^2 - 1)^2}{((\gamma - 1)\mathcal{M}_a^2 + 2)\mathcal{M}_a^2} = \sigma_b - \sigma_a \end{aligned} \tag{15}$$

Eqs. (15) generalize the result given in Marble and Candel [8] to the case where P_b^- is not zero and indicates that entropy fluctuations can be generated by the interaction between an acoustic wave and a shock.

3. Configuration

All the computations presented in this paper are related to the DLR experimental setup studied by Bake et al. [7]. A sketch of the so-called Entropy Wave Generator experiment is displayed in Fig. 3. It consists of an accelerated tube fed by entropy waves generated by an electric heating device located between the upstream plenum and the nozzle. The operating conditions are such that the nozzle is choked but not adapted so that a normal shock takes place just after the throat, within the divergent section. When accelerated through the nozzle, the small amplitude entropy fluctuations (of the order of 10 K) produce backward and forward propagating acoustic waves. The forward part of the generated noise is measured/analyzed by microphones located downstream the nozzle. The main physical parameters defining the operating conditions are presented in Table 1. Note that the heating duration is 100 ms which, with a bulk velocity of the order of 12 m/s, leads to an entropy perturbation of typical length of the order of 1200 mm while the nozzle is about 263 mm long. This is most likely not relevant to practical engine applications where the expected length of the entropy spots is more likely on the order of $100 - 200$ mm.

The numerical tool used in this study is the unstructured combustion code AVBP developed at CERFACS (AVBP [13]). AVBP solves the complete Navier–Stokes equations in two and three spatial dimensions. The unstructured approach allows computing not only the nozzle but also the whole air feeding line as well as the exhaust system. This code was selected because it solves the complete compressible Navier–Stokes equations and can naturally account for the energy transfer between the entropy and the acoustic modes of oscillation. The numerical method used is

Table 1
Main characteristics of the experimental/numerical experiment.

Plenum pressure 117,000 Pa	Outlet pressure 100,800 Pa	Inlet Mach 0.037	Shock Mach 1.340	Outlet Mach 0.023
Plenum temperature 298 K	Pulse amplitude 9 K	Pulse duration 100 ms	Pulse length 1000 ms	
Convergent length 13 mm	Divergent length 250 mm	Throat diameter 7.5 mm	Inlet diameter 30 mm	Outlet diameter 40 mm

Table 2
Main characteristics of the small scale simulations.

Run	Geometry	Length	BC	Heating
3D-1	3D	short	non-reflecting	uniform
2D-1	2D axi	short	non-reflecting	uniform
2D-2	2D axi	short	non-reflecting	non-uniform
2D-3	2D axi	short	reflecting	uniform
2D-4	2D axi	long	finite impedance	uniform

based on a weighted residual, Taylor–Galerkin discretization which is third order in both space and time (Colin and Rudgyard [14]) in order to minimize the dispersion/dissipation errors.

The main characteristics of the simulations performed are presented in Table 2. The entries “short” and “long” refer to the two types of computational domain depicted in Fig. 3. They both include the upstream plenum and the heating section but the “short” one extends only 500 mm downstream of the nozzle throat (length ℓ) while the “long” contains the exhaust duct until the entrance to the anechoic part, viz. approx. 2100 mm downstream of the nozzle. “BC” refers to the boundary condition prescribed at the outlet of the computational domain which can be either non-reflecting, fully reflecting or corresponds to a finite (neither zero nor infinite) acoustic impedance. The “heating” entries correspond to the shape of the temperature pulse: it is 1-D in most cases (viz. uniform in the plane normal to the duct) or it can depend on the distance r to the axis (viz. non-uniform in the cross-section; in the present case, the heating source term is proportional to $\cos(r/R \cdot \pi/2)$, with R the radius of the upstream duct). The uniform and non-uniform heatings correspond to the same overall energy so that the comparison between the runs 2D-1 and 2D-2 can provide relevant information regarding the effects of the inhomogeneity of the entropy perturbation on the noise generated. In the same way, comparing runs 2D-1 and 2D-3 will provide information about the sensitivity of the results to the outlet boundary condition while comparing 3D-1 and 2D-1 will be relevant to quantify the 3-D effects in the observed results. At last, run 2D-4 is designed to mimic, as much as possible, the experimental downstream acoustic impedance.[1] In all cases, the mesh resolution is enough to represent the propagation of the entropy and acoustic waves in the duct without significant dissipative/dispersive errors (mesh size on the order of 1 mm compared to the perturbation size on the order of 1200 mm; see Section 3). The 3-D mesh is rather coarse with 1.2 million tetraedras, corresponding to approximately 15 cells in a cross-section. The mesh density is equivalent for 2-D axisymmetric cases. Note that the mesh refinement is not sufficient to resolve the residual shock appropriately which, given the non-dissipative character of the numerical method, can lead to numerical instabilities. Thus extra numerical dissipation has been added in both 3-D and 2-D axisymmetric calculation in the region downstream of the throat of the nozzle.

In order to mimic the experimental heating device, a source term is added to the energy equation. It reads:

$$S(x,t) = S_0 \frac{1}{2}\left[\tanh\left(\frac{x - x_0 + L_s/2}{a}\right)\tanh\left(-\frac{x - x_0 - L_s/2}{a}\right) + 1\right] s(t)$$

where $L_s = 30$ mm is representative of the length of the experimental heating zone and $a = 3$ mm enables to smooth sufficiently the source term to avoid numerical issues. Moreover, the average location x_0 of the source term has been

---

[1] Not available in Bake et al. [5–7] but kindly provided by Dr. Ing. F. Bake during the course of this study.

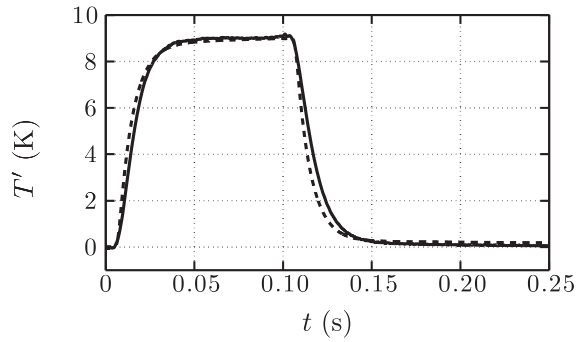

Fig. 4. Time traces of the experimental (———) and numerical (– – –) temperature downstream of the heating location.

consistently chosen with the location of the electrical device in the experiment (100 mm upstream of the nozzle throat). The temporal evolution $s(t)$ is defined as the following:

$$s(t) = \begin{cases} 1 - e^{-\frac{t-t_0}{\tau}} & \text{if } t \in [t_0, t_0 + T] \\ s(t_0 + T)e^{-\frac{t-t_0}{\tau}} & \text{if } t > t_0 + T \end{cases}$$

where t_0 is the time when the electrical device is triggered, T is the pulse duration and is equal to 100 ms and $\tau = 8$ ms. As shown in Fig. 4, those numerical parameters allow a fair representation of the temperature fluctuation produced in the experiment. The next section analyzes the results obtained in terms of pressure fluctuations generated downstream when the temperature perturbation displayed in Fig. 4 passes through the nozzle.

4. Results

The EWG setup has been studied both numerically and analytically during this study. Numerical simulations have the advantage of integrating all the possible effects involved in the entropy noise generation and contained in the Navier–Stokes equations. The analytical approach is valid only under the compact nozzle assumption and in the linear regime.

The time traces of the pressure computed 350 mm downstream of the throat are displayed in Fig. 5 for runs 2D-1, 2D-2, 2D-3 and 3D-1 together with the experimental signal. Clearly enough, these simulations do not reproduce the experimental data, neither in terms of amplitude, nor in terms of signal shape. For runs 2D-1 and 3D-1, the numerical pressure trace has a top-hat behavior similar to the temperature upstream fluctuation, while the experiment shows a wavy behavior at a frequency close to 30 Hz. The figure also indicates that 3D-1 leads to results very similar to 2D-1, indicating that the disagreement between the 2D-1 computation and the experimental data cannot be attributed to 3-D effects. The same conclusion can be drawn for the temperature inhomogeneity which appears to have no effect, at least for the configuration considered (comparing 2D-1 and 2D-2). On the other hand, Fig. 5 illustrates how large the effects of the downstream acoustic boundary condition can be. When a fully reflecting condition (which imposes pressure) is used instead of a non-reflecting one (which essentially sets the incoming acoustic wave to zero at the outlet), the amplitude decreases drastically. More importantly, the shape of the signal is also strongly modified by the superposition of the downward and backward pressure waves. A wavy behavior is obtained with run 2D-3, although with characteristic amplitude and frequency in quantitative disagreement with the experiment. The previous results suggest that the discrepancies observed in Fig. 5 might be related to an incorrect downstream acoustic impedance. Indeed, the short computational domain and non-reflecting BC used in runs 2D-1, 2D-2 and 3D-1 would only be representative of the actual experimental conditions if a perfect anechoic system would have been used by Bake et al. [7]. Actually, Fig. 6 demonstrates that this is not the case and that substantial reflection occurs, especially in the low frequency range: the modulus of the reflection coefficient, defined as the ratio of the backward wave to forward wave at the outlet, is as large as 0.5 at 30 Hz, the typical frequency of the reflections observed in the experimental signal (see Fig. 5). Accounting for a complex-valued, frequency-dependent reflection coefficient in a CFD code solving the flow equations in the time domain is not an easy task although it can be theoretically done by making use of recursive/non-recursive digital filters. A simpler approach has been followed in the present study. Instead of using a non-reflecting outlet boundary condition with zero entering wave L^-, it is common use to write

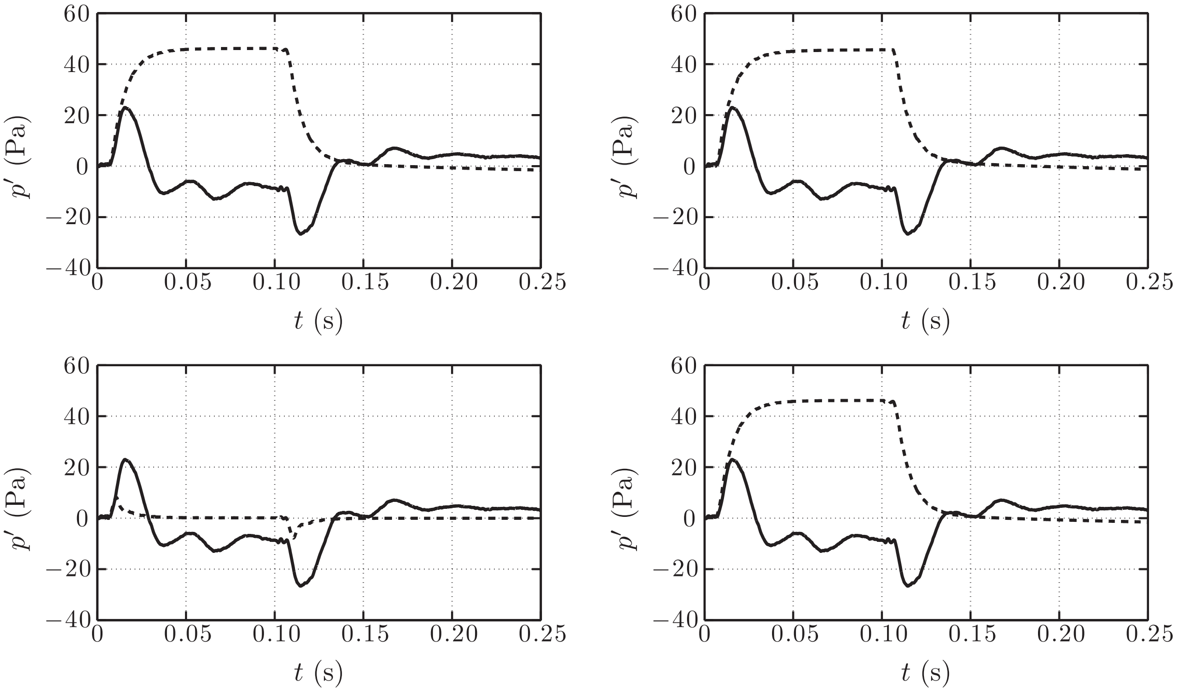

Fig. 5. Time traces of the fluctuating pressure 350 mm downstream of the nozzle. Experimental data: ———; Numerical result: – – –. Top left: run 2D-1; Top right: run 2D-2; Bottom left: run 2D-3; Bottom right: run 3D-1.

the latter as a pressure difference times a relaxation coefficient κ (Poinsot and Lele [15]), viz. $L^- = 2\kappa \Delta t \cdot (p_{\mathrm{ref}} - p_B)/(\rho c)$, with Δt the time step, p_B the nodal pressure at the outlet boundary and p_{ref} the reference pressure. In doing so, the outlet condition acts as a first-order low pass filter (Selle et al. [16]) whose cut-off frequency is inversely proportional to κ and the reflection coefficient R reads:

$$R = -\frac{1}{\imath\omega/\kappa + 1} \tag{16}$$

It is thus possible to tune the relaxation coefficient κ in order to mimic the amplitude of the experimental reflection coefficient, at least in the low-frequency range. The length ℓ of the downstream duct is then tuned in such a way as to mimic the experimental time delay as well as to compensate for the phase of the relaxation-based outlet partially reflecting condition. The experimental reflection coefficient is considered here to be measured at the nozzle throat ($x = 0$) while the reflection coefficient of numerical boundary condition (Eq. (16)) is given at the end of the computational domain ($x = \ell$). The experimental reflection coefficient is thus multiplied by $\exp(-2\imath\ell\omega/c)$ in order to shift it to the same position, at the end of the numerical domain ($x = \ell$). The experimental reflection coefficient obtained in this way is depicted in Fig. 6 where a fair agreement with the numerical one is apparent in the frequency range 20–40 Hz. The "optimized" relaxation coefficient κ and length ℓ are close to 160 s^{-1} and 2100 mm. As anticipated, Fig. 7 indicates that the numerical pressure signal is in better agreement with the measured one when accounting more accurately for the effective downstream boundary condition.

It is also possible to perform these calculations analytically. This can be done using the relations presented previously for the supercritical nozzle (Eq. (14)), the normal shock (Eq. (15)) and the subcritical nozzle (Eq. (9)). The supercritical nozzle starts at point 1 at the nozzle inlet and finishes at point 2 in the divergent section where the normal shock takes place. The normal shock relations are defined between point 2 and 3 and finally the subcritical nozzle starts at point 3, downstream of the shock, and finishes at point 4 at the end of the divergent section as shown in Fig. 8. Only the entropy wave generated by the electrical device is taken into account and the upstream part of the nozzle is assumed to be non-reflecting (even if this is not the case in the real configuration). The subsonic nozzle outlet is represented in a general manner by the reflection coefficient $R = P_4^-/P_4^+$, but it will be considered to be infinitely small for the non-reflecting calculation ($R \ll 1$ for numerical issues) and to be equal to the tuned reflection coefficient of the numerical computation 2D-4 for the "real" case. The entropy wave temporal evolution is proportional to that imposed on the source term on energy in the numerical computation. All the analytical calculations are performed in

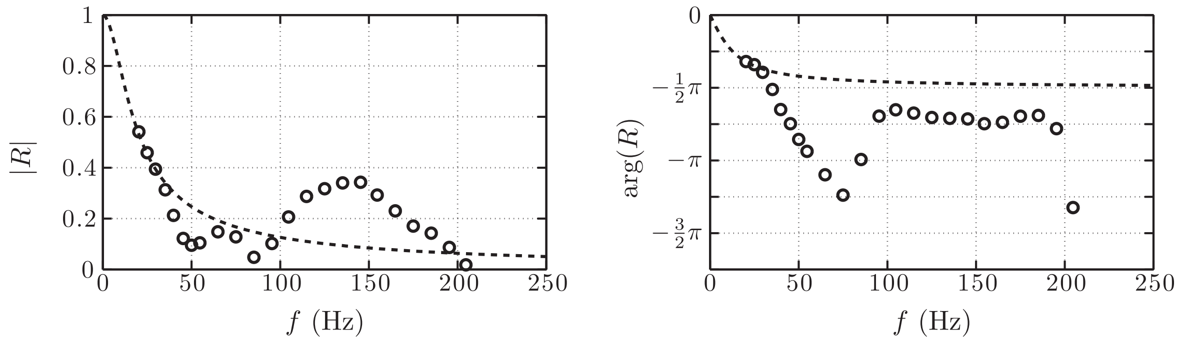

Fig. 6. Experimental reflection coefficient shifted 2100 mm downstream of the nozzle throat and numerical reflection coefficient. Shifted experimental data: o; Tuned relaxation coefficient: − − −.

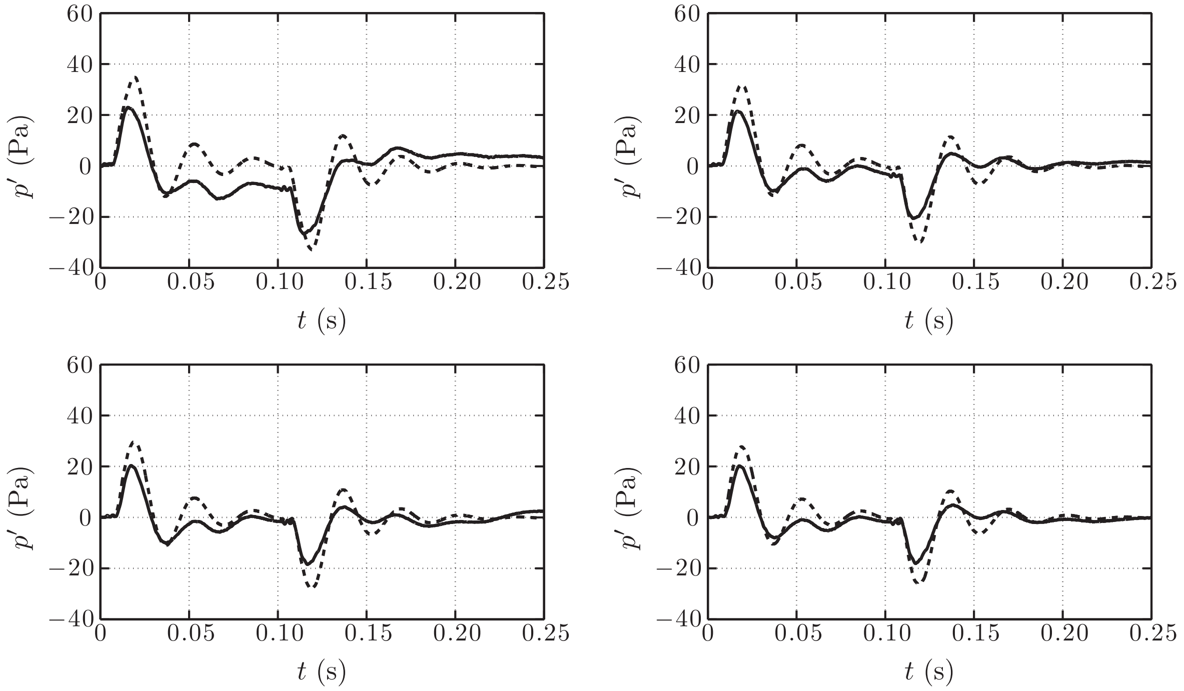

Fig. 7. Time traces of the fluctuating pressure downstream of the nozzle. Experimental data: ——; Run 2D-4: − − −. Distance downstream of the nozzle: Top left: 350 mm; Top right: 730 mm; Bottom left: 975 mm; Bottom right: 1150 mm.

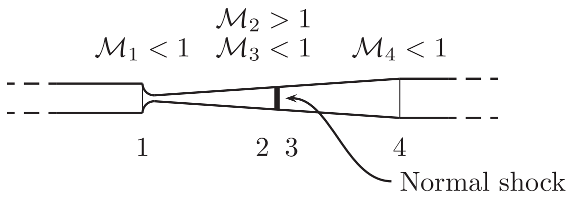

Fig. 8. Description of the analytic approach.

the frequency domain in order to take into account the frequency dependence of the outlet boundary condition in the real case, but the different nozzle elements are still assumed to be compact. Since the case of a shock in the divergent section is considered here, the supercritical nozzle (from 1 to 2) can be treated independently of the downstream elements, and provide explicitly the waves entering the downstream elements. The shock (from 2 to 3) and the subcritical nozzle with the outlet BC (from 3 to 4) have to be treated together since most of the waves are coupled. Finally, one obtains the reduced pressure fluctuation $(\mathrm{d}p/\gamma p)_4(\omega)$ in the frequency domain as a function of the four Mach numbers $\mathcal{M}_1$, $\mathcal{M}_2$, $\mathcal{M}_3$ and $\mathcal{M}_4$ ($\mathcal{M}_3$ and $\mathcal{M}_4$ are actually linked by the shock relations), the reflection coefficient

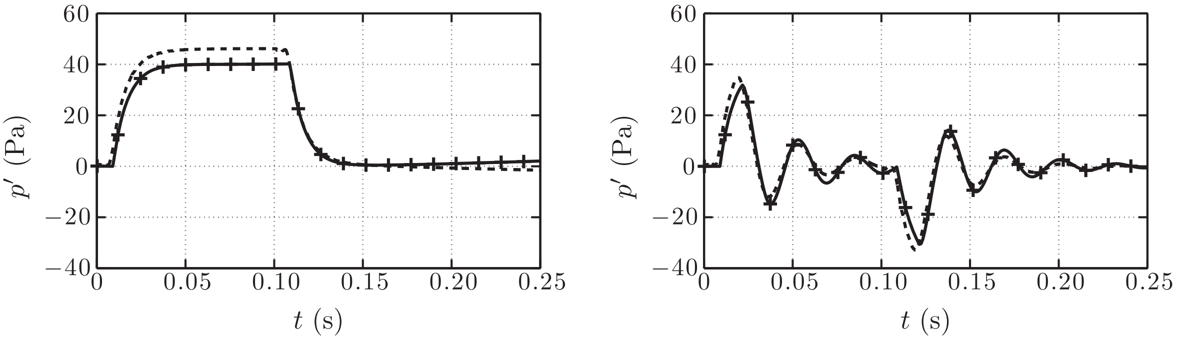

Fig. 9. Time traces of the fluctuating pressure downstream of the nozzle. Numerical results: $---$; Analytical results: $-+-$. Left: Non-reflecting case (analytic compared to run 2D-1); Right: Finite impedance case (analytic compared to Run 2D-4).

$R(\omega)$ and the reduced entropy fluctuation $\sigma_1(\omega)$. The time evolutions of the pressure fluctuations reconstructed from the analytical calculations are compared to the numerical computations. Fig. 9 shows a very good agreement between these two approaches. This demonstrates that the EWG experiment (for the given regime) is essentially driven by linear quasi-1-D acoustics.

5. Conclusions

The numerical and analytical analysis performed in this study demonstrates that the pressure signals obtained in the EWG experiment by Bake et al. [7] result from two main mechanisms:

- the entropy-to-acoustic conversion due the strong mean velocity gradient in the nozzle, including the normal shock that stands just downstream of the throat;
- the acoustic reflection within the exhaust system downstream of the nozzle and test section.

Moreover, in the low frequency range investigated, only 1-D planar waves are present and the compact nozzle approximation is valid, even for the entropy perturbations. As a result, the pressure signals observed experimentally and numerically can be nicely reproduced by a simple quasi-1-D analytical model derived in the zero frequency limit for the nozzle.

Acknowledgements

This work was performed during the Summer Program of CTR 2008. The authors gratefully acknowledge support from CINES for the computer resources and the DLR for providing the experimental data. This work was partly funded by the Fondation nationale de recherche pour l'aéronautique et l'espace within the BRUCO Project.

References

[1] M. Muthukrishnan, W. Strahle, D. Neale, Separation of hydrodynamic, entropy, and combustion noise in a gas turbine combustor, AIAA J. 16 (4) (1978) 320–327.
[2] N. Cumpsty, F. Marble, The interaction of entropy fluctuations with turbine blade rows; a mechanism of turbojet engine noise, Proc. R. Soc. Lond. 357 (1977) 323–344.
[3] G.F. Pickett, Core engine noise due to temperature fluctuations convecting through turbine blade rows, in: 2nd AIAA Aeroacoustics Conference, AIAA 1975-528, 1975.
[4] M. Ihme, H. Pitsch, D. Bodony, Radiation of noise in turbulent non-premixed flames, in: Proc. of the Combustion Institute, 2008.
[5] F. Bake, U. Michel, I. Rohle, C. Richter, F. Thiele, M. Liu, B. Noll, Indirect combustion noise generation in gas turbines, in: 11th AIAA/CEAS Aeroacoustics Conference, AIAA 2005-2830, 2005.
[6] F. Bake, U. Michel, I. Röhle, Investigation of entropy noise in aero-engine combustors, J. Eng. Gas Turbines Power 129 (2) (2007) 370–376.
[7] F. Bake, N. Kings, I. Röhle, Fundamental mechanism of entropy noise in aero-engines: Experimental investigation, J. Eng. Gas Turbines Power 130 (1) (2008) 011202, 6 pp.
[8] F. Marble, S. Candel, Acoustic disturbances from gas nonuniformities convected through a nozzle, J. Sound Vib. 55 (1977) 225–243.

[9] M. Leyko, F. Nicoud, T. Poinsot, Comparison of indirect and direct combustion noise in aircraft engines, in: 11th CEAS-ASC Workshop of X3-Noise, 2007.
[10] K. Mahesh, S. Lee, S. Lele, P. Moin, The interaction of an isotropic field of acoustic waves with a shock wave, J. Fluid Mech. 300 (1995) 383–407.
[11] K. Mahesh, S. Lele, P. Moin, The influence of entropy fluctuations on the interaction of turbulence with a shock, J. Fluid Mech. 334 (1997) 353–379.
[12] W. Moase, M. Brear, C. Manzie, The forced response of choke nozzles and supersonic diffusers, J. Fluid Mech. 585 (2007) 281–304.
[13] AVBP Code: http://www.cerfacs.fr/cfd/avbp_code.php and http://www.cerfacs.fr/cfd/CFDPublications.html, 2008.
[14] O. Colin, M. Rudgyard, Development of high-order Taylor–Galerkin schemes for unsteady calculations, J. Comput. Phys. 162 (2) (2000) 338–371.
[15] T. Poinsot, S. Lele, Boundary conditions for direct simulations of compressible viscous flows, J. Comput. Phys. 101 (1) (1992) 104–129.
[16] L. Selle, F. Nicoud, T. Poinsot, The actual impedance of non-reflecting boundary conditions: implications for the computation of resonators, AIAA J. 42 (5) (2004) 958–964.

Numerical and analytical modelling of entropy noise in a supersonic nozzle with a shock

M. Leyko*[,a], S. Moreau[b], F. Nicoud[c], T. Poinsot[d]

[a] *SNECMA, Villaroche, France - CERFACS, Toulouse, France*
[b] *GAUS, Faculté de Génie, Université de Sherbrooke, Canada*
[c] *I3M, Université Montpellier II, UMR CNRS 5149, France*
[d] *Institut de Mécanique des Fluides, Université de Toulouse, CNRS, France*

Abstract

Analytical and numerical assessments of the indirect noise generated through a nozzle are presented. The configuration corresponds to an experiment achieved at DLR by Bake *et al.* [F. Bake, C. Richter, B. Mühlbauer, N. Kings, I. Röhle, F. Thiele, B. Noll, The Entropy Wave Generator (EWG): A reference case on entropy noise, Journal of Sound and Vibration 326 (2009) 574-598] where an entropy wave is generated upstream of a nozzle by an electrical heating device. Both 3-D and 2-D axisymmetric simulations are performed to demonstrate that the experiment is mostly driven by linear acoustic phenomena, including pressure wave reflection at the outlet and entropy-to-acoustic conversion in the accelerated regions. Moreover, the spatial inhomogeneity of the upstream entropy fluctuation has no visible effect for the investigated frequency range (0-100 Hz). Similar results are obtained with a purely analytical method based on the compact nozzle approximation of Marble and Candel [F. Marble, S. Candel, Acoustic disturbances from gas nonuniformities convected through a nozzle, Journal of Sound and Vibration 55 (1977) 225-243] demonstrating that the DLR results can be reproduced simply on the basis of a low-frequency compact-elements approximation. Like in the present simulations, the analytical method shows

---

*Corresponding author.
Email addresses: `leyko@cerfacs.fr` (M. Leyko), `stephane.moreau@usherbrooke.ca` (S. Moreau), `franck.nicoud@univ-montp2.fr` (F. Nicoud), `thierry.poinsot@imft.fr` (T. Poinsot)

Preprint submitted to Elsevier *April 7, 2010*

that the acoustic impedance downstream of the nozzle must be accounted for to properly recover the experimental pressure signal. The analytical method can also be used to optimize the experimental parameters and avoid the interaction between transmitted and reflected waves.

Key words: aeroacoustics, indirect combustion noise, nozzle flow
PACS:

Nomenclature

$\mathcal{A}$	Nozzle cross-section area
c_p	Fluid specific heat at constant pressure
c_v	Fluid specific heat at constant volume
c	Speed of sound
d	Empirical smoothing constant
L^-	Entering wave at outlet boundary
ℓ_{in}	Length of the inlet duct upstream of the nozzle throat
ℓ_{out}	Length of the exit domain downstream of the nozzle throat
ℓ_h	Length of the experimental heating zone
$\mathcal{M} = u/c$	Fluid Mach number
$\dot{m}$	Fluid mass flow rate
p	Fluid static pressure
p_{ref}	Reference static pressure
p_B	Outlet nodal static pressure
P^-	Acoustic pressure propagating downstream
P^+	Acoustic pressure propagating upstream
r	Radial distance to the axis
R	Upstream duct radius
$\mathcal{R}_{\text{in}}, \mathcal{R}_{\text{out}}$	Acoustic reflection coefficient at the simulation inlet and exit
$\mathcal{R}_1, \mathcal{R}_4$	Acoustic reflection coefficient in planes 1 and 4
s	Fluid entropy
t	Time

t_0	Time of electrical device trigger
T	Fluid static temperature
T_p	Pulse duration
T_t	Fluid total or stagnation temperature
u	Fluid velocity
x	Axial coordinate of the nozzle
x_0	Average location of the source term and position of the heating device
γ	Ratio of specific heats
Δt	Time step
κ	Relaxation coefficient on pressure at the outlet boundary
ρ	Fluid density
σ	Reduced entropy fluctuation
τ	Relaxation time of the pulse model
ϕ	Temporal variation of the electrical device source term
Φ	Source term in the energy equation
Φ_0	Amplitude of the source term in the energy equation
ω	Angular frequency

1. Introduction

Over the last five decades, jet and external aerodynamic noises of aircraft have been substantially reduced. Further developments will be needed for modern aircraft design in order to meet the increasingly restrictive rules about noise reduction; there is no doubt that Computational AeroAcoustics (CAA) will play a major role in these future developments. With the drastic reduction of jet noise already achieved, the relative importance of other noise sources has increased and the contribution of these sources must be controlled if further global noise reduction is to be achieved. Among these sources, the noise coming from the turbulent flame within the combustor is already identified as significant at take-off, especially in the mid-frequency range.

Two main mechanisms controlling noise propagation from the combustion chamber to the far field have been identified (see Fig. 1). On the one hand, acoustic perturbations generated by the unsteady heat release from the turbulent flame propagate either upstream or downstream through the turbomachinery stages and can reach the far field after being distorted by the mean flow as well as diffracted and reflected by the solid walls within the diffuser and, the turbine and compressor blades. This sound generation is the *direct combustion noise* and has been theoretically investigated by Bragg (1), Strahle (2), Hassan (3), and nowadays for example experimentally by Lieuwen *et al.* (4) and numerically by Ihme *et al.* (5). According to the numerous studies in this field, the so-called direct noise is mainly caused by the unsteady heat release rate. On the other hand, entropy fluctuations generated within the combustion chambers (hot spots, imperfect mixing, etc.) are propagated downstream and interact with the accelerating mean flow. During this interaction, part of the energy contained in the entropy modes is transferred into the acoustic modes and the subsequent acoustic waves are transmitted to the far field through the turbine stages in a similar way as for the direct combustion noise. Candel highlighted this phenomenon during his PhD thesis (6) and showed that it can be an important source of noise in aero-engines. This mechanism is called the *indirect combustion noise* (or *entropy noise*) since the entropy spots are mostly caused by the unsteady combustion. Since direct and indirect noise have the same source (unsteady combustion), it is possible to compare them as proposed in (7). This comparison shows that entropy noise can dominate direct noise in engines and this explains why it is the focus of the present study.

In the seventies, a significant experimental and modeling effort of engine core noise was undertaken (2; 8; 9; 10; 11). In these experiments, however, the amplitude of the induced temperature fluctuation (about 1 K) was too low to clearly measure and characterize the indirect noise. An analytical model for the indirect combustion noise for compact nozzles was proposed by Marble and Candel (12). Moase *et al.* (13) have recently extended the analytical results of

Marble and Candel (12) for choked nozzles and supersonic nozzles of arbitrary geometry to study the conditions for unchoke, "over-choke" and unstart. By numerically solving the quasi-one-dimensional Euler equations they carefully studied the non-linear and non-compact phenomena to which the above analytical results do not apply. Stow *et al.* (14) also generalized the analytical results of Marble and Candel (12) by removing the quasi-one-dimensional assumption and moving to two-dimensional axisymmetric flow to study the reflection of azimuthal modes in choked nozzles. The resulting Euler equations were linearized and solved numerically. Yet no actual dedicated experimental validation of those theorical and numerical results with significant entropy waves generated were achieved until the recent entropy wave generator (EWG) experiment at DLR by Bake *et al.* (15; 16; 17; 18; 19). The corresponding experimental setup and the major measurements are summarized in Sec. 2.

From the current knowledge and expertise in Large Eddy Simulations (LES) of turbulent reacting flows in complex geometries and the accuracy requirements of Direct Noise Computation (DNC), computing the absolute level of combustion noise from a realistic combustor is probably out of reach of the present computing and modelling capabilities and starts from a *model* experiment such as the DLR EWG set-up is a logical first step. In this framework, the objectives of this study are threefold. First, the capability of a state-of-the-art LES code (ABVP) to compute compressible reacting flows and reproduce the entropy/acoustic interaction in the presence of a strong mean velocity gradient is assessed. The associated computational domain and simulations are discussed in Sec. 3.1 where a short description of the LES solver used here is also provided. The numerical results are then compared to the measurements from the EWG experiment and to the recent URANS computations achieved by Mühlbauer *et al.* (20). Secondly, the first-order physical mechanisms that drive the pressure signal measured in the experiment are explored. Notably the effects of (a) the entropy fluctuations shape and size, and (b) the boundary conditions are assessed. Finally, the application range of the analytical approach based on the compact nozzle approximation (12; 7) and valid for plane waves is investigated in Sec. 4. The analytical relationships that can be derived for unchoked and choked nozzles are first reviewed and applied to the EWG configuration and flow conditions. The analytical results are then compared with both the experimental data of Bake *et al.* (19) and the present unsteady simulations.

2. DLR experimental set-up and measurements

All computations presented in this paper are related to the DLR experimental setup studied by Bake *et al.* (16; 17; 18; 19). A sketch of the so-called Entropy Wave Generator (EWG) experiment is displayed in Fig. 2. It consists of a tube fed by entropy waves generated by an electric heating device located between the upstream plenum and the nozzle. The main geometrical parameters of the experiment are summarized in Table 1. The operating conditions were varied from unchoked conditions (nozzle Mach numbers, $\mathcal{M}_{\text{nozzle}}$, from 0.15 to 0.9) to choked flows ($\mathcal{M}_{\text{nozzle}} = 1$) with various exit Mach numbers, $\mathcal{M}_{\text{exit}}$. The averaged amplitude of the temperature fluctuations was also varied.

The present numerical simulations are restricted to the conditions termed reference test case 1 by Bake *et al.* (19). The nozzle is choked but not adapted so that a normal shock takes place just after the throat, within the divergent section. When accelerated through the nozzle, the small amplitude entropy fluctuations (in the order of 10 K) produce backward and forward propagating acoustic waves. The forward part of the generated noise is measured by microphones located downstream of the nozzle. The main physical parameters defining the operating conditions are presented in Table 2. It should be stressed that the heating duration is 100 ms which, with a bulk velocity in the order of 12 m/s, leads to an entropy perturbation longer than the nozzle (1200 mm against 263 mm). This might not be the case in practical engine applications where the expected length of the entropy spots is in the order of 100-200 mm. The present entropy spot (s') is made of a "raising", a "constant" and a "falling" fluctuation superimposed on the steady flow which all participate to the sound generation. Indeed, according to Marble and Candel (12), the pressure fluctuation (p') com-

Convergent length	Divergent length	Throat diameter	Inlet diameter	Exit diameter
13 mm	250 mm	7.5 mm	30 mm	40 mm

Table 1: Main geometrical characteristics of the DLR experimental nozzle

Plenum pressure	Outlet pressure	Inlet Mach
$117,000$ Pa	$100,800$ Pa	0.037
Outlet Mach	**Pulse duration, τ**	**Pulse amplitude**
0.023	100 ms	9 K

Table 2: Main physical parameters of the DLR Entropy Wave Generator experiment

ing from the linearized Euler equations is directly related to the entropy one, when considering indirect noise generation. It should also be stressed that in the so-called analytical approach, the entropy noise is not caused by the time-derivative of the entropy fluctuation: if there are no reflections, a Heaviside step function on the entropy perturbation produces the same result on the acoustic pressure. Therefore, the relevant length scale is believed to be the full pulse and not only its edges. Further details of the experiment and the associated measurements can be found in Bake *et al.* (17; 18).

3. Numerical simulation of indirect noise

3.1. Numerical set-ups and parameters

The numerical tool used in this study is the unstructured combustion code AVBP developed at CERFACS (21; 22). AVBP solves the complete three-dimensional compressible Navier-Stokes equations. It therefore integrates all possible non-linear effects involved in the entropy noise generation and contained in the these equations. The unstructured approach allows meshing and computing not only the nozzle but also the whole air feeding line as well as the exhaust system. This formulation then naturally accounts for the energy transfer between the entropy and the acoustic modes, and for the actual, possibly non-compact, nozzle geometry. The numerical method used in AVBP is based on a weighted residual, Taylor-Galerkin discretization which is third-order in both space and time (23) in order to minimize the dispersion and dissipation numerical errors.

All simulations termed "2D" correspond to 3-D calculations in an axisymmetric configuration on a slice with periodic boundary conditions. Only the simulation termed "3D" refers to the full cylindrical geometry. The main characteristics of the simulations are presented in Table 3. The entries "short" and "long" refer to the two types of computational domain depicted in Fig. 2. They both include the upstream plenum and the heating section but the "short" one extends only 500 mm downstream of the nozzle throat (length ℓ_{out}) while the "long" contains the exhaust duct up to the inlet of the anechoic section, viz. approx. 2100 mm downstream of the nozzle. The "long" configuration is meant to apply realistic impedance (especially the phase of the reflection coefficient) at the duct exit. In Table 3, "BC" refers to the boundary condition prescribed at the outlet of the computational domain which can be either non-reflecting, fully reflecting or corresponds to a finite (neither zero nor infinite) acoustic impedance. The "heating" entries correspond to the shape of the temperature pulse: it is 1-D in most cases (viz. uniform in the plane normal to the duct) expected for case 2D-2 where it depends on the distance r to the axis (viz. non-uniform in the cross-section; in the present case, the heating source term is proportional to $\cos[(r/R)(\pi/2)]$, with R the radius of the upstream duct). The uniform and non-uniform heating cases correspond to the same overall power in the cross-section so that the comparison between runs 2D-1 and 2D-2 can provide relevant information on the effects of the inhomogeneity of the entropy perturbation. In the same way, comparing runs 2D-1 and 2D-3 will provide information about the sensitivity of the results to the outlet boundary condition while comparing 3D-1 and 2D-1 will be relevant to quantify 3-D effects. Finally, run 2D-4 is designed to mimic, as much as possible, the experimental downstream acoustic impedance which was evaluated by DLR. In all cases, the mesh resolution is enough to represent the propagation of the entropy and acoustic waves in the duct without significant dissipative and dispersive errors. The mesh size is in the order of 1 mm and allows a sufficient resolution of the perturbation size (of the order of 1200 mm, see Sec.2), including its sharp raising and falling edges (in the order of 100 mm). The 3-D mesh contains 1.2 million tetraedras, corresponding to approximately 15 cells in a cross-section. The mesh density is equivalent for all 2-D axisymmetric cases. As the present simulations are not meant to resolve the boundary layer and vortex dynamics, the grid resolution is limited and slip boundary conditions are imposed on the walls.

In order to mimic the experimental heating device, a source term is added to the energy equation. It reads:

$$\Phi(x,t) = \Phi_0 \frac{1}{2}\left[\tanh\left(\frac{x - x_0 + \ell_h/2}{d}\right)\tanh\left(-\frac{x - x_0 - \ell_h/2}{d}\right) + 1\right]\phi(t)$$

where $\ell_h = 30$ mm is representative of the length of the experimental heating zone and $d = 3$ mm enables to sufficiently smooth the source term to avoid numerical issues. Moreover, the average location x_0 of the source term has been consistently chosen at the location of the electrical device in the experiment (100 mm upstream of the nozzle throat). The temporal evolution $\phi(t)$ is defined as following:

$$\phi(t) = \begin{cases} 1 - e^{-\frac{t-t_0}{\tau}} & \text{if } t \in [t_0, t_0 + T_p] \\ \phi(t_0 + T_p)e^{-\frac{t-t_0}{\tau}} & \text{if } t > t_0 + T_p \end{cases}$$

where t_0 is the time when the electrical device is triggered, T_p is the pulse duration set to 100 ms and τ is a relaxation time of the pulse set to 8 ms. As shown in Fig. 3, these numerical parameters allow a fair representation of the temperature fluctuation produced in the DLR experiment. This temperature perturbation passes through the nozzle, gets distorted and yields pressure fluctuations which are analysed in the next section.

3.2. Numerical results

The time traces of the pressure computed 350 mm downstream of the throat (solid lines) are displayed in Fig. 4 for runs 2D-1 (top left), 2D-2 (top right), 2D-3 (bottom left) and 3D-1 (bottom right). They are compared to the experimental

Run	Geometry	Length	BC	Heating
3D-1	3D	short	non-reflecting	uniform
2D-1	2D axi	short	non-reflecting	uniform
2D-2	2D axi	short	non-reflecting	non-uniform
2D-3	2D axi	short	reflecting	uniform
2D-4	2D axi	long	finite impedance	uniform

Table 3: Main characteristics of the small-scale simulations.

signal (dashed lines). Clearly enough, these simulations do not reproduce the experimental data, neither in terms of amplitude, nor in terms of signal shape. For runs 2D-1 and 3D-1, the numerical pressure trace has a top-hat behavior similar to the temperature upstream fluctuation, while the experiment shows a wavy behavior at a frequency close to 30 Hz. Figure 4 also indicates that 3D-1 leads to results very similar to 2D-1, indicating that the disagreement between the 2D-1 computation and the experimental data cannot be attributed to three-dimensional effects. The same conclusion can be drawn by comparing 2D-1 and 2D-2 for the temperature inhomogeneity which appears to have no effect, at least for this configuration. On the other hand, Fig. 4 illustrates how large the effects of the downstream acoustic boundary condition can be. When a fully reflecting condition (2D-3),which imposes pressure is used instead of a non-reflecting one (2D-1), which essentially sets the incoming acoustic wave to zero at the outlet, the amplitude decreases drastically. More importantly, the shape of the signal is also strongly modified by the superposition of the downward and backward pressure waves. A wavy behavior is also obtained in run 2D-3, although with a characteristic amplitude and a frequency in quantitative disagreement with the experiment and the simulations reported by Mühlbauer *et al.* (20; 24) (Fig. 10 in this reference). The amplitude is all the more reduced as the computational exit duct is shortened.

The previous results suggest that the discrepancies observed in Fig. 4 might be related to an incorrect downstream acoustic impedance as already suggested by Mühlbauer *et al.* (20; 24) and Leyko *et al.* (25; 26). Indeed, the short computational domain and non-reflecting BC used in runs 2D-1, 2D-2 and 3D-1 would only be representative of the actual experimental conditions if a perfect anechoic system would have been used by Bake *et al.* (19). It should also be noted that a slight reflectivity of the outlet boundary condition in the simulation distorts the pressure responses that get damped around 0.1 s as in the URANS simulation by Mühlbauer *et al.* (24) (Fig. 11 in this reference), which stresses the high sensitivity of the simulations to the exit flow condition. Actually, Fig. 5 demonstrates that substantial reflection occured in the experiment, especially in the low-frequency range: the modulus of the reflection coefficient, defined as the ratio of the backward wave to forward wave at the outlet, is as large as 0.5 at 30 Hz, the typical frequency of the reflections observed in the experimental signal (see Fig. 4). Accounting for frequency-dependent reflection coefficient in a CFD code solving the flow equations in the time-domain is feasible. For example, the boundary condition proposed by Reymen *et al.* can be used. However, all these models have parameters that need to be fitted over a large frequency range on the actual experimental impedance, and a specific implementation in the CFD code is required. Similarly to what was proposed by Mühlbauer *et al.* (20; 24), a simpler approach has been followed in the present study. Instead of using a non-reflecting outlet boundary condition with zero entering wave L^-, it is common use to write the latter as a pressure difference times a relaxation coefficient κ (27), viz. $L^- = 2\kappa\Delta t(p_{\mathrm{ref}} - p_B)/(\rho c)$, with Δt the time step, p_B the nodal pressure at the outlet boundary and p_{ref} the reference pressure. In doing so, the outlet condition acts as a first-order low pass filter (28) whose cut-off frequency is proportional to κ and the acoustic reflection coefficient $\mathcal{R}_{\mathrm{out}}$ reads:

$$\mathcal{R}_{\mathrm{out}} = -\frac{1}{\imath\omega/\kappa + 1} \tag{1}$$

It is thus possible to tune the relaxation coefficient κ in order to reproduce the amplitude of the experimental reflection coefficient, at least in the low-frequency range. The length ℓ_{out} of the downstream duct is then tuned to mimic the experimental time delay as well as to compensate for the phase of the relaxation-based outlet partially reflecting condition. The experimental reflection coefficient is expressed here at the nozzle throat ($x = 0$) while the reflection coefficient of the numerical boundary condition, Eq. (1), is given at the end of the computational domain ($x = \ell_{\text{out}}$). Assuming the Mach number to be small in the outlet duct, the experimental reflection coefficient can be multiplied by $\exp(-2\imath\ell_{\text{out}}\omega/c)$ in order to shift it to the same position, at the end of the numerical domain ($x = \ell_{\text{out}}$). The experimental reflection coefficient obtained in this way is depicted in Fig. 5 where a fair agreement with the numerical one is apparent in the frequency range 20-40 Hz. For higher frequencies the general trend is kept and the experimental peak at about 140 Hz cannot be captured, since the present reflection coefficient behaves like a first-order filter only. The best-fit relaxation coefficient κ and length ℓ_{out} are close to 160 s^{-1} and 2100 mm respectively. As soon as this corrected impedance is used at the outlet, results (run 2D-4) improve drastically: Fig. 6 indicates that the numerical pressure signal is in better agreement with the measured one when accounting for the effective downstream boundary condition, and so for all positions of the pressure sensor downstream of the nozzle.

4. An analytical method for indirect noise computation

An analytical model for the indirect combustion noise was proposed by Marble and Candel (12), which focused on the generation and the transmission of flow perturbations (acoustic and entropy) through a steady non-uniform nozzle flow. Assuming a quasi-one-dimensional nozzle flow and quasi-steady perturbations (nozzle compactness), they established the relationships linking the different perturbations using first principles only: mass flow, energy and entropy conservations. These developments are reviewed below and extended to the case of a shock in a nozzle to obtain an analytical tool which completely describes the DLR experiment and can replace the numerical simulation. The extended analytical results giving relations between waves in all possible cases (unchoked insentropic nozzle, choked insentropic nozzle and shock in nozzle) are then used to obtain the pressure fluctuations in the EWG experiments. Partially reflective boundary conditions identical to those used in the LES cases are also introduced in the model both at the inlet and outlet of the domain. By comparing with the above simulations using the same inlet and outlet acoustic impedances for both numerical and theoretical calculations, the domain of validity of the compact nozzle assumption and the linear regime inherent to the analytical approach can be assessed.

4.1. Isentropic nozzle

An isentropic flow of a homogeneous gas of density ρ, velocity u, pressure p, constant specific heats c_p and $c_v = c_p/\gamma$ is assumed in a quasi-1-D adiabatic duct of cross-section area $\mathcal{A}(x)$ as shown in Fig. 7. In this case, the mass flow rate

$$\dot{m} = \rho u \mathcal{A}, \tag{2}$$

the stagnation temperature

$$T_t = T\left(1 + \frac{\gamma - 1}{2}\mathcal{M}^2\right), \tag{3}$$

and the entropy

$$s = c_v \ln\frac{p}{\rho^\gamma}, \tag{4}$$

are constant throughout the duct. Eqs. (2), (3) and (4) can be differentiated to yield the corresponding fluctuations:

$$\frac{\dot{m}'}{\dot{m}} = \frac{1}{\mathcal{M}}\frac{u'}{c} + \frac{p'}{\gamma p} - \frac{s'}{c_p} \tag{5}$$

$$\frac{T_t'}{T_t} = \frac{1}{1 + \frac{\gamma-1}{2}\mathcal{M}^2}\left[(\gamma - 1)\mathcal{M}\frac{u'}{c} + (\gamma - 1)\frac{p'}{\gamma p} + \frac{s'}{c_p}\right] \tag{6}$$

and

$$\frac{s'}{c_p} = \frac{p'}{\gamma p} - \frac{\rho'}{\rho}, \tag{7}$$

where the speed of sound $c = \sqrt{\gamma p/\rho}$ and the Mach number $\mathcal{M} = u/c$ have been introduced.

If the wavelengths of the perturbations are large compared with the axial dimension of the nozzle (compact nozzle assumption), there is no delay and distortion between the inlet and the outlet sections of the nozzle. As a result, the instantaneous values of the mass flow, the total temperature and the entropy are conserved throughout the nozzle at each instant, as displayed in Fig. 8. In other words, the compact nozzle assumption allows writing the following equations:

$$[T_t']_a^b = 0 \quad ; \quad [\dot{m}']_a^b = 0 \quad ; \quad [s']_a^b = 0 \tag{8}$$

where $[\ ]_a^b$ stands for the jump between downstream (index b) and upstream (index a) of the related object (subcritical nozzle, supercritical nozzle and normal shock). At this point, it is useful to introduce the following acoustic waves and reduced amplitudes (12):

$$P^+ = \frac{1}{2}\left(\frac{p'}{\gamma p} + \frac{u'}{c}\right) \quad ; \quad P^- = \frac{1}{2}\left(\frac{p'}{\gamma p} - \frac{u'}{c}\right) \quad ; \quad \sigma = \frac{s'}{c_p} \tag{9}$$

4.1.1. Unchoked nozzle

By combining Eqs. (8) with Eqs. (5), (6) and (7), the following set of three equations can be obtained:

$$\begin{aligned}
\left(1+\frac{1}{\mathcal{M}_a}\right)P_a^+ + \left(1-\frac{1}{\mathcal{M}_a}\right)P_a^- - \sigma_a &= \\
\left(1+\frac{1}{\mathcal{M}_b}\right)P_b^+ + \left(1-\frac{1}{\mathcal{M}_b}\right)P_b^- - \sigma_b & \\
\frac{(\gamma-1)(1+\mathcal{M}_a)}{1+\frac{\gamma-1}{2}\mathcal{M}_a^2}P_a^+ + \frac{(\gamma-1)(1-\mathcal{M}_a)}{1+\frac{\gamma-1}{2}\mathcal{M}_a^2}P_a^- + \frac{1}{1+\frac{\gamma-1}{2}\mathcal{M}_a^2}\sigma_a &= \\
\frac{(\gamma-1)(1+\mathcal{M}_b)}{1+\frac{\gamma-1}{2}\mathcal{M}_b^2}P_b^+ + \frac{(\gamma-1)(1-\mathcal{M}_b)}{1+\frac{\gamma-1}{2}\mathcal{M}_b^2}P_b^- + \frac{1}{1+\frac{\gamma-1}{2}\mathcal{M}_b^2}\sigma_b & \\
\sigma_a &= \sigma_b
\end{aligned} \tag{10}$$

In each of the previous equations, the left-hand-side involves the three waves (P_a^+, P_a^-, σ_a) upstream of the nozzle at the inlet and the right-hand-side the three waves (P_b^+, P_b^-, σ_b) downstream of the nozzle at the outlet. As shown in Fig. 7, these waves propagate either outward or inward (toward the nozzle) depending on the flow-characteristic directions at these subsonic boundaries. In the particular case where $P_a^+ \neq 0$, $\sigma_a = 0$ and $P_b^- = 0$ (the ingoing waves can be fixed freely), Eqs. (10) allow recovering the expression given in (12) for the acoustic response of the unchoked nozzle to an acoustic excitation (AA):

$$\frac{P_b^+}{P_a^+}(\mathrm{AA}) = \frac{2\mathcal{M}_b}{1+\mathcal{M}_b}\,\frac{1+\mathcal{M}_a}{\mathcal{M}_a+\mathcal{M}_b}\,\frac{1+\frac{1}{2}(\gamma-1)\mathcal{M}_b^2}{1+\frac{1}{2}(\gamma-1)\mathcal{M}_a\mathcal{M}_b} \tag{11}$$

In the same way, if $P_a^+ = 0$, $\sigma_a \neq 0$ and $P_b^- = 0$ are assumed, the acoustic response to an entropy perturbation (SA) is recovered as in (12), viz.:

$$\frac{P_b^+}{\sigma_a}(\mathrm{SA}) = \frac{\mathcal{M}_b-\mathcal{M}_a}{1+\mathcal{M}_b}\,\frac{\frac{1}{2}\mathcal{M}_b}{1+\frac{1}{2}(\gamma-1)\mathcal{M}_a\mathcal{M}_b} \tag{12}$$

4.1.2. Isentropic choked nozzle

In the case of an isentropic choked nozzle, the flow is subsonic in the convergent nozzle part and supersonic in the divergent nozzle part. In this case, the acoustic wave P_b^- leaves the domain and cannot be imposed anymore (Fig. 9). Two waves enter the domain, namely P_a^+ and σ_a, and four must be determined, namely three transmitted/generated waves (P_b^+, P_b^- and σ_b) and one reflected/generated wave (P_a^-). The critical mass flow equation is then introduced in order to close the problem ($\mathcal{A}^\star$ being the critical section area and $\dot{m}^\star$ being the critical mass flow):

$$\dot{m}^\star = \frac{p_{t1}}{\sqrt{\gamma r T_{t1}}}\mathcal{A}^\star\gamma\left(\frac{\gamma+1}{2}\right)^{-\frac{1}{2}\frac{\gamma+1}{\gamma-1}} \tag{13}$$

By first differentiating Eq. (13) and combining the result with Eq. (5), the following additional condition can be obtained for the fluctuations:

$$\frac{u'}{c} - \frac{\gamma-1}{2}\mathcal{M}\frac{p'}{\gamma p} - \frac{1}{2}\mathcal{M}\frac{s'}{c_p} = 0 \tag{14}$$

which can be used to complete Eqs. (8) and close the system. After some algebra the following expressions for the four outgoing waves can be obtained:

$$\begin{aligned}
\left(1-\frac{\gamma-1}{2}\mathcal{M}_a\right)P_a^+ - \left(1+\frac{\gamma-1}{2}\mathcal{M}_a\right)P_a^- - \frac{1}{2}\mathcal{M}_a\sigma_a &= 0\\
\left(1-\frac{\gamma-1}{2}\mathcal{M}_b\right)P_b^+ - \left(1+\frac{\gamma-1}{2}\mathcal{M}_b\right)P_b^- - \frac{1}{2}\mathcal{M}_b\sigma_a &= 0\\
P_a^+ + P_a^- &= P_b^+ + P_b^-\\
\sigma_a &= \sigma_b
\end{aligned} \tag{15}$$

Once again, in the particular case where $P_a^+ \neq 0$ and $\sigma_a = 0$, Eqs. (15) allow recovering the expression given in (12) for the acoustic response of the choked nozzle to an acoustic excitation (AA):

$$\frac{P_b^+}{P_a^+}(AA) = \frac{1 + \frac{\gamma-1}{2}\mathcal{M}_2}{1 + \frac{\gamma-1}{2}\mathcal{M}_1} \tag{16}$$

In the same way, if $P_a^+ = 0$ and $\sigma_a \neq 0$ are assumed, the acoustic response to an entropy perturbation (SA) is recovered as in (12), viz.:

$$\frac{P_b^+}{\sigma_a}(SA) = \frac{\mathcal{M}_2 - \mathcal{M}_1}{2} \frac{\frac{1}{2}}{1 + \frac{\gamma-1}{2}\mathcal{M}_1} \tag{17}$$

Yet, for all cases where the back-pressure is below the critical pressure $p^\star$ yielding the sonic throat, a residual shock stands in the diverging section of the choked nozzle, the mean flow is no longer isentropic and the interaction of the waves with the shock must be accounted for as shown in the next section.

4.2. Waves for a shock

Even though the detailed interaction of acoustic, entropy or vorticity waves with a shock wave is a complex flow phenomenon (29; 30), the wave propagation can be fully described analytically in a simplified quasi-one-dimensional situation (13). By construction the flow immediately upstream and downstream of a normal shock is supersonic and subsonic, respectively. Four waves are ingoing in this case (Fig. 10), namely P_a^+, P_a^-, σ_a and P_b^-, while only two propagate in the outward direction, viz. P_b^+ and σ_b. The derivation of the outgoing waves as a function of the ingoing ones builds upon the classical jump relations through a normal shock which only depend on the upstream Mach number:

$$\begin{aligned} \frac{p_b}{p_a} &= \frac{\gamma\mathcal{M}_a^2 - \frac{\gamma-1}{2}}{\frac{\gamma-1}{2}} \\ \frac{\rho_b}{\rho_a} &= \frac{\frac{\gamma-1}{2}\mathcal{M}_a^2}{1 + \frac{\gamma-1}{2}\mathcal{M}_a^2} \end{aligned} \tag{18}$$

For small perturbations, and noting that $\mathcal{M}_a'/\mathcal{M}_a$ is related to the shock speed motion $-u_s'/u_a$ since the Mach number depends only on the cross-section area ratio in the supersonic regime, Eqs. (18) yield:

$$\begin{aligned}\left(\frac{p'}{\gamma p}\right)_b - \left(\frac{p'}{\gamma p}\right)_a &= -\frac{2\mathcal{M}_a^2}{\gamma \mathcal{M}_a^2 - \frac{\gamma-1}{2}}\left(\frac{u'_s}{u_a}\right) \\ \left(\frac{\rho'}{\rho}\right)_b - \left(\frac{\rho'}{\rho}\right)_a &= -\frac{2}{1+\frac{\gamma-1}{2}\mathcal{M}_a^2}\left(\frac{u'_s}{u_a}\right)\end{aligned} \tag{19}$$

The conservation of the mass-flow in the reference frame moving with the shock leads, for small perturbations, to:

$$\left(\frac{\rho'}{\rho}\right)_a + \frac{1}{\mathcal{M}_a}\left(\frac{u'}{c}\right)_a = \left(\frac{\rho'}{\rho}\right)_b + \frac{1}{\mathcal{M}_b}\left(\frac{u'}{c}\right)_b + \frac{1-\mathcal{M}_a^2}{1+\frac{\gamma-1}{2}\mathcal{M}_a^2}\left(\frac{u'_s}{u_a}\right) \tag{20}$$

Equations (19) and (20) are first combined to eliminate u'_s/u_a, noting that $[(\gamma+1)\mathcal{M}_a^2]/[(\gamma-1)\mathcal{M}_a^2+2] = \mathcal{M}_b^2$. Then, the pressure, mass-density and velocity perturbations in the two resulting equations are replaced by the waves defined in Eq. (9), and the following relations for the shock are finally obtained:

$$\begin{aligned}\left(1+\mathcal{M}_a^2+2\mathcal{M}_a^2\mathcal{M}_b\right)P_b^+ + \left(1+\mathcal{M}_a^2-2\mathcal{M}_a^2\mathcal{M}_b\right)P_b^- &= \\ \left(1+\mathcal{M}_a^2+2\mathcal{M}_a\mathcal{M}_b^2\right)P_a^+ + (1+\mathcal{M}_a^2-2\mathcal{M}_a\mathcal{M}_b^2)\,P_a^- & \\ \left(P_b^+ + P_b^- - P_a^+ - P_a^-\right)(\gamma-1)\frac{\left(\mathcal{M}_a^2-1\right)^2}{\left[(\gamma-1)\mathcal{M}_a^2+2\right]\mathcal{M}_a^2} &= \sigma_b - \sigma_a\end{aligned} \tag{21}$$

Equations (21) generalize the result given in (12) to the case where P_b^- is not zero and indicate that entropy fluctuations can be generated by the interaction between an acoustic wave and a shock. In the case of a perfectly reflecting outlet, a cycle of acoustic and entropic waves can be produced, which may yield an entropic-acoustic instability as described by Foglizzo and Tagger (31) in shocked accretion flows.

4.3. Application to the DLR configuration

Having derived the general transfer functions for the different types of flows in a compact converging-diverging nozzle, the relationships mimicking the EWG experiment can be derived based on the notations of Fig. 11. As mentioned above, the present focus is on the reference test case 1 in Bake *et al.* (19) of a choked nozzle with a maximum exit Mach number of 1.32. The supercritical nozzle starts at point 1 at the nozzle inlet and finishes at point 2 in the divergent section where the normal shock takes place. The normal shock relations are defined between point 2 and 3 and finally the subcritical nozzle starts at point 3, downstream of the shock, and finishes at point 4 at the end of the divergent region. Only the entropy wave generated by the electrical device, σ_1, is taken into account at the inlet. The upstream part of the nozzle with the large settling chamber is represented in a general manner by the reflection coefficient $\mathcal{R}_1 = P_1^+/P_1^-$. The subsonic nozzle outlet is also represented ~~in a general manner~~ by the reflection coefficient $\mathcal{R}_4 = P_4^-/P_4^+$.

For the supercritical nozzle upstream [Eqs. (15)], the in-going and out-going acoustic waves P_2^+ and P_2^- are given by

$$\begin{aligned} P_2^+ &= \xi_2^+ \sigma_1 \\ P_2^- &= \xi_2^- \sigma_1 \end{aligned}$$

with:

$$\xi_2^+ = \frac{\left[\mathcal{M}_2 - \mathcal{M}_1 - \mathcal{R}_1(\mathcal{M}_2 + \mathcal{M}_1)\right]\frac{1}{2}}{2\left[1 + \frac{\gamma-1}{2}\mathcal{M}_1 - \mathcal{R}_1(1 - \frac{\gamma-1}{2}\mathcal{M}_1)\right]} \tag{22}$$

$$\xi_2^- = -\frac{\left[\mathcal{M}_2 + \mathcal{M}_1 - \mathcal{R}_1(\mathcal{M}_2 - \mathcal{M}_1)\right]\frac{1}{2}}{2\left[1 + \frac{\gamma-1}{2}\mathcal{M}_1 - \mathcal{R}_1(1 - \frac{\gamma-1}{2}\mathcal{M}_1)\right]} \tag{23}$$

For the particular case where no reflection is considered at the inlet ($\mathcal{R}_1 = 0$) Eqs. (22) and (23) reduce to relations that can be found in (12)

$$\begin{aligned} \xi_2^+ &= \frac{\mathcal{M}_2 - \mathcal{M}_1}{2}\frac{\frac{1}{2}}{1 + \frac{\gamma-1}{2}\mathcal{M}_1} \\ \xi_2^- &= -\frac{\mathcal{M}_2 + \mathcal{M}_1}{2}\frac{\frac{1}{2}}{1 + \frac{\gamma-1}{2}\mathcal{M}_1} \end{aligned}$$

With the notations

$$\begin{aligned} \alpha_3^\pm &= 1 + \mathcal{M}_2^2 \pm 2\mathcal{M}_2^2\mathcal{M}_3 \\ \alpha_2^\pm &= 1 + \mathcal{M}_2^2 \pm 2\mathcal{M}_2\mathcal{M}_3^2 \end{aligned}$$

and

$$\Sigma = (\gamma - 1)\frac{\left(\mathcal{M}_2^2 - 1\right)^2}{\left[(\gamma - 1)\mathcal{M}_2^2 + 2\right]\mathcal{M}_2^2}$$

at the normal shock [Eqs. (21)], the following relationships hold

$$\alpha_3^+ P_3^+ + \alpha_3^- P_3^- = \alpha_2^+ P_2^+ + \alpha_2^- P_2^- \tag{24}$$

and

$$\left(P_3^+ + P_3^- - P_2^+ - P_2^-\right)\Sigma = \sigma_3 - \sigma_1 \tag{25}$$

For the subcritical nozzle downstream [Eq. (10)], the in-going and out-going acoustic waves P_3^+, P_3^-, P_4^+ and P_4^- are given by

$$\begin{aligned} \beta_3^+ P_3^+ + \beta_3^- P_3^- &= \beta_4^+ P_4^+ + \beta_4^- P_4^- \\ \delta_3^+ P_3^+ + \delta_3^- P_3^- &= \delta_4^+ P_4^+ + \delta_4^- P_4^- + (\zeta_3 - \zeta_4)\ \sigma_3 \end{aligned} \tag{26}$$

with

$$\beta^\pm = 1 \pm \frac{1}{\mathcal{M}}; \qquad \delta^\pm = \frac{(\gamma-1)\ (1 \pm \mathcal{M})}{1 + \frac{\gamma-1}{2}\ \mathcal{M}^2}; \qquad \zeta = \frac{1}{1 + \frac{\gamma-1}{2}\ \mathcal{M}^2}$$

Eqs. (24) and (25) combined with Eqs. (26) yield the following coupled system of equations

$$\begin{bmatrix} \alpha_3^+ & \alpha_3^- & 0 & 0 \\ \Sigma & \Sigma & -1 & 0 \\ \beta_3^+ & \beta_3^- & 0 & -\left(\beta_4^+ \mathcal{R}_4 + \beta_4^-\right) \\ \delta_3^+ & \delta_3^- & \zeta_4 - \zeta_3 & -\left(\delta_4^+ \mathcal{R}_4 + \delta_4^-\right) \end{bmatrix} \begin{bmatrix} P_3^+ \\ P_3^- \\ \sigma_3 \\ P_4^- \end{bmatrix} = \dots$$

$$\begin{bmatrix} \alpha_2^+ \xi_2^+ + \alpha_2^- \xi_2^- \\ \Sigma\left(\xi_2^+ + \xi_2^-\right) - 1 \\ 0 \\ 0 \end{bmatrix} \sigma_1 \tag{27}$$

which provide the remaining four unknowns.

4.4. Analytical results

Solving for the equations in Sec. 4.3 yields the time traces of the pressure fluctuations downstream of the throat. The acoustic waves in the duct upstream of the nozzle are assumed to propagate at the speed of sound since the Mach number is small, so that one can write $\mathcal{R}_1 = \mathcal{R}_{\text{in}} \exp(-2\imath \ell_{\text{in}} \omega / c)$, where $\mathcal{R}_{\text{in}}$ is the reflection coefficient at the duct inlet. The cross-section area of the settling chamber being large compared to the cross-section area of the duct, the pressure fluctuations can be assumed negligible for low-frequencies and thus one can write $\mathcal{R}_{\text{in}} = -1$. For a more general model, the plenum could also be considered as an extended Helmholtz resonator as described in Bake *et al.* (18). Similarly, the reflection coefficient of the subsonic nozzle outlet can be defined with the outlet reflection coefficient of the numerical simulation as $\mathcal{R}_4 = \mathcal{R}_{\text{out}} \exp(-2\imath \ell_{\text{out}} \omega / c)$ to match the condition used in the computation. The time evolution of the entropy wave is proportional to the one imposed in the source term of the energy equation in the numerical computation. The discrete Fourier transform of this signal $\sigma_1(\omega_k)$ is used for the analytical calculations.

Calculations [solving Eq. (27)] are performed for each frequency in order to take into account the frequency-dependence of the inlet and outlet boundary conditions, but the different nozzle elements are still assumed to be compact. Since a shock is present in the divergent part of the nozzle, the supercritical section (from 1 to 2) can be treated independently of the downstream elements, and provide explicitly the waves P_2^+, P_2^- and σ_2 entering the downstream elements. The shock (from 2 to 3) and the subcritical nozzle with the outlet BC (from 3 to 4) have to be treated together since most waves are coupled to yield the full system shown in Eq. (27). Finally, the reduced pressure fluctuation $[p'/\gamma p(\omega_k)]_4$ is obtained in the frequency domain as a function of the four Mach numbers $\mathcal{M}_1$, $\mathcal{M}_2$, $\mathcal{M}_3$ and $\mathcal{M}_4$ ($\mathcal{M}_3$ and $\mathcal{M}_4$ are actually linked by the shock relations), the reflection coefficients $\mathcal{R}_{\text{in}}(\omega_k)$, $\mathcal{R}_{\text{out}}(\omega_k)$ and the reduced entropy fluctuation $\sigma_1(\omega_k)$.

The time evolutions of the pressure fluctuations reconstructed from the analytical calculations (inverse discrete Fourier transform) are compared to the numerical computations in two cases at the outlet: the non-reflecting case on the one hand (run 2D-1), and the *real* reflecting case with the set of parameters of the tuned reflection coefficient (κ and ℓ_{out}) on the other hand (run 2D-4). Figure 12 shows these comparisons when no reflection is considered at the inlet. A good agreement is found which shows that the EWG experiment (for this regime) is essentially driven by linear quasi-1-D acoustics. Yet, the levels of the analytical calculation are slightly under-predicted. When considering a more realistic impedance at the inlet [$\mathcal{R}_1 = -\exp(-2\imath\ell_{\text{in}}\omega/c)$], Fig. 13 shows that the levels are now well recovered for both calculations with the two different outlet boundary conditions.

Finally, the analytical method can also be used to suggest improvements to the experimental set-up which would allow a clear separation of the indirect noise pressure signal and of acoustic reflection. An obvious solution would be to make the inlet and outlet termination fully anechoic to attenuate the reflections. This is difficult to achieve in practice, and a simpler solution is to perform the split between generated and reflected waves by either changing the duration of the temperature pulse upstream or modifying the length of the upstream and downstream ducts to increase the waves travel times. If one considers the original pulse duration T_p of 100 ms, the length of the ducts upstream and downstream of the nozzle would have to be of the order of 35 m to avoid interaction with the reflected waves before 200 ms. This is probably difficult to establish on the real experimental set-up. But, if shorter pulses are generated ($T_p = 5$ ms and to preserve the signal shape $\tau = 0.4$ ms) and if the inlet duct length is of the order of the outlet one ($\ell_{\text{in}} = 2100$ mm), the two emitted acoustic waves (upstream and downstream) can be separated from the reflected waves if one considers only the waves travel durations. For this last case, the analytical calculations show that the duration between two pulses has to be increased until about 10 s if one wants the cycle of reflections, to be sufficiently attenuated to avoid perturbation of the theoretical pressure signal. One can see Fig. 14 the temporal evolution of the pressure fluctuation with the previous parameters. These analytical calculations were performed with and without reflections at the inlet and outlet. The pressure signal is not perturbed until the noise generation is finished ($t \approx 20$ ms) so that the true indirect noise could be investigated in the absence of interference from reflected waves.

5. Conclusions

The DLR EWG experiment of Bake *et al.* (19) has been studied numerically and analytically. Simulations have been performed both in an axisymmetric and a fully three-dimensional configuration with various duct lengths and boundary conditions accounting for acoustic reflections. In parallel, an analytical model of the full experiment, based on an extension of the theory for compact nozzles originally derived by Marble and Candel (12), has been constructed: it takes into account the general acoustic impedances both at the inlet and outlet of the experimental set-up. The numerical and analytical analysis performed in this study demonstrate that the pressure signals obtained in the EWG experiment by Bake *et al.* (17) result from two main mechanisms: the entropy-to-acoustic conversion due the strong mean velocity gradient in the nozzle, including the normal shock that stands just downstream of the throat on the one hand; the acoustic reflection within the exhaust system downstream of the nozzle and test section on the other hand.The first mechanism is the indirect noise source and was the objective of the experiment. The second mechanism, however, is an undesired perturbation due to the non perfectly anechoic termination of the outlet, as well as the reflective inlet, which both must be understood to extract indirect noise signal from the measurements. The analysis also shows that, in the low-frequency range investigated, only 1-D planar waves are present and the compact nozzle approximation is valid, even for the entropy perturbations. As a result, the pressure signals observed experimentally and numerically can be nicely reproduced by a simple quasi-1-D analytical model derived in the low-frequency limit for the nozzle. This simpler model can also provide some guidance on how to re-design the experiment to remove or minimize the acoustic reflections in the measured pressure signals.

Acknowledgements

The authors gratefully acknowledge support from the *Centre Informatique National de l'Enseignement Supérieur* (CINES) for the computer resources and the DLR for making the experimental data available. This work was partly funded by the *Fondation Nationale de Recherche pour l'Aéronautique et l'Espace* (FNRAE) within the BRUCO Project and by SNECMA (SAFRAN Group).

References

[1] S. Bragg, Combustion noise, Journal of Institute of Fuel 36 (1963) 12–16.

[2] W. Strahle, On combustion generated noise, Journal of Fluid Mechanics 49 (2) (1971) 399–414.

[3] H. A. Hassan, Scaling of combustion-generated noise., J. Fluid Mech. 66 (3) (1974) 445–453.

[4] T. Lieuwen, S. Mohan, R. Rajaram, Preetham, Acoustic radiation from weakly wrinkled premixed flames, Combustion and Flame 144 (2006) 360–369.

[5] M. Ihme, H. Pitsch, D. Bodony, Radiation of noise in turbulent non-premixed flames, Proceedings of the Combustion Institute 32 (1) (2008) 1545–1553.

[6] S. Candel, Analytical studies of some acoustic problems of jet engines., Ph.D. thesis, California Institute of Technology, Pasadena, California (1972).

[7] M. Leyko, F. Nicoud, T. Poinsot, Comparison of direct and indirect combustion noise mechanisms in a model combustor, AIAA Journal 47 (11) (2009) 2709–2716.

[8] W. Strahle, M. Muthukrishnan, Thermocouple time constant measurement by cross power spectra, AIAA Journal 14 (11) (1976) 1642–1644.

[9] M. Bohn, Response of a subsonic nozzle to acoustic and entropy disturbances, Journal of Sound and Vibration 52 (2) (1977) 283–297.

[10] M. Muthukrishnan, W. Strahle, D. Neale, Separation of hydrodynamic, entropy, and combustion noise in a gas turbine combustor, AIAA Journal 16 (4) (1978) 320–327.

[11] W. Strahle, Combustion noise, Progress in Energy and Combustion Science 4 (3) (1978) 157–176.

[12] F. Marble, S. Candel, Acoustic disturbances from gas nonuniformities convected through a nozzle, Journal of Sound and Vibration 55 (1977) 225–243.

[13] W. Moase, M. Brear, C. Manzie, The forced response of choked nozzles and supersonic diffusers, Journal of Fluid Mechanics 585 (2007) 281–304.

[14] S. R. Stow, A. P. Dowling, T. P. Hynes, Reflection of circumferential modes in a choked nozzle, Journal of Fluid Mechanics 467 (2002) 215–239.

[15] F. Bake, U. Michel, I. Röhle, C. Richter, F. Thiele, M. Liu, B. Noll., Indirect combustion noise generation in gas turbines, in: 11th AIAA/CEAS Aeroacoustics Conference, AIAA-2005-2830, Monterey, CA, 2005.

[16] F. Bake, U. Michel, I. Röhle, Investigation of entropy noise in aero-engine combustors, Journal of Engineering for Gas Turbines and Power 129 (2) (2007) 370–376.
URL `http://elib.dlr.de/49128`

[17] F. Bake, N. Kings, I. Röhle, Fundamental mechanism of entropy noise in aero-engines: Experimental investigation, Journal of Engineering for Gas Turbines and Power 130 (1) (2008) 011202–1 – 011202–6.
URL `http://elib.dlr.de/57707`

[18] F. Bake, N. Kings, A. Fischer, I. Röhle, Experimental investigation of the entropy noise mechanism in aero-engines, International Journal of Aeroacoustics 8 (1) (2009) 125–142.

[19] F. Bake, C. Richter, B. Mühlbauer, N. Kings, I. Röhle, F. Thiele, B. Noll, The entropy wave generator (EWG): A reference case on entropy noise, Journal of Sound and Vibration 326 (2009) 574–598.

[20] B. Mühlbauer, B. Noll, M. Aigner, Numerical investigation of entropy noise and its acoustic sources in aero-engines, in: ASME Turbo Expo 2008, Vol. GT2008-50321, Berlin, Germany, 2008.

[21] P. Schmitt, T. Poinsot, B. Schuermans, K. P. Geigle, Large-eddy simulation and experimental study of heat transfer, nitric oxide emissions and combustion instability in a swirled turbulent high-pressure burner, Journal of Fluid Mechanics 570 (2007) 17–46.

[22] T. Poinsot, D. Veynante, Theoretical and Numerical Combustion, R.T. Edwards, 2nd edition, 2005.

[23] O. Colin, M. Rudgyard, Development of high-order Taylor-Galerkin schemes for unsteady calculations, Journal of Computational Physics 162 (2) (2000) 338–371.

[24] B. Mühlbauer, B. Noll, M. Aigner, Numerical investigation of the fundamental mechanism for entropy noise generation in aero-engines, Acta Acustica united with Acustica 95 (2009) 470–478.

[25] M. Leyko, F. Nicoud, S. Moreau, T. Poinsot, Numerical and analytical investigation of the indirect noise in a nozzle, in: Proceedings of the Summer Program, Center for Turbulence Research, NASA AMES, Stanford University, USA, 2008, pp. 343–354.

[26] M. Leyko, F. Nicoud, S. Moreau, T. Poinsot, Numerical and analytical investigation of the indirect combustion noise in a nozzle, Comptes Rendus Mécanique 337 (2009) 415–425.

[27] T. Poinsot, S. Lele, Boundary conditions for direct simulations of compressible viscous flows, Journal of Computational Physics 101 (1) (1992) 104–129.

[28] L. Selle, F. Nicoud, T. Poinsot, Actual impedance of nonreflecting boundary conditions: Implications for computation of resonators, AIAA Journal 42 (5) (2004) 958–964.

[29] K. Mahesh, S. Lee, S. Lele, P. Moin, The interaction of an isotropic field of acoustic waves with a shock wave, Journal of Fluid Mechanics 300 (1995) 383–407.

[30] K. Mahesh, S. Lele, P. Moin, The influence of entropy fluctuations on the interaction of turbulence with a shock, Journal of Fluid Mechanics 334 (1997) 353–379.

[31] T. Foglizzo, M. Tagger, Entropic-acoustic instability in shocked accretion flows, Astronomy and Astrophysics 363 (2000) 174–183.

List of Figures

List of Tables

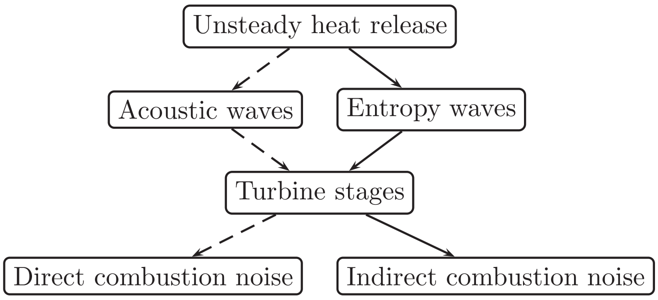

Figure 1: The two main mechanisms for noise generation from confined flames: direct (– – – –) and indirect (———) noise.

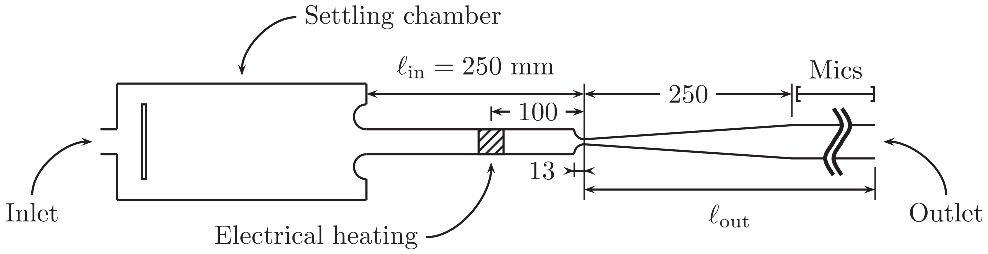

Figure 2: Sketch of the Entropy Wave Generator experimental set-up (lengths are given in mm). Short configuration: $\ell_{\mathrm{out}} = 500$ mm; Long configuration: $\ell_{\mathrm{out}} = 2100$ mm

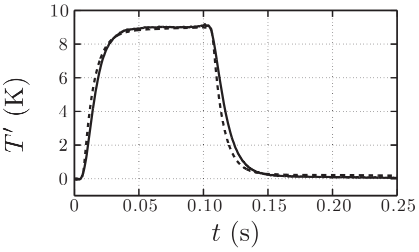

Figure 3: Time traces of the experimental (———) and numerical (- - - -) temperature downstream of the heating location.

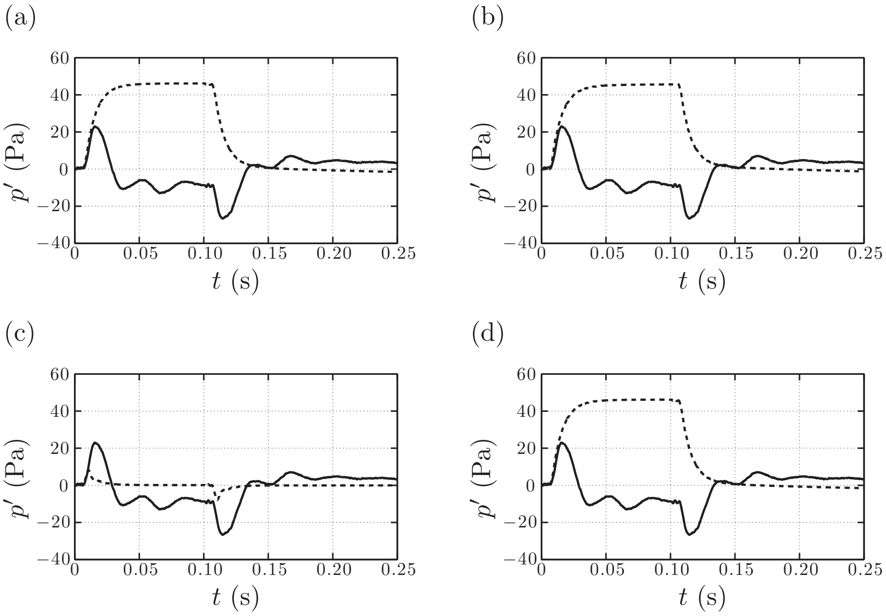

Figure 4: Time traces of the fluctuating pressure 350 mm downstream of the nozzle. Experimental data: ——— ; Numerical result: - - - - . (a) Run 2D-1; (b) Run 2D-2; (c) Run 2D-3; (d) Run 3D-1.

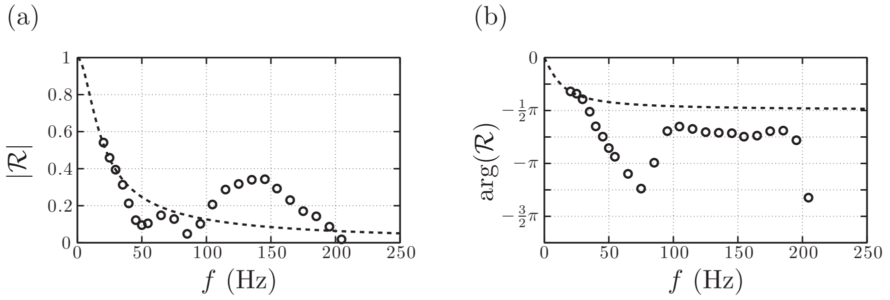

Figure 5: Experimental reflection coefficient shifted 2100 mm downstream of the nozzle throat and numerical reflection coefficient. Shifted experimental data: ○ ; Tuned relaxation coefficient: – – – – . (a) Modulus; (b) Argument.

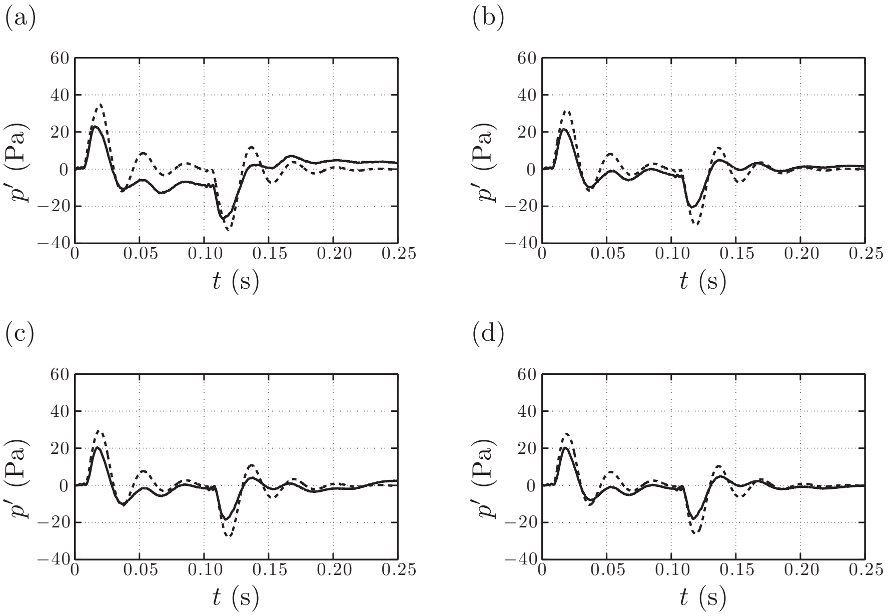

Figure 6: Time traces of the fluctuating pressure downstream of the nozzle. Experimental data: ——— ; Run 2D-4: - - - - . Distance downstream of the nozzle: (a) 350 mm; (b) 730 mm; (c) 975 mm; (d) 1150 mm.

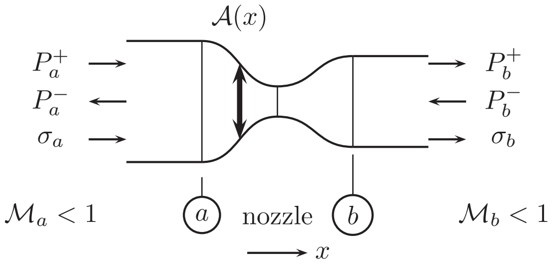

Figure 7: Sketch of the unchoked nozzle.

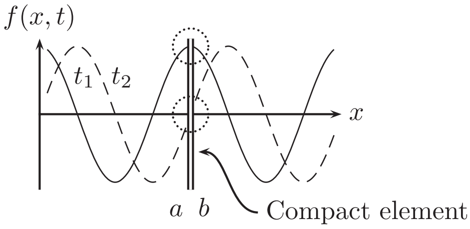

Figure 8: Compact element illustration: The quantity f, conserved throughout the element, is the same in upstream (a) and downstream (b) part of the compact element sketched by the vertical lines, at each instant t_1 and t_2.

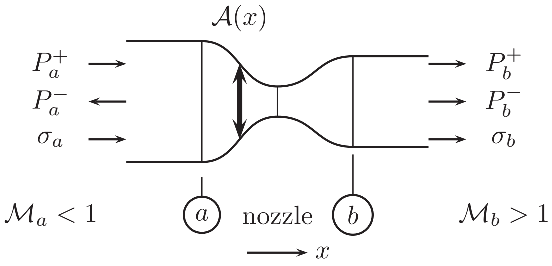

Figure 9: Sketch of the isentropic choked nozzle.

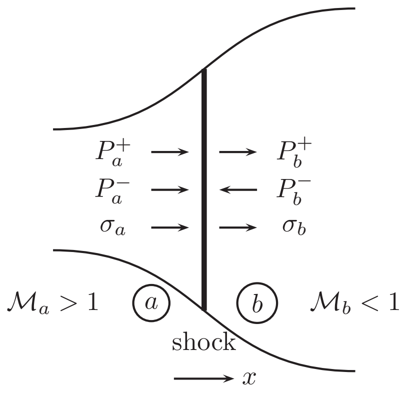

Figure 10: Sketch of the supersonic flow with normal shock.

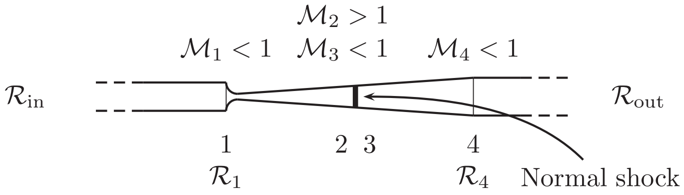

Figure 11: Description of the analytic approach

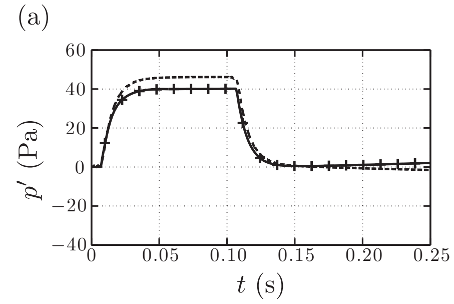

Figure 12: Time traces of the fluctuating pressure 350 mm downstream of the nozzle. Numerical results: $----$; Analytical results without reflections at the inlet and $\ell_{\text{out}} = 2100$ mm: $-+-$. (a) Non-reflecting case (Analytic compared to Run 2D-1); (b) Finite impedance case (Analytic compared to Run 2D-4).

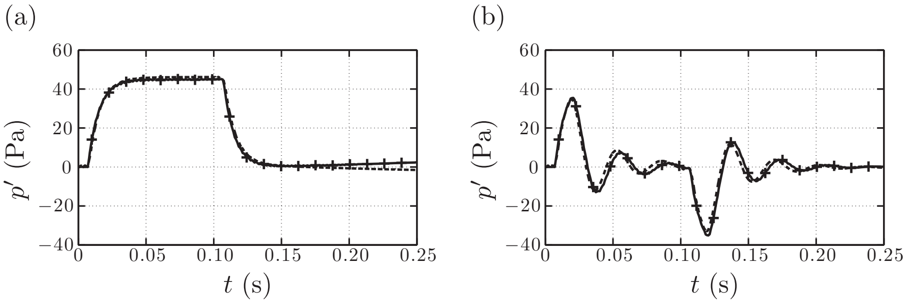

Figure 13: Time traces of the fluctuating pressure 350 mm downstream of the nozzle. Numerical results: ‒ ‒ ‒ ‒ ; Analytical results with reflections at the inlet and $\ell_{\text{out}} = 2100$ mm: $- + -$. (a) Non-reflecting case (Analytic compared to Run 2D-1); (b) Finite impedance case (Analytic compared to Run 2D-4).

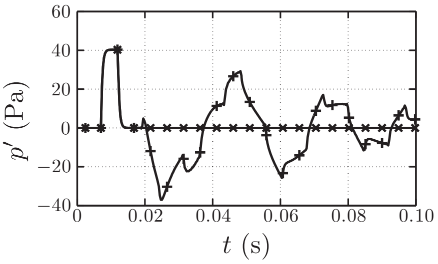

Figure 14: Analytical time traces of the fluctuating pressure downstream of the nozzle with shorter pulse duration. Totally non-reflecting at inlet and outlet: $- \times -$; Reflections at inlet and outlet: $- + -$.

Assessment of combustion noise in a premixed swirled combustor via Large-eddy simulation

Camilo F. Silva* and Matthieu Leyko †
CERFACS, 31057 Toulouse, France
Franck Nicoud ‡
Université Montpellier II, 34095 Montpellier, France
Stéphane Moreau §
Université Sherbrooke, 2500, boul. de l'Université Sherbrooke (Québec), Canada J1K 2R1

Abstract

Today, much of the current effort in the field of combustion noise is the development of efficient numerical tools to calculate the noise radiated by flames. Although unsteady CFD methods such as LES or DNS can directly provide the acoustic field radiated by noise sources, this evaluation is limited to small domains due to high computational costs. Hybrid methods have been developed to overcome this limitation. In these schemes, the noise sources are decoupled from the radiated sound. The sources are still calculated by DNS or LES codes whereas the radiated sound is evaluated by acoustic codes.

In the present paper the assessment of combustion noise is conducted by both direct (LES) and hybrid computations in a premixed swirled combustor. Some comparisons of the sound pressure levels resulting from both approaches will be shown, and the main differences between the two methods will be explained.

keywords: combustion noise, acoustic analogy, direct computations, hybrid computations.

1 Introduction

Large Eddy Simulation (LES) has become today an important tool for the simulation and posteriori analysis of turbulent flows. It offers the best promise in the foreseeable future for the estimation of noise from flows at Reynolds Numbers of interest in both open and closed systems. In aeroacoustics, LES plays an important role in the study of aerodynamical generated noise of numerous practical cases that range from air jets, high-lift devices or landing gears in an aircraft to the rear-view mirror of a car or the fan of a wind mill [1, 2]. Thermoacoustics is, on the contrary, less understood than aeroacoustics. This is due to the different physical phenomena implied such as the addition of unsteady heat release to the already turbulent flow. Still LES has been successfully applied to partially premixed and non-premixed open flames [3, 4] as well as in more complex cases such as gas turbine combustors. [5]

---

[*] Corresponding author. Ph.D. Student, CFD Team, 42, Av. Gaspard Coriolis; silva@cerfacs.fr. Tel: (33).(0)5.61.19.31.10

[†] Ph.D. Student, CFD Team, 42, Av. Gaspard Coriolis; leyko@cerfacs.fr

[‡] Professor, Université Montpellier II, I3M - CNRS UMR 5149 - CC51, franck.nicoud@univ-montp2.fr

[§] Professor, GAUS, Mechanical Engineering Department, Université de Sherbrooke, stephane.moreau@usherbrooke.ca.

Computational techniques for the estimation of sound can be classified into two broad categories: direct computations and indirect, or hybrid, computations. LES is well presented in these two categories. Direct computations resolve the flow field together with the sound radiation. A compressible LES code is therefore required in addition to high-resolution numerical schemes in order to minimize both dispersion and dissipation. Moreover, the computational domain must be large enough to include the sources of noise as well as part of the acoustic near field [6]. Very expensive computational costs can arise since hydrodynamic and acoustic scales differ to a large amount in typical applications where the Mach number is moderate. This is even more true when dealing with thermoacoustics since the transport equation of each species must be considered in order to solve the problem of compressible multicomponent reactive flows.

In hybrid approaches, the computation of sound is made at two different levels:

- model the sources of noise which requires a proper estimation of the flow and the flame dynamic properties. These sources are assumed independent of any acoustic quantity.
- predict the far field acoustic radiation due to the different noise sources. Acoustic propagation is calculated based on equations relevant to acoustic phenomena. The derivation of a wave equation governing sound propagation in an arbitrary mean flow (and therefore accounting for mean flow-acoustic interactions) remains a difficult and controversial task in aeroacoustics [7].

Since the sources of noise and the acoustic radiation are computed separately, the computational effort is less critical than in direct sound computations. The sources of noise can be computed by numerical codes with lower-resolution schemes provided that numerical dissipation is carefully controlled [8] and that the acoustic source formulations fulfill true radiation characteristics (dipole, quadripole, etc). Regarding thermoacoustics, and more specifically combustion noise, it has been established that turbulent flames behave like low frequency radiators of essentially monopole type [9]. After the different sources have been computed, the sound radiation, due to these sources, is evaluated by solving the wave operator coming from an acoustic analogy equation based on acoustic theories such as the Lighthill analogy [10], the Strahle formulation [11] (that follows Lighthill procedure and takes into account the conservation equation of multicomponent reacting flows), the Phillips analogy [12] or more recently the Linearized Euler equations or its APE formulation [13, 14]

These theoretical formulations are satisfactory for open systems, i.e. when the acoustic fluctuations produced by the source propagate to the infinite and anechoic far-field. Moreover, in these cases, it is relatively easy to distinguish pure acoustics from hydrodynamic pressure fluctuations in the region of interest (farfield): hydrodynamic pressure fluctuations are negligible in the far field since they typically decay at least as the inverse third power of the distance to the sources [15]. Less is known about aeroacoustics in confined domains where acoustic and hydroynamic pressure fluctuations are both present. Interesting developments have been done to account for turbulence-body interaction [16, 17] . More recently, Schram used a modified Curle's analogy combined with a boundary element method (BEM) for evaluating the acoustic field produced by a non-compact turbulent source in a confined domain[18].

In the field of thermo-acoustics, it seems that no significative work has been done for evaluating the noise produced by confined flames using hybrid approaches. In reactive flows, confined systems might present an important interaction between the flame, the turbulent flow and the walls of the system. However if this interaction is not strongly present, one can assume that the flame is independent of the acoustic field generated and acoustic analogies should apply. The general objective of this study is to investigate whether acoustic analogies might be considered for the evaluation of noise in confined domains.

2 Combustion noise through Phillips' analogy

The first attempt to include inhomogeneities of the mean flow into the acoustic wave operator is due to Phillips [19] who derived the following expression:

$$\begin{aligned}\frac{d^2\pi}{dt^2} - \frac{\partial}{\partial x_i}\left(c^2\frac{\partial \pi}{\partial x_i}\right) = \frac{\partial u_i}{\partial x_j}\frac{\partial u_j}{\partial x_i} + \frac{d}{dt}\left(\frac{\gamma-1}{\rho c^2}\dot{\omega}_T\right) \\ + \frac{d}{dt}\left[\frac{\gamma-1}{\rho c^2}\left(\nabla\cdot(\lambda\nabla T) - \rho\sum_k Y_k c_{p,k}\mathbf{v}_k\cdot\nabla T + \tau : \nabla\mathbf{u}\right)\right] \\ - \frac{\partial}{\partial x_i}\left(\frac{1}{\rho}\frac{\partial \tau_{ij}}{\partial x_j}\right) + \frac{d^2}{dt^2}(\ln r)\end{aligned} \tag{1}$$

where π is function of the logarithm of the pressure $\pi = (1/\gamma)\ln(p/p_\infty)$. The first term on the RHS is related to the noise created by turbulence. The second term is the monopole source of noise due to the unsteady heat release induced by the flame. The third one is linked to the noise produced by molecular transport whereas the gradient of the viscous tensor appears in the fourth term. Finally, the last term is known as the non-isomolar combustion source of noise.

In order to simplify this equation, one may consider different realistic assumptions in order to evaluate the acoustics for low mach number reactive systems [20]. Therefore, it is stated that

- The pressure level of the oscillations are small compared to the local mean pressure. $p'/p_0 \ll 1$.
- The system is nearly isobaric so that $p_0 \approx const.$
- The mean flow is small so that the convective terms in the equation are negligible.

As a consequence, the acoustic wave equation for low mach number reacting flows reads

$$\nabla\cdot(c_0^2\nabla p') - \frac{\partial^2 p'}{\partial t^2} = -(\gamma-1)\frac{\partial \dot{q}'}{\partial t} - \gamma p_0 \nabla\boldsymbol{v} : \nabla\boldsymbol{v} + \frac{\gamma p_0}{W_0}\frac{\partial^2 W'}{\partial t^2} \tag{2}$$

where c_0, p, γ, $\dot{q}$, $\boldsymbol{v}$, W represent respectivelly the speed of sound, the pressure, heat capacity ratio, the heat release rate, the velocity vector and the mixture molar weight. The symbols $()_0$ and $()'$ define respectively mean quantities and fluctuation quantities. As it can be noticed in the left hand side of eq. 2, the speed of sound c is placed inside the divergence operator. This ensures to capture acoustic fluctuations with strong variation of the mean temperature as it occurs close to the flame front.

In the combustion case exposed in this paper, the non-isomolar combustion noise does not play an important role since the reactant mixtures are highly dilluted in nitrogen. Further on, the aerodynamic source of noise is considered small with respect to the noise source associated with the perturbation of the heat release rate [21]. The inhomogeneous wave equation then reduces to

$$\boxed{\nabla\cdot(c_0^2\nabla p') - \frac{\partial^2 p'}{\partial t^2} = -(\gamma-1)\frac{\partial \dot{q}'}{\partial t}} \tag{3}$$

Under harmonic oscillation assumptions, the pressure fluctuation p' and the heat fluctuation $\dot{q}'$ are expressed as follows [22].

$$p'(\overrightarrow{x}, t) = \Re(\hat{p}(\overrightarrow{x})e^{-i\omega t}) \tag{4}$$
$$\dot{q}'(\overrightarrow{x}, t) = \Re(\hat{\dot{q}}(\overrightarrow{x})e^{-i\omega t}) \tag{5}$$

where $\omega = 2\pi f$. The quantities $\hat{p}$ and $\hat{\dot{q}}$ are complex amplitudes which depend on space only and are related by the so called Helmholtz equation :

$$\begin{cases} \nabla \cdot c_0^2 \nabla \hat{p} + \omega^2 \hat{p} = i\omega(\gamma - 1)\hat{\dot{q}} & \text{in } \Omega \\ + \text{ Boundary Conditions} & \text{on } \Gamma \end{cases} \tag{6}$$

3 Description of the acoustic Tool

When solving eq. 6 for pressure, the combustion term $\hat{\dot{q}}$ must be either known or modeled. If thermoacoustic eigen modes are sought for, $\hat{\dot{q}}$ is considered as a function of the acoustic pressure at some reference position, $\hat{\dot{q}} = \hat{\dot{q}}_{amp}(\hat{p}, \omega)$ so that eq. 6 is an eigenvalue problem which must be solved by using dedicated numerical methods [23]. On the contrary, when dealing with combustion noise the flame is considered as an autonomous acoustic source that generates combustion noise and $\hat{\dot{q}}$ reduces to a fixed forcing term:

$$\begin{cases} \nabla \cdot c^2 \nabla \hat{p} + \omega^2 \hat{p} = i\omega(\gamma - 1)\hat{\dot{q}}_{noise}(\omega) \\ + \text{ Boundary Conditions} \end{cases} \tag{7}$$

For eq. 7 the mathematical problem to solve is a linear system:

$$\underbrace{\mathcal{A}}_{\nabla \cdot c^2 \nabla + \omega^2 I} \underbrace{x}_{\hat{p}} = \underbrace{b}_{i\omega(\gamma-1)\hat{\dot{q}}_{noise}} \tag{8}$$

This Linear system is resolved by the Generalized Minimum REsidual (GMRES) method. This algorithm was chosen mainly due to its portability, simplicity, flexibility and efficiency . GMRES solves large, sparse and non Hermitian linear systems and belongs to the class of Krylov based iterative methods. This is an important feature that allows using only Matrix-vector products when solving eq. 8, instead of storing the full matrix $\mathcal{A}$.

The present numerical tool uses a CERFACS implementation of the GMRES algorithm for both real and complex, single and double precision arithmetics suitable for serial, shared memory and distributed memory computers [24].

4 Experimental Configuration

This article describes the evaluation procedure of noise due to the combustion within a swirled premixed combustor [25, 26] (EC2 Combustor) performing both direct and indirect computations. The experimental

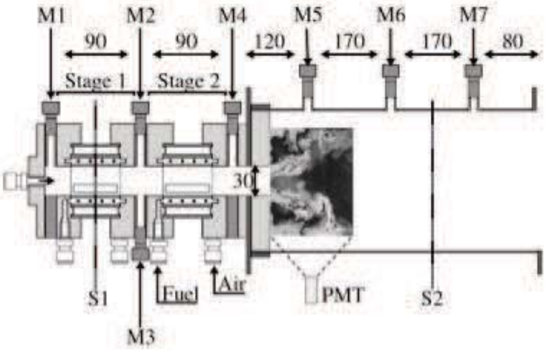

Figure 1: Two staged swirled premixed combustor. (Courtesy of École Centrale Paris)

study is carried out in the laboratory EM2C (École Centrale Paris). The EC2 combustor consists in two geometrical identical stages for air-fuel injection, a premixer and a combustion chamber. The flame is controlled by the Fuel-Air ratio imposed in each of the two stages and stabilized by a swirled premixed. The test rig accounts for 8 different measurement points of pressure (denoted $M1$ to $M7$ in fig.1) placed at equivalent distances along the combustor.

5 Combustion noise Analysis

5.1 Direct Approach

AVBP, developed by CERFACS, is the parallel solver used for the LES computations [27]. In this code, the full compressible Navier Stokes equations are solved on hybrid (structured and unstructured) grids with second order spatial and temporal accuracy. Subgrid stresses are described by the Smagorinksy model. The flame/turbulence interactions are modeled by the Thickened Flame (TF) model [28]. The spatial discretization is based on the finite volume method with a cell-vertex approach, combined to a numerical scheme derived from the Lax-Wendroff scheme. AVBP has been validated/used for a considerable number of configurations.[29, 30, 31]

Two different meshes were used to compute the flow and flame dynamics of the EC2 combustor. The ‘coarse’ mesh has 3 millions of cells whereas the ‘refined’ mesh is composed by 10 million cells. It has been found that both meshes reproduce sufficiently well the results given by PIV measurements when considering mean quantities. This can be observed in fig. 3.

Acoustics and flame dynamics of the system are, on the contrary, more difficult to evaluate than mean quantities. It is known that acoustics in the chamber is directly affected by the flame dynamics since acoustic pressure fluctuations produced by the turbulent flame are closely related to the rate of change in the flame surface area [32]. This rate of change in the flame surface area can be evaluated by computing the rate of change in the heat release produced by the flame [33]. As a consequence, one can expect that the bigger the rate of change of the heat release, the bigger the fluctuations of acoustic pressure produced by the flame. Figure 4 shows the value of the rate of change of heat release integrated over the whole volume of the combustor for the two different meshes. It is clear that by means of the refined mesh a quieter flame is modeled, considering the smaller values of rate of change of heat release in comparison to those obtained from the coarse mesh. As a consequence, one may state that pressure rms values

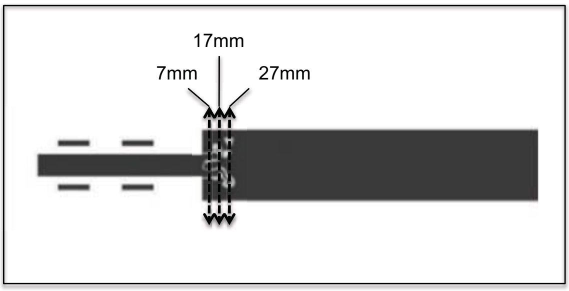

Figure 2: Section cuts for velocity profiles

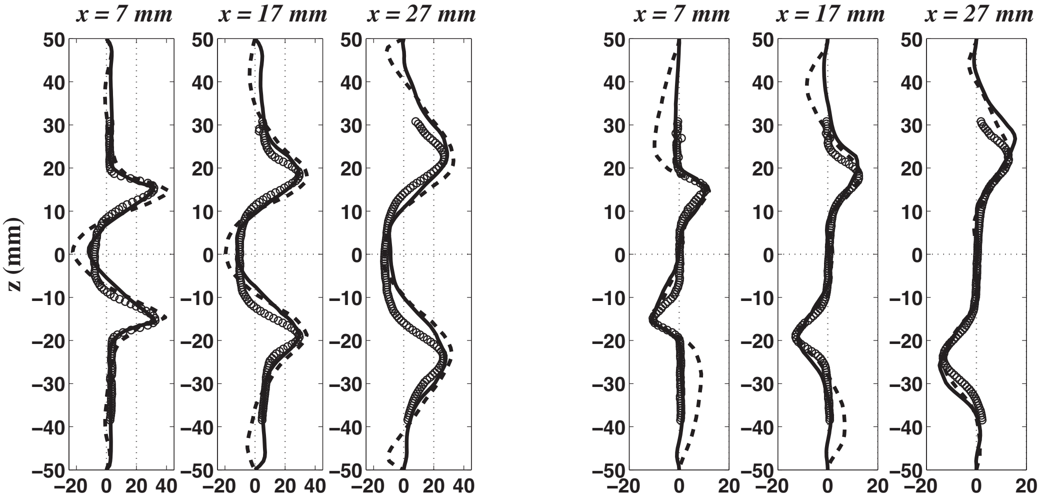

(a) Mean Axial Velocity

(b) Mean Radial Velocity

Figure 3: Velocity Profiles: ○ Experimental PIV measurements
− − − LES 3 million cells, ——— LES 10 million cells

and velocity rms values resulting from the refined mesh should be smaller than those obtained with the coarse mesh. This is supported by fig. 5 which compares the coarse and refined mesh results to the PIV experimental data.

The overall agreement is very good when the refined mesh is used to solve the compressible Navier-Stokes equations and poor when the coarse mesh is used instead. Note also that the computation with the coarse mesh proved unable to reproduce the proper recirculation zone and flame position. Acoustics in the chamber is better characterized by the Sound Pressure Level (SPL) at a given point rather than rms values of the pressure. Figure 6 shows the SPL values at the microphone 7 (see the location of $M7$ in fig. 1) for the computations with the refined and coarse mesh as well as the experimental measurements obtained.

As stated before, computing acoustic pressure fluctuations is very challenging since these values are very small by comparison to the aerodynamic fields. It has been observed that in order to correctly evaluate the dynamics of a flame and the acoustics generated by this one, the resolution of the computation

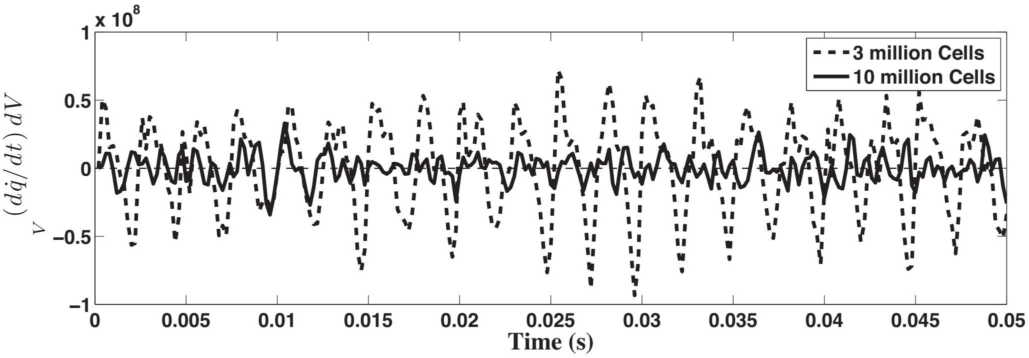

Figure 4: Rate of change of Heat release integrated over the combustor

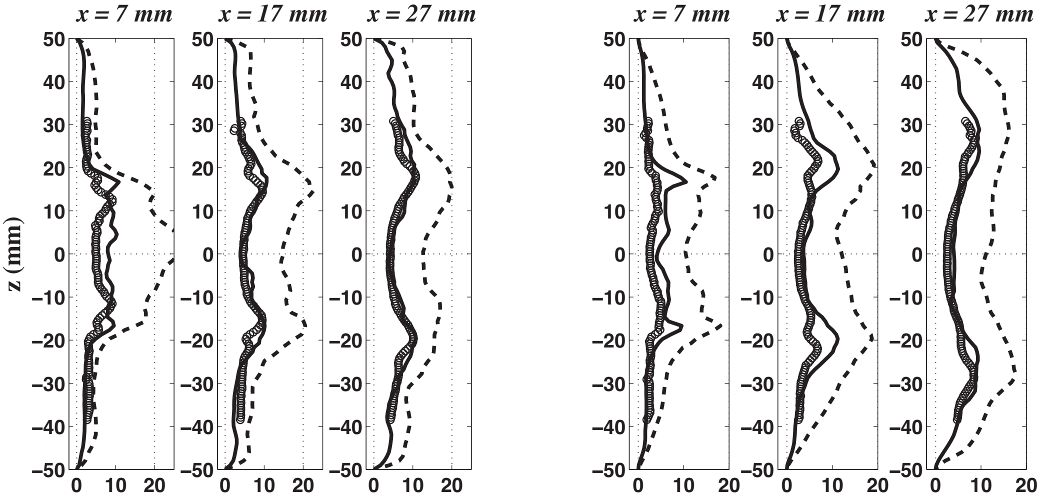

(a) RMS Axial Velocity

(b) RMS Radial Velocity

Figure 5: Velocity Profiles: ○ Experimental PIV measurements
− − − LES 3 million cells, ——— LES 10 million cells

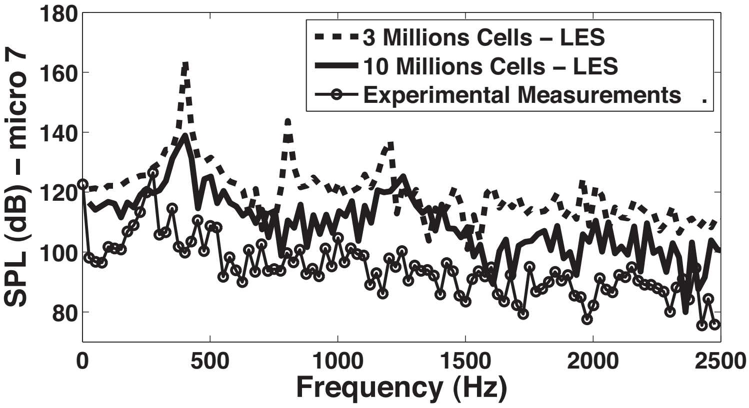

Figure 6: Sound Pressure Level

(resolution of the mesh and order of the numerical scheme) are of significative importance. The gap seen in fig. 6 between experimental results of the acoustic spectrum and the refined LES is problably due to the lack of resolution of the computation. For this purpose, a computation with 50 million cells is currently being conducted.

In the following the acoustic outputs from both direct and hybrid approaches will be compared. This comparison is carried out for the 10 million cells mesh and is independent from experimental data. It is assumed that hydrodynamic pressure fluctuations are small when considering direct approach results. Therefore, the acoustic field resulting from the hybrid approach is expected to be similar to the pressure fluctuation field coming from direct computations. This is further explained in fig. 7.

5.2 Hybrid approach

The hybrid computation accounts for two steps. First, the source of combustion noise is computed by postprocessing the data obtained from the LES computation (instantaneous heat release rate in addition to mean flow parameters taken from the 10 million cells numerical results). Second, the simplified Phillips equation written under the zero Mach number assumption is solved in the frequency domain (eq. 7) .

Overall good agreement is found between both direct and hybrid approaches, as shown if fig. 8 which shows the sound pressure levels obtained for microphones 5 and 7 (see the location of $M5$, $M7$ in fig. 1) .

It is interesting to notice that the hybrid computation succeed in recovering not only the magnitude of the acoustic pressure over almost all the spectrum, but also the shape of the acoustic waves. Figure 9 shows the strongest acoustic wave, the quarter wave mode, that resonates at 377 Hz. From this figure one can state that at this frequency the fluctuation of pressure recovered by the direct computation is almost completely due to acoustics since the pressure wave is clearly a resonant mode.

Observing with more attention fig. 8, it is noticeable that there are still some zones of the spectrum in which an important gap is present between hybrid and direct computations. For Microphone 5 for example, in the region around 1000 Hz, two different types of pressure waves are observed for the direct and hybrid computations (fig. 10). Whereas a pure acoustic standing wave is obtained by means of the hybrid approach, a perturbed pressure wave is obtained in the direct computation results. A pure

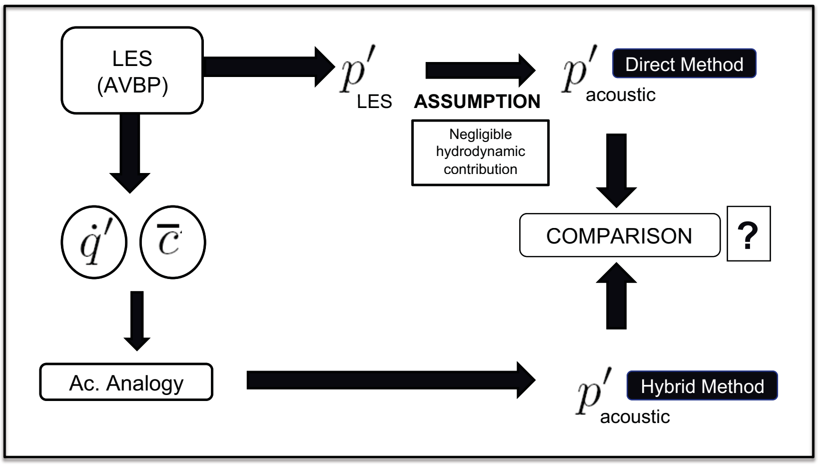

Figure 7: Exercise of comparison: Direct Approach Vs Hybrid Approach

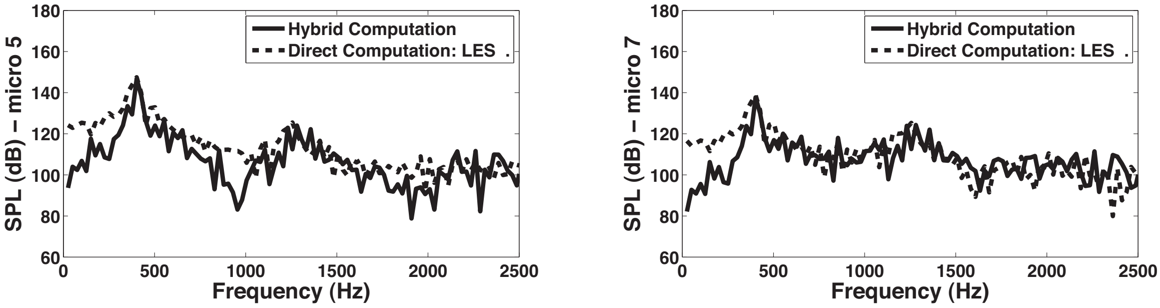

(a) Microphone 5

(b) Microphone 7

Figure 8: Sound Pressure Levels from the direct and hybrid approaches

standing acoustic wave can naturally have an acoustic pressure node. If this pressure node is present close to the region of the measurement device a low value of pressure fluctuation will be obtained. This is what happens for microphone 5 at the zone close to 1000 Hz (fig. 10a). Obviously, when the pressure fluctuations contain not only acoustics but also hydrodynamic perturbations as in the direct computations (fig. 10b), no pressure node can be observed and the resulting SPL is much higher than in the hybrid computation case.

Another difference between the SPL from the hybrid and direct approaches is observed at the two microphones in the very low frequency range. It is probable, considering the direct computation, that the fluctuations of pressure at very low frequencies (before the peak at 377 Hz) are composed by both acoustic and hydrodynamic contributions. On the other hand, presure fluctuations coming from the hybrid computation are totally due to acoustics. This could be the reason why, at low frequencies, the fluctuations of pressure coming from the direct computation are bigger than the ones coming from the hybrid approach.

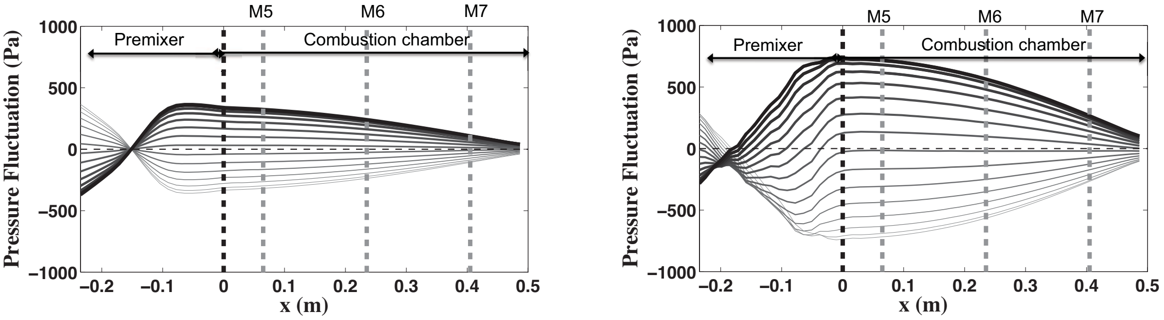

(a) Quarter pressure Wave from eq. 8
Hybrid Computation

(b) Quarter pressure Wave from LES
Direct Computation

Figure 9: Longitudinal pressure Waves oscillating at 377 Hz

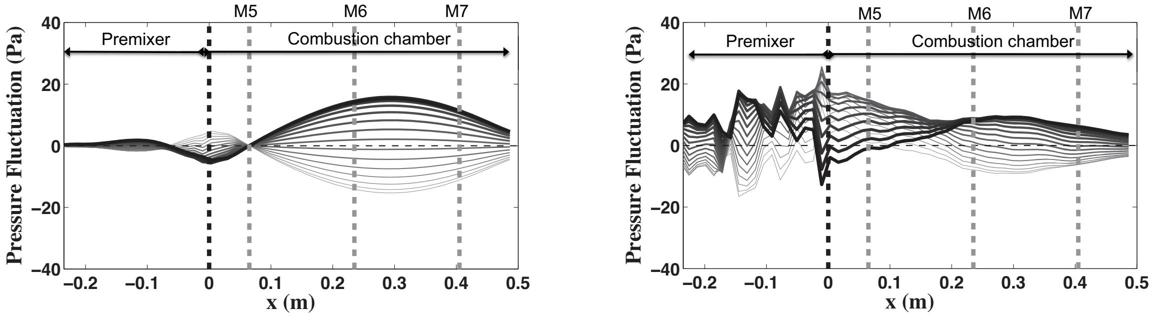

(a) Pressure Wave from eq. 8
Hybrid Computation

(b) Pressure fluctuation from LES
Direct Computation

Figure 10: Longitudinal pressure Waves oscillating at 954 Hz

6 Conclusions

Combustion noise of a premixed swirled combustor has been assessed by two different numerical approaches: a direct computation in which the noise produced by the flame is calculated together with the flow and flame dynamics, and a hybrid computation in which the acoustic field is evaluated apart from the sources of noise.

It has been found that in order to correctly estimate combustion noise by means of the direct computation it is mandatory to have a good resolution in the computation: a bad estimation of the flame dynamics leads to a wrong evaluation of the sound radiated by this one.

The output from the hybrid computation is a pure acoustic field due to the turbulent flame. Good agreement is found in almost the entire SPL spectrum when comparing the results of both direct and hybrid computation. Nevertheless, there are still some differences in specific zones of the spectrum. Hybrid computation results consider pure acoustic waves, and at given frequencies these pure acoustic waves present acoustic nodes that take place close to the acoustic sensor position. This fact leads to a low fluctuation of the pressure at this position and hence, to a low value of the SPL spectrum at these frequencies. At low frequencies, it is probable that the pressure fluctuations coming from the direct approach are composed not only by acoustics but also hydrodynamic fluctuations. This fact affect the comparison with the hybrid computation acoustic results.

Acknowledgments

This work was supported by the Fondation de Recherche pour l'aéronautique et l'espace (FRAE) through the BRUCO project. The authors also gratefully acknowledge the Centre Informatique National de l'Enseignement Supérior (CINES) for giving access to parallel computers and École Centrale Paris for the interesting discussions and experimental data.

References

[1] A. Oberai, F. Roknaldin and T. Hughes "Computation of Trailing-Edge Noise Due to Turbulent Flow over an Airfoil" AIAA Journal, **40** 2206 - 2216 (2002).

[2] D.J. Bodony and S. K. Lele "On the current status of jet noise predictions using Large-Eddy Simulation" AIAA Journal, **46** 364 - 380 (2008).

[3] H. Pitsch and H. Steiner, "Large-eddy simulation of a turbulent piloted methane/air diffusionn flame (Sandia flame D)" Phys. Fluids , **12**, 2541-2554 (2000).

[4] M. Ihme, H. Pitsch and H. Bodony "Radiation of Noise in Turbulent flames" Proc. Comb. Inst., **32**, 1545-1554 (2009).

[5] F. di Mare, W. Jones and K. Menzies "Large eddy simulation of a model gas turbine combustor" Combust. Flame, **137**, 278-294 (2004).

[6] A. S. Lyrintzis "Integral acoustic methods: From the (cfd) near-field to the (acoustic) far-field" Int. J. Aeroacoustics, **2**, 95-128 (2003).

[7] C. Bailly, C. Bogey and S. Candel "Modelling of sound generation by turbulent reacting flows" Submitted to Int. J. Aeroacoustics (2009).

[8] M. Wang, S. Moreau G. Iaccarisno and M. Roger "LES prediction of wall-pressure fluctuations and noise of a low-speed airfoil" Int. J. Aeroacoustics, **3** (2009).

[9] S. Bragg "Combustion noise" J. Inst. of Fuel, **36** 12-16 (1963).

[10] M. J. Lighthill "On sound generated aerodynamically: I. General theory" Proc. R. Soc. London Ser. A, **222** 1 - 32 (1954).

[11] W. C. Strahle "On Combustion Generated Noise" J. Fluid. Mech., **49** 399 - 414 (1971).

[12] S. Kotake "On combustion noise related to chemical reactions" J. Sound Vib., **42** 399-410 (1975).

[13] R. Ewert and W. Schröder. "Acoustic perturbation equations based on flow decomposition via source filtering" J. Comput. Physics, **188** 365 - 398 (2003).

[14] C. Bailly and D. Juvand "Numerical solution of acoustic propagation problems using Linearized Euler Equations" AIAA Journal, **38** 22 - 29 (2000).

[15] M. Roger "Aeroacoustics of wall-bounded flows" Von Karman Institute For Fluid Dynamics. Lecture Series. March 9-13 (2009).

[16] N. Curle "The influence of solid boundaries upon aerodynamic sound" Proc. R. Soc. London Ser. A 231, (1955).

[17] H.G. Davies, J.E. Ffowcs Williams "Aerodynamic sound generation in a pipe" J. Sound Vib., **161** 2 (1981).

[18] C. Schram "A boundary element extension of Curle's analogy for non-compact geometries at low-Mach numbers" J. Sound Vib., **322** 264-281 (2009).

[19] O. M. Phillips "On the generation of sound by supersonic turbulent shear layers" J. Fluid Mech., **9** 1-28 (1960).

[20] F. Williams "Combustion Theory" The Benjamin/Cummings Publishing Company (1985)

[21] H. Hassan "Scaling of combustion-generated noise" J. Fluid Mech., **49** 445-453 (1974).

[22] A. Pierce "Acoustics. An introduction to its physical principles and applications" Chapter 1 (1991).

[23] F. Nicoud et al. "Acoustic Modes in Combustors with Complex Impedances and Multidimensional Active Flame" AIAA Journal, (2007).

[24] V. Frayssé et al. "A Set of GMRES Routines fo Real and Complex Arithmetics on High Performance Computers." CERFACS Technical Report, (2003).

[25] A. Lamraoui et al. "Acoustic reconstruction of the fuel and air feeding line impedances in a swirled burner during combustion instabilites" In *3rd European Conference for Aerospace Sciences EUCASS* (2009).

[26] A. Lamraoui et al. "Methodology for on the fly acoustic characterization of the feeding lines impedances in a turbulent swirled combustor" In *Proceedings of ASME Turbo Expo 2010: Power for Land, Sea and Air* (2010).

[27] AVBP Code: *http://www.cerfacs.fr/4-26334-The-AVBP-code.php* and *http://www.cerfacs.fr/4-25719-Publications.php*, (2010)

[28] O. Colin et al "A thickened flame model for large eddy simulations of turbulent premixed combustion" Phys. Fluids **12**, 1843-1863 (2000)

[29] L. Selle et al. “Compressible Large-Eddy Simulation of turbulent combustion in complex geometry on unstructured meshes” Combust. Flame. **137**, 4, 489-505 (2004)

[30] S. Roux et al. “Studies of mean and unsteady flow in a swirled combustor using experiments, acoustic analysis and Large Eddy Simulations” Combust. Flame. **141**, 40-54 (2005)

[31] S. Mendez and F. Nicoud “Large eddy simulation of a bi-periodic turbulent flow with effusion” J. Fluid Mech., **46**, 2623-2633 (2008)

[32] P. Clavin, E. D. Siggia “Turbulent premixed flames and sound generation” Combust. Sci. Technol. **78** 147-155 (1991)

[33] T. Schuller, D.Durox and S.Candel “Dynamics of and Noise Radiated by a Perturbed Impinging Premixed Jet Flame” Combust. Flame. **128** 88-110 (2002)

[34] T.D. Butler, P.J. O’Rourke “A numerical method for two-dimensional unsteady reacting flows” 16th Symp. (Int.) on Combustion. The Combustion Institute. 1503-1515 (1977)